Cranfield University

Dimitrios Fouflias

An experimental and computational analysis of compressor cascades with varying surface roughness

School of Engineering

PhD. Thesis

Cranfield University

SCHOOL OF ENGINEERING

PhD Thesis

Academic Year 2008-2009

Dimitrios Fouflias

An experimental and computational analysis of compressor cascades with varying surface roughness

Supervisor: Dr. K. Ramsden

March 2009

This thesis is submitted in partial fulfilment of the requirements for the degree of Doctor of Philosophy.

Acknowledgements

I would like to express my deep appreciation to my supervisor Dr Ken Ramsden who helped me to run the compressor cascade project and to write this thesis by giving to me continuous instructions and advises and being always there when I needed his help. He really cares for his students. I will never forget the Saturday morning coffee brake with him, madame Jan and his project students.

Big appreciation I express as well to Prof. Pericles Pilidis who supervised performance parts of the project. I will never forget his gift.

I would also like to acknowledge the R-MC Power Recovery Ltd and their director Paul Lambart for funding this work and their support.

I express many thanks to Dr. Osvaldo Zuniga and to the PhD students and friends Jan Janicovic, Evdoksios Theodoridis, Arian Horoufi and Aiad Gannan who gave me considerable assistance.

In addition, I would like to extend sincere thanks to Prof. Joao Barbosa for his very important advises in terms of my thesis.

Above all, I have to say many thanks to my parents and my brother for supporting me with my studies at Cranfield University.

Abstract

This thesis presents a CFD and experimental analysis associated with the parameter compressor fouling and a CFD analysis associated with the parameter on-line compressor washing of industrial gas turbines.

On-line compressor washing is very popular and quite effective in the industrial gas turbine operational scheme. Many companies apply on-line washing with the engine running at normal speed so as to avoid downtime periods for off-line cleanings that could cause significant economic drawbacks. At this thesis vital parameters affecting compressor cleaning of an industrial gas turbine were examined and combined in such a way so as to provide adequate coverage of the frontal inlet guide vane area which is critical for effective cleaning. The parameters investigated were water injection nozzle position, inclination with respect to the engine centerline, injection velocity and nozzle spray angles.

However, before applying compressor washing, compressor fouling comes into consideration. For this purpose a compressor cascade tunnel (test rig) was designed and come into operation in order to examine different levels of fouling. The cascade test rig involved as well a washing kit for future cleaning of the cascade blades. This work related to the cascade design released a lot of information about designing suction type compressor cascade test rigs by analysing the flow inside the cascade rig computationally and three-dimensionally via CFD tools. The results in terms of the quality of flow obtained for the current test rig were also compared with modified versions of the test rig, one which involved a bigger plenum area behind the cascade test section and one involving the current rig running in a blowing type mode.

The CFD results coming out from the compressor cascade tunnel for the different fouling levels, were analysed in terms of mass flow capacity and polytropic efficiency reduction due to fouling by using Howell's theory (1945) and they were used as inputs for running performance simulation in terms of an industrial gas turbine engine using the performance simulation code Turbomatch. Therefore, a correlation between cascade fouling and real engine uniformly stage spread fouling was achieved. At high levels fouling where the 254 microns roughness height takes place, the non-dimensional air mass flow reduction can reach levels of 1.6% and the drop in compressor efficiency can touch the value of 5%.

The CFD results obtained after running all the simulation scheme for the different roughness levels, were compared to the actual experimental results coming from running the compressor cascade rig with the same fouling scheme of roughness.

Applying Howell's theory (1945), the fouled cascade was correlated to a uniformly fouled stage and a real industrial gas turbine. This time input in the Turbomatch code was the percentage deterioration in compressor efficiency calculated from correlated cascade data. This deterioration reaches a high level of 11 % when the fouling particle size is 254 microns.

Publications

Conferences

Fouflias D., Gannan A., Ramsden K. and Lambart P. CFD evaluation of water injection for industrial compressor washing. Cranfield Multi-Strand Conference, May 6-7, 2008, Cranfield University, UK.

Gannan A., Fouflias D. and Ramsden K. The influence of desert environment on gas turbine compressor fouling. Cranfield Multi-Strand Conference, May 6-7, 2008, Cranfield University, UK.

Fouflias D., Gannan A., Ramsden K. and Pilidis P. CFD predictions of cascade pressure losses due to compressor fouling. ASME Turbo Expo, Orlando, USA, June 8-12, 2009, GT2009-59158.

CONTENTS

List of figures

List of tables

Notation

a_1: cascade flow inlet angle
a_2: cascade flow outlet angle
$a_1^{'}$: cascade blade inlet angle
$a_2^{'}$: cascade blade outlet angle
a: Distance of maximum camber from the leading edge
A_{wire} : Wire surface area exposed to the fluid flow
$A^{'}, B^{'}$: Empirical constants
A : Cascade inlet cross sectional area
A : Cascade settling chamber cross sectional area
A_1: Inlet passage area
A_2: Outlet passage area
A_1 : Cascade test section inlet cross sectional area
A1: 1st rotor inlet cross sectional area
A2: First stage exit annulus area
A_{IGV} : Inlet guide vane annulus area
Aann: 1st rotor exit annulus area
A/D: Analog/digital
b: y-distance of maximum camber from the leading edge
B1: 1st rotor blade height
BS: British standard
c_m : Mean flow velocity
c_p : Specific heat at constant pressure
C_a : Axial air velocity
c_x : Axial velocity
c_1 : Cascade blade inflow velocity
c_1 : Cascade blade inflow velocity or rotor inlet absolute velocity
c_2 : Rotor exit absolute velocity or cascade blade outflow velocity
c_2: Cascade blade outlet velocity or rotor exit absolute velocity
c: Blade chord
c_3 : Stator exit absolute velocity
C_L : Lift coefficient
C_{Dp} : Blade profile drag coefficient
C_{Dp}: Cascade blade profile coefficient
C_D : Overall drag coefficient
C_{Da} : Drag coefficient related to wall annulus friction losses
C_{Ds} : Drag related to secondary losses
Cp: Specific heat at constant pressure
C_w : Wire heat capacity
C_0 , C_1, C_2, C_3, C_4 : Hot wire anemometer calibration constants
C_μ : Empirical constant (=0.09)
CFD: Computational Fluid Dynamics
CTA: Constant temperature anemometer

CW: Compressor power
d : Wire diameter
$\partial p / \partial r$: Pressure gradient
D : Drag force per unit blade depth
Dt1: 1st rotor tip diameter
Dhr1: 1st rotor hub diameter
Dmr1: 1st rotor medium diameter
Dt_{IGV}: IGV tip diameter
$Dhub_{IGV}$: IGV hub diameter
Dhr2: 1st rotor exit hub diameter
Dt2: 1st rotor exit tip diameter
Dmr2: 1st rotor exit medium diameter
e_n : Normal coefficient of restitution
E : voltage
E : Empirical constant (=9.793)
f_c : Cut-off frequency
f_r : Roughness function
f: Gas turbine operating frequency
g : gravitational acceleration
h_1 : Rotor inlet static enthalpy
h_{01} : Stagnation enthalpy at the rotor inlet
h_{01rel} : Rotor inlet relative stagnation enthalpy
h_2 : Rotor exit static enthalpy
h_{02} : Rotor exit stagnation enthalpy
h_{02rel} : Rotor exit relative stagnation enthalpy
h_3 : Stator exit static enthalpy
h_{03} : Stator exit stagnation enthalpy
h_{03s} : Stator exit stagnation enthalpy (isentropic)
h : Manometer reading at pressure p
h_{conv} : Convective heat transfer coefficient
h_a , h_b , h_c , h_d : Manometric heads of holes a, b, c and d respectively
$h_a^{'}$, $h_b^{'}$, $h_c^{'}$ and $h_d^{'}$: Manometric heads for a probe inclined in a parallel flow
$h_m^{'}$ Pressure head at hole m of a frictionless sphere in potential flow lying at an angle (β_m) in the direction of the parallel flow
H : Blade height
i: Incidence
i^* : Nominal incidence
i : Probe hole number
I : Current through the circuit
k_n : 5-hole yaw probe pressure recovery factor of hole n
k_0 : 5-hole yaw probe pressure factor
k_δ : 5-hole yaw probe inclination factor
k_i : 5-hole yaw probe hole pressure coefficient

k_β : 3- hole yaw probe direction coefficient

k_t : 3-hole yaw probe total pressure coefficient

k_s : 3-hole yaw probe static pressure coefficient

$\bar{k}$: Mean hole coefficient

k_s : Equivalent sand grain roughness

k'_i : Local weighted coefficient

k : Turbulence kinetic energy

k : Turbulent kinetic energy or fluid thermal conductivity

K : Dimensionless inclination factor

K_s : Roughness height

K_L : Cone loss coefficient

K_{B1}: 1st stage rotor exit blockage factor

K_{B2}: 1st stage exit Blockage factor

K_{Bexit}: Compressor exit blockage factor

l : Blade chord or sampling length

L : Lift force per unit blade depth

m : A variable in deviation (δ) rules

$\dot{m}$: Mass flow rate

m_{inlet}: Cascade inlet mass flow

M_{IGV} : Mach number on the IGV plane

M : Mach number

Ma: Rotor inlet axial Mach number

Mo: Rotor inlet absolute Mach number

M1: Rotor inlet relative Mach number

M_1 : Cascade inlet Mach number one chord upstream of the blades

M3: 1st rotor absolute exit Mach number

MRF: Multiple reference frame model

n_s : Stage efficiency

n_{tt} : Total to total stage efficiency

$n_{isentropic}$: Isentropic stage efficiency

n_c: Compressor overall efficiency

N: Shaft speed

N : Number of samples

Nu : Nusselt number

p: Static pressure

p : Static pressure

p_s : Static pressure

p_{IGV} : Static pressure on the IGV plane

p_{IGV} : Static pressure on the IGV plane

p_0 : Total pressure

p_o : Static pressure for a probe inclined in a parallel flow

p_i : Pressure sensed by hole i

p_t : Total pressure

$\bar{p}$: Mean hole pressure

p_1 : Cascade inlet static pressure one chord upstream or rotor inlet static pressure

p_1: Cascade inlet static pressure one chord upstream of the blades

p_{01rel} : Rotor inlet relative total pressure

p_2 : Cascade outlet static pressure

pstatic2: 1st stage outlet static pressure

p_2 : Rotor exit static pressure or cascade exit static pressure

p_{02} : Rotor exit total pressure

p_{02rel} : Rotor outlet relative total pressure

p_3 : Stator exit static pressure

p_{03} : Stator exit total pressure

p_n : Static pressure of hole n

P: Total pressure

P_{st} : Static pressure factor for probe hole 2

P_{stat} : Static pressure

P_{F1} : Flange total pressure

P_{IGV} : Total pressure on the IGV plane

P_t : Total pressure

P_{inlet}: Cascade tunnel inlet total pressure

P_1 : Cascade inlet total pressure one chord upstream

P_1: Cascade inlet total pressure one chord upstream of the blades

P1: 1st stage inlet total pressure

P_2 : Cascade outlet total pressure one chord downstream towards the exit flow streamtube or pressure of hole 2 of a five-hole yaw probe

P2: 1st stage exit total pressure

P_2 : Cascade outlet total pressure

P_2 / P_1 : Compressor pressure ratio

P3: 1st stage rotor exit total pressure

Pamb: Ambient pressure

Pr : Prandtl number

PR: Pressure ratio

PR : Pressure ratio

q : Dynamic head

Q : Heat transferred to the surroundings

Q_i : Thermal energy stored in the wire

r : Distance from the axis of rotation

Re:Reynolds number based to inlet velocity and chord length

R : Stage reaction

R_1, R_2: Fixed resistors

R_3: Variable resistor

R_w : Hot-wire probe resistor

R_w : Wire resistance

R_0 : Sensor (cold) resistance at ambient reference temperature T_0

R_{20} : Sensor resistance at 20^{o}C

R_{leads} : Probe leads resistance

$R_{\sup port}$: Resistance of the connection leads in the probe support

R_{cable} : Cable resistance

$R_{tot,0}$: Measured total resistance

$R_{\text{var}iable}$: Variable resistance

$R_x(\tau)$: Auto-correlation function

Ra : Roughness parameter

Rc: Overall pressure ratio

R: Ideal gas constant or stage reaction

Rstage1: 1st stage pressure ratio

SMM: Sliding mesh model

SST: Shear Stress Transport

t: Blade thickness

t : Time

t_1 : Cascade inlet static pressure one chord upstream of the blades

t_{IGV}: IGV face static temperature

T : Total temperature or total sampling time

T_0 : Wire reference temperature

T_1 : Integral time scale

T_1 : Cascade test section inlet total temperature

T1: 1st stage inlet total temperature

T_1 : Cascade inlet total pressure one chord upstream of the blades

T_2 : Rotor exit static temperature

T_2 / T_1 : Compressor total temperature ratio

T2: 1st stage exit total temperature

T3: 1st stage rotor exit total temperature

T_{03} : Stator exit stagnation temperature

Tamb: Ambient temperature

Texit: Compressor exit total temperature

T_{inlet}: Cascade tunnel inlet total temperature

T_w : Wire temperature

Tu : Turbulence intensity

T_s : Static temperature

TET: Turbine entry temperature

TW: Turbine power

u_τ : Friction velocity

u_P : Mean fluid velocity at point P

υ : Velocity vector magnitude

υ_o : Velocity vector magnitude for a probe inclined in a parallel flow

υ_θ : Tangential velocity

$\upsilon^2 / 2g$: Velocity head

U_{tip} : Blade tip velocity

U : Mean blade radius speed or fluid velocity

U_{mean} : Mean velocity

U_i : Instantaneous velocity

U_{rms} : Standard deviation of velocity

U : Mean air velocity or blade speed

Umr1: 1st rotor inlet mean blade speed
Umr2: 1st rotor outlet mean blade speed
UW: Useful power
v: Element velocity
V : Air velocity
$V_{12}, V_{14}, V_{13}, V_{15}$: Dimensionless velocity coefficients
$V_{2,n}$: Particle velocity normal to the wall after collision
$V_{1,n}$: Particle velocity normal to the wall before collision
Vo: 1st rotor absolute inlet velocity
Va1: Rotor inlet mean axial velocity
Va2: 1st rotor exit axial velocity
V1: Relative rotor inlet velocity
V2: 1st rotor relative exit velocity
V3: 1st rotor absolute exit velocity
V4: 1st stator exit flow absolute velocity
Vw0 : Absolute rotor inlet whirl velocity
Vw1: Relative rotor inlet whirl velocity
Vw2: 1st rotor relative exit whirl velocity
Vw3: 1st rotor absolute whirl velocity
w_1 : Rotor inlet relative velocity
w_2 : Rotor exit relative velocity
w_n : Tangential velocity at hole n of the yaw probe
w : Air flow velocity or test section mass flow rate
w: Flow velocity vector magnitude or angular velocity
w_1, w_2, w_3 : Normal velocity components for holes 1, 2 and 3 of a three-hole yaw probe
W : Power generated by heating the wire
W: Mass flow
W_1: Cascade inlet mass flow
$W_1T_1^{0.5}/P_1$: Compressor non-dimensional mass flow or cascade non-dimensional mass flow
x: x-distance from leading edge of maximum blade thickness
$x(t)$: Infinitely long time record
X : Axial force
X : Referred total pressure loss coefficient
y^+ : Wall y plus
y_P : Distance from point to the wall
y: Distance to the wall

Y : Aerodynamic total pressure loss coefficient or tangential force
$z(x)$: Absolute departure of the roughness profile from the mean line
$a_1^{'}$: Cascade blade inlet angle
$a_2^{'}$: Cascade blade outlet angle
a_1 : Cascade inlet flow angle
a_2 : Cascade outlet flow angle
α_1: Blade inlet flow angle
α_2: Blade outlet flow angle
α_1 : Cascade inlet flow angle
α_2 : Cascade outlet flow angle
α : Pitch angle
a : Overheat ratio
α_{20} : Temperature coefficient (at 20^{o}C)
α_2': Blade outlet metal angle
α_2*: Nominal outflow angle
a_r : Ratio of Reynolds shear stress to turbulent kinetic energy
α_m: mean cascade flow angle
α_m: Cascade blade mean flow velocity
α_m : Mean flow angle
α1: Relative rotor inlet air angle
α2: 1st rotor relative exit flow angle
α3: 1st rotor absolute exit flow angle
α4: 1st stator exit flow angle
α0: IGV outflow absolute blade angle
α'0: IGV outlet blade metal angle
α'1: Rotor blade inlet metal angle
α'2: Rotor outlet blade metal angle
α'3: Stator blade inlet metal angle
α'4: Stator outlet blade metal angle
β_1 : Flow inlet angle
$\beta_1^{'}$: Inlet blade metal angle
β_2 : Flow outlet angle
$\beta_2^{'}$: Outlet blade metal angle
β_2^{*} : Nominal outflow angle
β_m : Blade mean flow angle
β : Yaw angle
γ : Conical angle between the pressure hole and the probe axis or specific weight or ratio of specific heats
γ_0 : Identical to the conical angle ϕ
γ'0: IGV blade inlet metal angle
γ0: IGV blade inlet flow angle
γ_n : Angle between the velocity vector and any *nth* pressure hole radial line
δ: Deviation angle

δ : Dihedral angle between the flow plane and the meridian plane or Angle between the normal and the inclined position of the stem or 3-hole yaw probe wedge angle
δ*: Nominal deviation
δ^* : Nominal deviation
δ1: IGV blade deviation
δ2: Rotor blade deviation
δ3: Stator blade deviation
$\Delta H/(Umr2)^2$: Stage loading coefficient
$\Delta I=\eta_{pclean}-\eta_{pfouled}$: Deterioration in polytropic efficiency
Δm: Deterioration in cascade mass flow
Δp_0 : Total pressure loss
Δp_{0rotor} : Rotor total pressure loss
$\Delta p_{0stator}$: Stator stagnation pressure loss
Δp : Stage static pressure rise
$\Delta P_s / 0.5\rho U^2$: Stage pressure rise coefficient
ΔP_s : Stage static pressure rise
Δpstatic: Cascade static pressure increase
Δp_0: Cascade total pressure loss
Δpo: Cascade total pressure loss
ΔTc : Compressor temperature rise
ΔT_t : Stage total temperature increase
ΔT_s : Stage total temperature rise
ΔTc: Compressor temperature rise
ΔTstage: Stage temperature rise
ΔW : Actual work
$\Delta(W_1T_1^{0.5}/P_1)$: cascade deterioration in non-dimensional mass flow due to fouling
$\Delta\beta$: Yaw angle
ε: blade deflection
ε*: Nominal deflection
ε^* : Nominal deflection
ζ : Stagger angle
ζ : Total pressure loss coefficient
ζ_S : Stator total pressure loss coefficient
ζ_R : Rotor total pressure loss coefficient
ζ1: IGV stagger angle
ζ2: Rotor stagger angle
ζ3: Stator stagger angle
η_c : Compressor isentropic efficiency
η_c : Compressor overall efficiency
η_p: polytropic efficiency
η_s: Stage efficiency
η_t : Turbine isentropic efficiency
η_{th} : thermal efficiency
θ: Camber angle
θ : Camber angle

θ1: IGV camber angle
θ2: Rotor camber angle
θ3: Stator camber angle
θ_n : The angle between the velocity vector and the radial line through the nth pressure hole of a 5-hole yaw probe
κ : Von Karman constant (=0.4187)
λ: Work done factor
λ_s: Spacing parameter
μ : Dynamic viscosity
μ_t : Turbulent viscocity
v_i : Local velocity
ν_t : Turbulence viscosity
ξ: Stagger angle
ρ: Air density
ρ : Fluid density
ρ_s : Density at entrance to the stage
$\rho_x(\tau)$: Autocorrelation coefficient function
τ : Turbulent shear stress
τ_w : Time constant
τ_w : Wall shear stress
ϕ : Flow coefficient or conical angle between the velocity vector and the probe axis
Φ : Flow coefficient
Ψ^T : Stage work coefficient
ψ : Stage loading coefficient
ψ: Stage loading coefficient
ψ : Five-hole probe yaw angle or angle between the vertical plane and the meridian plane
$\overline{\omega}$: Total pressure loss coefficient
ω: Total pressure loss coefficient or turbulence energy dissipation
ω : Blade profile total pressure loss coefficient
Ω : Vorticity tensor

Chapter 1 - Introduction

1.1 Overview

Gas turbines consume large quantities of air which contain foreign particles that stick on the blades of the compressor causing the phenomenon of fouling. These undesirable deposits on the blades cause an increase of the blade surface roughness and boundary layer thickening which leads to reduction of the air mass flow through the gas turbine engine. The mass flow reduction causes compressor pressure ratio degradation and it's isentropic efficiency goes down as well. In order to avoid all these negative effects and to combat fouling, manufacturers apply compressor cleaning off-line and on line, where off-line washing is defined by no fuel being burnt during the washing process while with on line washing the engine is firing fuel.
In the present study, the effect of cleaning on the performance of axial compressor stages is to be investigated. This will be achieved through a series of two-dimensional cascades experiments. The focus of the research programme will include the effects of surface roughness by reproducing fouling conditions found in the compressors of many gas turbine engines. In order to analyse the effects of cleaning, a suction test rig is under construction split in two parts, the blade cascade part and the washing system part. Beginning with the blade cascade part, this comprises an intake flare, a blade test section with nine two-dimensional blades of NACA 65 profile, a plenum chamber, an exit cone and a centrifugal fan.
The design of the cascade part took into consideration all the main parameters necessary for design like ambient pressure and temperature, pressure loss in the intake, de Haller number, blade test section boundary layer effects, space/chord ratio, nominal deviation, nominal outflow angles, streamlines direction and test rig air mass flow rate. Another parameter taken into consideration very carefully was the positioning of the pitot pressure tube in the cascade tunnel. In addition, an appropriate yawmeter has been identified for flow pressure and velocity measurements in the air-stream. These measurements will be made both upstream and downstream of the cascade blades.
The washing system already constructed involves a piston pump, a driving motor and an injection nozzle arrangement. This has been used for on-line compressor cleaning of an industrial Alstom Typhoon gas turbine of low power output. For the setting of this washing system all the necessary characteristics have been taken into account. For example, the positioning of the injection nozzle, droplet sizes, system operating pressure, nozzle type, washing fluid mass flow rate, injection velocity and spray angle. Also, the cleaner used for this washing system was a water based cleaner provided by the R-MC Power Recovery company.
In order to understand better the parameters influencing compressor cleaning of an industrial gas turbine, several simulations took place using an intake of an ABB GT13 D2 gas turbine (98MW). In this case water injection has been applied, using various droplet diameters, droplet injection velocities and nozzle positions.
Based on the data obtained for this industrial gas turbine intake, simulations have also been run involving the current cascade test rig arrangement. However, for the cascade test rig of this project, in order to apply blade cleaning, blade fouling is planned. For

this purpose, the blades have to be coated with some kind of contaminants uniformly spread on the blade surfaces. Initially, the cascade test rig will be run with clean blades. Subsequently, fouled blades will be tested and finally, the impact of washing will be investigated.
The current project will involve several steps. Initially, for example, fixed cascade blades at a nominal incidence angle of zero degrees will be chosen. In particular, the inlet and outflow air angles will be measured. The initial clean blade measurement programme will include variation of the mass flow rate. The corresponding changes in Mach number and exit flow direction will be recorded. At the same time, the blade chord Reynolds number will be calculated so that an accurate assessment of the boundary layer state over the cascade blades can be established. The latter is vital in the understanding of the role of the boundary layer in the penetration of cleaning fluid. This is, of course, important in understanding the subsequent effectiveness of the washing (wetting) process. The measured loss of stagnation pressure across the cascade blades will lead to an assessment of the profile losses. The latter will lead to an assessment of profile drag coefficient of the cascade blades.

1.2 Project objectives

The aims of the current research are as follows:

- Investigating via CFD tools the parameters affecting the water coverage of the inlet guide vane frontal area of an industrial gas turbine subjected to on-line compressor washing and trying to combine them in such a way so as to achieve optimum coverage.
- Analysing designing aspects of suction type compressor cascade tunnels.
- Taking cascade measurements of pressures, flow velocities and outflow angles at certain intake Mach number level for clean and fouled cascade blades.
- Investigating a correlation between fouled cascade and fouled actual gas turbine engine.
- Checking the effect of fouling in terms of gas turbine performance.

1.3 Thesis structure

The current thesis structure has been divided in several chapters.

Chapter 2 presents the literature review done for the theoretical bases of the current project. Informations from several researchers in the same field of study is presented in this chapter.

Chapter 3 presents a computational study using CFD tools for an industrial ABB GT13 D2 gas turbine intake and its front stage subjected to water injection. This study focuses on the water concentration in front of the first stage of the engine in order to check for adequate water coverage of this area and therefore effective cleaning using different nozzle position arrangements. Also, in this chapter the water droplet flow in

the area of the first stage of the gas turbine has been analyzed and possible existence of intake air swirl has been examined.

Chapter 4 involves all the considerations and calculations that have been taken place for the design of the cascade test rig of the present project. It involves information about the instrumentation and the washing kit that will be attached on the rig, as well.

Chapter 5 presents all the necessary preliminary CFD simulations done in order to examine the flow in the volume of the cascade test rig. The effect of plenum chamber attached on the rig was analyzed and the pressure and velocity distributions in specific areas of the rig were investigated. The cases of increasing the plenum chamber of the test rig and running the rig in a blow type mode were investigated, as well.

Chapter 6 involves CFD simulations done by applying roughness on the blades of the cascade test rig. The effect of roughness on the velocity, total pressure loss and exit flow angles at one chord distance behind the blades towards the cascade exit flow streamtube has been analysed. A correlation between the cascade results and a real industrial gas turbine ABB GT13 E2 has been used in terms of polytropic efficiency and mass flow capacity degradation due to fouling. Performance results in terms of the gas turbine ABB GT13 E2 were obtained using the performance simulation tool Turbomatch developed in Cranfield university.

Chapter 7 presents experimental results obtained from the cascade test rig of the current project. These results are compared to the CFD results obtained using the experimental boundary conditions. Also, a correlation between cascade results and a real engine stage and engine performance is established applying Howell's theory and the Turbomatch code for various fouling cases examined.

Chapter 8 gathers all the conclusions and recommendations which have been arrived at the findings of the present study.

1.3 Previous and current research

1.3.1 Compressor fouling and on-line compressor washing

This project has established its basis on the research done by the Gas Turbine Performance Engineering group of Cranfield university in the last ten years in terms of on-line compressor washing. The company supporting this research is the R-MC Power Recovery Ltd. Three previous PhD researches were done in terms of on-line compressor washing and compressor fouling. Mund (2006) analyzed the water droplet distribution in front of the inlet guide vane area of an industrial compressor and Mustafa (2005) analysed the water droplet trajectories in an axial compressor. Zuniga (2007) analyzed in parallel the parameters compressor fouling and on-line compressor washing.
The current research associated to this project has been done under the supervision of Doctor Ramsden and Professor Pilidis. The experimental work was done with the contribution of Aryan Horoufi (PhD-candidate) and the technical support of Paul Lambart, Jonathon O'Donnell, Ross Gordon and Andy Lewis from the R-MC Power

Recovery Ltd. The performance part of the project in terms of using the Turbomatch code of Cranfield university took place under the supervision of Jan Janicovic (PhD candidate). Significant support in terms of the CFD analysis was given by Doctor Rubini and Doctor Joao Texeira.

1.3.2 Application software and programming languages

The two-dimensional design of the compressor cascade test rig geometry of the current project was achieved by using the 2007 version of the design package AUTOCAD. The three-dimensional design of the rig involved the version 11 of the design package I-DEAS.
A commercial CFD package Fluent 6.3 was used for developing the computational solution for the cascade geometry of the current project. This CFD package gives the ability to analyze flows associated with complex geometries in two and three dimensions incorporating structured and unstructured meshes using the preprocessor Gambit 2.4.
The program Turbomatch written in Fortran and developed in Cranfield university was used for the gas turbine performance simulation. This program can handle different engine configurations thermodynamically. It involves nine compressor and nine turbine maps using them for design and off-design engine performance calculations. Scaling factors can be applied to these maps in terms of efficiency and mass flow capacity in order to simulate performance deterioration which in this case of the project is caused by the parameter roughness. Special routines called “bricks” are used in order to handle these scaling factors. After running the performance simulation code the results obtained are mainly engine power output, compressor pressure ratio, compressor and turbine efficiency and fuel consumption.
The version 5.0 of the programming language Visual Basic was used to acquire the whole pressure readings coming out from the instrumentation attached on the cascade test rig of the current research and the version 6.0 for acquiring hot-wire anemometer data originated from the intake area of the cascade arrangement.
The version 6.1 of Matlab was used in order to post-process the data coming out from the hot-wire anemometer equipment as far as air flow mean velocity and turbulence intensity is concerned.

1.4 Study contribution

The work done on this research project will illustrate for the first time CFD and experimental information about the mechanism of fouling and the correlation between fouled cascade and fouled gas turbine engine in terms of performance. Also, the results of this project will give some further aspects in terms of optimising on-line compressor washing and significant contribution in terms of designing suction type compressor cascade test rigs.

Chapter 2 - Literature

2.1 Compressor fouling

Before analysing the effects of cleaning on axial compressors the reason that leads to the need for compressor cleaning must be analysed first which is the parameter fouling. Nowadays the competitive gas turbine market for power and propulsion generation leads the gas turbine operators to the direction of maximizing and controlling the performance deterioration. Deterioration problems arise for many reasons and one that is very important is the compressor fouling. Compressor fouling is caused from impurities present in the air flow that stick on the blades and vanes changing their aerodynamic profile and causing compressor mass flow and pressure ratio reduction, which lead in significant drop in terms of efficiency and power output.

The mass flow reduction happens due to the fact that the deposits on the blade surfaces cause an increase of the surface roughness of the initially polished blades and this increase in roughness causes boundary layer thickening which finally leads to reduction of the compressor passage cross sectional area and engine mass flow rate.

The fouling problem comes out to be more intensive in terms of the gas turbines used for power generation where high levels of intake air mass flow are involved.

According to Bromley et al (2004), output losses range between 2% and 5% under favourable conditions and 15% to 20% under adverse conditions.

The aerodynamic performance of each stage of an axial compressor depends on that of the earlier stages, so fouling on the first stages which are usually fouled the worst can have a significant negative effect in performance of the whole compressor unit.

The size of the fouling particles extends up to 10 microns, but sizes above 10 microns up to 20 microns can cause blade erosion according to Bromley et al (2004). Also, the high temperatures involved in compressors cause air impurity deposits to be baked on which make them difficult to remove.

However, even if high quality inlet filtration systems have been fitted in order to prevent gas turbine fouling, fouling inevitably occurs and compressor washing needs to take place in order to remove it as much as possible.

In majority, the fouling deposits on compressor blades of the gas turbines are usually mixtures of water wettable, water soluble and water insoluble materials. According to Stalder (2001) pH values of 4 and even lower have been found on fouling materials existing on compressor blades indicating the danger for blade corrosion. These materials, if not subjected to washing, are bonding continuously on the blade surfaces as the time passes and at the end it is very difficult to be removed.

Water soluble deposits can cause corrosion since they are hydroscopic or contain chlorides. Water insoluble deposits are organic such as hydrocarbon residues or from silica.

Gbadebo et al (2004) performing experiments on a large-scale single stage low speed compressor and on a single stator by applying roughness only on the vanes using strips of emery paper, observed that when roughness is applied from the leading edge up to peak suction (20% chord) all the way through the span it has significant negative effect on the performance of the compressor stage while when it is applied downstream of the suction peak the stage seems to be almost insensitive. In terms of

his experiments on the single vane roughened from leading edge to peak suction, he illustrated, using oil flow visualisation, large hub corner separation at the design flow coefficient which gave high total pressure loss at the exit of the vane and increased exit flow angle deviation, however the vane was almost unaffected when roughness applied at mid chord and towards the trailing edge performing in a similar level as the smooth blade. The results of the author illustrating which part of the blade is more sensitive to fouling, give a good hinge to the researchers involved in compressor washing to understand where the blade suffers in terms of performance when fouling presents and where on the blade surface washing must be more effective.

2.2 Compressor cleaning

Nowadays compressor washing can be obtained via regular cleaning. The cleaning techniques that are usually applied for regular compressor cleaning are the off-line and online cleaning and in order to achieve optimum levels of compressor cleaning, a program involving systematic online washing and periodic off-line washing is recommended.

2.2.1 Online compressor washing

The main scope of online compressor washing is to maintain a level of cleanliness for the compressor which however is not as high as the level approached by cleaning the compressor off-line. The reason for online cleaning is attributed to the need for minimising the shutdowns of the gas turbine that have serious economic effects especially for gas turbine power plants. In other words online cleaning extends the period between shutdowns required for off-line cleaning and minimises the revenue that would be lost since the gas turbine continues to operate during the cleaning process producing power.
Online cleaning is performed while the gas turbine is running at full load via injection of washing fluid from atomizing spray nozzles positioned around the air intake duct of the gas turbine. Usually online washing involves the use of particular detergents but sometimes the cleaning is performed by applying just water if the deposits are water soluble. The frequency of online washings is very important and the time intervals between washings are kept short such as one washing every third day of gas turbine operation during the week. The duration of online cleaning cycles ranges from ten to twenty minutes depending on the degree of fouling and if detergent is used a rinse cycle of the same duration follows employing only demineralised water.
Online washing cannot be as effective as off-line washing and this can be attributed to many reasons. One of them is that the centrifugal forces existed in the compressor rotor unit rotating at high speed enforce the cleaning fluid to move towards the outer periphery (casing) and as a result most portion of the span of the blades cannot be cleaned. In addition, the velocity of the air in the compressor is so high that the residence time of the cleaning fluid in the compressor is very short. Another reason explaining why the online cleaning is not as complete as the off-line cleaning is the temperature rise inside the compressor of the running engine which causes cleaning liquid to start boiling about halfway through the compressor (Carl Hjerpe 2004). Also,

the turbulence levels existing in running conditions result in washing fluid being lost on the duct walls before reaching the compressor.
One can realise how important is the online washing with just a small example reported by Stalder (2001) of compressor blade inspection after one month operating period which involves compressor washings every four days (see figure 2-1).

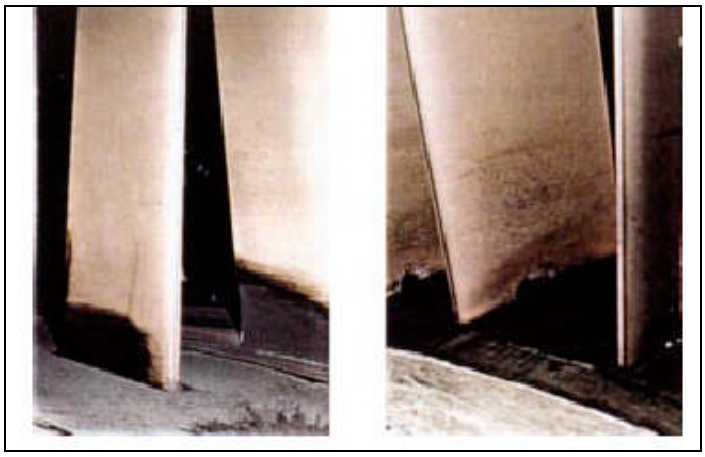

Figure 2–1: Fouling deposits on the root and tip of a compressor First stage guide vanes, subjected to online washing every four days during a period of about one month (Stalder, 2001).

From figure 2-1 it is obvious that the frequent online washings prevented the severe fouling of the compressor front stage vanes leaving only an increment of fouling on the surface areas close to the tips and the roots where fouling is more difficult to be removed due to boundary layer effects.

2.3 Cleaners

The cleaning fluids used for compressor washing comprise water and kerosene with or without an emulsifier, solvent based cleaners and water based cleaners. The more commonly used are the water based cleaners which are solutions of detergent in water containing sometimes corrosion inhibitors. They are diluted with water (1 plus 4 parts water) before usage, they contain little amount of solvent and mainly they are not flammable. They tend to freeze at about 0 ^{o}C and for this reason anti icing agents are added. In the mean time another one advantage of water based cleaners is that they are biodegradable.
The corrosion inhibitors contained in water based cleaners even if they neutralize the influence of salts on the compressor blades, they tend to form a film on the blades which sometimes, during online cleaning, produces a decomposed deposit at about 200^{o}C in the middle part section of the compressor.
Depending on the nature of the fouling deposits hence if they are water wettable or water soluble, sometimes online washing is performed with water alone. However, if there are water insoluble deposits then cleaning with just water is quite dangerous since the insoluble material will not be washed off and the fouling deposits will further built up especially in the front stages of the compressor.

2.4 Injection systems for compressor washing

The design characteristics of the cleaner injection systems involve:

- Positioning of the nozzles
- Droplet size
- System operating pressure
- Type of nozzles
- Washing fluid mass flow rate levels
- Injection velocity
- Spray angle

2.4.1 Positioning of injection nozzles

The positioning of the injection nozzles with respect to the gas turbine intake is of main importance in order to obtain uniform wetting and efficient removing of fouling products from the compressor blades. The nozzles inject into the intake air stream a low quantity of cleaning fluid that is atomised and mixes with the air which carries it uniformly into the cross sectional plane determined from the IGVs (inlet guide vanes) in order to wet them. Different nozzle positions for various gas turbine washing systems were illustrated by a research made by F. Mund (2006), see figure 2-2.

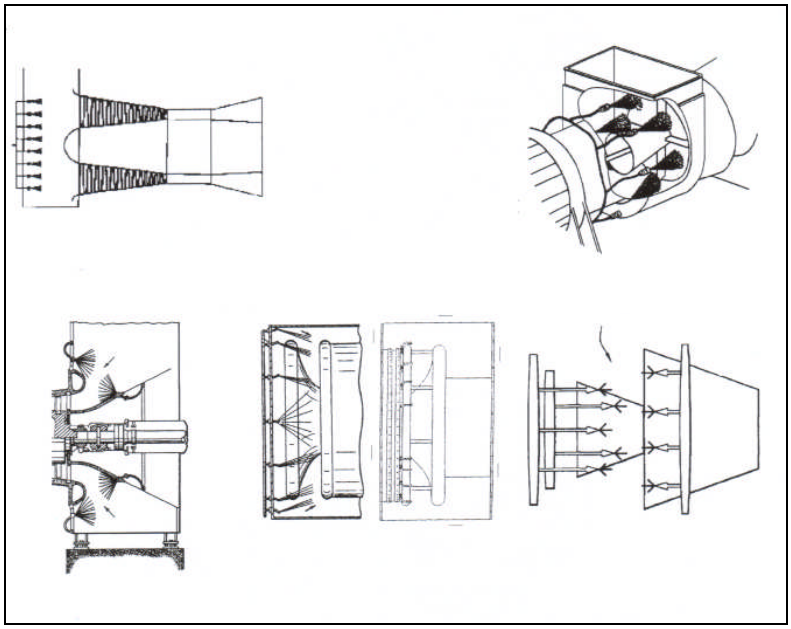

Figure 2–2: Various washing systems nozzle positioning (F. Mund 2006).

The number of nozzles used for compressor cleaning vary between different washing system units, however the higher the number of the injection nozzles in the air intake casing both upstream and downstream of the bellmouth, the better the distribution of the cleaning fluid in the intake air will be.
In parallel the penetration of the injection nozzles into the air stream must be kept minimum in order to prohibit possible loss of parts into the intake air stream.

2.4.2 Washing system operating pressure

The compressor washing systems are divided in systems of low operating pressure usually up to 9 bar and high operating pressure about 70 bar.
In terms of these systems a lot of advantages and disadvantages exist as reported from Carl Hjerpe (2004):
Low pressure systems for online and off-line compressor cleaning

- Large number of nozzles required since there is low capacity per nozzle
- Possibility of clogging of small nozzle orifices
- Low liquid exit nozzle velocity may cause liquid streaking
- Separate nozzles for online and off-line cleaning
- Low risk for nozzle wear

High pressure systems for online and off-line compressor cleaning

- Fewer nozzles required (higher liquid capacity per nozzle than low pressure nozzles) leading to low installation and maintenance costs
- Less amount of liquid used
- Better online cleaning fluid penetration due to higher fluid-air velocity ratio
- Small possibility of blade erosion due to low droplet sizes
- Easily retrofittable
- Same set of nozzles used for online and off-line cleaning

2.4.3 Droplet size

According to Bromley et al (2004) the droplet size for safe and effective online washing must be in the range between 50 to 250 microns. Droplets of too small sizes can be easily deflected by the air stream and there are possibilities not to reach the inlet guide vanes. However, too large droplets may not lead to effective compressor cleaning since they are affected by the parameter gravity making them to move close to the lower part of the gas turbine intake plenum. Large droplet sizes can cause blade erosion as well.

2.4.4 Type of nozzles

The nozzles used for compressor washing can be of hydraulic type or air assisted atomizers and the spray patterns that they produce vary from solid steams, full or hollow cone sprays and even flat fan sprays.

2.4.5 Washing fluid mass flow rate levels

The mass flow of the injection fluid must be as low as possible but without meaning a loss of cleaning efficiency which must be kept in the highest possible levels. Using

low mass flow rates for online washing problems like clogging of blade film cooling systems due to deposits washed off from the front stages onto the rear stages, penetration of the effluent water into the internal engine piping systems, fogging of the flame detector lenses and high CO emissions during online washing can be eliminated as much as possible. Using low injection quantity of cleaning solution the cleaning cost goes down due not only to lower washing fluid consumption but also to lower demineralised water consumption. In relation to these, the cost goes further down since the size of the washing skid has to be smaller.
For compressor washing the injection mass flow depends on the area to be wetted which is usually the area between two struts (see figure 2-3) and the distance between the location of the nozzles and the area of impact.

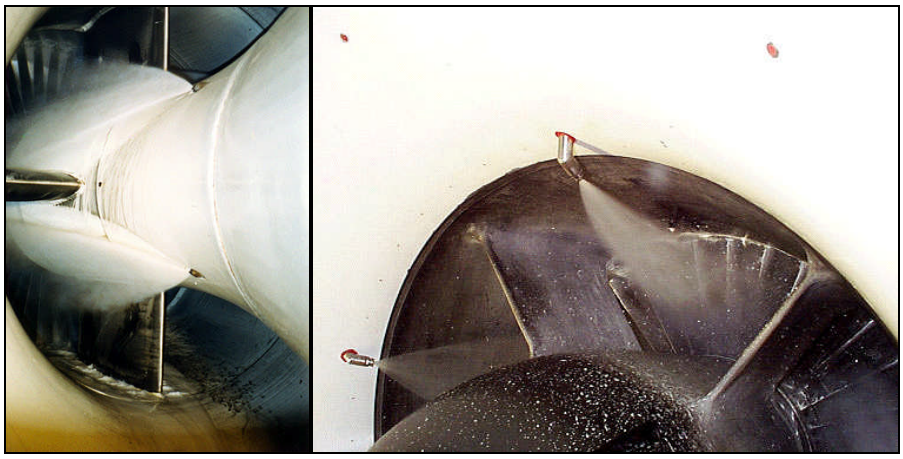

Figure 2–3: Wetted areas between struts (www.gtefficiency.com).

2.4.6 Injection velocity

The parameter injection velocity varies for different washing systems. High velocity sprays penetrate into the core air stream and little washing liquid is lost to the walls. Further away the velocity of the spray droplets will have almost the same velocity as the air entering the compressor but in the meantime they will have already penetrated the compressor in depth.

2.4.7 Spray angle

The spray angle is a parameter that has to do with the area to be wetted. This area is usually the area between two struts and the spray angle must be appropriate in order to cover this area during injection especially at on-line washing cases. In such cases a spray angle of e.g. 90 degrees injected into the still air will reduce to about 60 degrees when injected into the engine running at full load and this effect has to be taken into account in order for the washing system manufacturer to estimate the spray angle.

2.5 Online water injection investigation

The combination of online and off-line washing is very important for keeping the engine as efficient as possible. Stalder (2001) reported a set of tests involving online and off-line gas turbine washing that took place in a combined cycle plant in The Netherlands at the outskirts of Utrecht. The plant involved two gas turbines of 30.7 MW output and one steam turbine of 38.6 MW. The tests were performed over a time interval of 4000 hours and all measurements of power were made with the gas turbine running at base load.

The author concluded that power recovery after an off-line washing is higher than after an online washing and that this recovery extends for longer time for shorter online washing time intervals, preventing incremental degradation of output power.

A second set of tests was carried out on a 66MW gas turbine (year 1990) operating in the Lage Weide 5 combined cycle plant located on the same area. The test took place over a period of 18 months involving 8089 operating hours in total. During this period 83 online compressor washes were performed and the average power recovery measured after an online washing was found to be 712 KW. Online cleaning was performed once every four days.

The period of the 8089 hours involved was split into two time periods the first consisting of 3915 operating hours and the second 4174 hours due to an overhaul that was conducted after the end of the first period. In the first period three off-line washes were performed after 760, 2435 and 605 operating hours respectively from the beginning of the time period and the average power output increase after an offline washing was about 1.8 MW. This gain in power output was further reduced in the second period to a value of about 1MW, where two off-line washings were performed, one 1143 operating hours after the overhaul and the second after 1381 hours. This reduction in power gain was attributed to the aging of the unit during this period of time. However, even if the second period involved fewer off-line washes in the mean time it involved more online washes 45 instead of 38 performed in the first one and this indicates the first sign of extending the time period between off-line cleanings.

Stalder (2001) states in parallel, that for the total time interval of 4000 hours the loss in power output without compressor washing being performed would be very significant close to a value of 10%.

Syverud et al (2005) performed systematic online water wash tests after ingestion of salt water on a GE J85-13 jet engine (with 8 stage compressor) at the test facilities of the Royal Norwegian Air Force. The droplet sizes of the water injected were 25, 75 and 200μm and the water-air ratios were in the range between 0.4% to 3% by mass. Two different manifolds were used one with 12 air assisted flat spray nozzles producing droplet sizes of 25 μm and one with 18 full cone spray nozzles with droplet sizes of 75 or 200 μm based on volume mean diameter. The operating pressure of the washing system was 24 bars. For the experiments conducted, the droplet sizes were obtained by using laser diffraction spray analyser in still air and at a distance of 44cm from the nozzles. Seven online cleanings were performed and the compressor online wash duration was 5 minutes at engine speeds varying from full speed to idle for two complete cycles and the flow rate of tap water used for cleaning was 17.6 litres per minute (droplet size of 200 μm).

The effects on compressor performance were analysed through changes in the compressor stage work efficiency. The engine performance was measured after 30sec,

60sec, 90 sec, 4 and 10 minutes online water wash and the test data referred by the author represent engine operation at 95% shaft speed.
The authors state that water to air ratios above 3% can cause excessive blade loads and erosion damage and due to this reason they are not recommended for online water washing. The water-air ratios referred by the author for effective cleaning on aeroderivative engines are in the range between 0.8 to 2%. Also, the authors concluded that higher water flow rate always for safe cleaning is the main parameter for effective online water wash and low flow rates and smaller droplet sizes cause redeposition of fouling on the rear compressor stages.
The effect of the parameter water-air ratio is illustrated in the following figures 2-4 & 2-5 presented by the work of the authors.

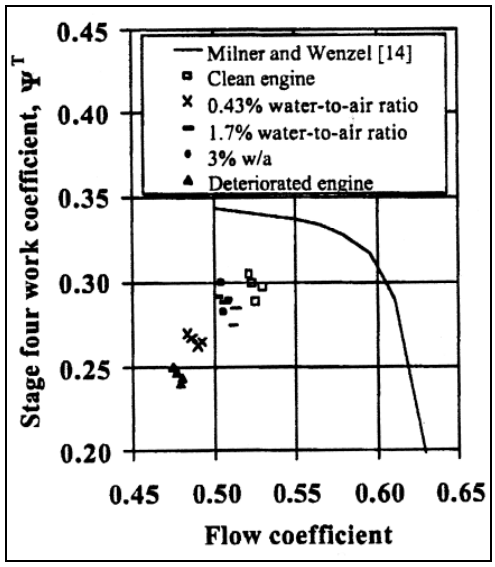

Figure 2–4: Stage four work coefficient after 60 sec water wash with 200 µm droplets (Syverud and Bakken, 2005).

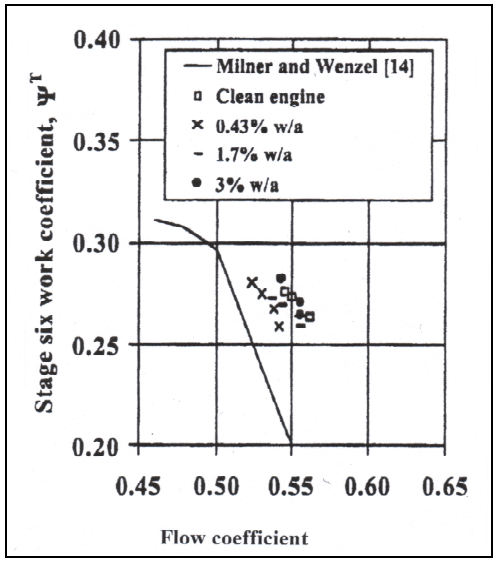

Figure 2–5: Stage six work coefficient after 60 sec water wash with 200 µm droplets (Syverud and Bakken, 2005).

From these figures one can see that the higher the water-air ratio is, the better the stage four and six work coefficients are with respect to the respective flow coefficients.
The quantities plotted in figures 2-4 and 2-5 are the work and flow coefficients defined as follows:

$$\Psi^{T} = c_p \Delta T_t / U_{tip}^2 \ \text{(kJ/kg)/(m/s)}^2 \quad (1)$$

Ψ^{T} : stage work coefficient
c_p : specific heat at constant pressure (kJ/kgK)
ΔT_t : stage total temperature increase (K)
U_{tip} : blade tip velocity (m/s)

$$\Phi = C_a / U_{tip}^2 \quad (2)$$

Φ : flow coefficient
C_a : axial air velocity (m/s)

According to Mund et al (2005), the cleaning of the first stage of a gas turbine is very important in order to reinstate the engine mass flow and a uniform fluid distribution is necessary covering the full engine annulus. The parameters studied in Mund's (2005) report were airflow reduction, injection location, injection direction, droplet mass and injection velocity. The effect of the operating condition of the engine on the fluid distribution at the compressor inlet was investigated as well.
According to the authors droplet trajectories are based on the force balance between the droplet and the airflow and increasing droplet diameter or droplet density hence droplet mass, enables droplets to penetrate the air stream. However, the larger droplets impinging on the blades with higher impact force can cause blade erosion. Very small droplets are carried with the airstream and they are not able to penetrate the boundary layer and reach the blade surfaces in order to clean them. The authors mention that the droplet range suggested for compressor washing applications ranges from 50 to 500 μm up to 800 μm.
In Mund's (2005) simulation, part of the intake of an industrial gas turbine of about 19m height and 12m width (260 MW) was modelled excluding the silencer and the filters (see figure 2-6). For the filters which were high-velocity filters a pressure drop of 400 KPa was taken under assumption. After an initial study which generated boundary conditions, the author cut away a large part of the vertical duct (block A) and used the remaining part (block B) in order to be able to achieve grid refinement, using always half of the intake domain with respect to the vertical symmetry plane.

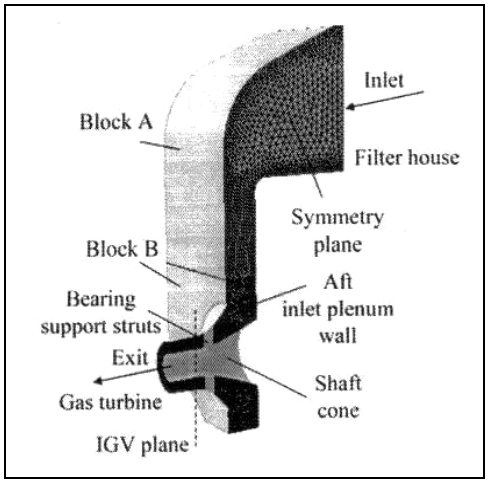

Figure 2–6: Computational grid domain (Mund and Pilidis, 2005).

The operating conditions involved in the simulation were the design point of the engine specified at sea level in an international standard atmosphere (ISA) climate at full load condition and an off-design condition with the engine running at a high desert altitude of 871m with 32 ^{o}C ambient temperature. The turbulence model used for the simulation was the Spalart-Almaras model applying standard wall functions.
The authors referred to velocities of 27 m/s after the 90 degrees intake bend and 173 m/s and 167 m/s at the compressor inlet for design and off-design conditions respectively.
The flow passing towards the vertical duct of the intake, approaching the inlet annulus was separated by the shaft cone and trapped at the end of the duct, forming a big vortex close to the shaft cone redirecting the flow in the compressor (see figure 2-7).

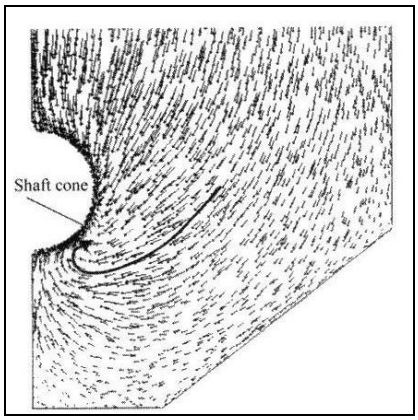

Figure 2–7: Close to shaft cone vortex illustration (Mund and Pilidis, 2005).

The researchers examined two modelling configurations in terms of injection location, one with 20 nozzles fitted circumferentially around the shaft cone at the aft plenum wall with the first nozzle shifted 9 degrees from the 12 o'clock position (configuration A, see figure 2-8) and another one with similar nozzle arrangement mounted on the opposite side of the gas turbine intake (configuration B, see figure 2-9).

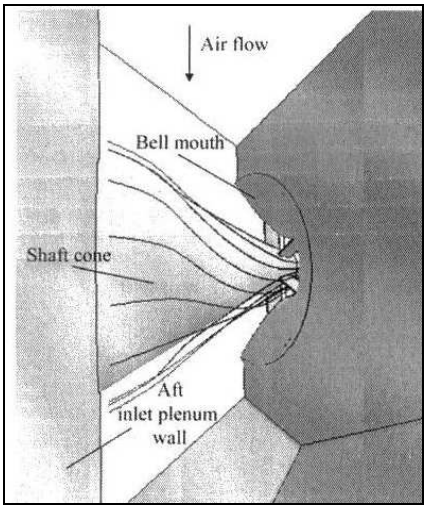

Figure 2–8: Configuration A droplet trajectories (Mund and Pilidis, 2005).

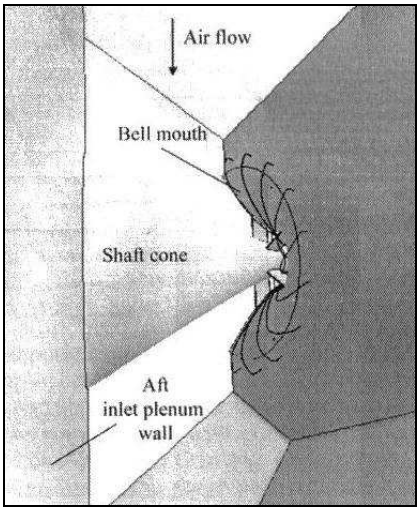

Figure 2–9: Configuration B droplet trajectories (Mund and Pilidis, 2005).

All injections were parallel to the shaft and modelled under design point engine condition. The injections were single point injections representing the centreline of the spray patterns. The droplet diameters chosen for the simulation were 50 μm and the injection velocity 150 m/s.

Comparing these two configurations of single jet injections the authors showed that injecting fluid away from the compressor (configuration B) appears to give better distribution on the IGV plane positioned on the leading edge of the IGVs (see figure 2-10). The majority of the droplets managed to reach the mid-span of the vanes.

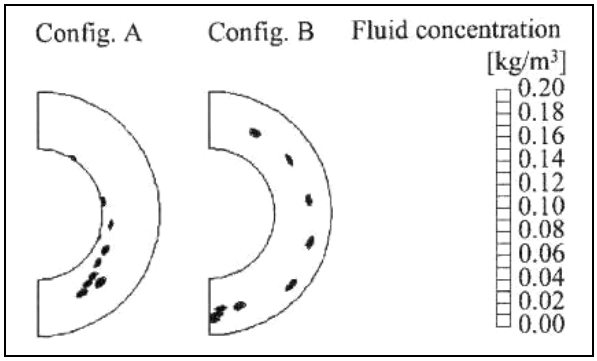

Figure 2–10: IGV plane fluid concentration contours (50μm droplet diameter, 150 m/s injection velocity, Mund and Pilidis, 2005).

Injecting fluid towards the compressor (configuration A) better droplet coverage on the IGV plane was obtained by increasing the droplet diameter above 50 μm (see figure 2-11).

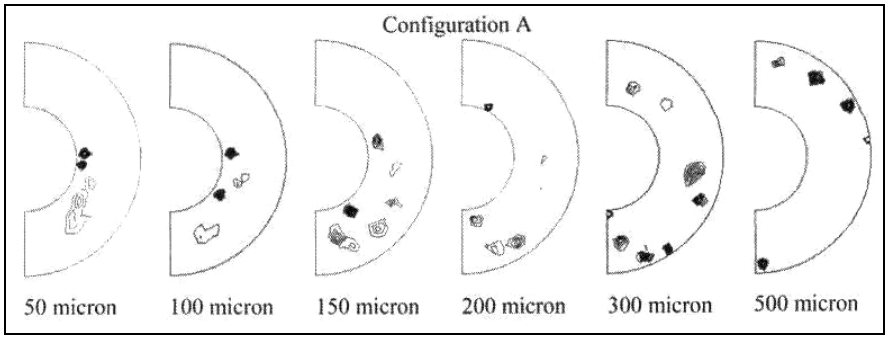

Figure 2–11: IGV plane droplet distribution increasing droplet diameter (injection velocity 100 m/s, configuration A, Mund and Pilidis, 2005).

To investigate the droplet distribution more realistically, solid cone spray patterns were simulated incorporating 40 and 80 degrees spray angles. In terms of configuration A with the injection nozzles pointing towards the compressor the 80 degrees sprays did not seem to give much better results compared to the 40 degrees sprays as far as the IGV plane droplet coverage is concerned (see figure 2-12).

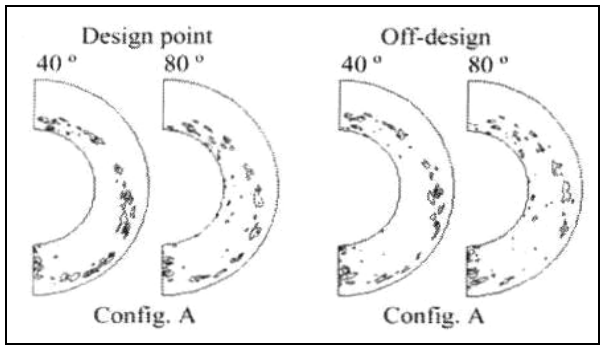

Figure 2–12: Configuration A IGV plane fluid concentration (solid cone, 300 μm droplet diameter and 100 m/s injection velocity, Mund and Pilidis, 2005).

However, better coverage on the upper part of the intake was obtained for the off-design engine running condition (higher altitude and temperature) since the airflow achieved lower velocities and the droplet trajectories were less deflected from it.
Investigating more the parameter injection direction, the authors run simulations with injection angles of 10 degrees towards the shaft cone (configuration D). This increment of injection direction angle given on the nozzles resulted in a higher deflection of the jets above the shaft cone downwards and a stronger influence of the vortex below the shaft cone on the droplets (see figure 2-13).

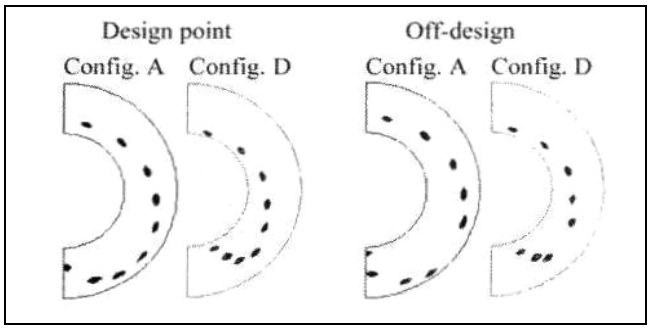

Figure 2–13: IGV plane fluid concentration contours for different injection directions (Mund and Pilidis, 2005).

Another simulation was run by injecting ethyl alcohol droplets with density lower than water's density, with a velocity of 100 m/s and droplet diameter of 300 μm. The simulation showed that the trajectories of the ethyl alcohol droplets were subjected to higher deflection by the airflow especially on the upper part of the shaft cone (see figure 2-14).

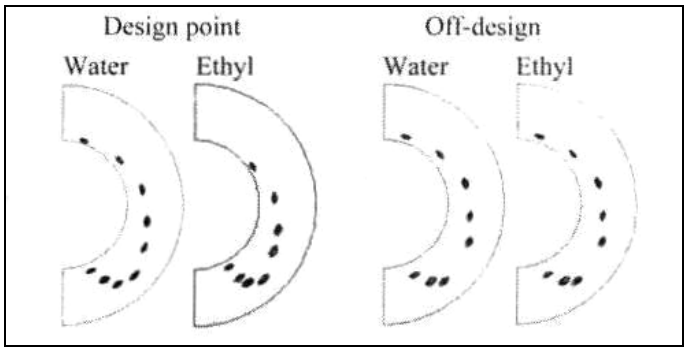

Figure 2–14: IGV plane fluid concentration contours for different fluid densities (Mund and Pilidis, 2005).

Running simulations for configuration D the authors investigated different droplet diameters from 50 μm to 500 μm and different injection velocities in the range between 75 and 200 m/s, employing single jet injections in order to check the IGV plane coverage from droplets. Introducing an IGV plane coverage angle θ (see figure 2-15) the authors found that increasing the droplet diameter a significant increase in coverage was obtained while increasing the injection velocity such an increase could not be obtained. A rapid increase in the coverage angle for droplet sizes of 150-300 μm was predicted and it was attributed to the Stokes number which exceeded unity for droplet diameters above 180 μm. According to the authors, the Stokes number St is the ratio of particle response time to a characteristic time-scale of the flow and for

St<<1, particles follow the flow streamlines but for St>>1, particles resist changing their direction as the flow streamlines change direction.

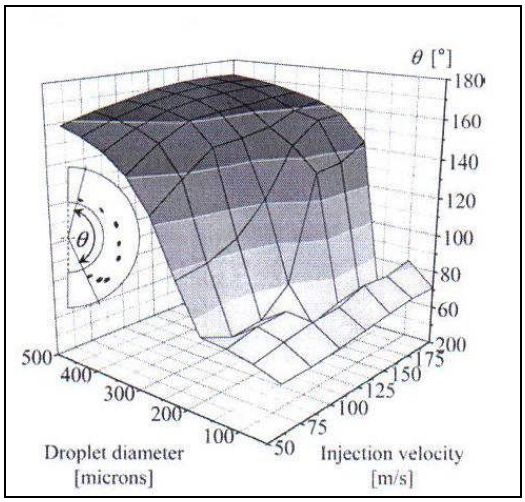

Figure 2–15: Configuration D IGV plane coverage against droplet diameter and injection velocity (Mund and Pilidis, 2005).

Mund et al (2004) illustrated for the same intake geometry the coverage of the IGV plane from droplets for design and off-design conditions varying the injection velocity between 75 and 125 m/s and keeping the droplet diameter at 300 μm (see figure 2-16). The operating pressure of the washing system was between 4500 and 9000 kPa.

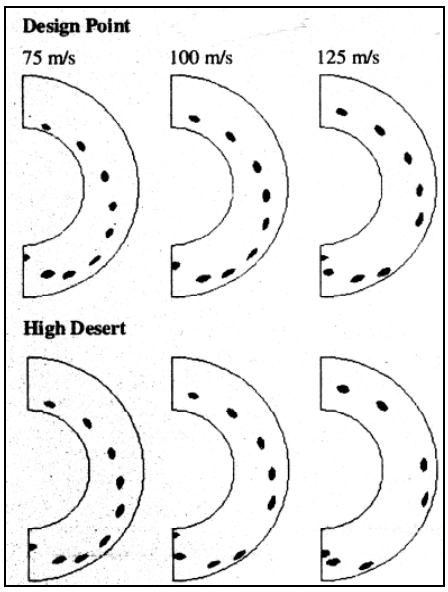

Figure 2–16: Concentration plots at the compressor inlet plane for single jet injection and droplets of 300 μm diameter (Mund and Pilidis, 2004).

At this point the authors illustrated that increasing the injection velocity the water droplets deviate more from the shaft cone in the upper half of the annulus. However, most important is the comparison between the design point and the different operating condition of high desert where the droplets deviate more from the shaft cone

compared to the design point case for the same droplet diameter and injection velocity conditions.
Hayward et al (1999) investigating the fact that the rear stages of a compressor cannot be cleaned efficiently with conventional cleaning methods since at these stages the temperatures are elevated and the droplets evaporate, they suggested a new invention of compressor washing. The washing system they used involves a pressure regulator in order to control the droplet sizes that the system can provide through the injection nozzles. More specifically, this regulator had to be adjusted in order to provide for the washing system small droplets initially so as to enable the first stages to be cleaned effectively. Then after a small time interval during the cleaning the regulator was adjusted again, so the droplet sizes that are going to be produced are bigger enabling the rear compressor stages to be cleaned effectively as well.
The authors at this point described the application of their invention on a LM 1600 General Electric aero derivative gas turbine having a low pressure compressor of three stages and a high pressure compressor of seven stages. They state that the whole washing process is separated into four steps as shown in table 1:

Table 1: GE LM 1600 washing process (Hayward et al, 1999)

1^{st} step	2^{nd} step	3^{rd} step	4^{th} step	5^{th} step
Covers the first two stages (low pressure compressor)	Covers the third stage (low pressure compressor)	Covers the fourth stage (high pressure compressor)	Covers the fifth, sixth and seventh stage (high pressure compressor)	Covers the eighth, nineth and tenth stage (high pressure compressor)
Duration	Duration	Duration	Duration	Duration
60 sec	45 sec	45 sec	90 sec	90 sec
Operating pressure	Operating pressure	Operating pressure	Operating pressure	Operating pressure
90-100 bar	60-70 bar	45 bar	30-35 bar	20 bar
Droplet diameter	Droplet diameter	Droplet diameter	Droplet diameter	Droplet diameter
120 μm	150 μm	180 μm		

2.6 Compressor cascade blade notation, forces and coefficients

In order to illustrate the relation between a cascade and real compressor stage the notation (figure 2-17), forces and velocities (figure 2-18) applicable to a cascade arrangement must be indicated.

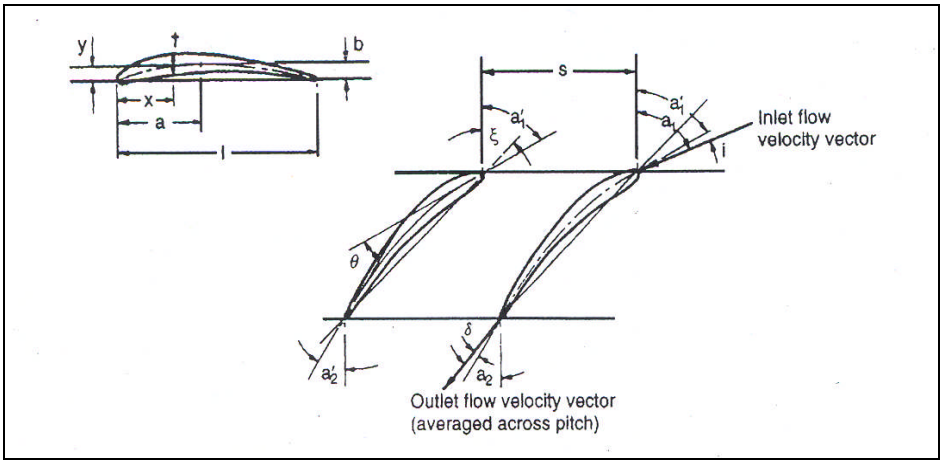

Figure 2–17: Compressor cascade blade notation (Dixon, 1998).

x: x-distance from leading edge of maximum thickness
a: distance of maximum camber from the leading edge
l : blade chord
b: y-distance of maximum camber from the leading edge
s: blade passage space
ξ: stagger angle
δ: deviation
i: incidence
a_1: cascade flow inlet angle
a_2: cascade flow outlet angle
a_1' : cascade blade inlet angle
a_2' : cascade blade outlet angle
θ : camber angle
a_1': cascade blade inlet angle
a_2': cascade blade outlet angle

a_1: cascade flow inlet angle
a_2: cascade flow outlet angle

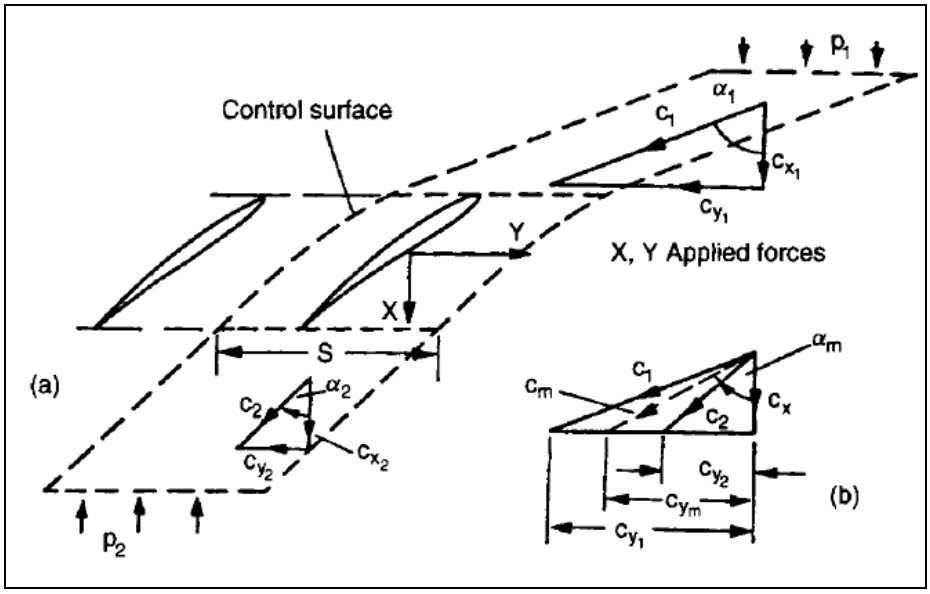

Figure 2–18: Forces and velocities in a blade cascade (Dixon, 1998).

According to the control surface of figure 2-18, the forces X and Y are exerted by unit depth of blade upon the fluid, exactly equal and opposite to the forces exerted by the fluid upon unit depth of blade (Dixon 1998). Assuming condition of incompressibility through the control surface the axial and tangential forces X and Y respectively can be expressed as follows.

$$X = (p_2 - p_1)s \qquad (3)$$

$$Y = \rho\ s\ c_x(c_{y1} - c_{y2}) \qquad (4)$$

The loss in total pressure can be expressed in the following form:

$$\frac{\Delta p_0}{\rho} = \frac{p_1 - p_2}{\rho} + \frac{1}{2}(c_1^2 - c_2^2) \qquad (5)$$

Δp_0 : total pressure loss
p_1 : inlet static pressure
p_2 : outlet static pressure
c_1 : inflow velocity
c_2 : outflow velocity

The total pressure loss coefficient can be expressed in the following two forms one based on the axial velocity (c_x) which is assumed to be constant and the other based on the inflow velocity (c_1):

$$\zeta = \frac{\Delta p_0}{\frac{1}{2}\rho c_x^2} \qquad (6)$$

$$\overline{\omega} = \frac{\Delta p_0}{\frac{1}{2}\rho c_1^2} \quad (7)$$

The difference of the squares of inlet and outflow velocities can be extended more which gives the following formula:

$$c_1^2 - c_2^2 = (c_{y_1}^2 + c_x^2) - (c_{y_2}^2 + c_x^2) = (c_{y_1} + c_{y_2})(c_{y_1} - c_{y_2}) \quad (8)$$

Combining (3), (4), (5) & (8) the total pressure loss can be expressed from the formula that follows:

$$\frac{\Delta p_0}{\rho} = \frac{1}{\rho s}(-X + \tan \alpha_m Y) \quad (9)$$

where $\tan \alpha_m = \frac{1}{2}(\tan \alpha_1 + \tan \alpha_2)$ (10)

In order to correlate the axial and tangential forces with the lift and drag forces one has to analyse the diagram that these forces create (see figure 2-19).

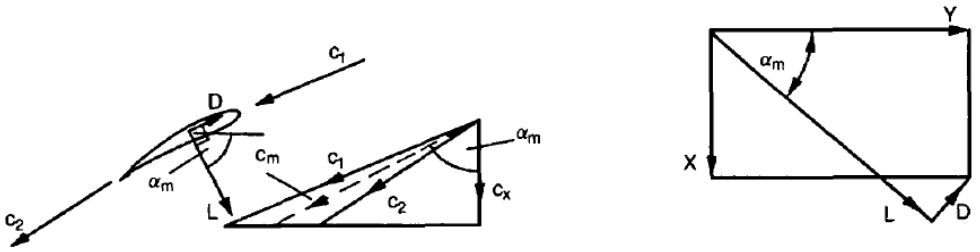

Figure 2–19: Lift and drag exerted by a cascade unit span blade upon the fluid (Dixon 1998).

According to figure 19 the lift and the drag forces can be resolved in terms of axial and tangential forces as follows:

$$L = X \sin \alpha_m + Y \cos \alpha_m \quad (11)$$

$$D = Y \sin \alpha_m - X \cos \alpha_m \quad (12)$$

Combining equations (9) and (12) one can obtain a very important expression in terms of the drag force exerted on the blade of unit depth which is the following:

$$D = s\Delta p_0 \cos \alpha_m \quad (13)$$

Combining equations (11), (12), (13) and (4) the following important formula in terms of lift force per unit blade depth is obtained:

$$L = \rho s c_x^2 (\tan\alpha_1 - \tan\alpha_2)\sec\alpha_m - s\Delta p_0 \sin\alpha_m \quad (14)$$

The lift and drag coefficients are expressed according to the following formulas:

$$C_L = \frac{L}{\frac{1}{2}\rho c_m^2 l} \quad (15)$$

$$C_D = \frac{D}{\frac{1}{2}\rho c_m^2 l} \quad (16)$$

Combining formula (13), (14), (15) and (16) the lift coefficient can be expressed from the following formula:

$$C_L = 2\frac{s}{l}\cos\alpha_m(\tan\alpha_1 - \tan\alpha_2) - C_D \tan\alpha_m \quad (17)$$

Combining (16), (13) and (6) the drag coefficient is expressed as follows:

$$C_D = \zeta \frac{s}{l}\cos^3\alpha_m = C_{Dp} \quad (18)$$

C_{Dp} : blade profile drag coefficient

The following stage velocity triangles of figure 2-20 are going to be used in order to illustrate the derivation of the total to total stage efficiency.

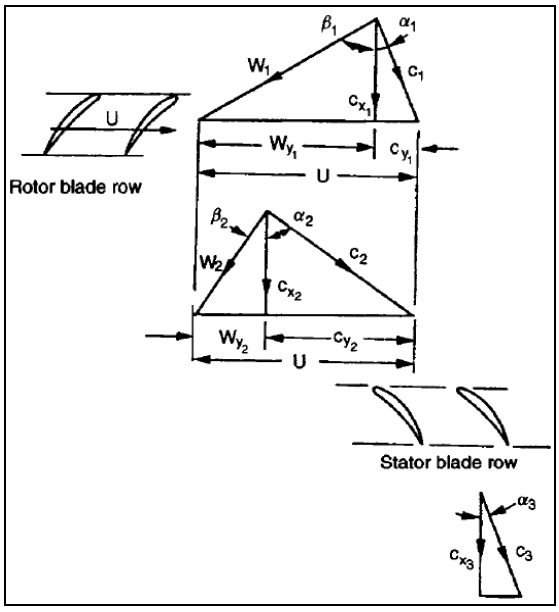

Figure 2–20: Compressor stage velocity triangles (Dixon, 1998).

Dixon (1998) analysed the Mollier's diagram (see figure 2-21) applying to an axial compressor stage in order to derive the expression for the total-to-total stage efficiency.

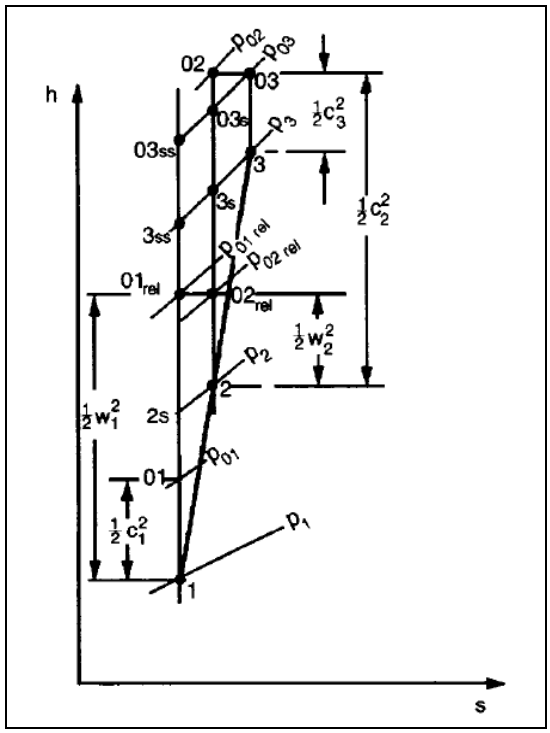

Figure 2–21: Mollier's diagram for an axial compressor stage (Dixon, 1998).

The actual work ΔW performed by the rotor on unit mass of fluid is expressed as the difference between the stagnation enthalpy at the rotor exit h_{02} and the rotor inlet h_{01}, however since there is no stagnation enthalpy change at the stator the actual work done can be expressed as the difference between the stator exit stagnation enthalpy h_{03} and the rotor inlet stagnation enthalpy:

$$\Delta W = h_{03} - h_{01} \quad (19)$$

Analysing Mollier's diagram (figure 2-21), the minimum work required to attain the same final stagnation pressure as in the real process can be obtained as follows:

$$\begin{aligned} \Delta W_{\min} &= h_{03ss} - h_{01} = (h_{03} - h_{01}) - (h_{03s} - h_{03ss}) - (h_{03} - h_{03s}) \\ &= (h_{03} - h_{01}) - (T_{03}/T_2)(h_2 - h_{2s}) - (T_{03}/T_3)(h_3 - h_{3s}) \end{aligned} \quad (20)$$

Since the compressor stage temperature rise is only a small fraction of the absolute temperature level then formula (19) takes the following form:

$$\Delta W_{\min} = (h_{03} - h_{01}) - (h_2 - h_{2s}) - (h_3 - h_{3s}) \quad (21)$$

Also, because of the small temperature rise in the stage, the density change is small and it is reasonable to assume the fluid as incompressible.

Analysing more the terms stator exit stagnation enthalpy h_{03}, rotor exit stagnation enthalpy h_{02}, stator exit total pressure p_{03} and rotor exit total pressure p_{02} then:

$$h_{03} = h_3 + \frac{1}{2}c_3^2 \quad (22)$$

h_3: stator exit static enthalpy

$$h_{02} = h_2 + \frac{1}{2}c_2^2 \quad (23)$$

h_2: rotor exit static enthalpy

$$p_{03} = p_3 + \frac{1}{2}\rho c_3^2 \quad (24)$$

p_3: stator exit static pressure

$$p_{02} = p_2 + \frac{1}{2}\rho c_2^2 \quad (25)$$

p_2: rotor exit static pressure

Combining equations (22), (23), (24) & (25) and taking into account that the stagnation enthalpy remains constant along the stator $h_{02} = h_{03}$ then:

$$h_3 - h_2 = \left[(p_{02} - p_2) - (p_{03} - p_3)\right]/\rho \quad (26)$$

Using the thermodynamic relationship $Tds = 0 = dh - (1/\rho)dp$ according to the isentrope 2-3s of Mollier's diagram:

$$h_{3s} - h_2 = (p_3 - p_2)/\rho \quad (27)$$

Relating formulas (26) and (27) then:

$$h_3 - h_{3s} = (p_{02} - p_{03})/\rho = (1/\rho)\Delta p_{0\,stator} \quad (28)$$

According to the isentrope 1-2s of Mollier's diagram:

$$h_{2s} - h_1 = (p_2 - p_1)/\rho \quad (29)$$

Analysing more the terms rotor inlet relative stagnation enthalpy h_{01rel}, rotor exit relative stagnation enthalpy h_{02rel}, rotor inlet relative total pressure p_{01rel} and rotor outlet relative total pressure p_{02rel} then:

$$h_{01rel} = h_1 + \frac{1}{2}w_1^2 \quad (30)$$

h_1: rotor inlet static enthalpy

$$h_{02rel} = h_2 + \frac{1}{2} w_2^2 \quad (31)$$

$$p_{01rel} = p_1 + \frac{1}{2} \rho w_1^2 \quad (32)$$

p_1 : rotor inlet static pressure

$$p_{02rel} = p_2 + \frac{1}{2} \rho w_2^2 \quad (33)$$

Taking into account that the rotor inlet relative stagnation enthalpy equals the rotor outlet stagnation enthalpy and relating equations (30), (31), (32) and (33) one can obtain:

$$h_2 - h_{2s} = (p_{01rel} - p_{02rel}) / \rho = (1/\rho) \Delta p_{0rotor} \quad (34)$$

Using formulas (19), (21), (28) and (34) the formula expressing the total to total stage efficiency n_{tt} can be obtained:

$$n_{tt} = \frac{\Delta W_{\min}}{\Delta W_{actual}} = \frac{(h_{03} - h_{01}) - (h_2 - h_{2s}) - (h_3 - h_{3s})}{(h_{03} - h_{01})} = 1 - \frac{\Delta p_{0stator} + \Delta p_{0rotor}}{\rho (h_{03} - h_{01})} \quad (35)$$

Howell (1945) separated the compressor losses into three categories

- Blade profile losses
- Wall annulus skin friction losses
- Secondary losses (all the remaining losses)

In terms of a compressor the overall drag coefficient C_D for each blade row is obtained from the summation of all the drag forces related to the three categories of losses mentioned.

$$C_D = C_{D_p} + C_{D_a} + C_{D_s} \quad (36)$$

$$C_{Da} = 0.02 \ s/H \quad (37)$$

C_{Da} : Drag related to wall annulus friction losses

s : blade pitch

H : blade height

$$C_{Ds} = 0.018 C_L^2 \quad (38)$$

C_{Ds} : Drag related to secondary losses

2.7 Correlation between cascade and compressor stage

In order to proceed closer to the correlation with a real compressor stage some basic assumptions have to be done:

- Stage reaction R 50% ($\alpha_2 = \beta_1$ & $\beta_2 = \alpha_1$)
- Density at entrance to the stage ρ_s
- Mean blade radius speed U
- Work done factor λ
- Axial velocity across the stage is constant

where $R = \dfrac{rotor\ \ static\ \ pressure\ \ rise}{stage\ \ static\ \ pressure\ \ rise}$ (39) (Saravanamuttoo 2001)

$$\lambda = \frac{actual\ \ change\ \ of\ \ whirl\ \ velocity}{ideal\ \ change\ \ of\ \ whirl\ \ velocity} \quad (40)$$ (Ramsden 2002)

The flow inlet angle β_1 and flow outlet angle β_2 correspond now to the cascade flow angles α_1 & α_2 respectively (figure 2-17). The parameter $\beta_1^{'}$ represents the inlet cascade blade metal angle.
Having these parameters been established the values of flow coefficient ϕ and stage loading coefficient ψ can be obtained as follows:

$$\phi = \frac{c_x}{U} = \frac{1}{\tan\beta_1 + \tan\beta_2} \quad (41)$$

$$U = c_{x_1}(\tan\alpha_1 + \tan\beta_1) = c_{x_2}(\tan\alpha_2 + \tan\beta_2) \quad (42)$$

$$\psi = \frac{\Delta h_0}{U^2} = \frac{\lambda U(c_{y_2} - c_{y_1})}{U^2} = \frac{\lambda U c_x(\tan\alpha_2 - \tan\alpha_1)}{U^2} = \lambda\phi(\tan\alpha_2 - \tan\alpha_1) \quad (43)$$

The lift coefficient according to the formula obtained from cascade basis (17) can be obtained as follows:

$$C_L = 2\frac{s}{l}\cos\beta_m(\tan\beta_1 - \tan\beta_2) \quad (44)$$

$$\tan\beta_m = \frac{\tan\beta_1 + \tan\beta_2}{2} \quad (45)$$

The profile drag coefficient according to the formula obtained from cascade basis (18) can be obtained as follows:

$$C_{D_p} = \frac{s}{l}\left(\frac{\Delta p_0}{\frac{1}{2}\rho w_1^{\,2}}\right)\frac{\cos^3\beta_m}{\cos^2\beta_1} \quad (46)$$

Then knowing the blade pitch s, the blade height H and the blade lift coefficient values the overall drag coefficient can be calculated:

$$C_D = C_{D_p} + C_{D_a} + C_{D_s} = C_{D_p} + 0.02(s/H) + 0.018C_L^2 \quad (47)$$

To calculate the total to total stage efficiency, formula 35 is related with the flow and stage loading coefficients first according to Dixon (1998):

$$n_{tt} = 1 - \frac{\Sigma\Delta p_0 / \rho}{\psi U^2} = 1 - \frac{\Sigma\Delta p_0 / \frac{1}{2}\rho c_x^2}{2\psi / \phi^2} = 1 - \frac{(\zeta_R + \zeta_S)\phi^2}{2\psi} \quad (48)$$

Applying equation 18 based on cascade analysis on equation 48 applying on real compressor stage the stator total pressure loss coefficient can be obtained:

$$\zeta_S = \frac{l}{s} C_D \sec^3\beta_m \quad (49)$$

where $\zeta_S = \zeta_R$

Combining equations 48 and 49 assuming stator and rotor total pressure losses equal the total to total stage efficiency can be calculated as follows:

$$n_{tt} = 1 - \frac{\phi^2 C_D (l/s)}{\psi \cos^3\beta_m} \quad (50)$$

Except the total to total stage efficiency calculation that is supported on cascade basis analysis and shows clearly the correlation between cascade and real compressor stage, another step further involves the calculation of pressure rise across the stage Δp.

$$n_{isentropic} = n_{tt} = \frac{\Delta h_{isentropic}}{\Delta h} = \frac{\Delta p(1/\rho_s)}{\Delta h} \quad (51)$$

$$\Delta p = n_{tt}\rho_s \Delta h = n_{tt}\rho_s \psi U^2 \quad (52)$$

Howell and Bonham (1950) in doing this correlation between cascade and stage characteristics, knowing already the cascade values $\beta_1^{'}$, $\beta_2^{'}$, θ and s/l, they started by determining the nominal fluid outlet angle β_2^* of cascade blading by combining equations 30 ($\delta^* = m\theta\sqrt{\frac{s}{l}}$) and 31 ($\beta_2^* = \delta^* + \beta_2^{'}$) with the following equation in terms of m:

$$m = 0.23(2a/l)^2 + (\frac{\beta_2^*}{500}) \qquad (53)$$

a : distance of point of maximum camber from blade leading edge

Then using the diagram (figure 2-22) of fluid outlet angle versus fluid deflection the value of nominal deflection ε^* was found. Using the values of nominal fluid outlet angle β_2^* and nominal deflection ε^*, by substituting into the relations $\varepsilon^* = \beta_1^* - \beta_2^*$ and $i^* = \beta_1^* - \beta_1'$, the values of nominal inflow angle β_1^* and nominal incidence i^* were calculated.

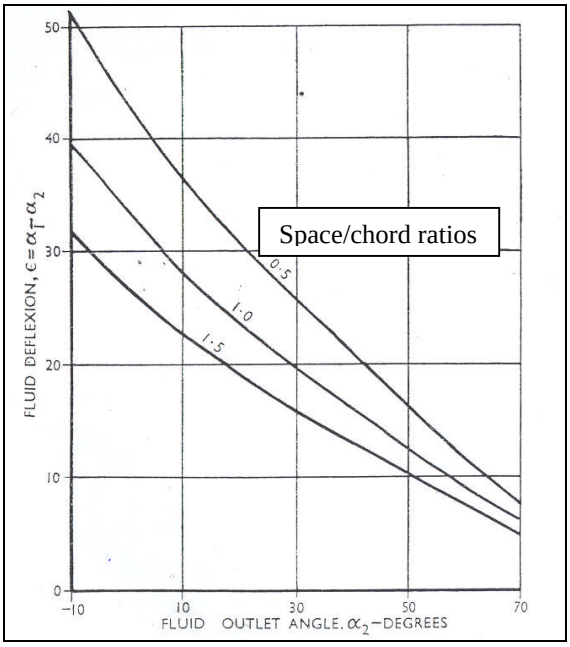

Figure 2–22 : Nominal values of fluid deflection (Howell, 1945).

Then using cascade characteristic curve data extrapolated in terms of nominal incidence and fluid deflection (figure 2-23), several points of the stage characteristics were obtained by using each time different values of $(i - i^*)/\varepsilon^*$, hence different values of incidence.

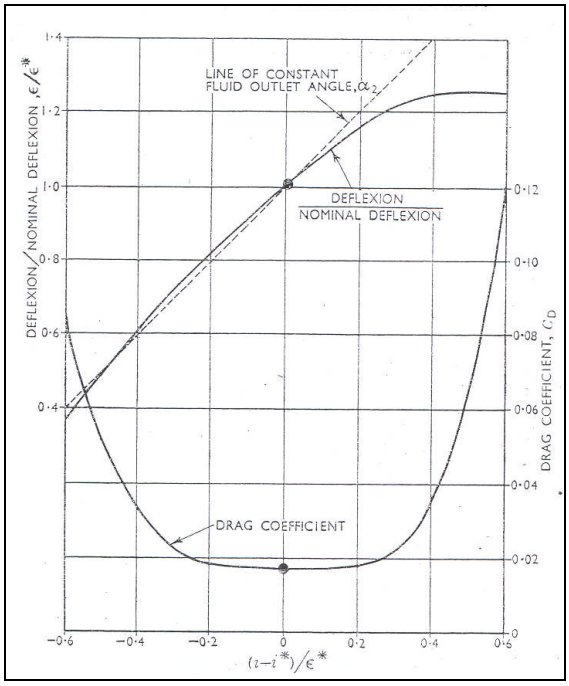

Figure 2–23 : Deflections and drag coefficients at other than nominal incidences (Howell, 1945).

In order to plot the stage characteristics curve (example figure 2-24) the stage temperature rise coefficient $c_p \Delta T_s / 0.5U^2$, stage efficiency n_s and stage pressure rise coefficient $\Delta P_s / 0.5\rho U^2$ had to be calculated for different incidences according to the following formulae:

$$\frac{c_p \Delta T_s}{\frac{1}{2}U^2} = 2\lambda(\frac{c_x}{U})(\tan\beta_1 - \tan\beta_2) \qquad (54)$$

ΔT_s : stage total temperature rise

$$n_s = 1 - \frac{2}{\sin 2\beta_m}\ \frac{C_D}{C_L} \qquad (55)$$

$$\frac{\Delta P_s}{\frac{1}{2}\rho U^2} = n_s(\frac{c_p \Delta T_s}{\frac{1}{2}U^2}) \qquad (56)$$

ΔP_s : stage static pressure rise

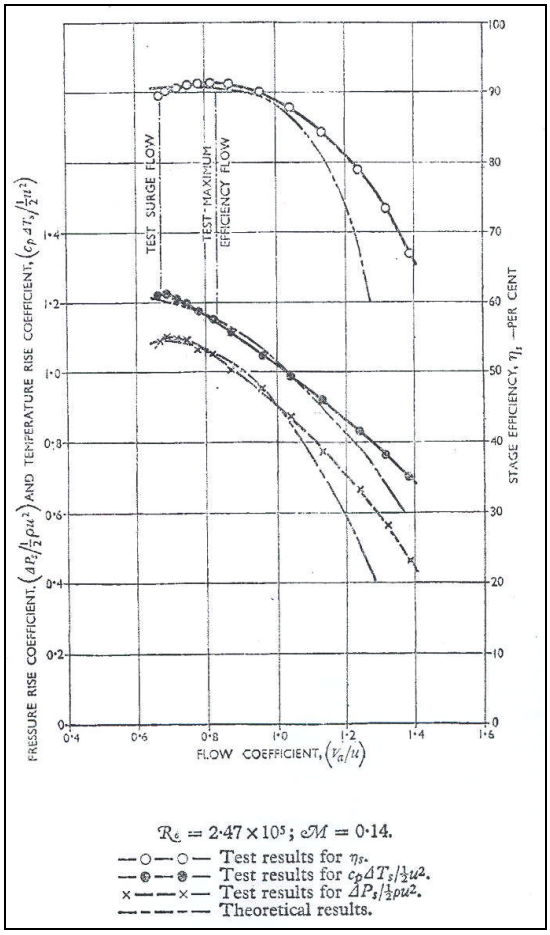

Figure 2–24 : Test stage compressor characteristics (Howell and Bonham, 1950).

2.8 Instrumentation for cascade exit flow angle measurements

The probes used for the measurement of flow direction behind turbomachinery equipment are the five-hole and the three-hole pressure probes depending on the nature of the flow if it is three-dimensional or two-dimensional.

2.8.1 Five-hole pressure probes

The theory of the five-hole spherical probe according to Nowack (1970) is based on the energy equation between a point in the free stream air and a point (n) on the surface of a sphere (see figure 2-25).

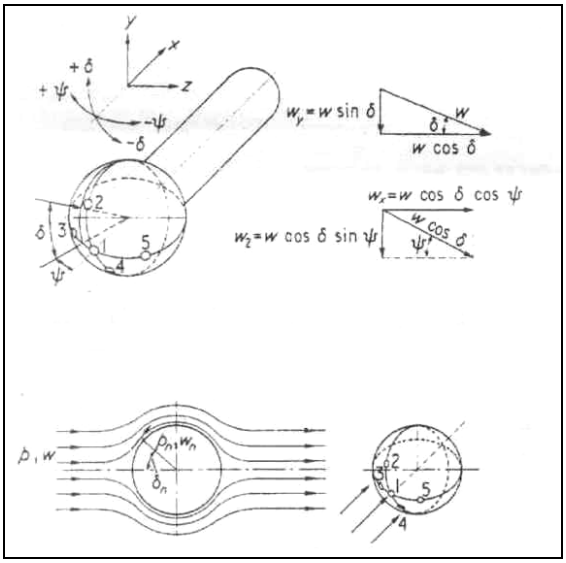

Figure 2–25: Relation between yaw and pitch angles (Nowack, 1970).

Applying Bernoulli's equation between these two points the following relation arises:

$$p + \frac{1}{2}\rho w^2 = p_n + \frac{1}{2}\rho w_n^2 \Rightarrow p_n = p + \frac{1}{2}\rho w^2 \left\{1 - (w_n / w)^2\right\} \quad (57)$$

Assuming $k_n = 1 - (w_n / w)^2$ and $q = \frac{1}{2}\rho w^2$

then

$$p_n = p + qk_n \quad (58)$$

Therefore for points in the meridian plane

$$p_1 = p + qk_1 \quad (59)$$
$$p_2 = p + qk_2 \quad (60)$$
$$p_4 = q + qk_4 \quad (61)$$

For points on the meridian plane w_n is a function of angle δ, so

$$k_n = 1 - (w_n / w)^2 = f(\delta) \quad (62)$$

If h is the manometer reading at pressure p the following relations can be written

$$\frac{p_1 - p_2}{q} = \frac{h_1 - h_2}{h_q} = k_1 - k_2 = f(\delta) \quad (63)$$
$$\frac{p_1 - p_4}{q} = \frac{h_1 - h_4}{h_q} = k_1 - k_4 = f(\delta) \quad (64)$$

Combining these equations a dimensionless inclination factor K is obtained for the equatorial plane by keeping the angle ψ constant. K is a function of pitch angle δ.

$$\frac{p_1 - p_2}{p_1 - p_4} = \frac{h_1 - h_2}{h_1 - h_4} = \frac{k_1 - k_2}{k_1 - k_4} = K_\delta = f(\delta) \qquad (65)$$

For points 1, 3 & 5 that belong on a meridian plane and keeping the angle δ constant an analogous relation arises:

$$\frac{p_1 - p_3}{p_1 - p_5} = \frac{h_1 - h_3}{h_1 - h_5} = \frac{k_1 - k_3}{k_1 - k_5} = K_\psi = f(\psi) \qquad (66)$$

These inclination factors K_δ and K_ψ are used for determining the direction of the velocity vectors. Also, dimensionless velocity coefficients can be expressed as follows:

$$V_{12} = \frac{h_1 - h_2}{h_q} = k_1 - k_2 = f(\delta, \psi) \qquad (67)$$

$$V_{14} = \frac{h_1 - h_4}{h_q} = k_1 - k_4 = f(\delta, \psi) \qquad (68)$$

$$V_{13} = \frac{h_1 - h_3}{h_q} = k_1 - k_3 = f(\psi, \delta) \qquad (69)$$

$$V_{15} = \frac{h_1 - h_5}{h_q} = k_1 - k_5 = f(\psi, \delta) \qquad (70)$$

For determining the static pressure, the static pressure factor P_{st} can be formed which for the probe hole number 2 takes the following form

$$P_{st2} = \frac{P_2 - P_{stat}}{q} = \frac{h_2 - h_{stat}}{h_q} = f(\delta, \psi) \qquad (71)$$

P_2 : pressure of hole 2

P_{stat} : static pressure

2.8.1.1 Probe calibration

Nowack (1970) used a calibration method in which the direction of the velocity vector is determined by two Cartesian angles, a yaw angle in a horizontal equatorial plane and a pitch angle in a vertical meridian plane which contains the velocity vector and is perpendicular to the equatorial plane. For this kind of calibration a special rig was used (see figure 2-26).

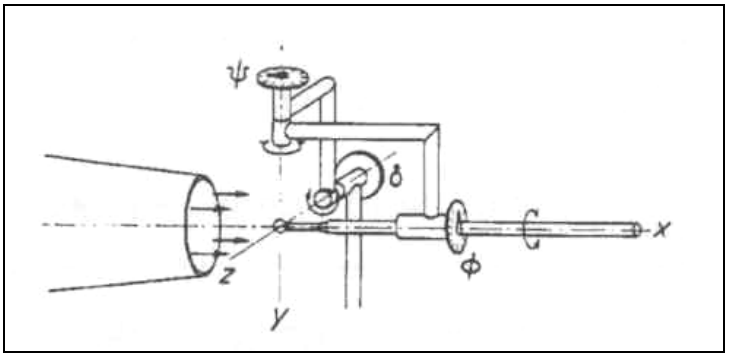

Figure 2–26: Calibration rig (Nowack, 1970).

This rig involved three perpendicular axes x, y and z, intersecting all at the centre of the sphere, so this point remained fixed relevant to the position of the axes. Protractor scales were provided for each axes x, y and z, giving readings of the angles ϕ, ψ and δ respectively, with respect to the calibration flow direction. The air flow for the calibration was provided via a radial compressor coupled to a convergent stream tube. The velocity profile at the end of the tube was flat with a velocity magnitude of 24 m/s. This magnitude was obtained via a Pitot probe which was also used to note static pressures. The calibration took place as well at different flow speeds between 2 and 40m/s corresponding to Reynolds numbers from 2.3×10^3 to 4.1×10^4. The calibration process was as follows (see figure 2-27).

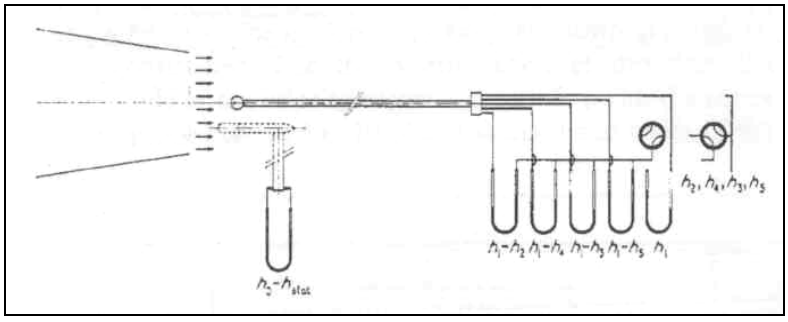

Figure 2–27: Calibration procedure scheme (Nowack, 1970).

The head of the spherical probe was set at a distance of 7cm from the stream tube end along it's axis. The holes 2 and 4 were set in the vertical plane, holes 3 and 5 in the horizontal plane and pressure readings of the five holes were obtained via five Betz water micromanometers. In order to obtain zero readings of the protractor scales careful adjustment of the probe took place until the manometer readings related to the holes 2, 3, 4 and 5 were equal. During the calibration process the yaw angle ψ was changed at increments of 5 degrees by keeping the pitch angle δ constant and manometer readings were obtained for all these different probe positions. Also, the pitch angle δ was varied in increments of 5 degrees by keeping the yaw angle constant. Both yaw and pitch angles were varied in the range between -90 and +90 degrees. Using this method of calibration the main chart of inclination factor versus yaw and pitch angle was obtained (see figure 2-28).

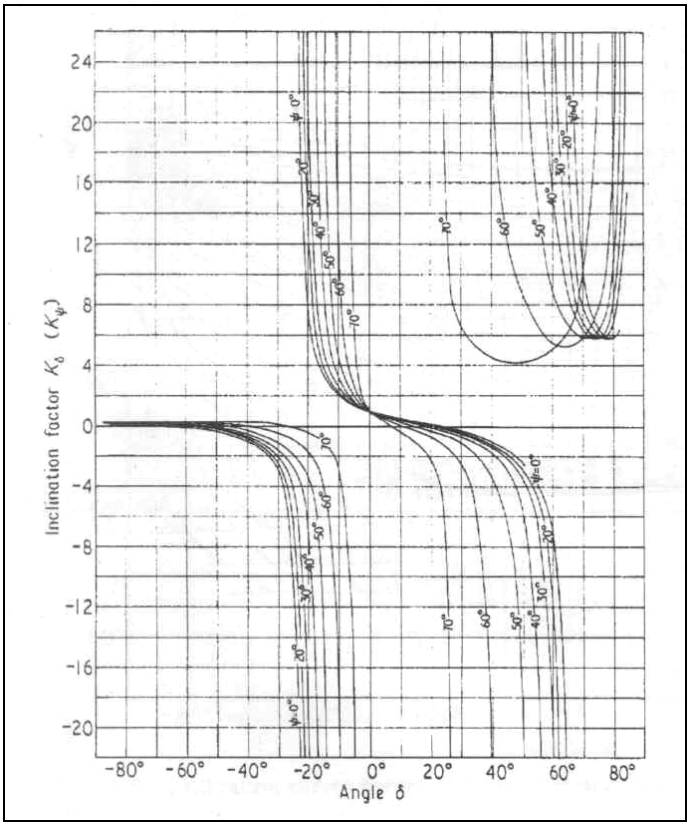

Figure 2–28: Inclination factor versus pitch and yaw angle variation (Nowack, 1970).

Therefore, depending on the values of the inclination factors K_δ and K_ψ, the velocity vector direction can be found straight forward from the calibration curves for the inclination factor K. Also, calibration curves were produced for the velocity and static pressure factors (or coefficients) as a function of yaw and pitch angles. In terms of possible errors involved, the author states that errors may occur when the probe is used in steep velocity gradient flow fields and for this reason probe heads of smaller dimension should be preferable.

According to Wright (1970), the pressure recovery factor k_n for sufficiently high velocities ($4x10^3<Re<1.5x10^5$) is independent of Reynolds number and for a given probe design it is only a function of the angle θ_n, which is the angle between the velocity vector and the radial line through the nth pressure hole (see figure 2-29).

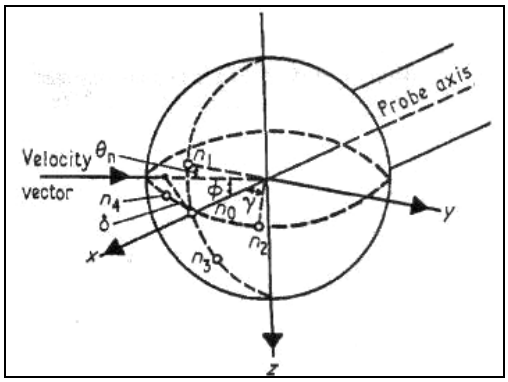

Figure 2–29: Spherical sensing head notation (Wright, 1970).

ϕ : conical angle between the velocity vector and the probe axis
δ : dihedral angle between the flow plane and the meridian plane
γ : conical angle between the pressure hole and the probe axis

The angle θ_n is expressed usually in terms of the following angles the pitch α and yaw β angles (see figure 2-30) and the conical ϕ and dihedral δ angles.

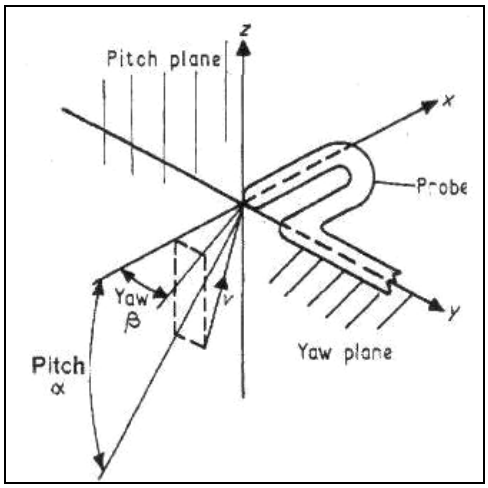

Figure 2–30: Pitch and yaw angles (Wright, 1970).

The author in order to get the angles ϕ and δ and to specify the velocity direction uses certain combinations of the recovery factors as follows:

$$\frac{k_1 - k_3}{k_0 - k_2} = f(\phi, \delta) \qquad (72)$$

$$\frac{k_4 - k_2}{k_0 - k_2} = F(\phi, \delta) \qquad (73)$$

The velocity magnitude and the system static pressure are given from the following expressions respectively:

$$k_0 - k_2 = 2(p_0 - p_2)/\rho V^2 \qquad (74)$$

$$k_0 = 2(p_0 - p_s)/\rho V^2 \qquad (75)$$

The author refers that the distribution of these pressure recovery factor combinations results in complicated families of curves which can be simplified by using three new factors K_ϕ, K_v and K_p as follows:

$$K_\phi = \left[1 - \sum_{n=1}^{4} (p_0 - p_n) \;/\; 2 \left\{ \sum_{n=1}^{4} (p_0 - p_n)^2 \right\}^{1/2} \right]^{1/2} \qquad (76)$$

$$K_v = \left[\rho V^2 \left\{ \sum_{n=1}^{4} (p_0 - p_n)^2 \right\}^{-1/2} \right]^{1/2} \qquad (77)$$

$$K_p = 2(p_0 - p_s)/\rho V^2 \qquad (78)$$

The dihedral angle δ is obtained from the following equation:

$$\tan\delta = -(p_1 - p_3)/(p_2 - p_4) \qquad (79)$$

The author states that the factors K_ϕ and K_v are functions of the flow angles ϕ and δ, while K_p is only a function of ϕ and independent of the dihedral angle δ. Also, after experimental calibration of a spherical and hemispherical probe, the author observed that the results related to the hemispherical probe are closer to the theoretical ones in terms of the factors K_ϕ, K_v and K_p. This happens due to the improved flow conditions coming out of moving of the boundary layer separation point further away from the pressure holes of the hemispherical probe (see figure 2-31) in comparison with the spherical probe, obtaining so better calibration characteristics closer to the theory.

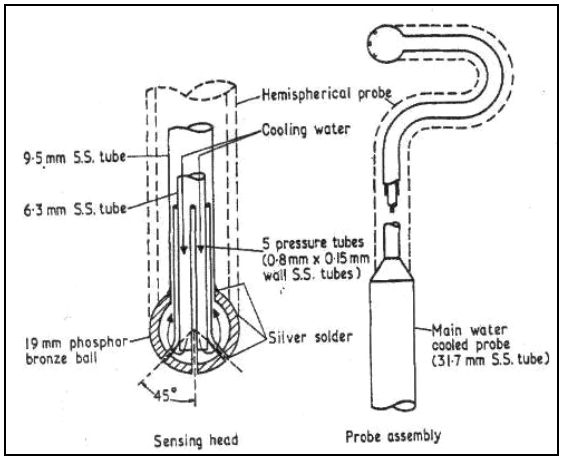

Figure 2–31: BCURA five-hole spherical and hemispherical pitotmeter (Wright, 1970).

According to the experimental calibration conducted by the author, the data were obtained in a circular free stream jet of uniform velocity profile cross sectional area. A standard pitot-static tube was used to obtain the dynamic and static pressures of the jet and flow conditions of the calibration took place in the range between 5.5 and 23m/s (7000<Re<29000).
After determining the value of the dihedral angle δ, in order to specify the quadrant that contains the velocity vector the following inequalities were used:

If $-\dfrac{p_1 - p_3}{p_2 - p_4} > 0$ and $p_2 - p_4 > 0$ then $0 < \delta < \pi/2$

If $-\dfrac{p_1 - p_3}{p_2 - p_4} < 0$ and $p_2 - p_4 < 0$ then $\pi/2 < \delta < \pi$

If $-\dfrac{p_1 - p_3}{p_2 - p_4} > 0$ and $p_2 - p_4 < 0$ then $\pi < \delta < 3\pi/2$

If $-\dfrac{p_1 - p_3}{p_2 - p_4} < 0$ and $p_2 - p_4 > 0$ then $3\pi/2 < \delta < 2\pi$

The usual method of doing three-dimensional flow measurements using a five-hole spherical pitot probe involves either adjustment of the probe until its axis points in the flow direction (nulling method), or yawing of the probe until the meridian plane contains the flow angle and then making use of two-dimensional calibration curves for the flow determination in this plane. Both methods require probe adjustment and in order to avoid this difficulty Lee and Ash (1956) used a five-hole spherical pitot probe that was developed and calibrated to measure static pressure and the magnitude and direction of the velocity vector for any arbitrary flow angle without requiring adjustment (see figure 2-32).

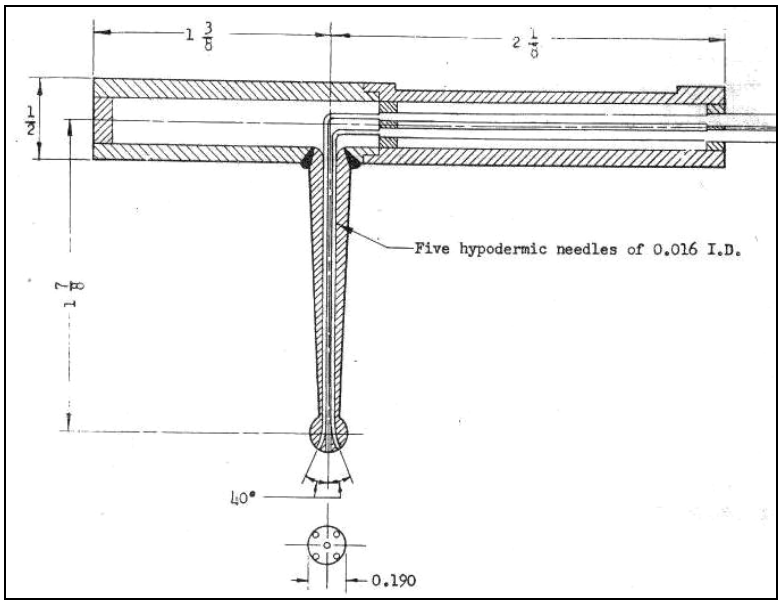

Figure 2–32: Construction details of spherical pitot (Lee and Ash, 1965).

The head of the probe had a diameter of 0.19 inches bearing five pressure holes of 0.016 inches diameter, one along the shaft axis and four located symmetrically on the equatorial and meridian planes. Each of the four holes lied on a sphere radius making an angle of 40 degrees with the axis of the probe (see figure 2-33).

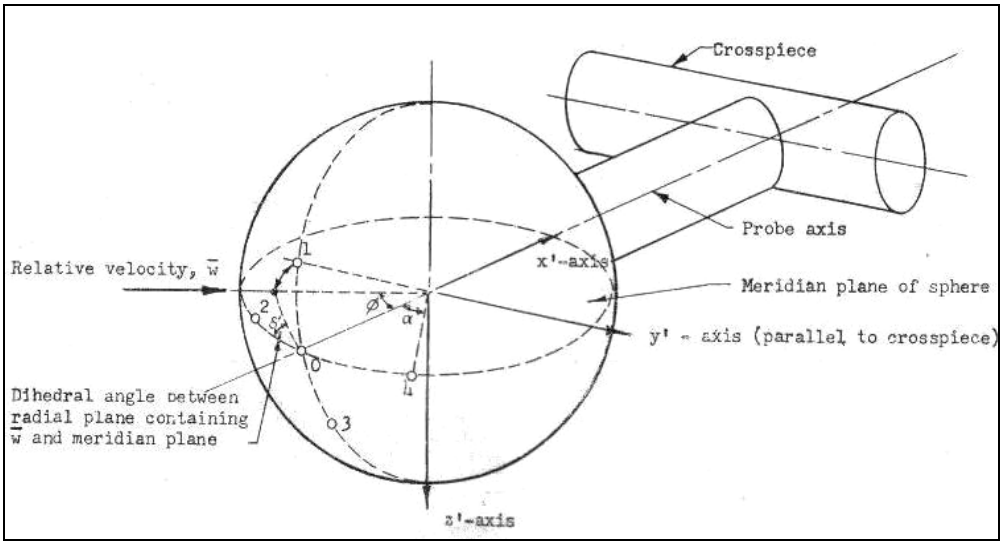

Figure 2–33: Notation for spherical probe head (Lee and Ash, 1965).

The author states that the pressure recovery factor k_n is a function of the Reynolds number and the angle γ_n which is the angle between the velocity vector and any *nth* pressure hole. This factor for sufficiently high velocities becomes independent of the Reynolds number and then it's only a function of the conical angle ϕ and the dihedral angle δ.

The author uses the following relations of pressures (80) and (81) in terms of the holes of the spherical probe for a known orientation of the probe with respect to the velocity vector of the free stream in order to determine the direction of the velocity vector in relation to the angles ϕ and δ respectively:

$$\frac{k_1 - k_3}{k_0 - k_3} = \frac{p_1 - p_3}{p_0 - p_3} = X_{133}(\phi, \delta) \qquad (80)$$

$$\frac{k_2 - k_4}{k_0 - k_3} = \frac{p_2 - p_4}{p_0 - p_3} = Y_{243}(\phi, \delta) \qquad (81)$$

According to Milne-Thomson (1950), the velocity at any point on the surface of the sphere corresponding to a radial line making an angle γ_n with respect to the direction of the velocity vector w is given by the following relation:

$$w_n = (\frac{3}{2}\sin\gamma_n)w \qquad (82)$$

Lee and Ash 1956 use the above relation in order to determine the pressure recovery factor k_n:

$$k_n = 1 - \frac{9}{4}\sin^2\gamma_n \qquad (83)$$

Then the pressure recovery factor ratios can be given as follows:

$$\frac{k_1 - k_3}{k_0 - k_3} = \frac{\sin^2\gamma_3 - \sin^2\gamma_1}{\sin^2\gamma_3 - \sin^2\gamma_0} = \frac{\cos^2\gamma_1 - \cos^2\gamma_3}{\cos^2\gamma_0 - \cos^2\gamma_3} \quad (84)$$

Using equations of spherical trigonometry the angle γ_n is related to the angles ϕ and δ as follows:

$$\cos\gamma_0 = \cos\phi \quad (85)$$

$$\cos\gamma_1 = \cos\phi \ \cos\alpha + \sin\alpha \ \sin\delta \ \sin\phi \quad (86)$$

$$\cos\gamma_2 = \cos\phi \ \cos\alpha + \sin\alpha \ \cos\delta \ \sin\phi \quad (87)$$

$$\cos\gamma_3 = \cos\phi \ \cos\alpha - \sin\alpha \ \sin\delta \ \sin\phi \quad (88)$$

$$\cos\gamma_4 = \cos\phi \ \cos\alpha - \sin\alpha \ \cos\delta \ \sin\phi \quad (89)$$

Using the above relations, the author managed to obtain the theoretical ratios of the pressure recovery factors:

$$X_{133} = \frac{k_1 - k_3}{k_0 - k_3} = \frac{2 \ \sin 2\alpha \ \sin\delta \ \sin 2\phi}{2 \ \sin^2\alpha \ (\cos^2\phi - \sin^2\delta \ \sin^2\phi) + \sin 2\alpha \ \sin\delta \ \sin 2\phi} \quad (90)$$

$$Y_{243} = \frac{k_2 - k_4}{k_0 - k_3} = \frac{2 \ \sin 2\alpha \ \cos\delta \ \sin 2\phi}{2 \ \sin^2\alpha \ (\cos^2\phi - \sin^2\delta \ \sin^2\phi) + \sin 2\alpha \ \sin\delta \ \sin 2\phi} \quad (91)$$

The velocity magnitude was determined as follows combining pressure holes number 0 and 3:

$$p_0 - p_3 = \rho\frac{w^2}{2}(k_0 - k_3) \Rightarrow w = \sqrt{\frac{2}{\rho}\frac{p_0 - p_3}{k_0 - k_3}} \quad (92)$$

where:

$$k_0 - k_3 = \frac{9}{4}(\cos^2\gamma_0 - \cos^2\gamma_3)$$
$$= \frac{9}{4}\left[\sin^2\alpha \ (\cos^2\phi - \sin^2\delta \ \sin^2\phi) + \frac{1}{2}(\sin 2\alpha \ \sin 2\phi \ \sin\delta)\right] \quad (93)$$

The static pressure of the airstream was given from the following equation:

$$p_s = p_0 - k_0\rho\frac{w^2}{2} \quad (94)$$

where the theoretical pressure factor value k_0 is given from the following relation (γ_0 is identical to the conical angle ϕ)

$$k_0 = 1 - \frac{9}{4}\sin^2\phi \qquad (95)$$

Shukry (1949) used a five-hole spherical pitot probe (see figure 2-34) in order to investigate spiral (three-dimensional flow) motion around bends.

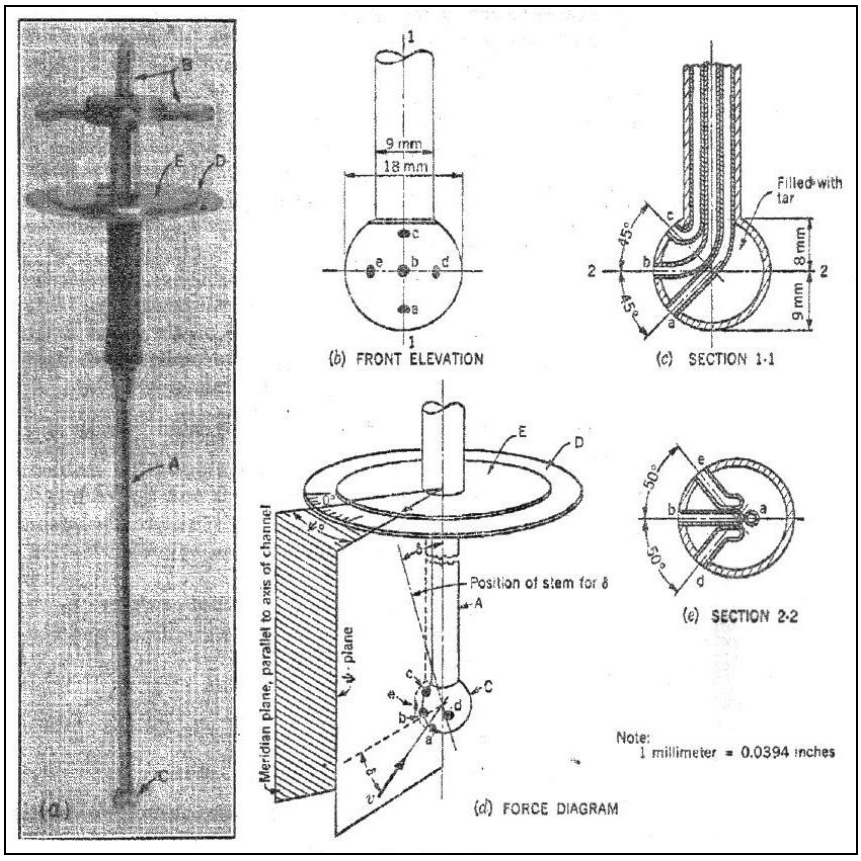

Figure 2–34: The pitot sphere (Shukry, 1949).

The probe was consisted of a spherical head with five holes a, b, c, d and e, a vertical stem and two discs one graduated in degrees (disk D) and one which was fixed on the stem and containing a pointer lying in the plane of holes a, b and c (disk E). The stem of the probe passed through a hole in disk D which was selected to be fixed in certain position and as a result when the stem was rotated the angle of deviation in degrees ψ could be obtained. According to the author, the procedure to use this kind of five-hole spherical pitot probe is as follows:

(Step 1) The probe is positioned in the channel of air flow with its stem perpendicular to the longitudinal axis of the channel. Then the probe is adjusted in such a way that the meridian plane comprising holes a, b and c and the zero of the graduated disk D, is parallel to the longitudinal axis.

(Step 2) The stem of the probe is then rotated until the pressure manometers connected to holes d and e indicate the same pressure values. This means that the velocity vector υ lies in the vertical plane passing through holes a, b, and c and the pointer of the disk E. Also, the angle ψ between the vertical plane and the meridian

plane can be read on disk D. Then the manometric heads h_a, h_b, h_c and h_d can be obtained.

(Step 3) In order to find the angle δ between the velocity vector and the direction of the longitudinal axis of the air flow channel, the stem of the probe should be rotated in the plane ψ about the center of the sphere until the manometer readings of holes a and c are equal. At this position, the velocity vector would directly pointing towards hole b and the pressure reading related to this hole would be the velocity head $\upsilon^2/2g$ from which the velocity magnitude could be obtained. The angle δ would be the angle between the normal and the inclined position of the stem.

But, since the angle δ could not be easily determined directly during the experiments the author referred to another method based on calibration data.

(Step 4) After getting the values of angles ψ and δ and the velocity magnitude of the velocity vector υ, the components of the vector in terms of x, y and z axis were determined from the following equations (see figure 2-35):

$$\upsilon_x = \upsilon \cos\delta \sin\psi \qquad (96)$$

$$\upsilon_y = \upsilon \sin\delta \qquad (97)$$

$$\upsilon_z = \upsilon \cos\delta \cos\psi \qquad (98)$$

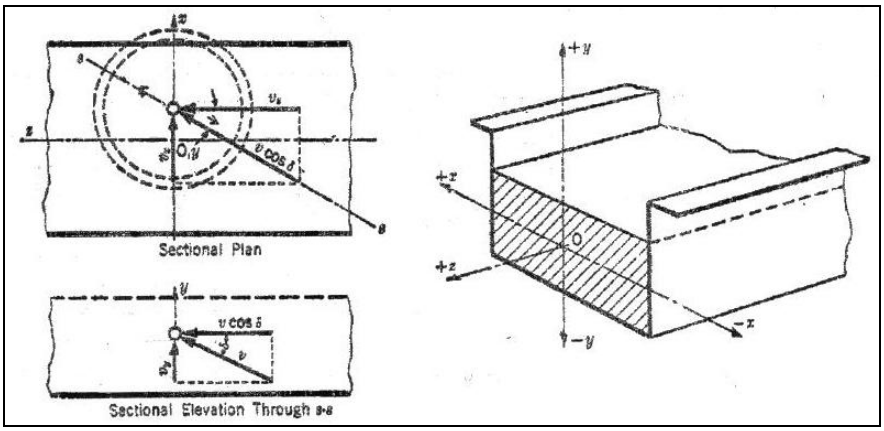

Figure 2–35: Flow coordinates and velocity components (Shukry, 1949).

For the calibration of this probe, the probe was inclined in terms of angle δ via small increments in the range between -60 and 60 degrees with a direction of parallel flow of known velocity υ_o and static pressure p_o (see figure 2-36). For any angle δ the manometers linked with holes e and d were first adjusted to give the same pressure readings and then the readings of manometric heads h_a', h_b', h_c' and h_d' were taken.

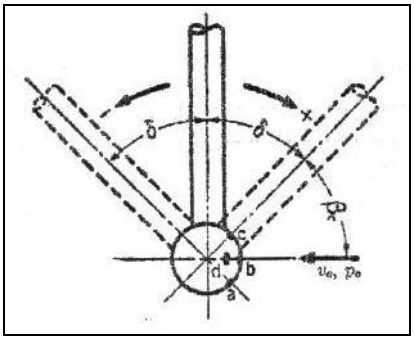

Figure 2–36: Angle of inclination δ (Shukry, 1949).

In order to obtain the pressure recovery factors or dynamic coefficients k or of holes a, b, c and d, the author referred to the theory of fluid mechanics (Springer 1934) which states that the pressure head at any hole m of a frictionless sphere in a potential flow, lying at an angle β_m (see figure 2-37) in the direction of the parallel flow is given by the following relation:

$$h_m^{'} = \frac{p_o}{\gamma} + \frac{\upsilon_o^2}{2g}\left(1 - \frac{9}{4}\sin^2\beta_m\right) = \frac{p_o}{\gamma} + k_m\frac{\upsilon_o^2}{2g} \qquad (99)$$

γ : specific weight

Therefore, knowing the values of velocity magnitude υ_o, static pressure p_o and hole manometric pressure heads $h_a^{'}$, $h_b^{'}$, $h_c^{'}$ and $h_d^{'}$ for each specified angle δ, the values of each hole pressure coefficients k_a, k_b, k_c and k_d were found.

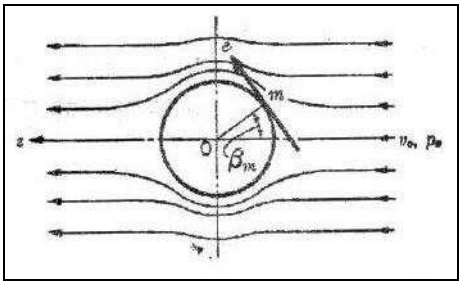

Figure 2–37: Steady flow pattern around a sphere (Shukry, 1949).

Combining all the above pressure coefficients an inclination factor k_δ was determined for every different value of angle δ :

$$k_\delta = \frac{h_c^{'} - h_a^{'}}{h_b^{'} - h_d^{'}} = \frac{k_c - k_a}{k_b - k_d} \qquad (100)$$

Having all these pressure coefficient values and the inclination factor determined for different angles δ , then a calibration chart was obtained as follows (figure 2-38):

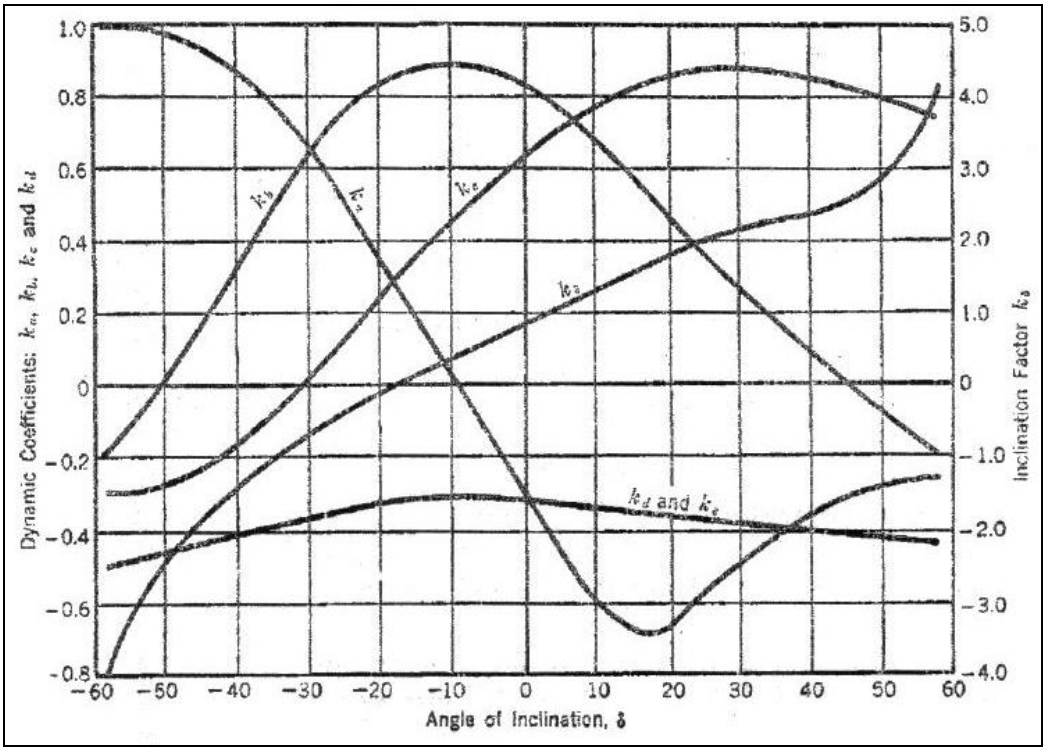

Figure 2–38: Dynamic coefficients and inclination factors versus angle δ (Shukry, 1949).

This calibration chart was used in order to define the flow angle δ during the normal experiments. Also, one must notice that the values of υ_o, p_o and h' for a probe inclined in a parallel flow are equal to the values of υ , p_s and h respectively when the probe is positioned normal to the channel axis and the velocity vector υ points at an angle δ with respect to the probe axis.
The manometric heads of the holes obtained experimentally can be expressed as follows:

$$h_a = \frac{p_s}{\gamma} + k_a \frac{\upsilon^2}{2g} \qquad (101)$$

$$h_b = \frac{p_s}{\gamma} + k_b \frac{\upsilon^2}{2g} \qquad (102)$$

$$h_c = \frac{p_s}{\gamma} + k_c \frac{\upsilon^2}{2g} \qquad (103)$$

$$h_d = \frac{p_s}{\gamma} + k_d \frac{\upsilon^2}{2g} \qquad (104)$$

Then combining all these manometric heads an expression of the velocity head can be obtained as follows which can give the magnitude of the velocity vector:

$$\frac{\upsilon^2}{2g} = \frac{h_a - h_b}{k_a - k_b} = \frac{h_b - h_c}{k_b - k_c} \qquad (105)$$

And the static pressure head can be obtained as follows:

$$\frac{p_s}{\gamma} = h_a - k_a \frac{\upsilon^2}{2g} = h_b - k_b \frac{\upsilon^2}{2g} \qquad (106)$$

Al-Hassani (1982) used a similar with Shukry's (1949) five-hole spherical pitot probe (see figure 2-39) in order to determine direction of velocity vectors behind cascade blades, velocity magnitude of the vectors and static pressure head.

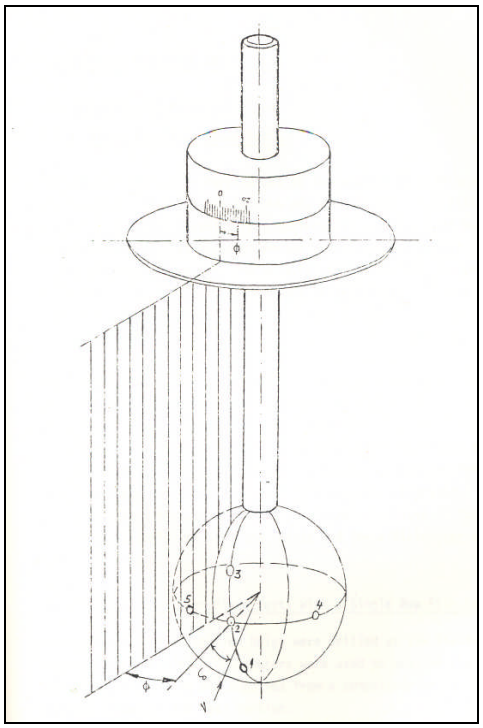

Figure 2–39 : Spherical tube yaw meter (Al-Hassani, 1982).

The spherical head (8 mm diameter) of the probe was set in such a position with respect to the flow so as the zero and 180 degree points of the circular dial of the probe coincide with the plane of the probe shaft axis of the tube. The probe was turned in it's guide until the pressure readings linked to the holes 4 and 5 were equal and then the angle ϕ was recorded from the dial of the fixed marker. In order to calculate the flow angle δ the following coefficient k_{1234} was estimated whose distribution in relation to the particular angle was given via a calibration chart (see figure A1 appendix):

$$k_{1234} = \frac{p_3 - p_1}{p_2 - p_4} \qquad (107)$$

p_1, p_2, p_3, p_4: differential pressures of point 1, 2, 3 and 4 in relation to free air

The velocity of the flow was given by using the following formula including data from holes 2 and 4:

$$V = \sqrt{\frac{p_2 - p_4}{k_{24}(1/2)\rho}} \qquad (108)$$

k_{24}: coefficient given from calibration chart

The static pressure was calculated as follows:

$$p = p_2 - k_2(\frac{1}{2}\rho V^2) \qquad (109)$$

k_2: coefficient given from calibration chart

2.8.2 Three hole cobra pressure probes

Three-hole pressure probes are frequently used for two-dimensional flow analysis related to turbomachinery components.The three hole pressure probes involve three pressure holes lying in one plane. They have mainly three different types of head geometries: cobra, trapezoidal and cylinder head. Probes can operate in two different ways by nulling or not nulling them. Nulling the probe means that the probe is oriented and aligned at the axis parallel to the air flow. Then the central hole measures approximately the total pressure and the pressures sensed by the side holes should be equal however, small differences caused by manufacturing imperfections or flow field variability are usually observed. Nulling the probe provides accurate measures but requires a device that nulls the probe continuously. For cases where the direction of the flow field varies significantly, nulling the probe is not recommended since it can take long time for the device that nulls the probe to find the nulling position. The non-nulling mode is less accurate but provides installation simplicity and it takes place by setting the probe at constant pitch and yaw angles. The pressures related to each hole are recorded by traversing the probe over the flow field and from these pressure values the direction and the velocity magnitude of the flow are determined. The geometry of a cobra three-hole pressure probe is illustrated in figure 2-40.

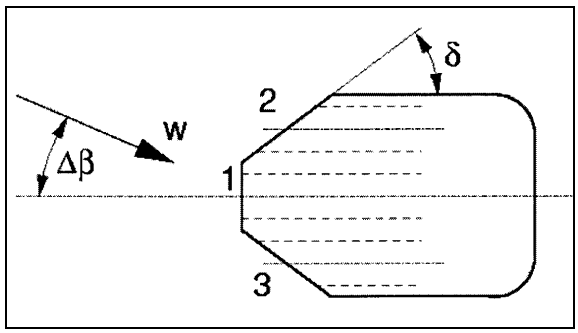

Figure 2–40: Three-hole cobra probe geometry (Rafel Giralt I Cubi, 2008).

For each probe hole the pressure can be non-dimensionalised according to the following coefficient:

$$k_i = \frac{p_i - p}{\frac{1}{2}\rho w^2} \quad (110)$$

i : probe hole number
k_i : hole coefficient
p_i : pressure sensed by hole i
p : static pressure
w : velocity

The air velocity w of the wind tunnel where the probe is located can be calculated from measurements of the pressure difference of total and static pressure according to:

$$w = \sqrt{\frac{p_t - p}{\rho / 2}} \quad (111)$$

According to Rafel Giralt I Cubi (2008), the coefficients related to the three-hole probe are used to reduce the data on the non-dimensional coefficients by Treaster and Yocum (1979). They found that the dynamic pressure expressed by the difference between the total pressure p_1 and the mean hole pressure $\overline{p}$ was a normalizing parameter which reduced the scatter of calibration data compared to the case of using the true dynamic pressure.

Direction coefficient k_β

$$k_\beta = \frac{p_2 - p_3}{p_1 - \overline{p}} = \frac{k_2 - k_3}{k_1 - \overline{k}} \quad (112)$$

Total pressure coefficient k_t

$$k_t = \frac{p_1 - p_t}{p_1 - \overline{p}} = \frac{k_1 - 1}{k_1 - \overline{k}} \quad (113)$$

Static pressure coefficient k_s

$$k_s = \frac{\overline{p} - p}{p_1 - \overline{p}} = \frac{\overline{k}}{k_1 - \overline{k}} \quad (114)$$

$$\overline{p} = \frac{p_2 + p_3}{2} \quad (115)$$

$\overline{p}$: mean hole pressure

p_t : total pressure

$$\overline{k} = \frac{k_2 + k_3}{2} \quad (116)$$

$\overline{k}$: mean hole coefficient

2.8.2.1 Streamline projection method

The streamline projection method is a simple method which can predict the calibration coefficients related to a three-hole pressure probe. The streamline projection method assumes that the free air stream velocity is projected on each pressure hole of the probe. In this case the probe holes sense the sum of free stream static pressure and dynamic pressure which velocity component is normal at them as follows:

$$p_i = p + \frac{1}{2}\rho w_i^2 \quad (117)$$

Relating the equation that defines the probe hole coefficient

$$p_i = p + \frac{k_i}{2}\rho w^2 \quad (118)$$

the hole coefficient can be written as follows:

$$k_i = \left(\frac{w_i}{w}\right)^2 \quad (119)$$

Figure 2-41 illustrates the projection of the velocity vectors of magnitude w normal to each pressure hole.

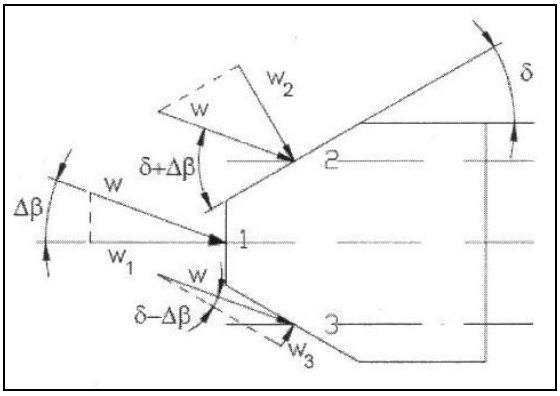

Figure 2–41: Velocity components over a cobra probe head (Rafel Giralt I Cubi, 2008).

The normal velocity components for each hole are obtained which are the following:

$$w_1 = w\cos\Delta\beta \qquad (120)$$

$$w_2 = w\sin(\delta + \Delta\beta) \qquad (121)$$

$$w_3 = w\sin(\delta - \Delta\beta) \qquad (122)$$

$\Delta\beta$: yaw angle

δ : wedge angle

Substituting the normal velocity components on the hole pressure formula, the pressures sensed by each probe hole are obtained:

$$p_1 = p + \frac{1}{2}\rho(w\cos\Delta\beta)^2 \qquad (123)$$

$$p_2 = p + \frac{1}{2}\rho[w\sin(\delta + \Delta\beta)]^2 \qquad (124)$$

$$p_3 = p + \frac{1}{2}\rho[w\sin(\delta - \Delta\beta)]^2 \qquad (125)$$

So, the coefficients relevant to each hole are found as follows:

$$k_1 = \cos^2\Delta\beta \qquad (126)$$

$$k_2 = \sin^2(\delta + \Delta\beta) \qquad (127)$$

$$k_3 = \sin^2(\delta - \Delta\beta) \qquad (128)$$

2.8.2.2 Three-hole cobra probe calibration procedure

Before being used for turbomachinery measurements a probe has to be calibrated. Lerena Diaz (2003) used an open jet wind tunnel (see figure 2-42) in order to calibrate a three-hole cobra probe which was positioned at a number of certain angular increment settings with constant free air jet velocity and low turbulence intensity. The calibration took place at a Mach number level between 0.05 and 0.14 at different Reynolds numbers by varying the yaw angle of the probe from -30^o to +30^o in increments of 2.5^o for zero pitch angles. The objective of the project was to investigate the influence of different head geometries and Reynolds numbers on the calibration coefficients of three-hole pressure probes.

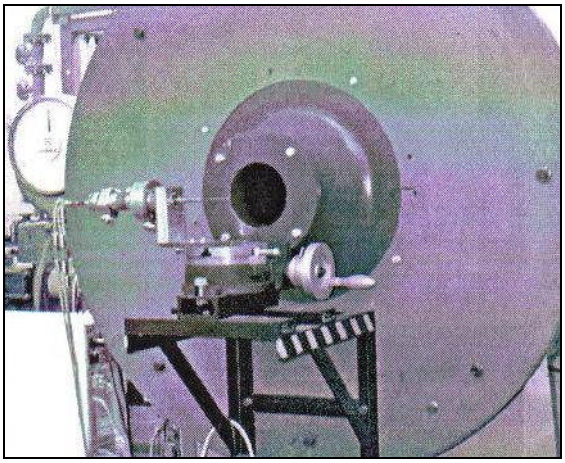

Figure 2–42: Cobra probe calibration facility (Rafel Giralt I Cubi, 2008).

Calibration curves regarding the hole coefficients k_1, k_2 and k_3 against yaw angle $\Delta\beta$ were obtained and good agreement between the experimental and streamline projection method results were achieved in terms of the hole coefficient k_1. Discrepancies were observed in terms of the hole coefficients k_2 and k_3 since the streamline projection method does not take into consideration the probe head suction side separation. In terms of the direction coefficient k_β and total pressure coefficient k_t good agreement was obtained between experimental calibration and streamline projection method results, however, good agreement was not observed for the static pressure coefficient k_s.

The author calibrated the three hole pressure probes at two different Reynolds numbers of 3750 and 7500 and reported that the direction coefficient k_β and the total pressure coefficient k_t were unaffected. However, the static pressure coefficient k_s was found to be affected from the Reynolds number variation for the whole range of yaw angles, in a sense that increasing the Reynolds number the value of the coefficient decreases.

2.9 Hot wire anemometer

2.9.1 Hot wire anemometer units

The study of turbulence in wind tunnels is very important and such studies can be carried out by using proper instrumentation like hot-wire anemometers often called constant temperature anemometers (CTA).
The measuring equipment of a hot wire anemometer typically involves a probe with it's support, cabling, a CTA anemometer, a signal conditioner, an Analog/Digital converter and a computer with a special application software for CTA set-up, data acquisition and data analysis (see figure 2-43).

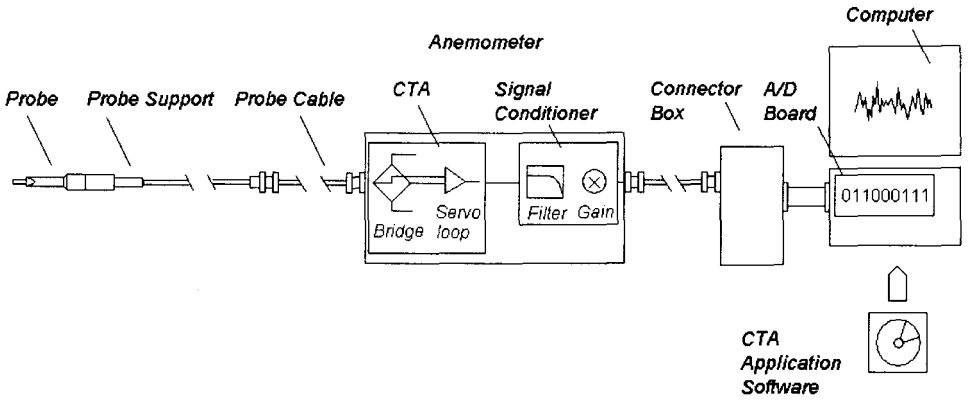

Figure 2–43: Typical CTA measuring chain (Jorgensen, 2002).

2.9.2 Probes

Anemometer probes (see figure 2-44) are provided with four types of sensors: miniature wires, gold-plated wires, fibre-film and film-sensors.

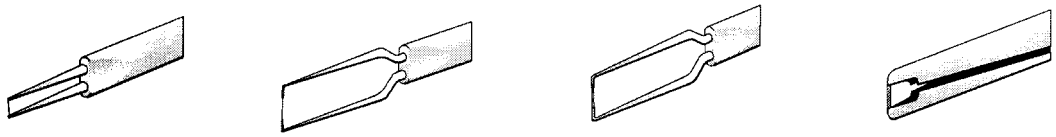

Figure 2–44: Sensor types (Jorgensen, 2002).

Wires normally have a 5 μm diameter and a length of 1.2 mm and they are suspended between two needle-shaped prongs. Miniature wires can be used in air flows with turbulence intensity up to 5-10%, they have the highest frequency response, they can be repaired and they are the most affordable sensors. Gold-plated sensors can be used in air flows with turbulence intensities up to 20-25% and their frequency response is inferior to miniature wires.

Fibre-film sensors are more rugged than wire sensors, their frequency response is inferior to wires and they can be used in less clean air. Film-sensors can operate in air at moderate-to-low fluctuation frequencies, they are the most rugged probe type, they can be used in less clean air than the fibre-sensors and they are not repairable.
Hot wire anemometer probes can be split in single, dual and triple sensor probes according to the number of sensors (see figure 2-45) representing the one, two and three-dimensional versions of the probes respectively.

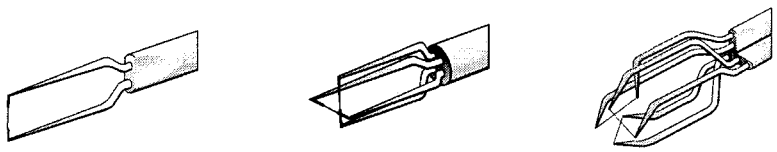

Figure 2–45: Sensor arrays (Jorgensen, 2002).

In terms of positioning the probe is preferably set with the wire perpendicular to the flow and the prongs parallel to the flow (see figure 2-46). According to Jorgensen (2002) it is recommended that the probe coordinate system (X, Y, Z) coincides with that of the laboratory (U, V, W).

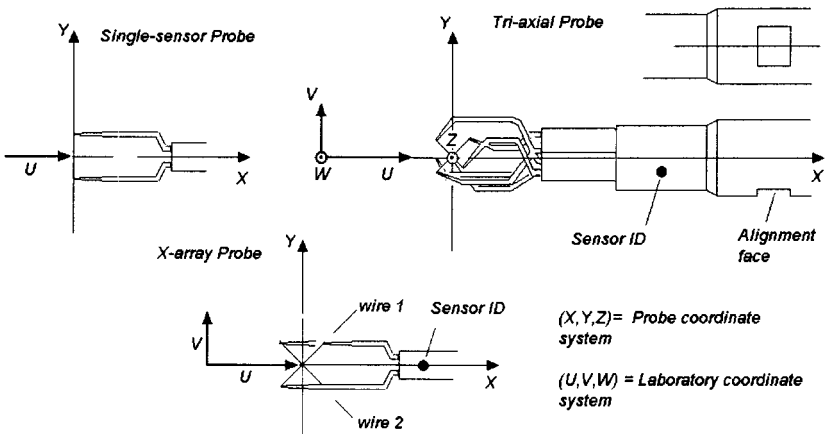

Figure 2–46: Probe orientation (Jorgensen, 2002).

The hot wire anemometers can be research type anemometers which are multi-channel systems with up to six or more CTA channels, or they can be dedicated anemometers involving a single channel and supporting one sensor. Most of the CTA anemometers include a signal conditioners for high-pass and low-pass filtering and for amplification of the anemometer signal. The high-pass filter removes the DC-part of the signal and the low-pass filter removes the electronic noise from the signal. After the CTA, the signal passes through an analogue-to-digital A/D converter board and then it is saved as data series in a computer which is equipped with an application software for running the anemometer.

2.9.3 Constant temperature anemometer unit

The measure of the instantaneous flow velocity using such an instrument is based on the heat transfer between the sensor of it and the surrounding fluid medium. An electric current is sent through the wire and the wire heats up. As the air flows over the wire, it cools the wire and removes some of it's heat energy. An energy balance equation can be used to for the heating and cooling of the wire and solving this equation the velocity of the fluid over the wire can be found. Hot-wire anemometers are used as part of a Wheatstone bridge configuration (see figure 2-47).

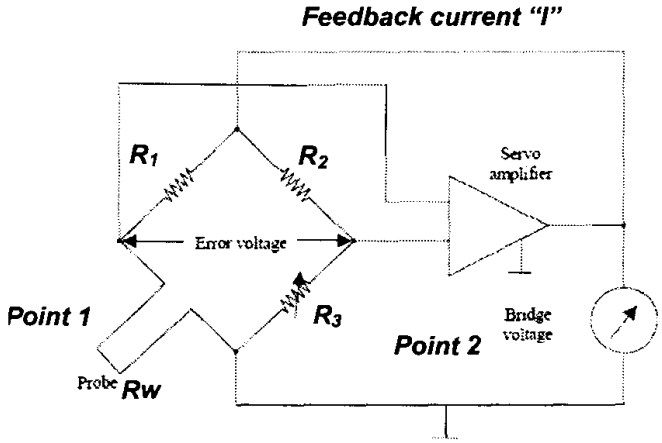

Figure 2–47: CTA anemometer principle diagram (www.qats.com).

The circuit of the bridge comprises two known fixed resistors R_1 and R_2 and a third variable resistor R_3. The hot-wire probe is the forth resistor R_w completing the Wheatstone bridge. The bridge is balanced when $R_1/ R_w= R_2/ R_3$ and then the voltage difference (error voltage) between points 1 and 2 is zero. This can be achieved by adjusting the variable resistor R_3. As the speed of air passing over the wire increases or decreases, the wire temperature changes and it's resistance as well. Then the bridge becomes unbalanced and a voltage difference exists between points 1 and 2. The amplifier of the anemometer detects this voltage difference and adjusts a feedback current accordingly in order to keep the wire temperature and resistance constant and to bring the bridge in the balanced condition again. These current changes can be measured and used to calculate the velocity of the flow over the wire.

$$W = Q + \frac{dQ_i}{dt} \quad (129)$$

$$Q_i = C_w T_w \quad (130)$$

W : power generated by heating the wire
Q : heat transferred to the surroundings
Q_i : thermal energy stored in the wire
C_w : wire heat capacity
T_w : wire temperature

Assuming that the wire heat storage is zero then

$$W = Q = I^2 R_w = h_{conv} A_{wire} (T_w - T_0) \quad (131)$$

h_{conv} : convective heat transfer coefficient
A_{wire} : wire surface area exposed to the fluid flow
T_0 : wire reference temperature
R_w : wire resistance
I : current through the circuit

Since $Nu = \frac{h_{conv} d}{k}$ (132)

Nu : Nusselt number
d : wire diameter
k : fluid thermal conductivity

Then

$$I^2 R_w = A_{wire} \frac{Nuk}{d} (T_w - T_0) \quad \text{(a)(133)}$$

According to Perry (1982)

$$Nu = 0.42 \,\mathrm{Pr}^{0.2} + 0.57 \,\mathrm{Pr}^{0.33} \,\mathrm{Re}^{0.5} \quad (134)$$

$$\mathrm{Pr} = \frac{\mu C_p}{k} \quad (135)$$

Pr : Prandtl number
μ : fluid dynamic viscosity
C_p : specific heat of the fluid at constant temperature

$$\mathrm{Re} = \frac{\rho U d}{\mu} \quad (136)$$

Re : Reynolds number
ρ : fluid density
U : fluid velocity

Therefore the Nusselt number can be expressed in the form:

$$Nu = A_1' + B_1' \,\mathrm{Re}^n = A_2' + B_2' U^n \quad (137)$$

and substituting into equation (133) then:

$$I^2 R_w^2 = E^2 = (T_w - T_0)(A' + B' U^n) \quad \text{(S)(138)}$$

A', B': empirical constants

Hence the voltage of the hot wire is a measure of the fluid velocity U according tp King's law (1914) and the magnitude of the exponent n was found to be 0.5.

2.9.4 Signal conditioner and A/D converter

The signal coming out from the constant temperature anemometer (output voltage) is fed to a signal conditioning unit. This unit is used in order to match it's output voltage to the input voltage range of the A/D converter. The scope of the analog/digital converter is to change it's analog input signal into the equivalent value in digital format.

2.9.5 Hot wire set-up

The set-up of the constant temperature hot wire anemometer includes static bridge balancing (overheat adjustment) and dynamic balancing (square wave test). The hardware set-up also includes low-pass filter and optional gain settings when a signal conditioner is part of the CTA anemometer.
The overheat adjustment takes place in order to determine the sensor working temperature. The variable resistor is adjusted, so that the desired sensor operating temperature is established when the bridge is set into Operate. The relation between the hot and cold resistor is given by the overheat ratio a (recommended value in air 0.8):

$$a = \frac{R_w - R_0}{R_0} \quad (139)$$

$$R_w = R_{20}[1 + \alpha_{20}(T_w - 20)] \quad (140)$$

R_w: sensor (heated) resistance at operating temperature T_w
R_0: sensor (cold) resistance at ambient reference temperature T_0
R_{20}: sensor resistance at 20^oC
α_{20}: temperature coefficient (at 20^oC)

The active sensor resistance R_0 can be calculated by subtracting the probe leads resistance R_{leads}, the resistance of the connection leads in the probe support $R_{\sup\ port}$ and the cable resistance R_{cable} from the measured total resistance $R_{tot,0}$:

$$R_0 = R_{tot,0} - (R_{leads} + R_{\sup\ port} + R_{cable}) \quad (137)$$

The variable resistance can then be calculated as follows:

$$R_{\text{var}\,iable} = (1+a)R_0 + R_{leads} + R_{\text{sup}\,port} + R_{cable} \qquad (141)$$

The variable resistance is adjusted to the calculated value $R_{\text{var}\,iable}$.

The square wave test allows measurement and optimization of the system frequency response. A square wave generator is placed in parallel with the probe in order to add a square wave of small amplitude to the sensor heating current. According to Lomas (1986) the square wave test is based on the assumption that sensor heating and cooling by varying the velocity of the fluid is thermodynamically identical to heating and cooling of the sensor by varying the heating current. When the square wave current is introduced, the current passing through the sensor increases and then drops to it's original value due to the interference of the amplifier via a feedback signal reducing the heating current in order to balance the anemometer bridge and this has the same effect as a sudden decrease in the velocity of the fluid. When the square wave current decreases, the amplifier increases the heating current to bring the resistance of the sensor at it's original value and to balance the bridge again.
According to Bruun (1995) the optimum response to a square wave test can be obtained by adjusting the controls until the response signal in figure 2-48 is achieved having a 15% undershoot relative to the maximum. Defining the time constant τ_w as the time between the start of the pulse and the point where the response signal has decayed to 3% of it's maximum value, the bandwidth of the probe-anemometer system (cut-off frequency) f_c can be determined:

$$f_c = \frac{1}{1.3\tau_w} \qquad (142)$$

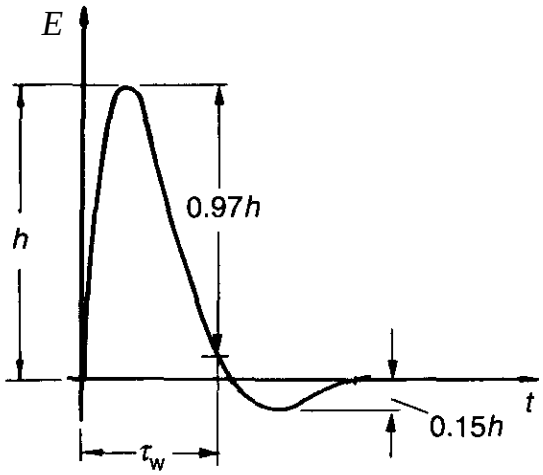

Figure 2–48: Hot-wire probe square-wave test response (Bruun, 1995).

The system response can be optimised by adjusting the amplifier filter and gain but, most manufacturers recommend default settings. Low-pass filtering is applied in order to decrease the electronic noise, high pass filtering is used to clean the signal and to

make it stationary and gain is applied to amplify the anemometer signal in order to utilise an A/D board with a resolution that is too small for the application.

2.9.6 Hot wire anemometer calibration

Calibration of a hot wire anemometer can be performed either in a dedicated calibrator with a low-turbulent free jet whose velocity is calculated from the pressure drop over its exit or in the wind-tunnel where the experiments are going to take place using a pitot-static tube. For the calibration the probe is exposed to a range of known velocities U and then the voltages E of the anemometer are recorded. Plotting the voltage and the velocity data points one curve fit through all these points can be constructed (see figure 2-49) representing the transfer function that is going to be used when converting data records from voltages into velocities. Therefore, via the calibration a relation is established between the anemometer output and the velocity of the flow.

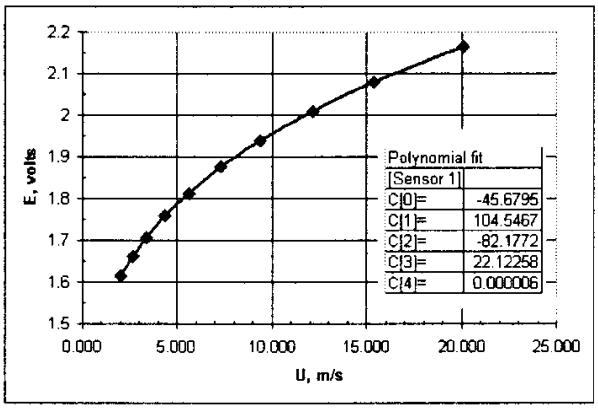

Figure 2–49: Curve fitting of calibration data (Jorgensen, 2002).

The curve fit can be expressed with a 4th order polynomial trend line as follows:

$$U = C_0 + C_1 E + C_2 E^2 + C_3 E^3 + C_4 E^4 \qquad (143)$$

C_0, C_1, C_2, C_3, C_4: constants

2.9.7 Data acquisition

The signal coming out from a hot wire anemometer is a continuous analogue voltage and in order the signal to be processed digitally it has to be sampled as a time series consisting of discrete values digitized by an A/D converter. The time series can be analysed either in the amplitude domain, the time domain or in the frequency domain. The analysis in the amplitude domain provides information about the amplitude distribution of the signal and according to Jorgensen (2002) it is based on one or more time series sampled on the basis of a single integral time-scale in the flow. A velocity time series represents data from one sensor converted into a velocity component. A

single velocity time series provides mean velocity U_{mean} and standard deviation of velocity U_{rms} in order to estimate turbulence intensity:

$$U_{mean} = \frac{1}{N}\sum_{1}^{N} U_i \qquad (144)$$

N : number of samples

U_i : instantaneous velocity

$$U_{rms} = \left(\frac{1}{N-1}\sum_{1}^{N} (U_i - U_{mean})^2 \right)^{0.5} \qquad (145)$$

$$Tu = \frac{U_{rms}}{U_{mean}} \qquad (146)$$

Tu : turbulence intensity

A typical mean velocity and standard deviation of velocity distribution with respect to time is illustrated in figure 2-50:

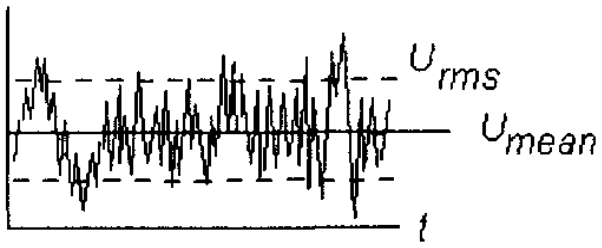

Figure 2–50: Mean and rms velocity versus time (Jorgensen, 2002).

In terms of analysing the time series in the time domain an integral length scale can be calculated from an auto-correlation function $R_x(\tau)$. The autocorrelation function describes the dependence of the data at one time on the values at another time. Considering an infinitely long time record, $x(t)$, with a zero mean (see figure 2-51), the autocorrelation between the values of $x(t)$ at times t and $t+\tau$ can be expressed as follows:

$$R_x(\tau) = \lim_{T\to\infty} \frac{1}{T}\int_{0}^{T} x(t)x(t+\tau)\ dt \qquad (147)$$

T : total sampling time

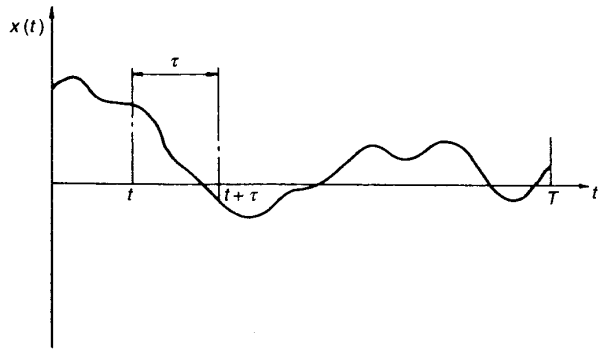

Figure 2–51: Autocorrelation measurements (Bruun, 1995).

Most of the hot wire anemometer application softwares comprise an autocorrelation coefficient function $\rho_x(\tau)$ which is calculated and graphically displayed (see figure 2-52).

$$\rho_x(\tau) = \frac{R_x(\tau)}{R_x(0)} \qquad (148)$$

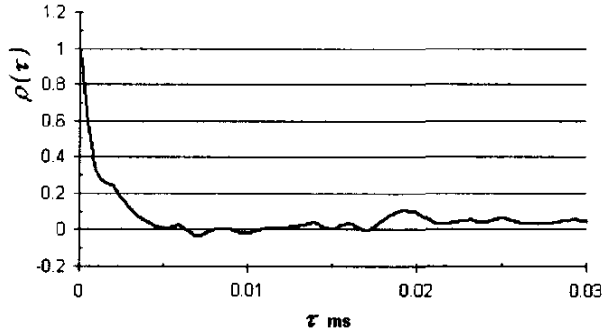

Figure 2–52: Drop of auto-correlation coefficient (Jorgensen, 2002).

At time zero it starts with a value of 1 and falls down to 0 and usually continues oscillating around this value and the time it takes the coefficient to drop from the value of 1 to the value of 0 is the integral time scale T_1

$$T_1 = \int_0^\infty \rho_x(\tau) d\tau \qquad (149)$$

2.9.8 Turbulent length scale

The length scale is a very useful concept for examining turbulent field structures. According to Lenschow and Stankov (1986), for fixed-point boundary layer observations, a time scale can be related to a length scale by multiplying the mean wind speed by the time scale and this requires the assumption of "frozen turbulence" involved in the Taylor's hypothesis (Taylor, 1938). To illustrate these ideas Panofsky and Dutton (1984) consider the record of an atmospheric variable A observed at a

fixed point as shown in figure 2-53. Assuming that the turbulent eddies are carried by the mean wind velocity U and change slowly as they move, it can be assumed that the flow pattern is produced by having a spatial pattern in the x direction moving past the observer with speed U without change of shape. The spatial pattern could be depicted with the axis relabelled as x=Ut and this notion is called the frozen wave hypothesis or Taylor's hypothesis.

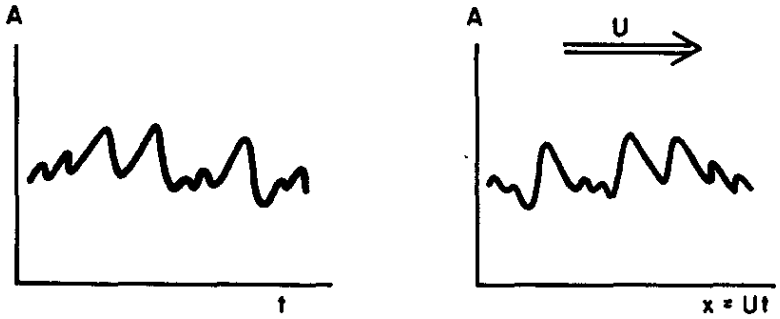

Figure 2–53: Taylor's hypothesis illustration (Panofsky and Dutton, 1984).

2.10 Roughness issues

The effect of surface roughness on turbomachinery flows has been examined by many engineers in order to improve as many as possible gas turbine performance issues. Gbadebo et al (2004), applying surface roughness on stator blading of a single-stage low-speed axial compressor, found that it has major effect on the three dimensional separation at the hub. Surface flow visualization and exit loss measurements showed that the size of separation was increased with the presence of roughness. The authors illustrated experimentally that when roughness is applied between the leading edge and suction peak it has a significant negative effect on the performance of the stage, whereas when it is applied downstream of the suction peak the effect is negligible.
Leipold et al (2000) investigated the effect of surface roughness on the flow around a highly loaded compressor cascade by measuring profile pressure distribution and the local total pressures at the exit measuring plane of a smooth and a roughened blade for a variation of inlet flow angle and inlet Reynolds number. They found that at low Reynolds numbers and small inlet angles, the surface roughness reduces slightly the separation bubble created. However, this reduction is overcompensated by the negative effect of roughness on the turbulent boundary layer downstream of the bubble. Also, at higher Reynolds numbers roughness causes turbulent separation associated with high total pressure losses.
Zhang et al. (2004) investigated the effects of surface roughness on the aerodynamic performance of turbine airfoils for different inlet turbulence intensity levels of 0.9%, 5.5% and 16.2%. Their work showed that changing the surface roughness condition, the effect on the integrated aerodynamic losses is significant, whereas altering the inlet turbulence intensity level the effect is small. The magnitudes of integrated aerodynamic losses were determined by integrating profiles of exit free-stream stagnation pressure minus exit local stagnation pressure with respect to a normal coordinate measured from airfoil centerline in the traverse flow direction across the wake.

Bammert and Sandstede (1980) carried out measurements of boundary layer development in a cascade wind tunnel representing a section through the stator blades of a gas turbine of 50 percent reaction. The authors tested smooth and roughened blades and they stated that surface roughness increases the friction factor and causes a shift of the transition point forward.

Suder et al (1995) reported the performance deterioration of a high-speed axial compressor rotor by varying the airfoil surface roughness and thickness. A smooth and a rough coating were applied to different portions of the blade surface to determine the blade portions that are most sensitive to thickness/roughness variations. The authors found that at design speed the areas that are most sensitive to roughness, are the leading edge and the front half of the suction surface in terms of performance degradation and based on flow field predictions generated using quasi and full three-dimensional dimensional Navier-Stokes codes they indicated that adding thickness to the rotor has a small impact in terms of performance. Applying roughness on the blades causes boundary layer thickening of the suction surface downstream of the shock/boundary layer interaction, hence causing a passage blockage which reduces the diffusion process and reduces the rotor pressure and temperature rise. Examining relative Mach number variations pitchwise at 15% chord distance behind the trailing edge at a blade height of 70% span, it was illustrated that an increase in Mach number and in wake momentum deficit takes place as the roughness increases.

Bammert and Milsch (1972) carried out experiments on compressor cascades consisted of roughened NACA 65 series blade sections in different geometrical variations. They illustrated that loss coefficients rise by increasing the roughness grade which is the ratio of sand roughness over the chord length. Testing profiles of smaller thickness the losses were lower than those corresponding to profiles of higher thickness. The authors illustrated that increasing the surface roughness the turning angle decreases, as well.

A lot of researchers have also correlated roughness results in terms of equivalent sand grain roughness k_s in order to use a common language of surface roughness characterization translating turbomachinery roughness into roughness associated with pipe and external flows. The equivalent sand grain roughness was first used by Nikuradse (1993) and Schlichting (1936) and it represents the sand grain size giving the same skin friction coefficient as the roughness evaluated for internal flow passages.

Chapter 3 - Industrial gas turbine intake water injection simulation

3.1 Industrial intake geometry

CFD results are very important in order to provide a basis of optimizing the position of injecting water within an industrial gas turbine intake. The intake of an industrial gas turbine ABB GT13 D2 (5 m height, 2.8 m length and 5.6 m width) located at Baran district of Rajasthan, India at an altitude of 240 m with 27 ^{o}C ambient temperature was investigated via CFD tools (Fluent 6.3, 2007) in terms of airflow and on-line water injection for compressor washing (see figure 3-1).

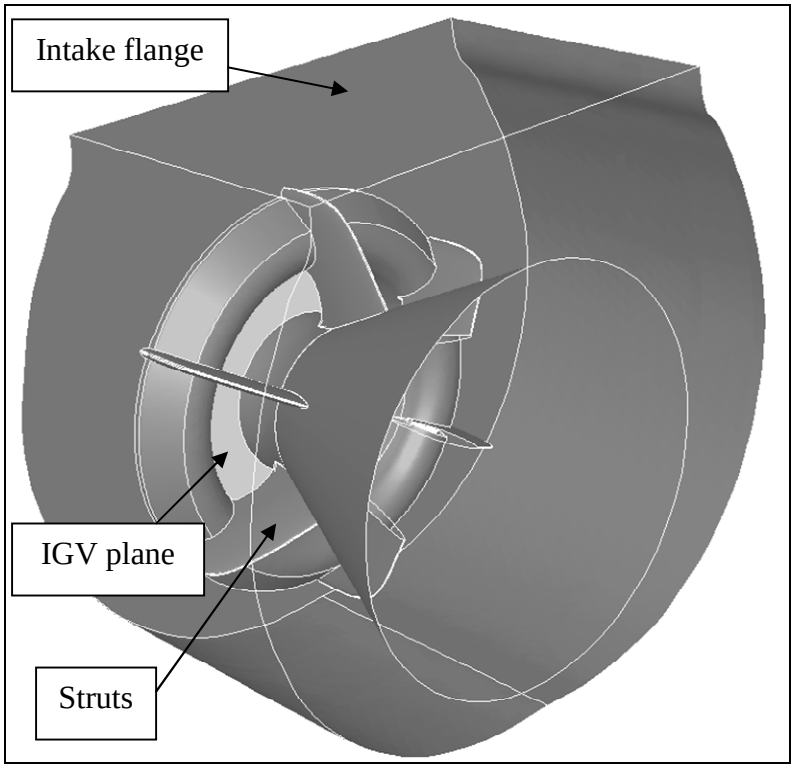

Figure 3–1: Industrial gas turbine (ABB GT13 D2) intake.

The intake of the gas turbine manifold involved six struts starting from the 12 o'clock position and spreading circumferentially at 60 degrees apart. To avoid any possible swirl components into the annulus flow, the camber angle of the strut cross-sectional profile was set at zero.

3.2 Boundary conditions for the industrial intake

In order to run the simulation the filters attached to the intake were not included. The pressure drop along the filters was assumed to be 400 Pa which corresponds to a

pressure drop for high velocity filters. The total pressure at the exit of the filters was set to be 97900 Pa at 27 ^{o}C total pressure. Assuming that the flow between the inlet of the intake part simulated and the outlet is adiabatic and knowing the air mass flow rate (370 kg/s), the IGV plane area (2.305 m^2), the total pressure on the IGV plane (97450 Pa) and the total temperature there (300.15 K), from compressible flow tables the value of the Mach number on the IGV plane was calculated to be approximately 0.5. Then using the following formula for compressible flow the static pressure on the IGV plane was calculated to be 84082 Pa:

$$\frac{P_{IGV}}{p_{IGV}} = (1 + \frac{\gamma - 1}{2} M_{IGV}^{2})^{\frac{\gamma}{\gamma - 1}} \qquad (150)$$

P_{IGV} **:** Total pressure on the IGV plane

p_{IGV} **:** Static pressure on the IGV plane

M_{IGV} **:** Mach number on the IGV plane

γ : 1.4

3.3 Industrial gas turbine intake meshing

The volume geometry of the industrial gas turbine was filled with tetrahedral and hexahedral cells. The zone close to the struts and the compressor intake (IGV plane) was comprised from structured grid for better accuracy, while the zone outside the struts was filled with tetrahedral cells hence course mesh, in order to save grid cells for the area of the zone close to the IGV plane (see figure 3-2).

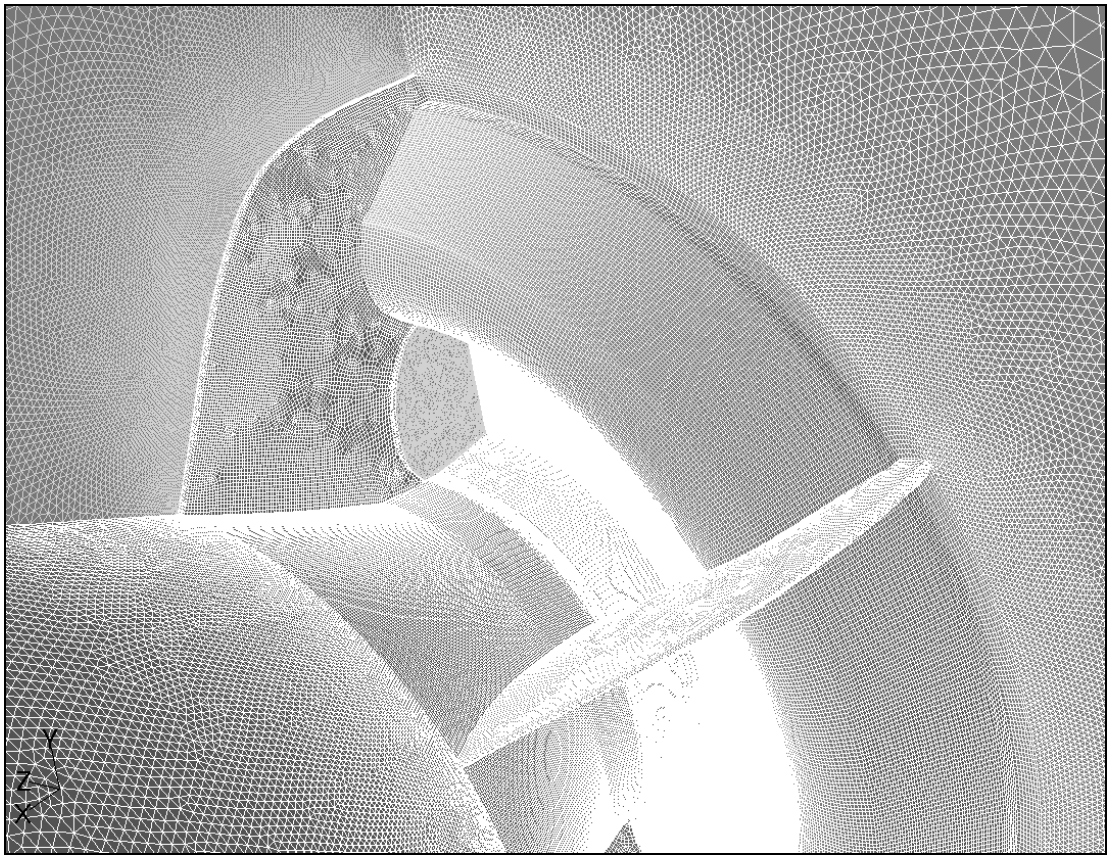

Figure 3–2: ABB GT13 D2 intake mesh resolution.

In order to investigate the intake computationally, six different meshes were generated:

Course mesh: 1,997,814 million tetrahedral cells
Pre medium mesh: 6,280,953 mixed cells (tetrahedral and hexahedral cells)
Medium mesh: 10,370,992 mixed cells
Better medium mesh: 10,564,770 mixed cells
Less fine mesh: 11,364,941 mixed cells
Fine mesh: 12,286,906 mixed cells
All these meshes were investigated in order to get grid independency for the simulation. The parameters checked for grid independency were the aerodynamic total pressure loss coefficients (Y) between the intake flange (F1) and the IGV (inlet guide vane) plane and the referred total pressure loss coefficient (X) according to Biesinger's (2002) definitions for a similar industrial gas turbine intake (see figure 3-3):

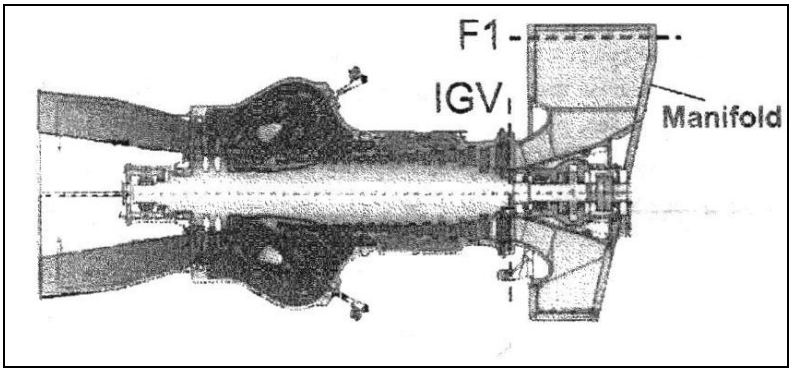

Figure 3–3: Typical manifold with flange F1 (Biesinger and Lepel, 2002).

$$Y = \frac{P_{F1} - P_{IGV}}{P_{IGV} - p_{IGV}} \quad (151)$$

$$X = \frac{P_{F1} - P_{IGV}}{P_{IGV}}(\%) \quad (152)$$

P_{F1}: flange total pressure

P_{IGV}: total pressure on the IGV plane

p_{IGV}: static pressure on the IGV plane

Plotting the total pressure loss coefficients (Y) and (X), one can see that after about 10 million cells these parameters seem to stabilize (see figures 3-4 and 3-5) and as a result for further simulation runs the grid involving the fine mesh was selected.

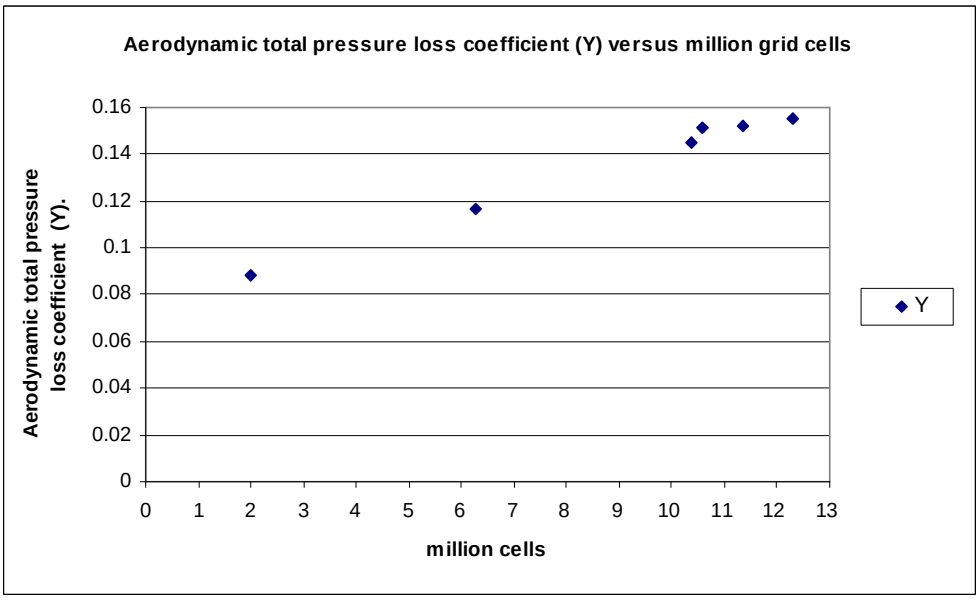

Figure 3–4: Y parameter versus number of grid cells.

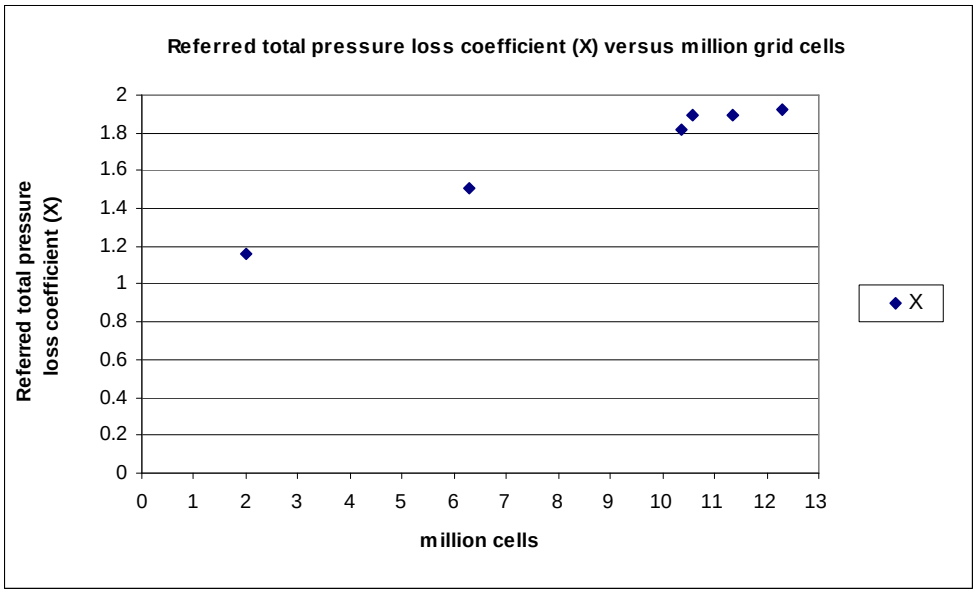

Figure 3–5: X parameter versus number of grid cells.

3.4 Turbulence model and solver selection

For the simulation of the industrial gas turbine intake the standard k-ε model was selected. The standard k-ε model is characterized by its robustness, economy, and reasonable accuracy for a wide range of turbulent flows which explains its popularity in industrial flow and heat transfer simulations.
The pressure based solver of Fluent was used for solving the continuous phase, involving the SIMPLE algorithm for pressure-velocity coupling and the second order discretization scheme was implemented for the flow equations.

3.5 Spray (discrete phase) parameters

The two phase flow for the present simulation was assumed to be sufficiently diluted meaning so that particle-particle interactions and the effects of the dispersed phase (droplets) on the continuous phase (air) are negligible. For sufficiently diluted flows involving a dispersed phase which does not exceed a volume fraction of 10-12 %, Fluent uses a Lagrangian frame of reference for the dispersed phase which is consisted of spherical particles.
The trajectories of the dispersed or discrete phase are obtained by applying under integration a force balance on the particle. This balance equates the inertia of the particle with the forces acting on the particle, including the hydrodynamic drag and the gravity force.
The water droplets for the simulation were modelled as inert particles not subjected to evaporation since the temperature rises halfway within an industrial gas turbine intake duct. For the current simulation particle-particle interactions were not taken into account since a very small amount of dispersed fluid was injected approximately 0.2 % per cent mass fraction. Droplet collision, deformation or break up was not taken into account either.
The type of discrete phase boundary condition was selected to be the default “reflect” type with a coefficient of restitution value equal to 1. “Reflect” according to Fluent 6.3 means rebound the particle off the boundary in question with a change in it’s momentum as defined by the coefficient of restitution (see figure 3-6):

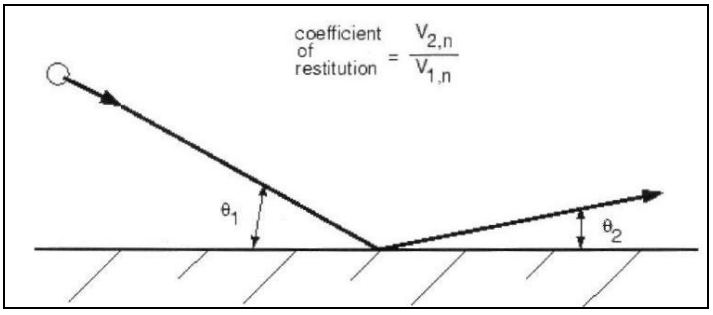

Figure 3–6: ‘Reflect’ boundary condition for the discrete phase (Anonymous, Fluent 6.3, 2007).

The normal coefficient of restitution defines the amount of momentum in the direction normal to the wall that is retained by the particle after the collision with the boundary.

$$e_n = \frac{V_{2,n}}{V_{1,n}} \qquad (153)$$

e_n : normal coefficient of restitution

$V_{2,n}$: particle velocity normal to the wall after collision

$V_{1,n}$: particle velocity normal to the wall before collision

A normal or tangential coefficient of restitution equal to 1 means that the droplet retains all of its normal or tangential momentum after the rebound implying an elastic

collision. The default setting for both coefficient of restitution is a constant value 1 implying that all normal and tangential momentum is retained.

3.6 Nozzle Injection arrangements and CFD analysis

The first simulation was run with 19 nozzles injecting towards the gas turbine IGV plane, positioned according to normal set (see figures 3-7 and 3-8). The upper nozzles 1, 2, 3, 4, 5, 16, 17, 18 and 19 were pointing 5 degrees upwards away from the shaft core surface, while nozzles 7, 8, 9, 10, 11, 12, 13 and 14 located at the lower half part of the intake perimeter were pointing at 13 degrees towards the cone surface. Nozzles 6 and 15 were pointing horizontally towards the centreline of the gas turbine.

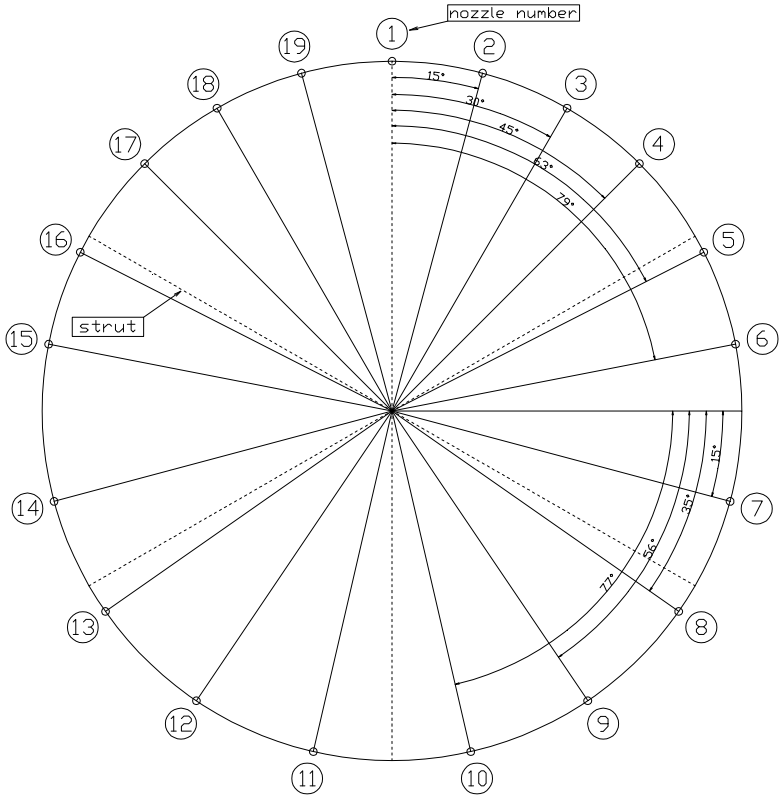

Figure 3–7: Normal set water injection nozzle positions.

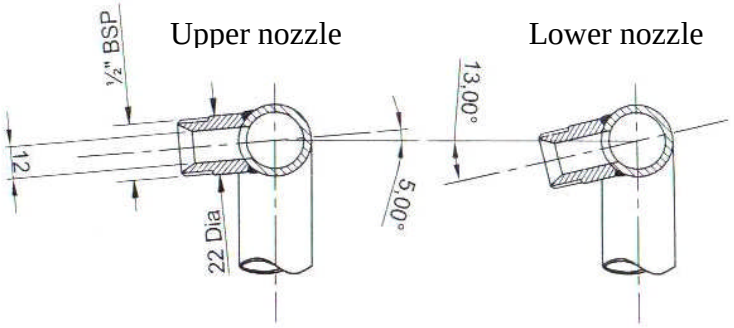

Figure 3–8: Normal set nozzle angles with respect to the horizontal centerline passing though the gas turbine.

After taking results by running simulations with the normal nozzle settings, then a second set of simulations was run involving 19 nozzles injecting towards the engine (see figure 3-9).

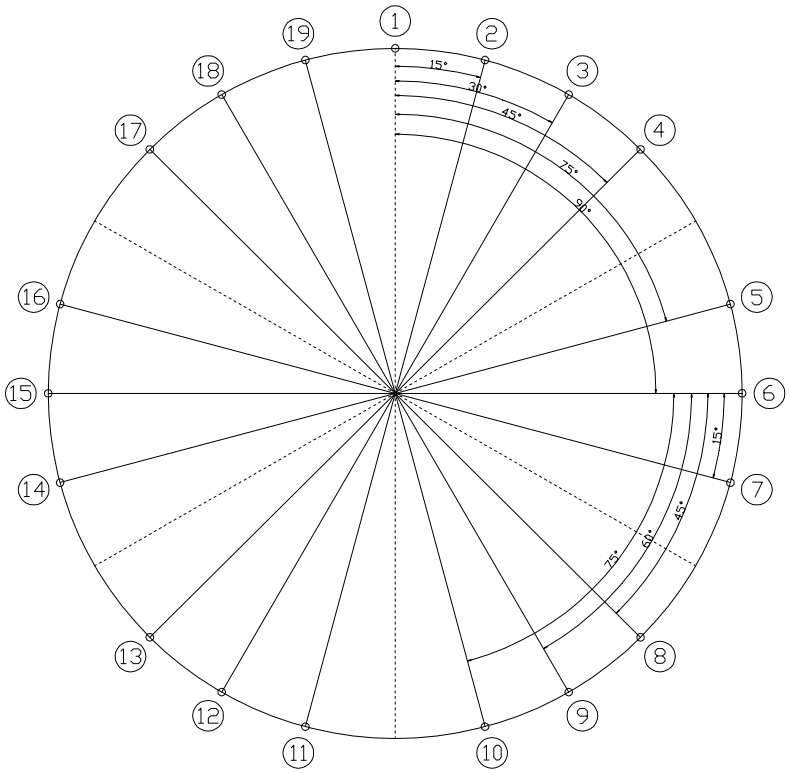

Figure 3–9: Water injection nozzle arrangement 1.

Injection nozzles 1,2,3,18,19 were set at zero degrees with respect to the gas turbine centreline while all the other nozzles were set in such a way so as to point towards the mid span area of the IGV plane (18 degrees with respect to gas turbine centreline, see figure 3-10).

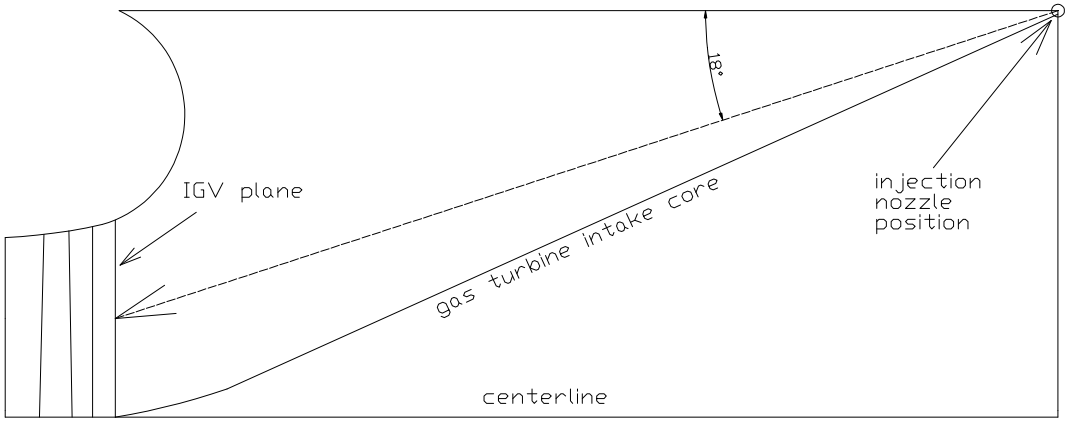

Figure 3–10: Nozzle pointing towards IGV plane.

The third simulation involved 18 nozzles (see figure 3-11) positioned at spaces of 20 degrees from one another. Nozzles 1, 2, 3, 17 and 18 were positioned at zero degrees with respect to the gas turbine center line while the remaining nozzles were pointing towards the midspan of the IGV annulus.

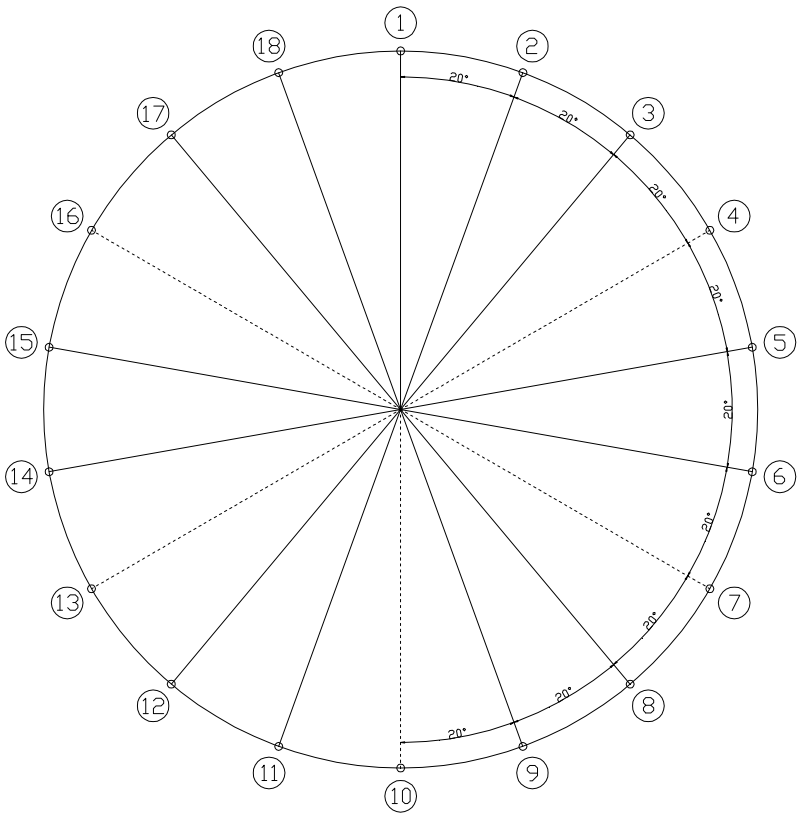

Figure 3–11: Water injection nozzle arrangement 2.

Initially, the CFD simulation involved the ABB GT13 gas turbine intake subjected to water injection of 135 litters in 4 minutes time. The simulation was run with nozzle spray angles of 40 degrees, nozzle injection velocity of 143 m/s and with different droplet diameters of 150, 300, 400 and 500 μm (see figures 3-12, 3-13, 3-14 and 3-15).

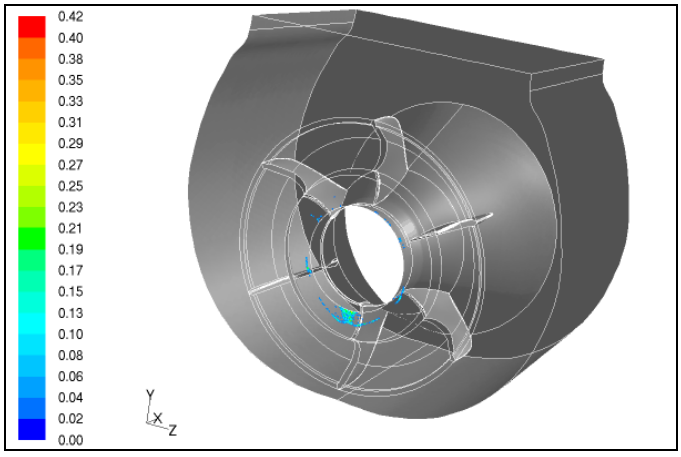

Figure 3–12: Normal set droplet concentration contours (kg/m^3) , 40 deg cone angle, injection velocity 143 m/s, diameter 150 μm.

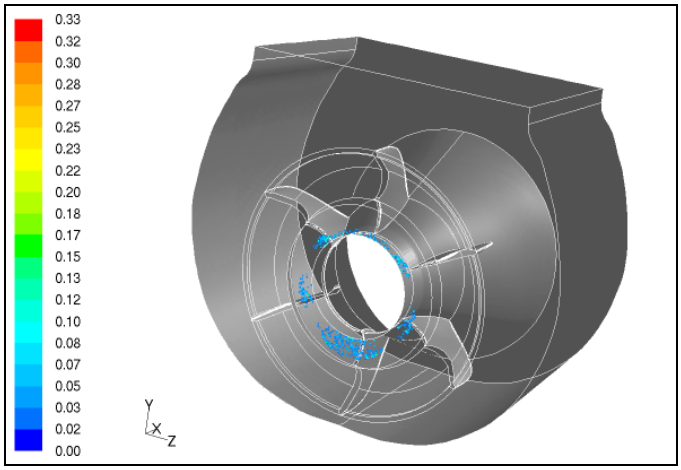

Figure 3–13: Normal set droplet concentration contours (kg/m^3), 40 deg cone angle, injection velocity 143 m/s, diameter 300 µm.

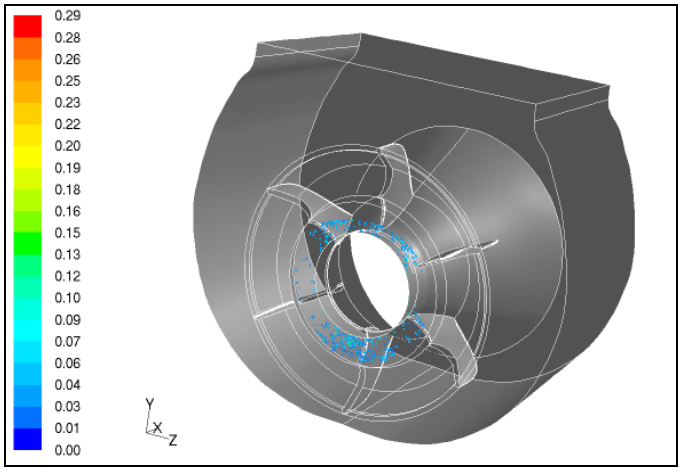

Figure 3–14: Normal set droplet concentration contours (kg/m^3), 40 deg cone angle, injection velocity 143 m/s, diameter 400 µm.

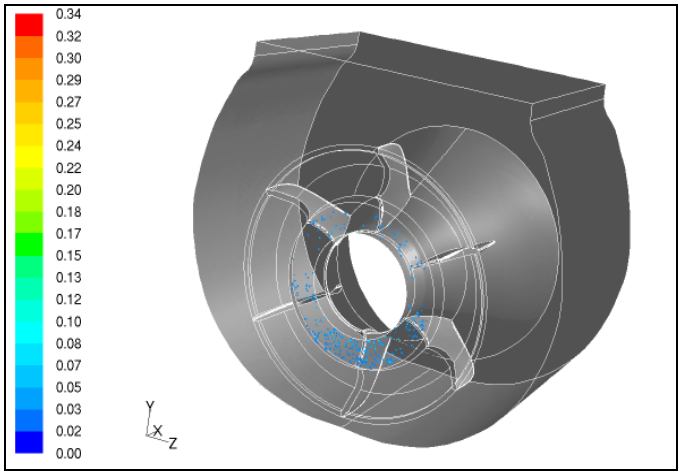

Figure 3–15: Normal set droplet concentration contours (kg/m^3), 40 deg cone angle, injection velocity 143 m/s, diameter 500 µm.

From the figures above one can see that the IGV plane is covered more efficiently as the droplet diameter increases from 150 microns to 500 microns. This can be attributed to the fact that the momentum of the larger droplets is higher and as a result they are deflected less than the smaller droplets from the gas turbine intake air flow towards the bottom of the intake. This is even more obvious by checking the droplet trajectories of the nozzles injections (see figures 3-16, 3-17, 3-18 and 3-19).

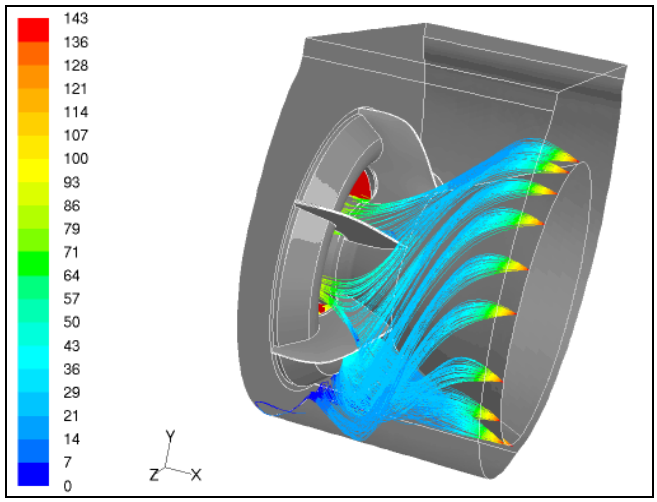

Figure 3–16: Normal set particle tracks coloured by velocity magnitude (m/s), 40 deg cone angle, injection velocity 143 m/s, diameter 150 µm.

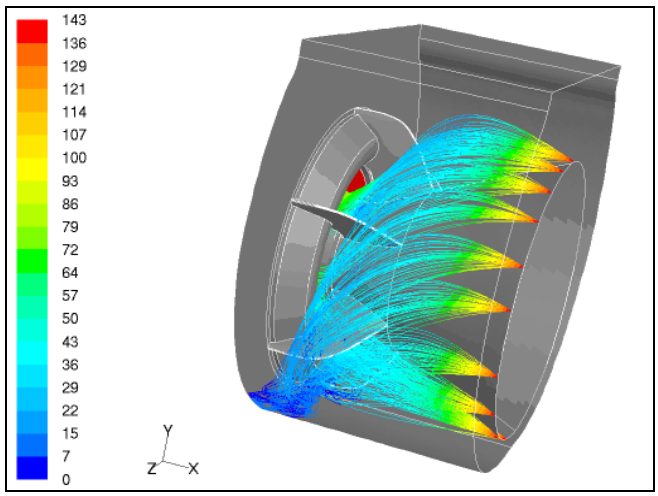

Figure 3–17: Normal set particle tracks coloured by velocity magnitude (m/s), 40 deg cone angle, injection velocity 143 m/s, diameter 300 µm.

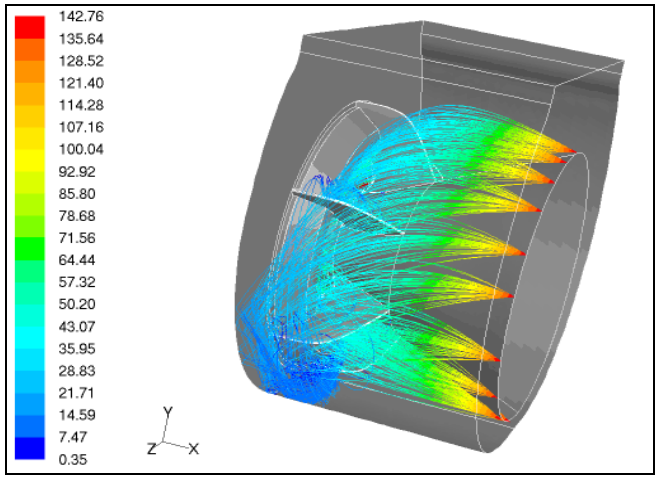

Figure 3–18: Normal set particle tracks coloured by velocity magnitude (m/s), 40 deg cone angle, injection velocity 143 m/s, diameter 400 µm.

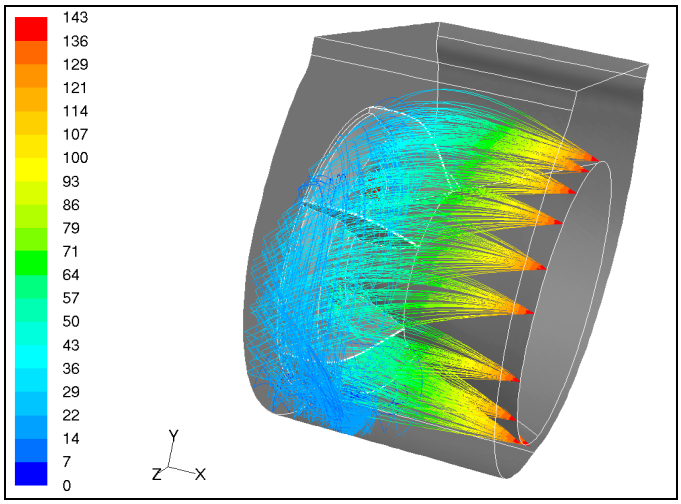

Figure 3–19: Normal set particle tracks coloured by velocity magnitude (m/s), 40 deg cone angle, injection velocity 143 m/s, diameter 500 µm.

From all the above figures involving droplet concentration contours and droplet trajectories one can see that the size of 300 microns is the most efficient in terms of unavoidable water on the walls around the IGV plane. Also, it is the safest in terms of blade erosion. Using larger droplet sizes above 300 microns the droplet trajectories hit the walls around the IGV plane, however the IGV plane coverage is higher.
Then using as reference the size of 300 microns and 40 degrees spray cone angle, the water injection velocity was increased to 212 m/s by increasing the doses of water from 135 litters to 200 litters in 4 minutes period. However, the results were not better than the cases corresponding to injection velocity of 143 m/s (see figures 3-20 and 3-21).

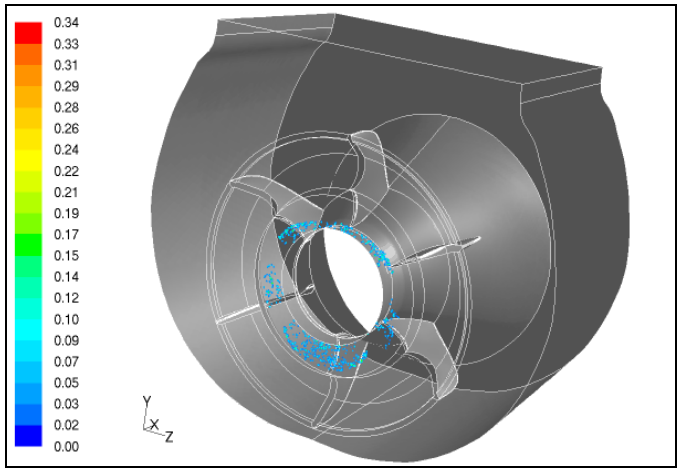

Figure 3–20: Normal set droplet concentration contours (kg/m^3), 40 deg cone angle, injection velocity 212 m/s, diameter 300 μm.

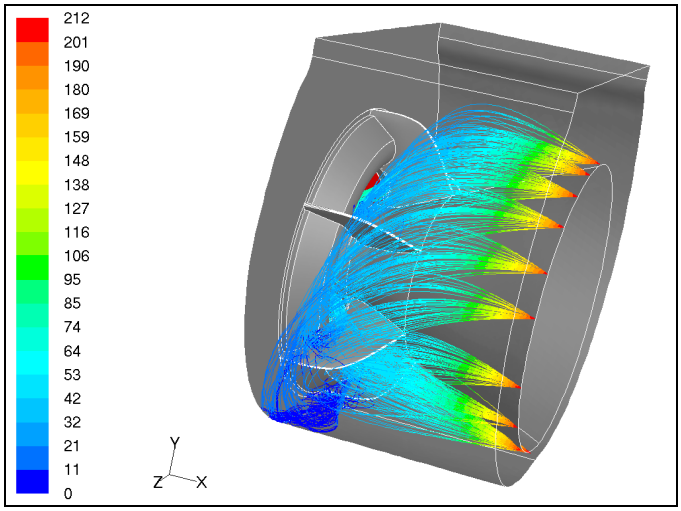

Figure 3–21: Normal set particle tracks coloured by velocity magnitude (m/s), 40 deg cone angle, injection velocity 212 m/s, diameter 300 μm.

Then keeping the droplet reference size to 300 μm, the spray cone angle to 40 degrees and the water doses to 135 litters, arrangements 1 and 2 were examined and not much differences were appeared in terms of IGV plane coverage (see figures 3-22 and 3-23), however less waste of water on the walls around the IGV plane was achieved (see figures 3-24 and 3-25).

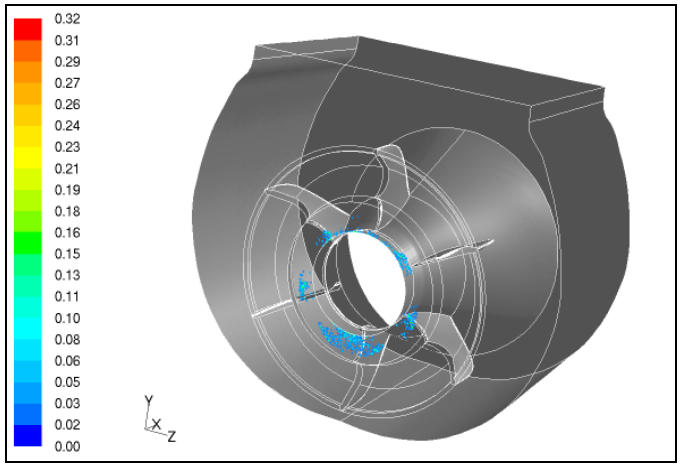

Figure 3–22: Arrangement 1 droplet concentration contours (kg/m^3), 40 deg cone angle, injection velocity 143 m/s, diameter 300 µm.

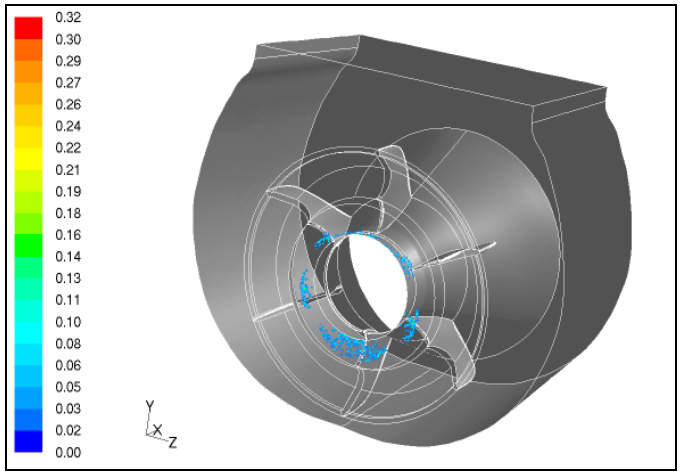

Figure 3–23: Arrangement 2 droplet concentration contours (kg/m^3), 40 deg cone angle, injection velocity 151 m/s, diameter 300 µm.

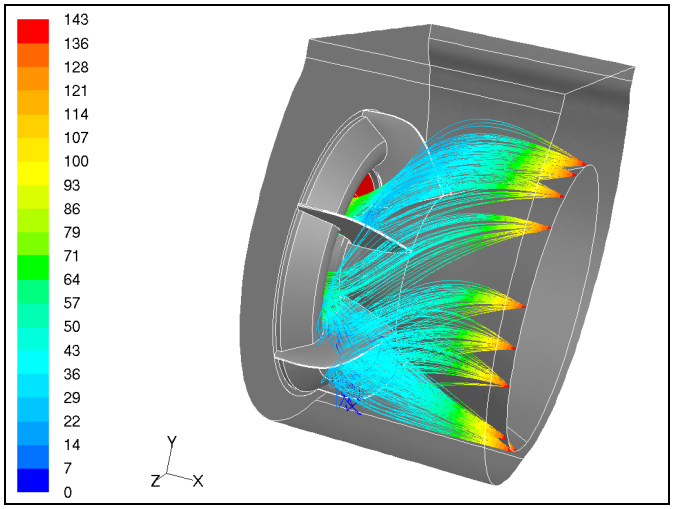

Figure 3–24: Arrangement 1 particle tracks coloured by velocity magnitude (m/s), 40 deg cone angle, injection velocity 143 m/s, diameter 300 µm.

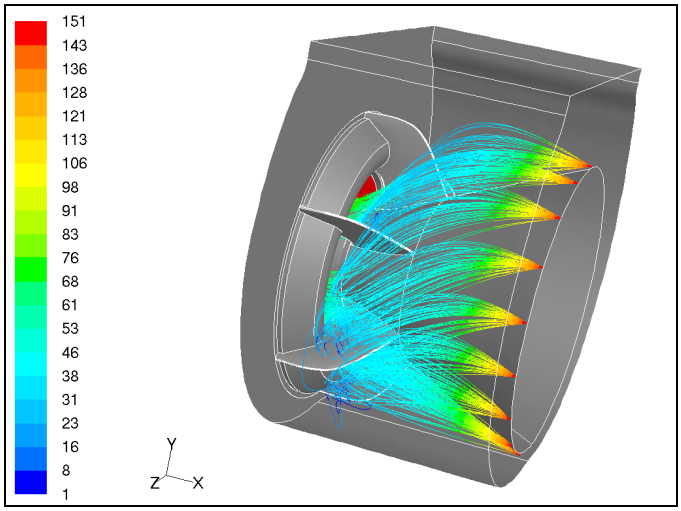

Figure 3–25: Arrangement 2 particle tracks coloured by velocity magnitude (m/s), 40 deg cone angle, injection velocity 151 m/s, diameter 300 µm.

Running the simulation for arrangements 1 and 2 with increased water supply of 200 litters per 4 min and therefore increased injection velocity, better IGV coverage was obtained (see figures 3-26 and 3-27) with a very small amount of droplet trajectories wasted on the walls around the IGV plane especially for arrangement 1 (see figures 3-28 and 3-29).

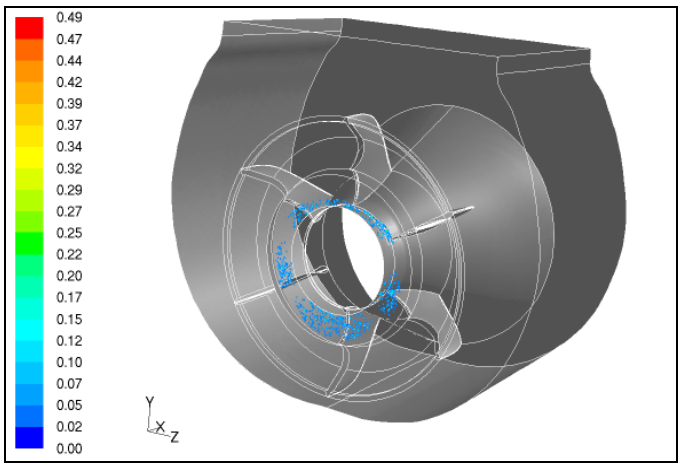

Figure 3–26: Arrangement 1 droplet concentration contours (kg/m^3), 40 deg cone angle, injection velocity 212 m/s, diameter 300 µm.

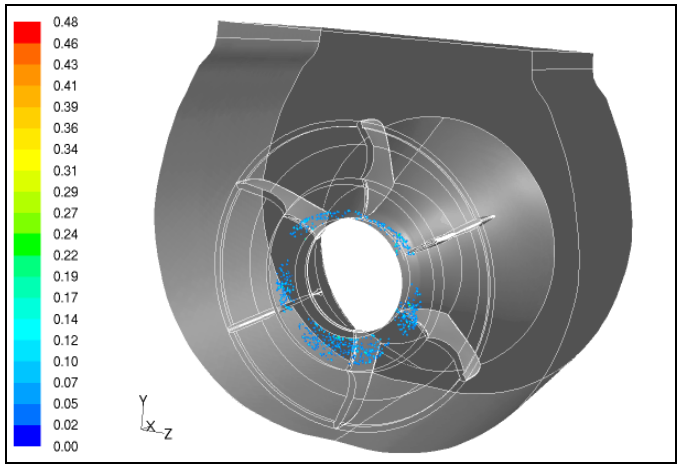

Figure 3–27: Arrangement 2 droplet concentration contours (kg/m^3), 40 deg cone angle, injection velocity 223 m/s, diameter 300 µm.

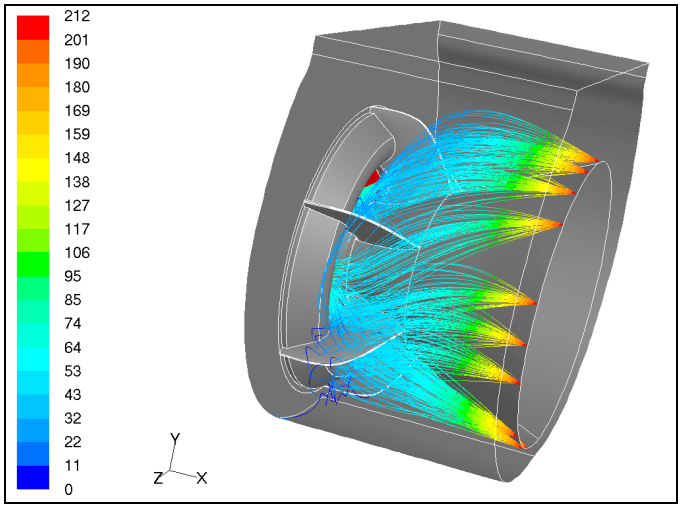

Figure 3–28: Arrangement 1 particle tracks coloured by velocity magnitude (m/s), 40 deg cone angle, injection velocity 212 m/s, diameter 300 µm.

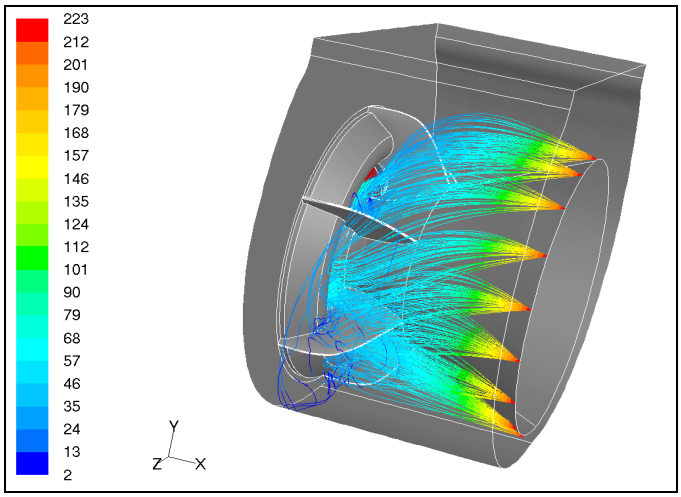

Figure 3–29: Arrangement 2 particle tracks coloured by velocity magnitude (m/s), 40 deg cone angle, injection velocity 223 m/s, diameter 300 µm.

After examining different nozzle arrangements with 40 degrees spray injection angles, then a value of 80 degrees cone injection angle was used for the simulations (see figures 3-30, 3-31, 3-32, 3-33, 3-34 and 3-35). The results in terms of IGV plane coverage and droplet trajectories were not better than these from the simulations run with 40 degrees spray angle.

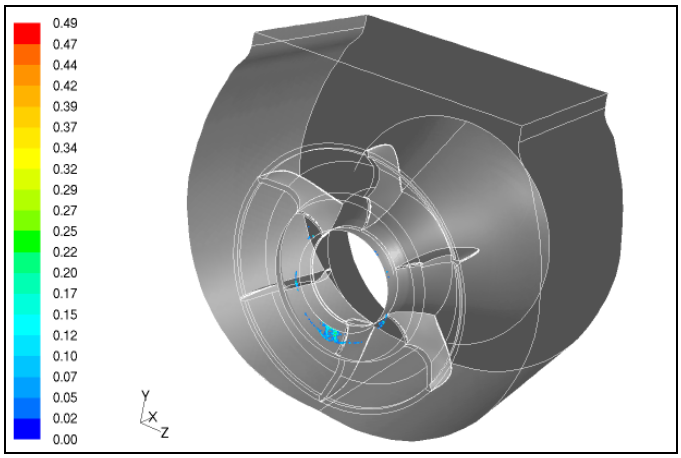

Figure 3–30: Normal set droplet concentration contours (kg/m^3), 80 deg cone angle, injection velocity 143 m/s, diameter 150 µm.

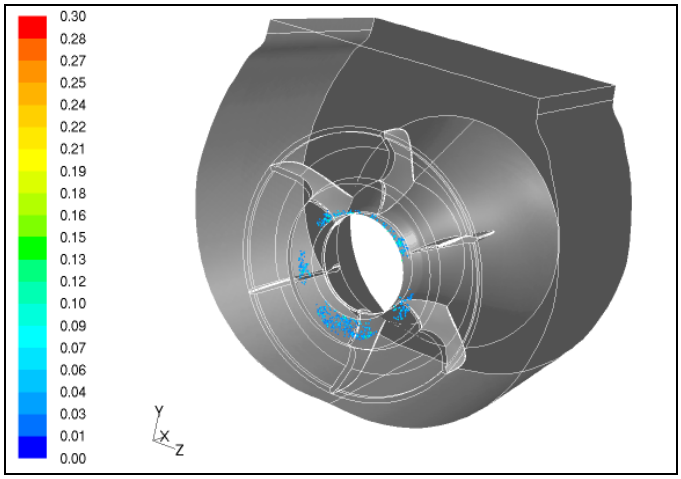

Figure 3–31: Normal set droplet concentration contours (kg/m^3), 80 deg cone angle, injection velocity 143 m/s, diameter 300 µm.

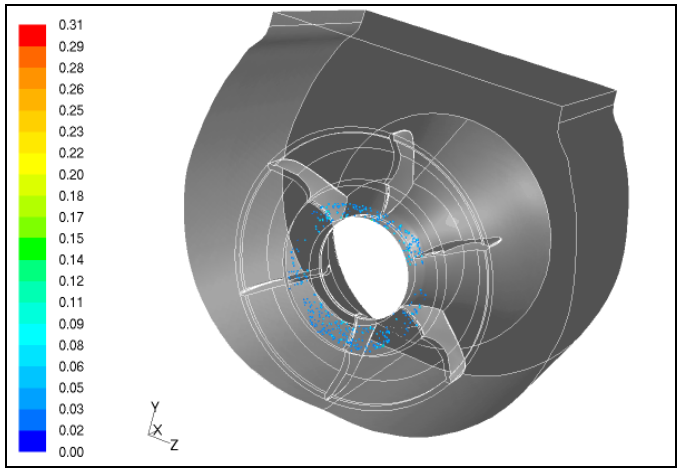

Figure 3–32: Normal set concentration contours (kg/m^3), 80 deg cone angle, injection velocity 143 m/s, diameter 400 µm.

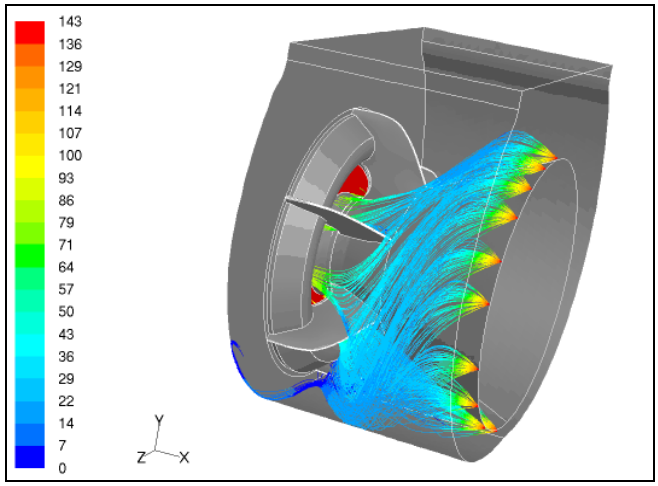

Figure 3–33: Normal set particle tracks coloured by velocity magnitude (m/s), 80 deg cone angle, injection velocity 143 m/s, diameter 150 µm.

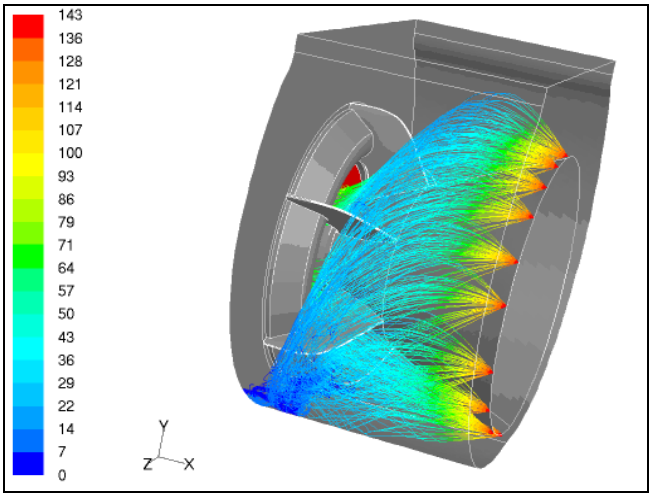

Figure 3–34: Normal set particle tracks coloured by velocity magnitude (m/s), 80 deg cone angle, injection velocity 143 m/s, diameter 300 µm.

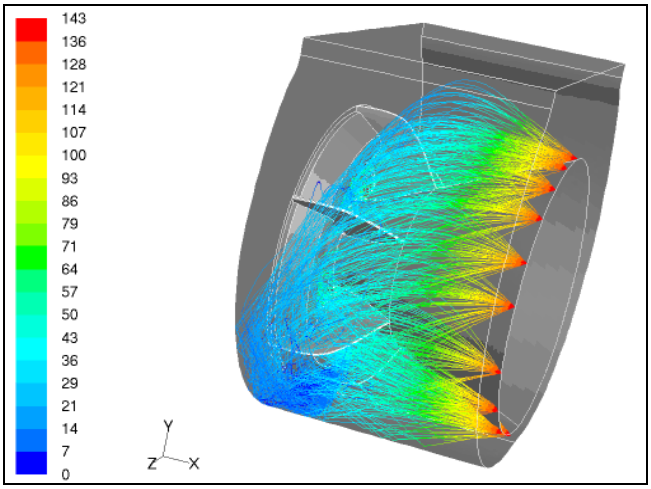

Figure 3–35: Normal set particle tracks coloured by velocity magnitude (m/s), 80 deg cone angle, injection velocity 143 m/s, diameter 400 µm.

Running arrangements 1 and 2 with 80 degrees cone angle the simulations showed no better results in terms of IGV water coverage (see figures 3-36, 3-37, 3-38 and 3-39) however, the spillage of water on the walls around the IGV plane was higher (see figures (3-40, 3-41, 3-42 and 3-43).

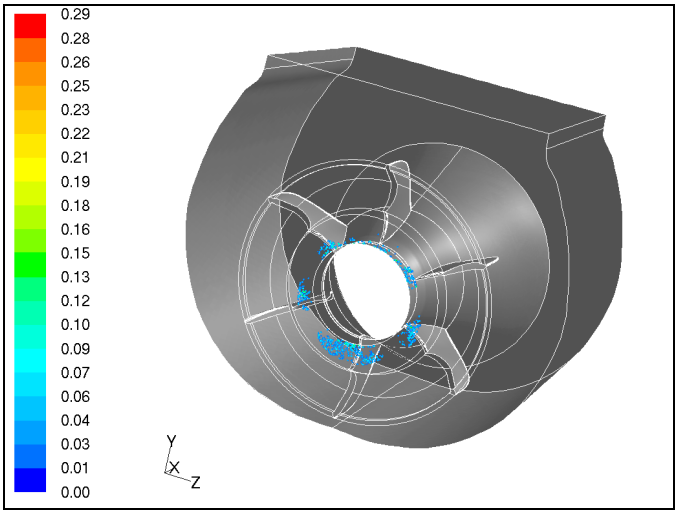

Figure 3–36: Arrangement 1 droplet concentration contours (kg/m^3), 80 deg cone angle, injection velocity 143 m/s, diameter 300 µm.

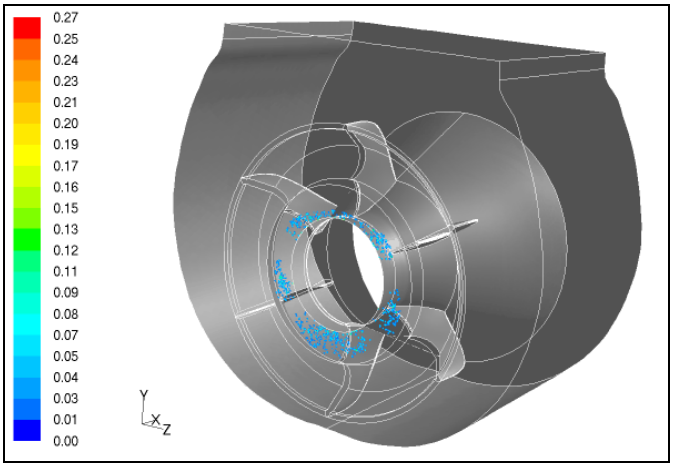

Figure 3–37: Arrangement 1 droplet concentration contours (kg/m^3), 80 deg cone angle, injection velocity 143 m/s, diameter 350 µm.

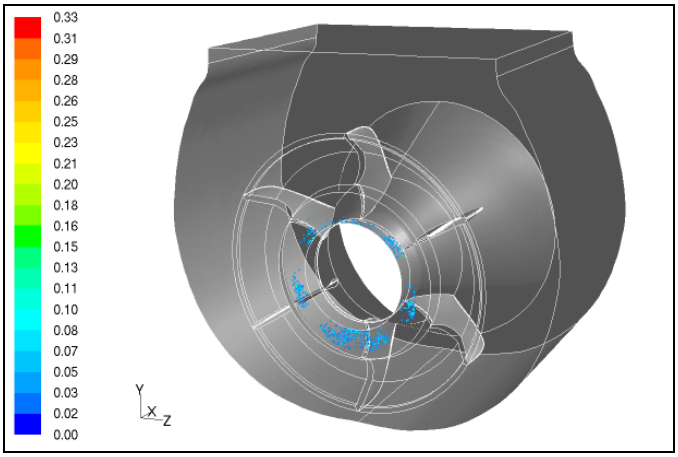

Figure 3–38: Arrangement 2 droplet concentration contours (kg/m^3), 80 deg cone angle, injection velocity 151 m/s, diameter 300 µm.

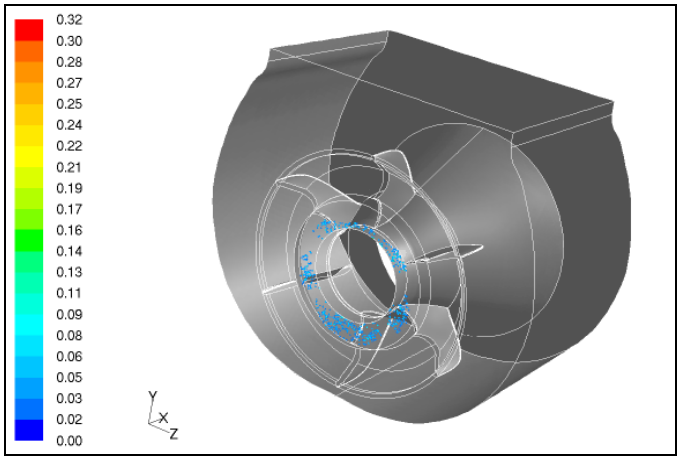

Figure 3–39: Arrangement 2 droplet concentration contours (kg/m^3), 80 deg cone angle, injection velocity 151 m/s, diameter 350 µm.

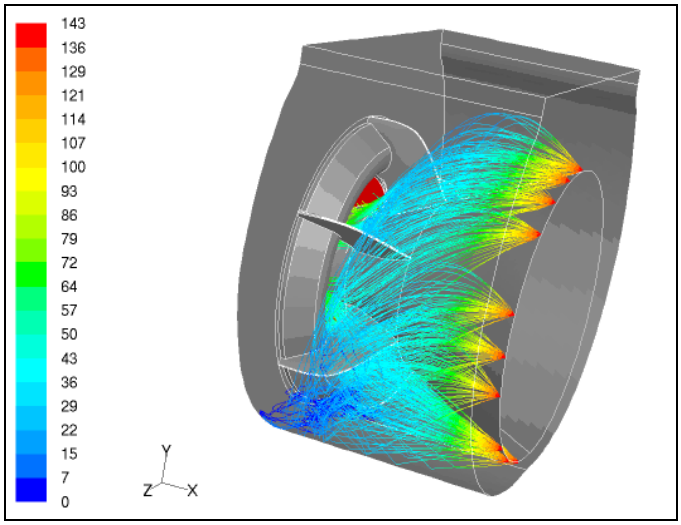

Figure 3–40: Arrangement 1 particle tracks coloured by velocity magnitude (m/s), 80 deg cone angle, injection velocity 143 m/s, diameter 300 µm.

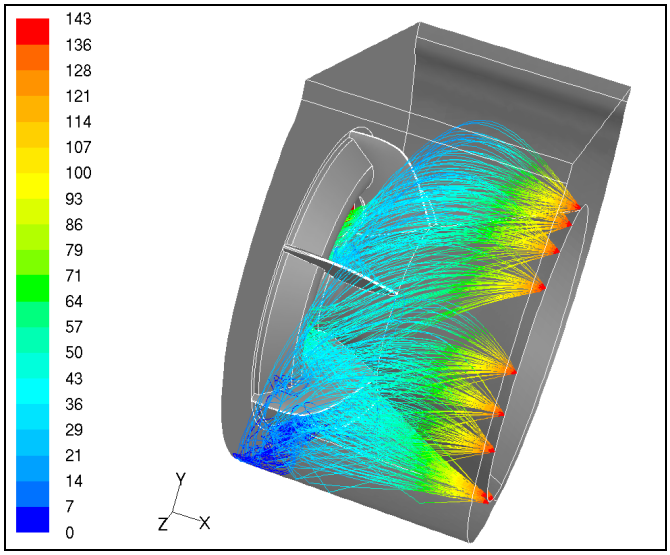

Figure 3–41: Arrangement 1 particle tracks coloured by velocity magnitude (m/s), 80 deg cone angle, injection velocity 143 m/s, diameter 350 µm.

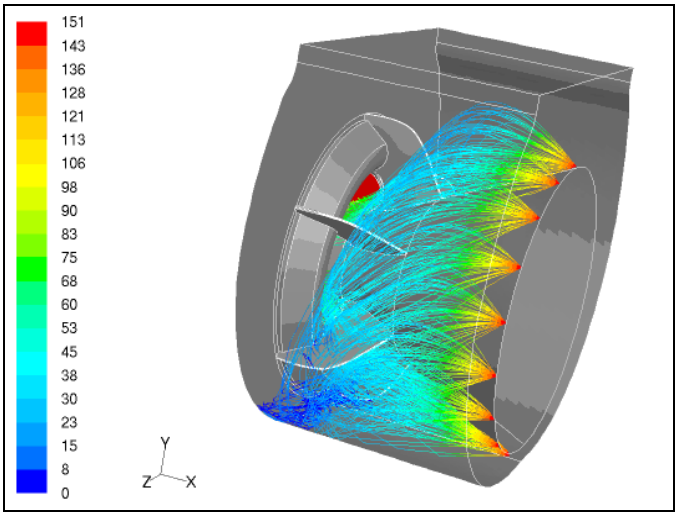

Figure 3–42: Arrangement 2 particle tracks coloured by velocity magnitude (m/s), 80 deg cone angle, injection velocity 151 m/s, diameter 300 µm.

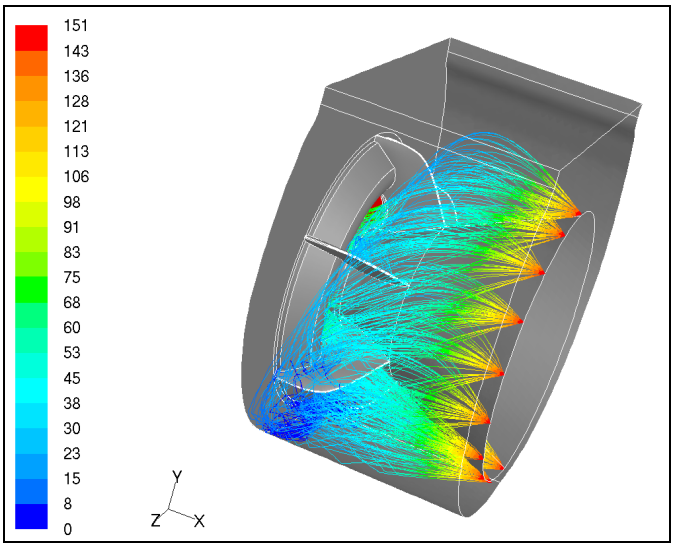

Figure 3–43: Arrangement 2 particle tracks coloured by velocity magnitude (m/s), 80 deg cone angle, injection velocity 151 m/s, diameter 350 µm.

Analysing the flow at the lower part of the industrial compressor intake, it was found that a big vortex exists on a plane set midways of the intake (see figures 3-44 and 3-45). There the air streams coming from the right and the left part of the intake shaft cone meet creating so a vortex that is directed towards the IGV plane of the engine.

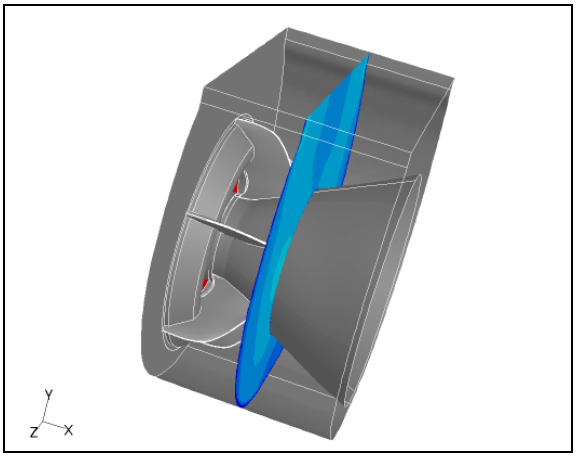

Figure 3–44: Middle vertical plane illustration.

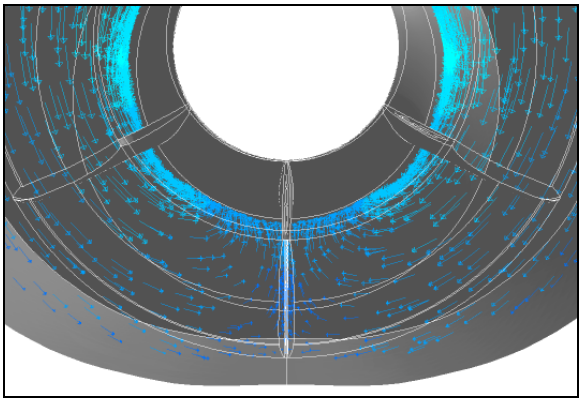

Figure 3–45: Lower vortex illustration.

In order to see how cleaning fluid particles and air behaves along the path of a particle trajectory, the first trajectory of the first nozzle injection was analysed (see figure 3-46) for a case of 80 degrees cone injection. The number of trajectories for each nozzle injection was 50.

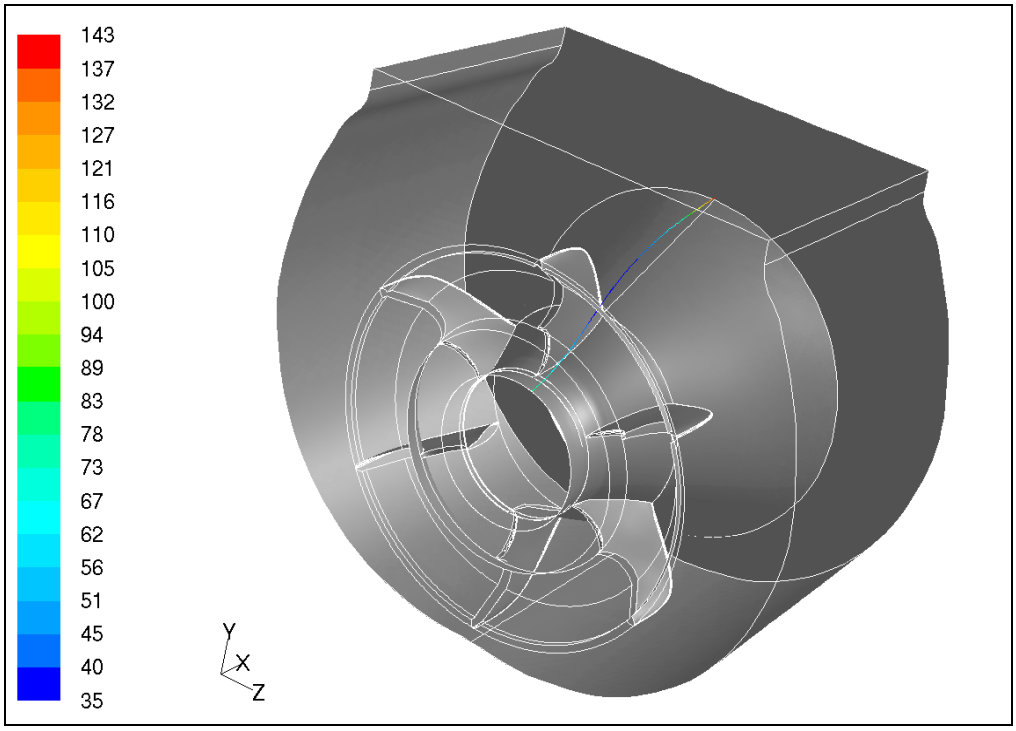

Figure 3–46: Normal set single particle track coloured by velocity magnitude (m/s), 80 deg cone angle, injection velocity 143 m/s, diameter 300µm.

Along the first fluid particle trajectory it can be seen from figure 3-47 that the droplets and the air behave differently in terms of velocity. The droplets leave the nozzle with an estimated velocity of 143 m/s and the velocity magnitude drops to 39 m/s at approximately half way between the injection point and the IGV plane. The droplets then start to accelerate reaching a value of around 80 m/s at the IGV plane.

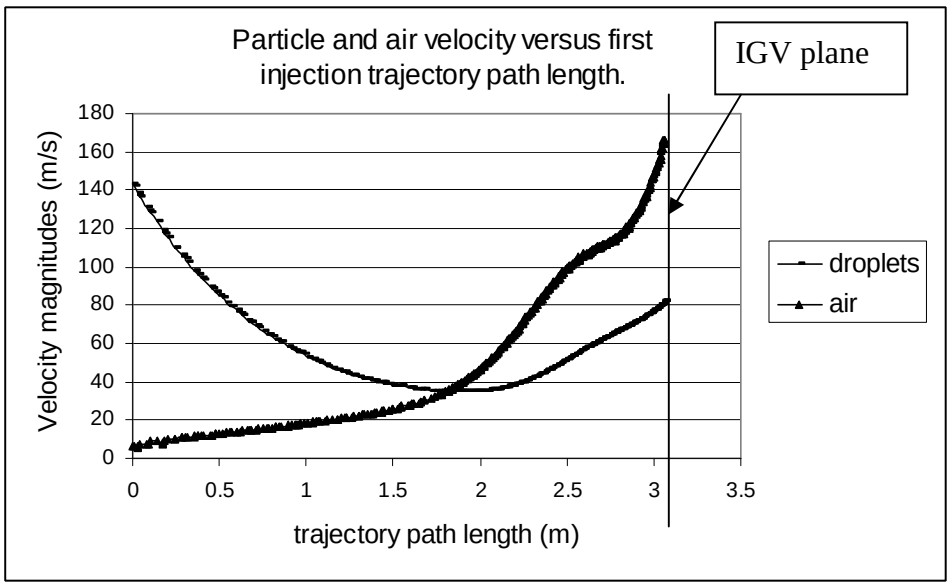

Figure 3–47: Particle and air velocity distribution along first injection trajectory path.

The initial decrease of the kinetic energy of the droplets shown in figure 3-47 is due firstly to the fluid particles gravitational deceleration. Another one reason for this

velocity decrease can be the fact that the air trajectories coming from the top part of the intake are directed vertically downwards opposing so the trajectories of the droplets of the first nozzle that are directed upwards. Hence, the resultant velocity in terms of water is lower in value than the initial droplet flow velocity (see figure 3-48).

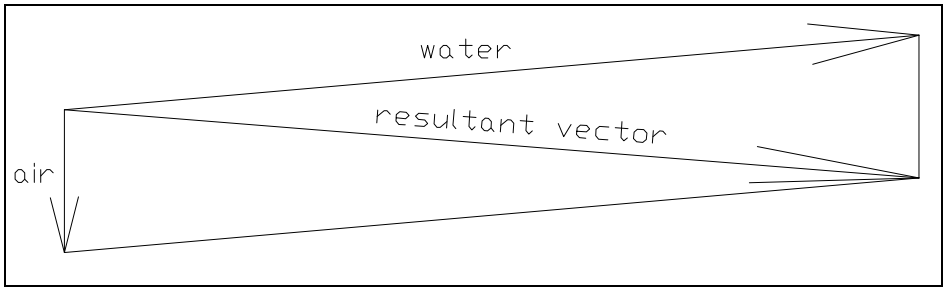

Figure 3–48: Air and droplet vectors illustration.

Beyond the halfway point however, the air flow is accelerating rapidly around the inside wall towards the tips of the IGV's. This creates a falling pressure gradient along the corresponding streamlines and encourages the particles to accelerate.
However, along the same trajectory the air gains continuously kinetic energy reaching a velocity of about 165 m/s next to the IGV plane which corresponds approximately to a Mach number value of 0.5 which is typical for industrial compressor intakes.
The same trajectory in terms of time was analysed (see figure 3-49) and the results displayed that the total time involved for a trajectory to reach the IGV plane was approximately 0.06 sec.

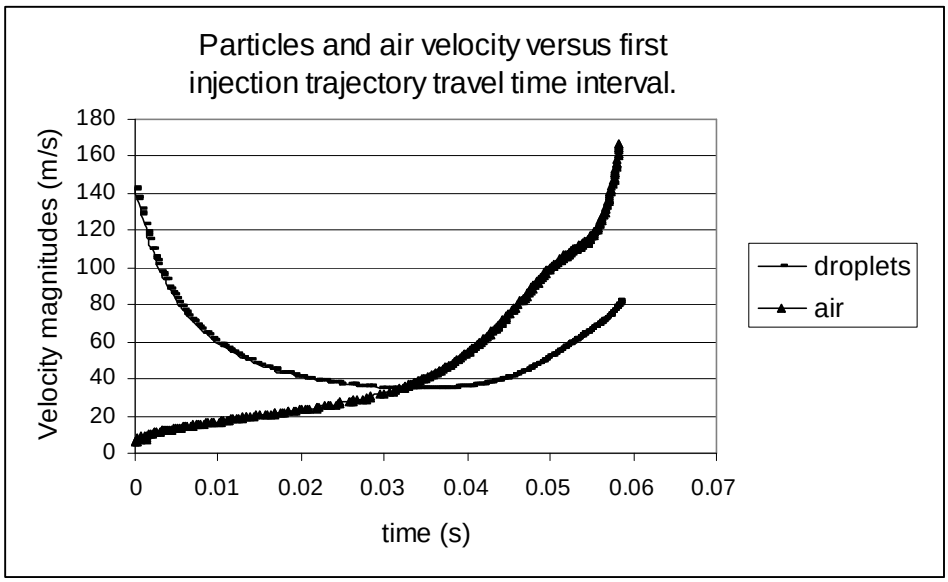

Figure 3–49: Particle and air velocity distribution with respect to trajectory time interval.

3.7 Compressor stage-intake connected geometry and meshing

The CFD simulation that took place in order to analyse the flow between the inlet of the intake after the filters and the IGV plane has been extended further more towards the first stage of the compressor, so as to examine the effect of the first rotating unit (rotor row) on the intake flow and the droplet path crossing it (see figure 3-50).

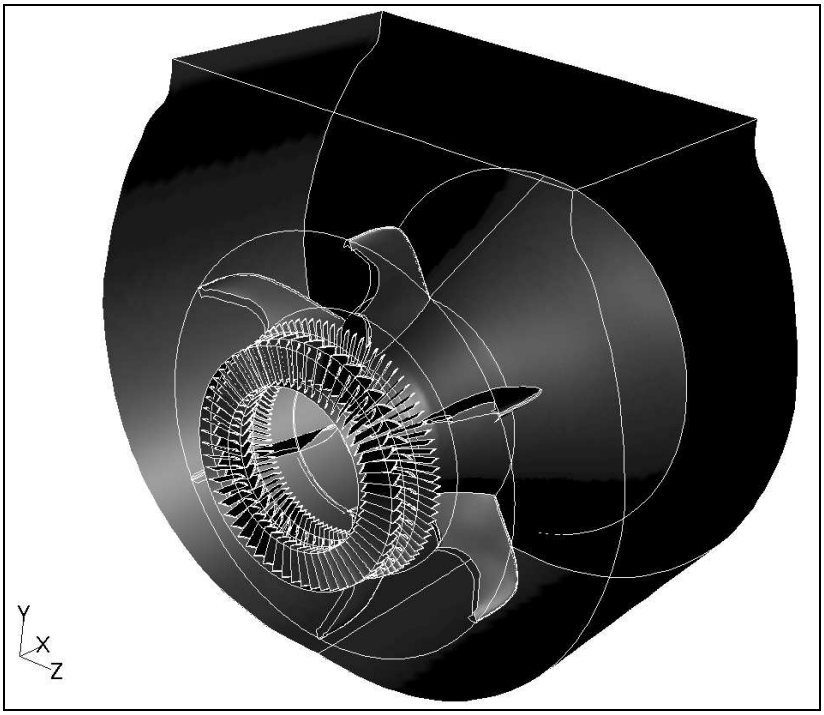

Figure 3–50: Representation of compressor first stage and intake connected.

In order to investigate the geometry computationally, five different meshes were generated comprised of tetrahedral cells:

Mesh 1: 7,695,340 million cells
Mesh 2: 8,750,243 million cells
Mesh 3: 10,048,019 million cells
Mesh 4: 10,918,693 million cells
Mesh 5: 11,453,516 million cells

All these meshes were investigated in order to get grid independency for the simulation. The parameter checked for grid independency was the aerodynamic total pressure loss coefficients Y which was stabilized in terms of it's value after about 9 million cells. As a result for further simulation runs the grid involving the finer fifth mesh was selected (see figures 3-51 and 3-52).

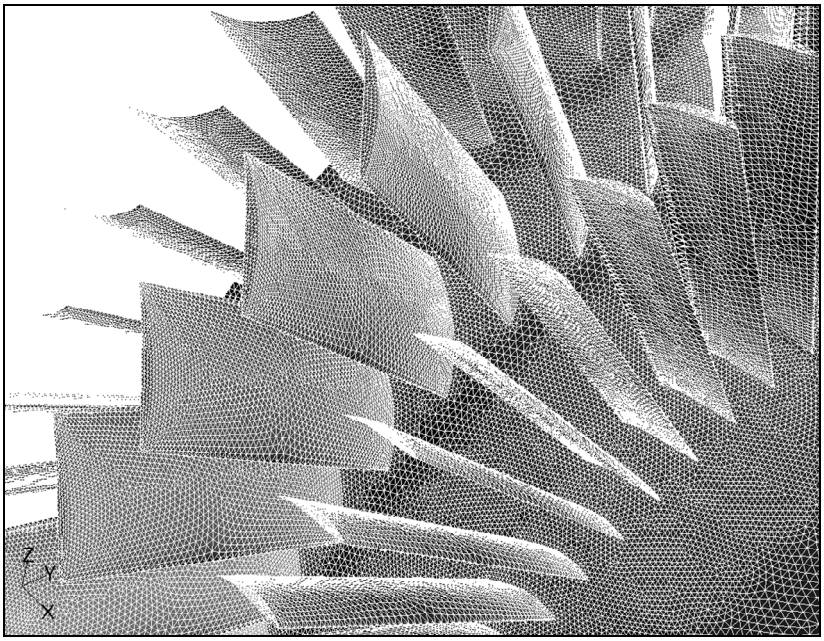

Figure 3–51: Blade grid distribution.

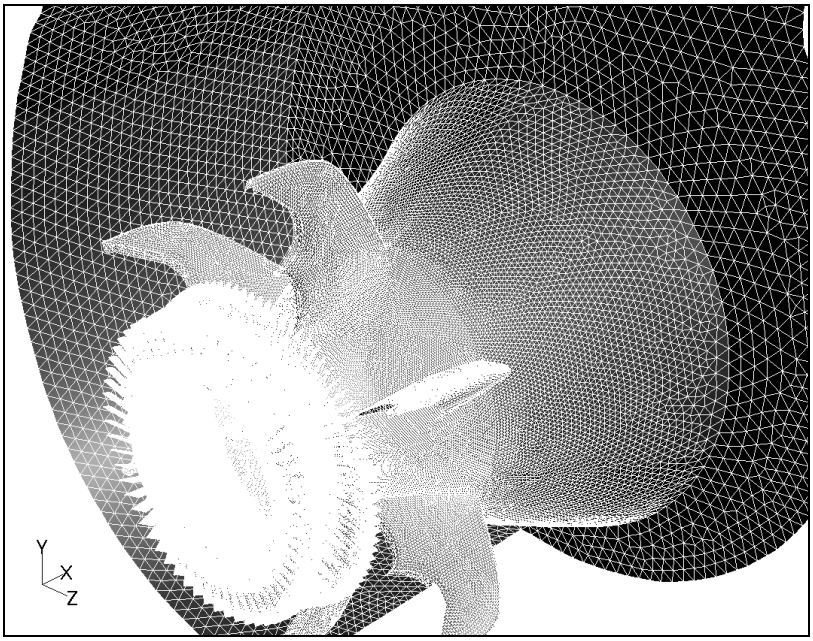

Figure 3–52: Intake surface grid distribution.

3.7.1 Turbulence model, solver and boundary conditions

The simulation took place under steady state conditions and the continuous phase was solved using the pressure based solver of Fluent with implicit formulation, employing the SIMPLE algorithm for pressure-velocity coupling. The equations of flow were solved to first order accuracy. The k-ε turbulence model with standard wall functions was employed for the simulation. The absolute velocity formulation was used for the simulation since the flow in most of the domain is not rotating.

The converged solution of the finest mesh of the continuous phase was used as the input for the discrete phase modelling (water droplets). The droplet trajectories were calculated using a coupled Lagrangian formulation including drag, inertia and gravity for the droplet spheres. The density of liquid water was given to the droplets. The mass fraction of water liquid injected into the airflow was very low 0.2% and interactions between droplets were neglected. The droplets impinging on the walls of the industrial intake geometry were subjected to reflection and no consideration was taken in terms of droplet breakup, evaporation, collision and deformation.
The volume simulated involved an inlet and an outlet which were considered as mass flow inlet and pressure outlet boundaries respectively. The air mass flow at the inlet was set at 370 kg/s and the total temperature at 300.15 K. Default Fluent settings for turbulent kinetic energy (value of 1 m^2/s^2) and turbulent dissipation rate (value of 1 m^2/s^3) at the inlet boundary were used for the simulation.
The static pressure at the outlet just after the stator row was calculated to be 110831.5 Pa and radial equilibrium pressure distribution was taken into account. According to Fluent 6.3 (2007), when this feature is active, the specified gauge pressure applies only to the position of minimum radius (relative to the axis of rotation) at the boundary and the static pressure on the rest of the zone is calculated from assumption that radial velocity is negligible, so that the pressure gradient is given by:

$$\frac{\partial p}{\partial r} = \frac{\rho \upsilon_\theta^2}{r} \quad (154)$$

p : static pressure
r : distance from the axis of rotation
υ_θ : tangential velocity
ρ : density

This boundary condition can be used even for zero rotational velocity and for this reason it has been used for the flow through the annulus pressure outlet boundary behind the first stage stator row.
At this pressure outlet boundary the turbulence intensity and viscosity ratio were set by default according to Fluent 6.3 (2007), getting values of 10% and 10 respectively. The total temperature at this boundary which represents the exit of the first stage, the total temperature was set to be 326.896 K declaring a stage total temperature increase of 26.741 K (see Appendix: preliminary axial compressor design, figure A2).
Many problems involve multiple moving parts or contain stationary surfaces which are not surfaces of revolution. According to Fluent 6.3 (2007), for these problems the model can be broken up into multiple fluid/solid cell zones, with interface boundaries separating the zones. Zones which contain the moving components can then be solved using the moving reference frame equations, whereas stationary zones can be solved with the stationary frame equations. The manner in which the equations are treated at the interface lead to two approaches which are supported from Fluent:

- Multiple rotating reference frames
  Multiple reference frame model (MRF)
  Mixing plane model

- Sliding mesh model (SMM)

Both the MRF and mixing plane approaches are steady-state approximations and differ in the manner in which conditions at the interfaces are treated, however, the sliding mesh model is an unsteady approximation due to the motion of the mesh with time.

The Multiple reference frame approximation involves individual cell zones which move at different rotational and or translational speeds. At the interfaces between cell zones, a local reference frame transformation is performed to enable flow variables in one zone to be used to calculate fluxes at the boundary of the adjacent zone. The MRF approach does not account for the relative motion of a moving zone with respect to adjacent zones (which may be moving or stationary), the grid remains fixed for the computation. This is analogous to freezing the motion of the moving part in a specific position and observing the instantaneous flow field with the rotor in that position. Hence, the MRF is often referred to as the 'frozen rotor approach'. The MRF model can be used for turbomachinery applications in which rotor-stator interaction is relatively weak and the flow is relatively uncomplicated at the interface between the moving and the stationary zones. Steady-state flow conditions are assumed at the interface between the two reference frames. That is, the velocity at the interface must be the same (in absolute terms) for each reference frame. The grid does not move.

The mixing plane model is useful for predicting steady-state flow in a turbomachine stage, where local interaction effects (such as wake and shock interaction) are secondary. If local effects are important, then an unsteady, sliding mesh calculation is required. In the mixing plane approach, each fluid zone is treated as a steady-state problem. Flow-field data from adjacent zones are passed as boundary conditions that are spatially averaged or mixed at the mixing plane interface. This mixing removes any unsteadiness that would arise due to circumferential variations in the passage-to-passage flow field (wakes, shock waves, separated flow) thus yielding a steady-state result

The sliding mesh model is the most accurate method for simulating flows in multiple moving reference frames, but also the most computationally demanding.

For the present simulation the Multiple rotating reference frame approach was used employing the Multiple reference frame model. The volume of the geometry simulated has been divided into three fluid zones. The first zone covers the volume between the intake and the IGV-rotor interior face, the second zone the volume between the IGV-rotor interior face and the Rotor-stator interior face and the third one occupies the rest of the volume up to the outlet of the stage (see figure 3-53). All these separating faces have been selected as interiors since they are occupied by fluid cells on both sides.

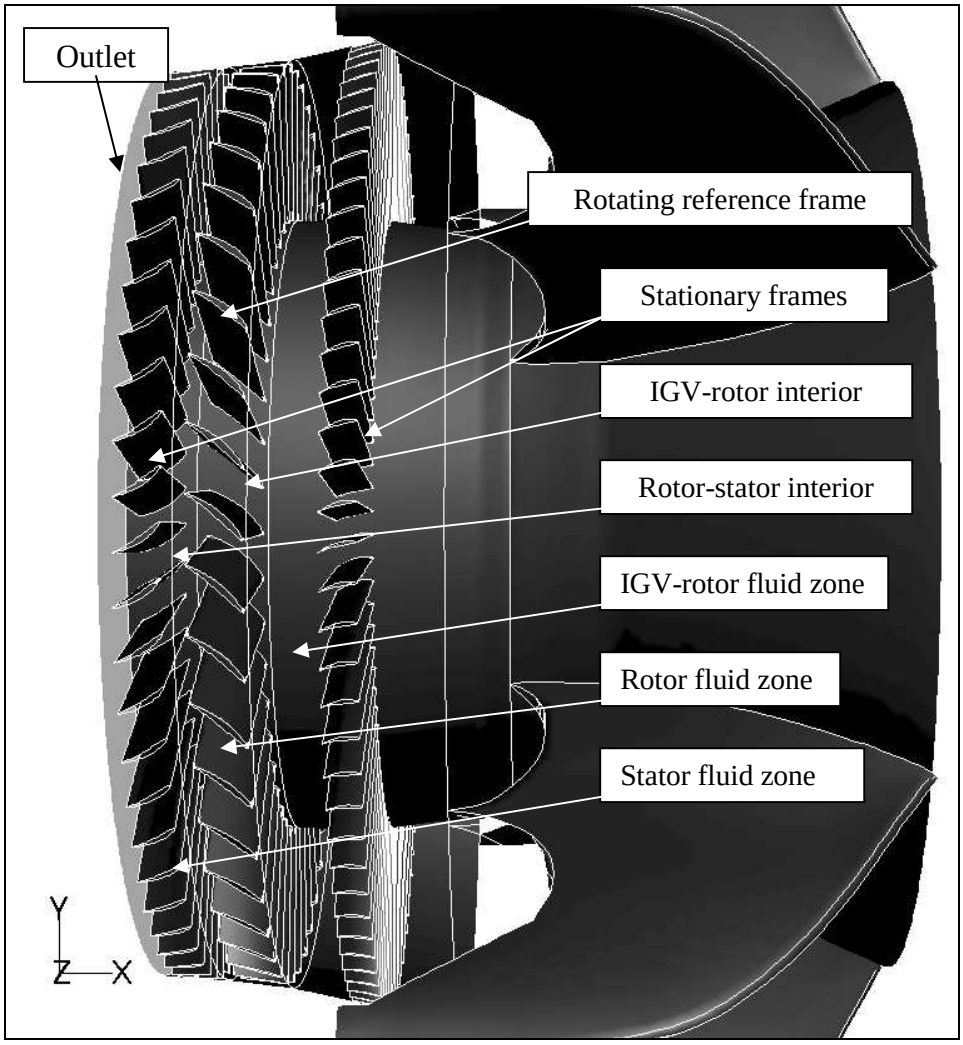

Figure 3–53: Reference frame representations.

The IGV-rotor fluid zone was set as a stationary fluid zone. All the walls related to this zone including the IGV blades were set as stationary walls as well.
The Rotor fluid zone was set to a rotating reference frame with a rotational velocity of 2970 rpm with respect to the x-axis of the stage. For a rotating reference frame, Fluent 6.3 (2007) assumes by default that walls rotate with the grid and hence are moving with respect to the stationary (absolute) reference frame. So the rotor walls and the rotor hub were defined as stationary relative to the adjacent Rotor fluid zone. The shroud of the rotors was defined as moving (rotating) wall in the absolute reference frame.
The Stator fluid zone was set to a stationary reference frame. The stator shroud, blades and hub of this zone were set as stationary walls.
All the walls involved in the three fluid zones were set to be under no slip shear conditions with a roughness height of 0 mm according to the default Fluent setting.
Examining the Mach number contours along an isosurface crossing the midspan of the IGVs, it can be seen that the Mach number in front of the IGVs gets a reasonable value of 0.5 which is typical for industrial gas turbines (see figure 3-54). Mach number values close to unity were observed at the rotor blade throat areas as it was expected.

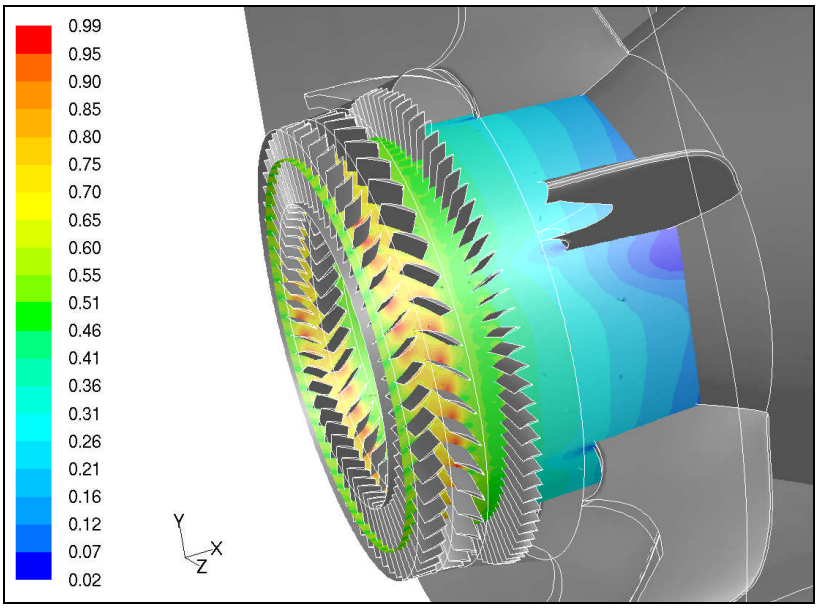

Figure 3–54: Mach number contours.

Investigating the geometry in terms of swirl, according to figures 3-55, 3-56 and 3-57 no swirl was detected in front of the IGVs either on the upper or the lower part of the intake geometry. However, significant swirl of the air flow was observed behind the IGVs and this was expected since they induce a substantial amount of turning on the air flow.

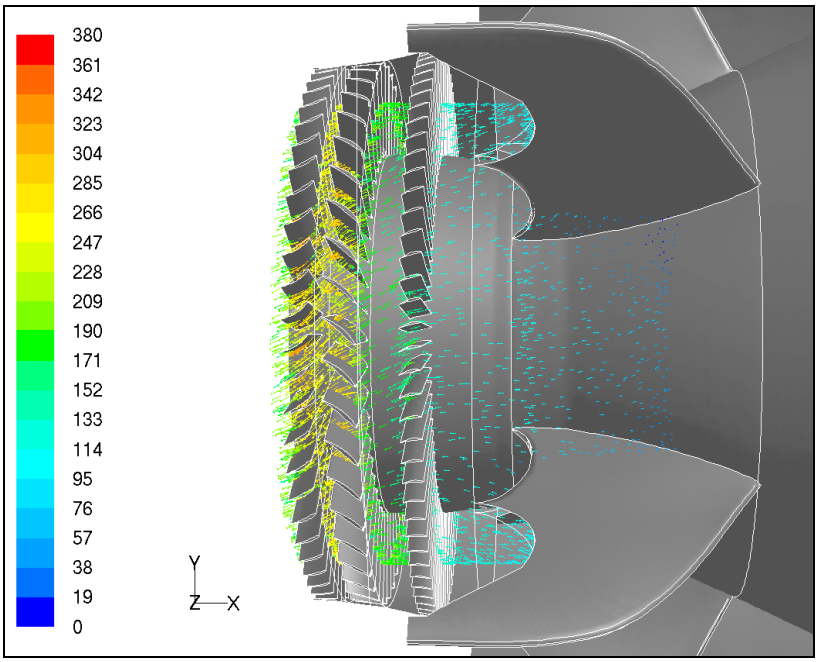

Figure 3–55: Velocity vectors coloured by velocity magnitude (m/s).

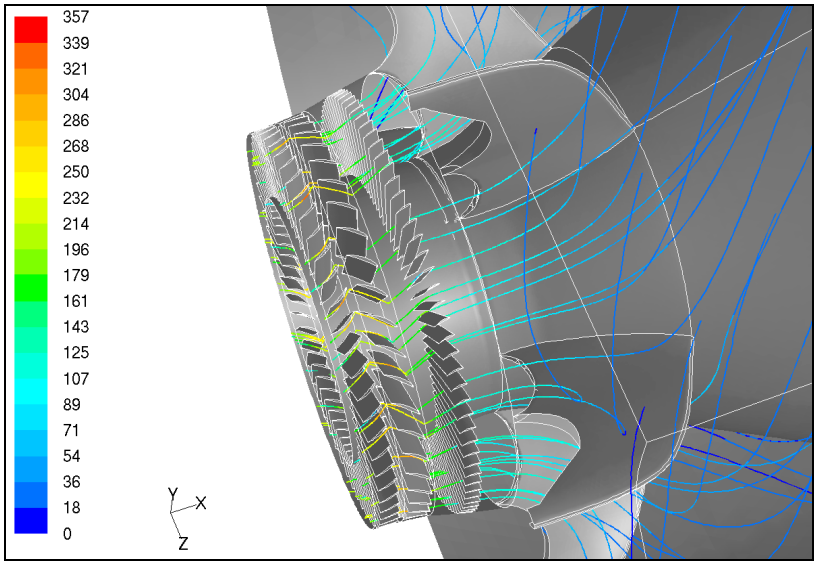

Figure 3–56: Air flow path lines above shaft cone coloured by velocity magnitude (m/s).

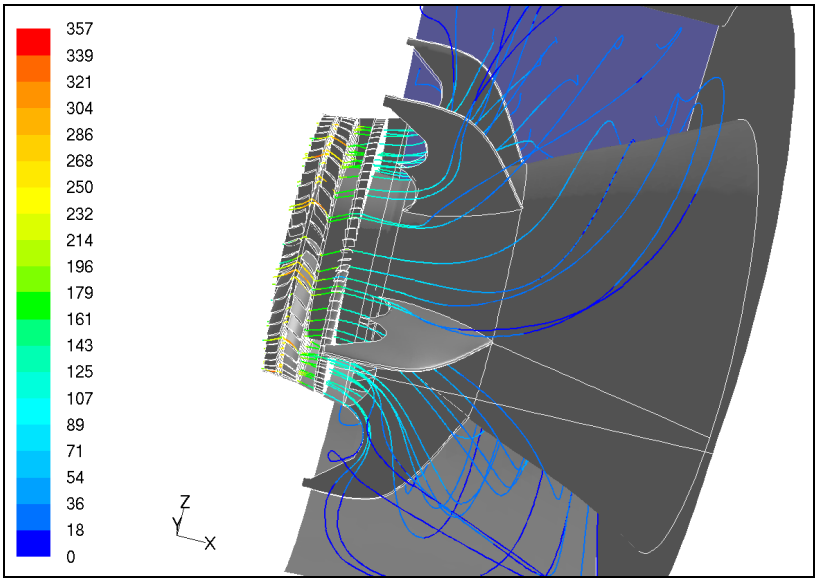

Figure 3–57: Air flow path lines below shaft cone coloured by velocity magnitude (m/s).

Examining the air flow path vertically towards the rear view of the intake, one can see that the air streamlines are quite symmetrical in both parts of the intake separated by the imaginary plane formed by the x and y axes (see figure 3-58).

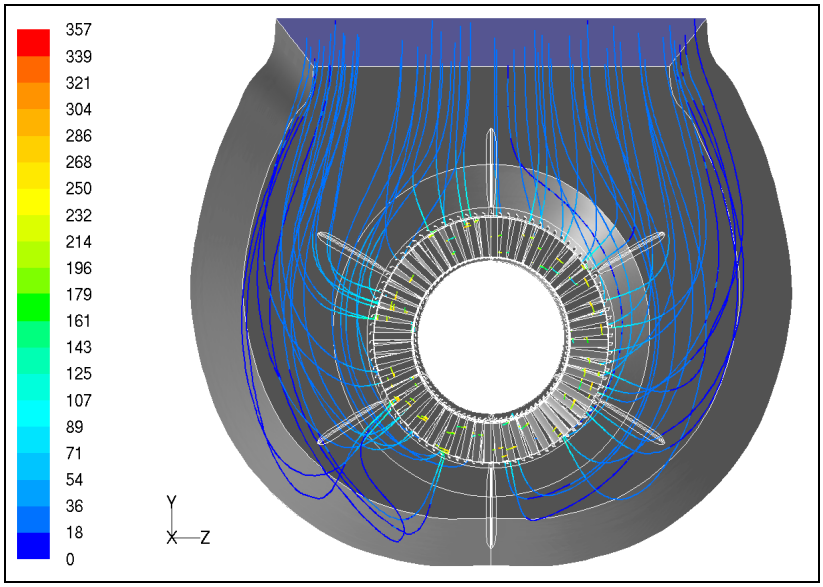

Figure 3–58: Pathlines coloured by velocity magnitude (m/s).

3.8 Connected geometry subjected to water injection

Examining the Arrangement 1 injection setting, it was found (see figure 3-59) that the trajectories of the nozzle number 1 hit the hub area before the IGV entrance annulus area and then these trajectories follow a lifting path towards the compressor stage.

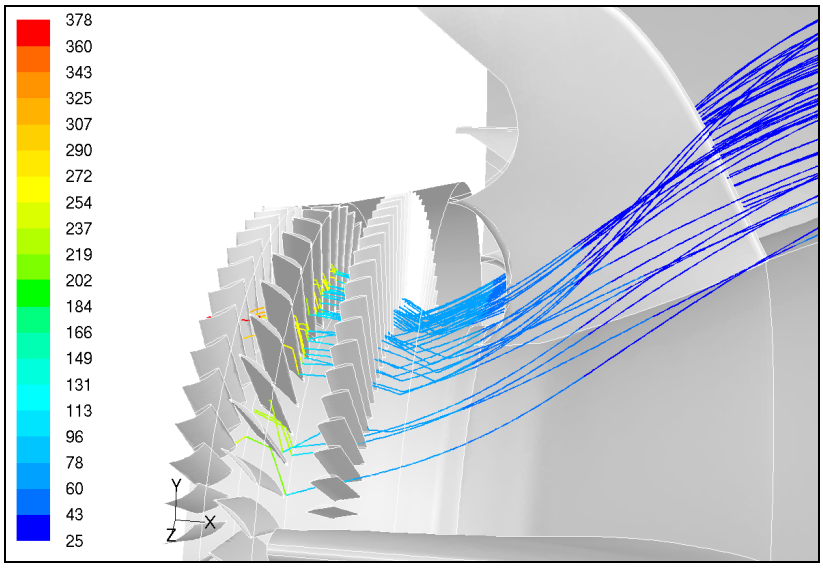

Figure 3–59: Nozzle 1 particle tracks coloured by velocity magnitude (m/s).

However, the trajectories of nozzles 2 and 19 meet the IGVs at midspan and this is quite satisfactory in terms of compressor washing (see figure 3-60). The trajectories of the remaining nozzles were performing in a similar way.

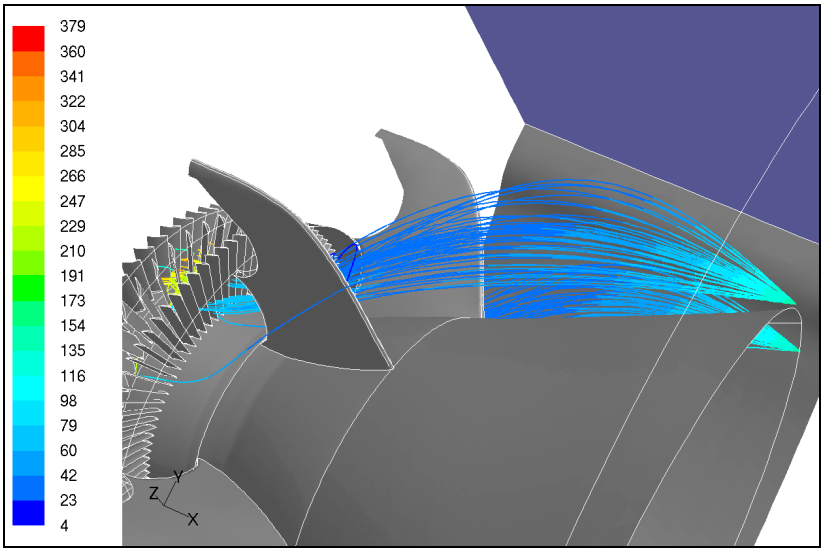

Figure 3–60: Nozzles 2 and 19 particle tracks coloured by velocity magnitude (m/s).

Some water spillage over the rear wall of the industrial intake was unavoidable (see figure 3-61) however, without affecting seriously the washing of the compressor stage.

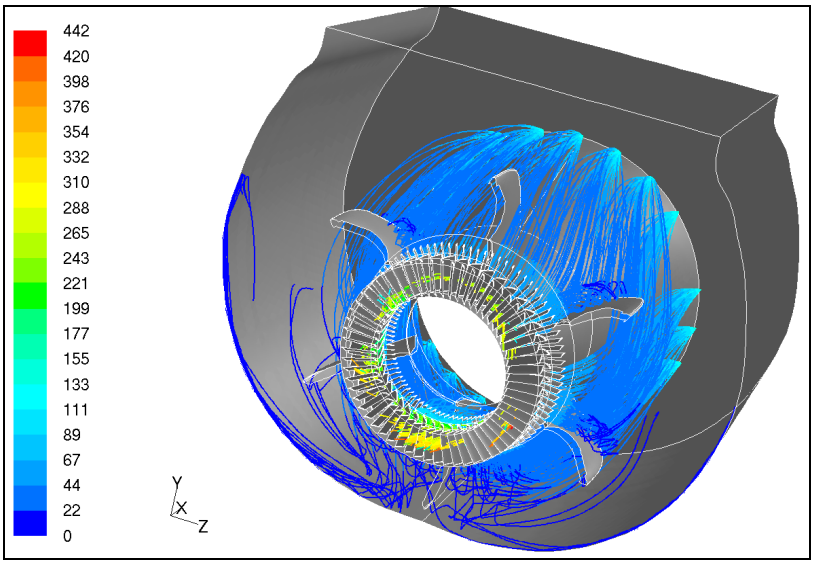

Figure 3–61: Nozzles 1-19 particle tracks coloured by velocity magnitude (m/s).

The upper nozzles droplet lifting path can be seen as well from figures 3-62, 3-63 and 3-64 representing different cross sections along the compressor stage. In front of the IGVs the droplets on the upper part of the engine cone hub seem to be very close to the hub surface however, the droplets on the lower part of the hub seem to be spread along the whole span of the IGVs (see figure 3-62). At the left and right part of the stage not many droplets have arrived.

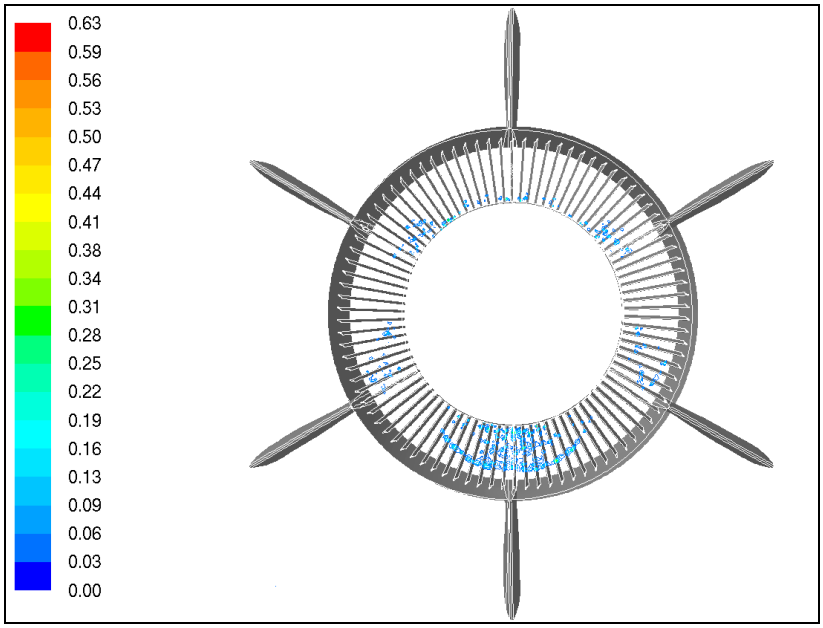

Figure 3–62: IGV-cross sectional-face droplet concentration contours (kg/m^3).

Checking the cross sectional area in front of the rotor (see figure 3-63), it can be seen that the droplets on the upper and lower part of the stage have been shifted up and there are quite a few droplets on the right and left side, as well. This can be attributed to the rotational effect of the rotor that is getting stronger and stronger as the droplets approach the rotor area.

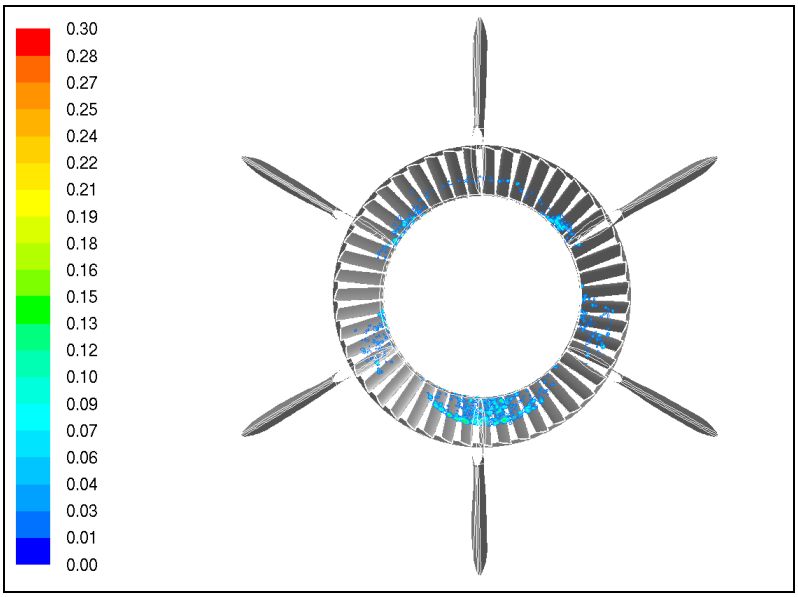

Figure 3–63: IGV-rotor-cross sectional-face droplet concentration contours (kg/m^3).

At the cross sectional face just behind the rotors and in front of the stators (see figure 3-64) the droplets seem to rise even more at the upper and lower part of the face.

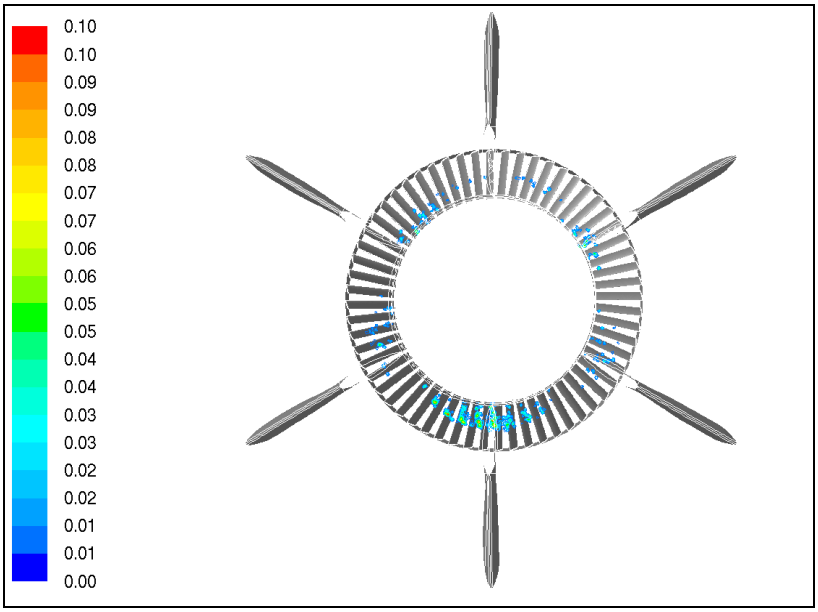

Figure 3–64: Rotor-stator-cross sectional-face droplet concentration contours (kg/m^3).

At the outlet of the stage (see figure 3-65), it was found that a high concentration of droplets took place at the bottom part of the stage.

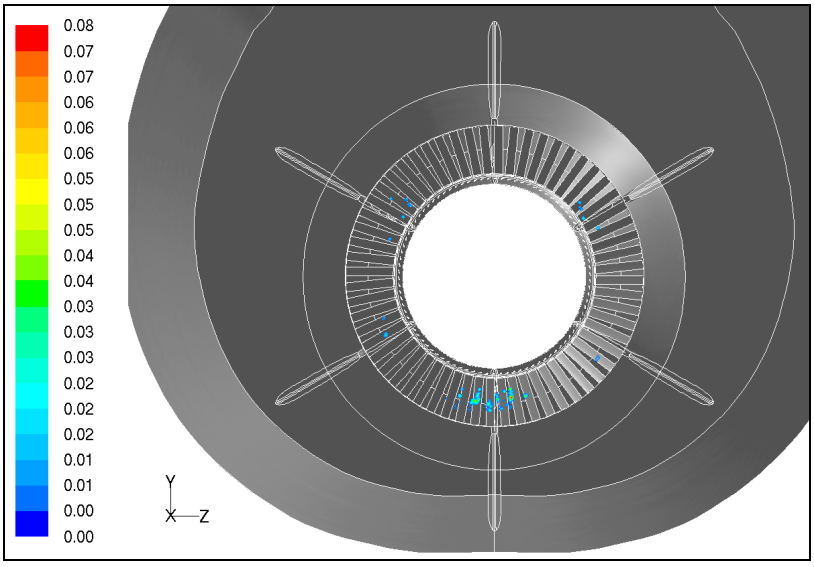

Figure 3–65: Stage outlet-face droplet concentration contours (kg/m^3).

3.9 Examining possible swirl experimentally

In order to examine the possibility of existing swirl in the intake flow of a gas turbine a short test took place at the laboratories of Cranfield university. This test can provide a lot of interesting information to the field of compressor washing since possible swirl found in the intake will have serious effect on the trajectories of cleaning fluid injected for washing.
The engine tested was a Rolls-Royce Avon turbojet gas turbine consisted of a sixteen stage axial compressor, a three stage turbine and a fixed area convergent propelling

nozzle (see figure 3-66). The hub diameter of the engine was 0.31 m and the tip diameter 0.88 m as well. The engine was run at idle conditions at 3300 rpm sucking a mass flow of approximately 68 kg/s.

Figure 3–66: Rolls-Royce Avon jet engine.

Examining the flow images it was found (see figure 3-67) that there is a swirl flow component towards the direction of the engine rotation at the 6 o'clock position of the intake.

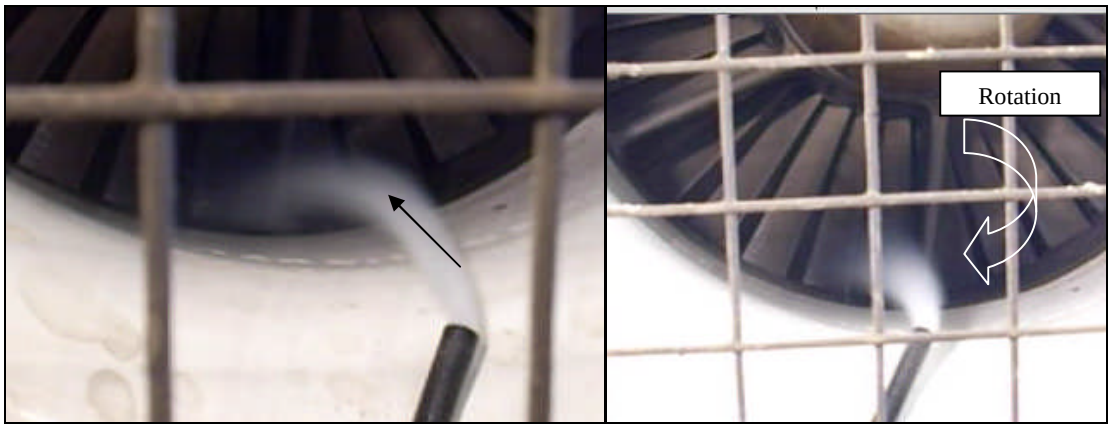

Figure 3–67: Smoke injection at 6 o'clock inlet position.

The 9 and 10 o'clock positions did not indicate any significant swirl component in the flow and the smoke streams seemed to flow axially towards the intake (see figures 3-68 and 3-69).

Figure 3–68: Smoke injection at 9 o'clock inlet position.

Figure 3–69: Smoke injection at 3 o'clock inlet position.

At the 12 o'clock position the flow seemed to have a swirl component towards the engine direction of rotation (see figure 3-70).

Figure 3–70: Smoke injection at 12 o'clock inlet position.

The swirl components appeared at the 6 and 12 o'clock positions of the engine can be attributed to vortices imparted into the flow due to the presence of obstacles existed next to the engine intake in the test house where it is located.

Chapter 4 - Cascade work

4.1 Cleaning fluid and injection nozzle characteristics

The cleaning fluid that is going to be used for the experimental work is the R-MC Power Guard that is a water based cleaner diluted in a ratio of 1:4 with demineralised water. The density of the mixture of the cleaning fluid and water was calculated and it was found to be 992 kg/m^3.
This particular fluid was used for compressor on-line washing of an Alstom Typhoon industrial gas turbine having ten compressor stages, compression ratio of 14.2, air inlet mass flow 18.7 kg/s and producing 4.7 MW of power. The washing system involved for the compressor cleaning of this gas turbine run at an operating pressure of 90 bar for 4 minutes comprising 6 flat fan spray nozzles delivering 1.25 lt/minute each (see figure 4-1). The cleaning mixture of fluid and water was heated at a temperature of 50^{o}C as well.

Figure 4–1: Flat fan spray nozzle.

Each of these injection nozzles used for the Alstom Typhoon compressor cleaning has an orifice width of 0.78mm and orifice height of 0.33mm capable of producing under operating pressure of 90 bar spray width angle of 85 degrees, spray height angle of 42 degrees and droplet diameters of between 50 and 150 μm.

4.2 Washing system part units

The washing system that is going to be used for the test rig experimental work is the ATOMAX MSC system of the R-MC company with just a few modifications. The rig washing system comprises a tank of 40 litres capacity of cleaning fluid (see figure 4-2).

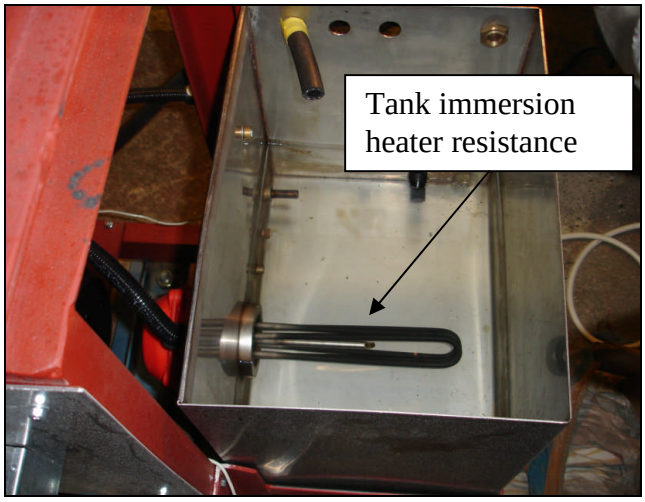

Figure 4–2: Test rig washing system tank.

The tank involves a three phase (440 Volt, 1x3 KW) immersion heater in order to heat up the cleaning fluid in it up to a temperature of 50 ^{o}C. In case the fluid level drops below the level of the heater a float switch for heater protection is involved and if below the intake of the pump another float switch is activated to prevent the pump from running dry (see figure 4-3).

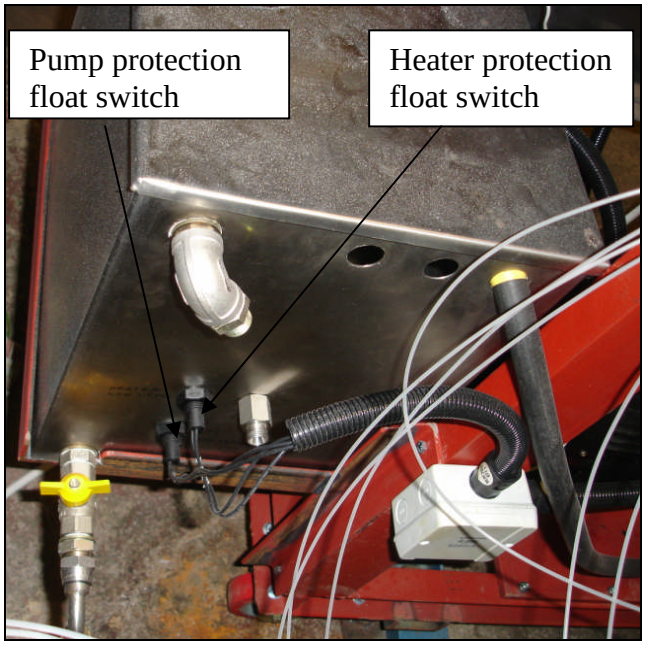

Figure 4–3: Tank float switches.

A temperature gauge is also fitted in the tank in order to display the temperature level of the fluid (see figure 4-4).

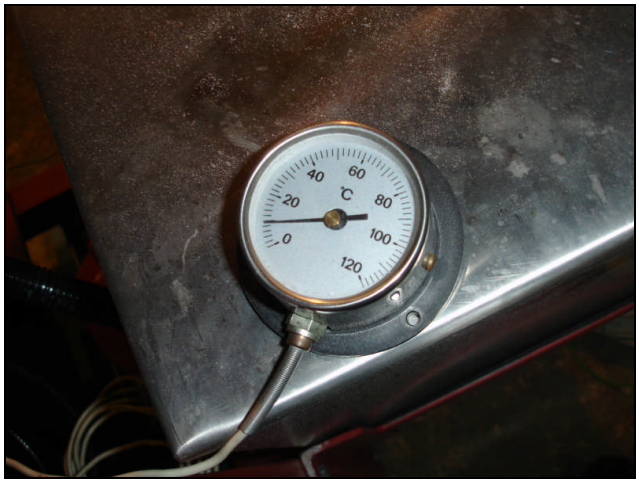

Figure 4–4: Temperature gauge.

The washing fluid is directed to the injection nozzle via a three cylinder plunger pump (5.5HP) capable to deliver 150 bar maximum pressure at 1450 rpm. The pump (figure 4-5) was driven by a three phase electric motor of 2.2 KW running at 1128 rpm. At the outlet of the pump a pressure regulator existed in order to provide the injection nozzle with the desirable pressure which is 90 bar (figure 4-6).

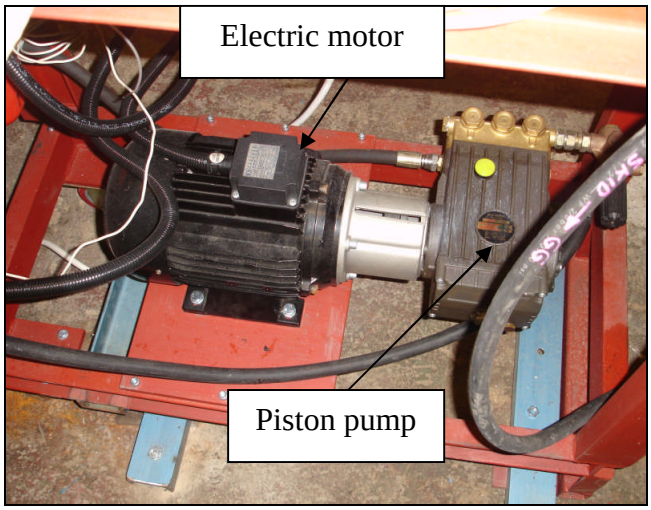

Figure 4–5: Pump and electric motor arrangement.

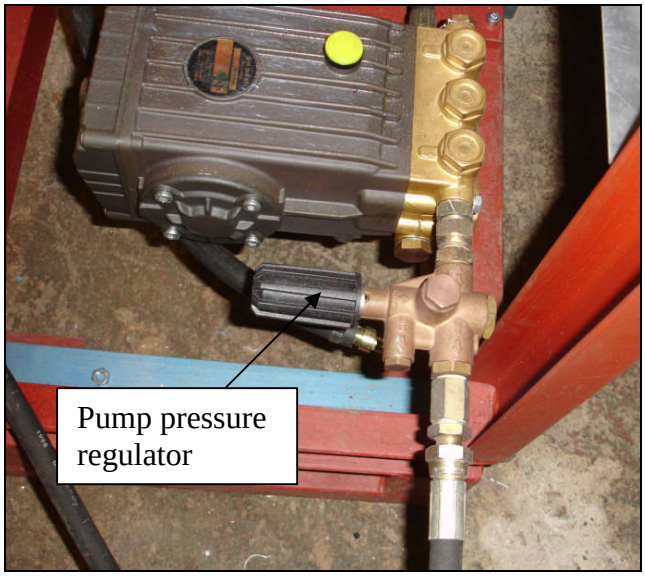

Figure 4–6: Pump pressure regulator.

The reading of the pressure is taken from a pressure gauge fitted next to the injection nozzle (see figure 4-7).

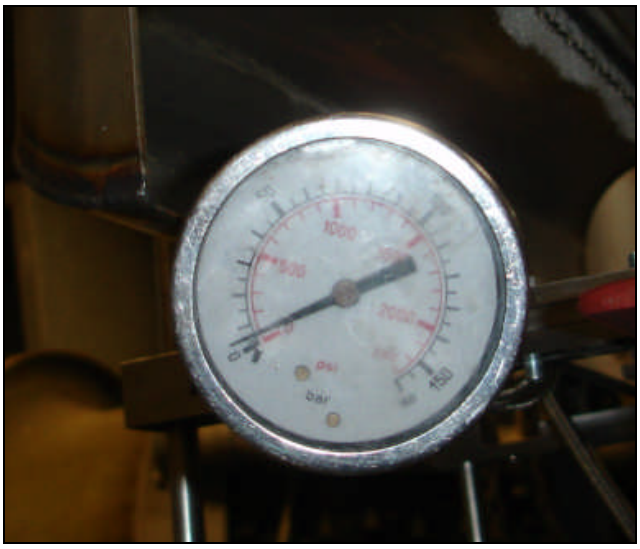

Figure 4–7: Pressure gauge.

In terms of the electrics three important switches are involved in the system. On the electric line there is initially the main power supply electric switch which supports the main pump switch and the heater normal and emergency switch (see figure 4-8).

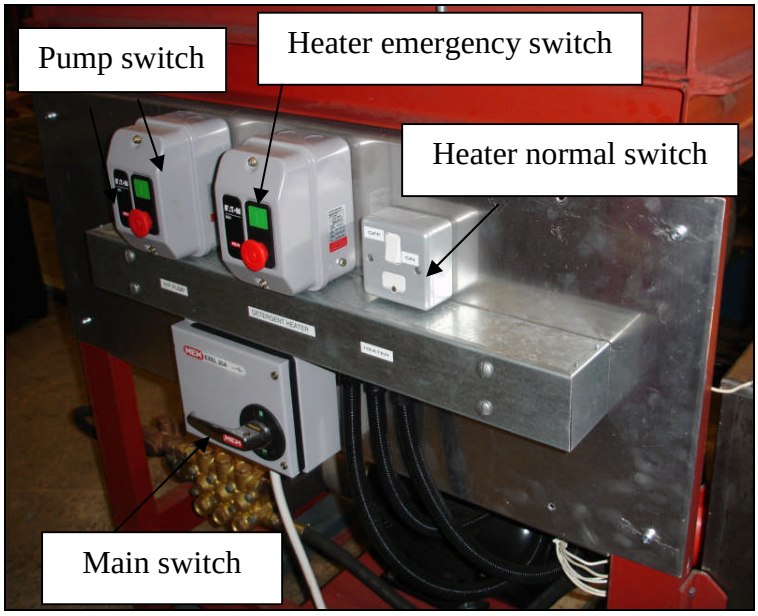

Figure 4–8: Main electric switches.

The nozzle of the injection system involves three degrees of freedom in terms of it's movement with respect to the intake of a compressor cascade test rig. This flexibility in terms of movement comes out from the design of a nozzle adjustable support rack that can be used for various intake compressor cascade suction geometries (see figure 4-9).

Figure 4–9: Nozzle adjustable support rack.

With this nozzle support arrangement different nozzle positions can be investigated with respect to the entry of the cascade intake in order to check their effect on blade washing.

4.3 Designing aspects of the cascade test rig

The design of the compressor cascade test rig comprises a test section involving nine untwisted two dimensional blades. These blades are of NACA 65 thickened profile particular for industrial gas turbines (see figure 4-10).

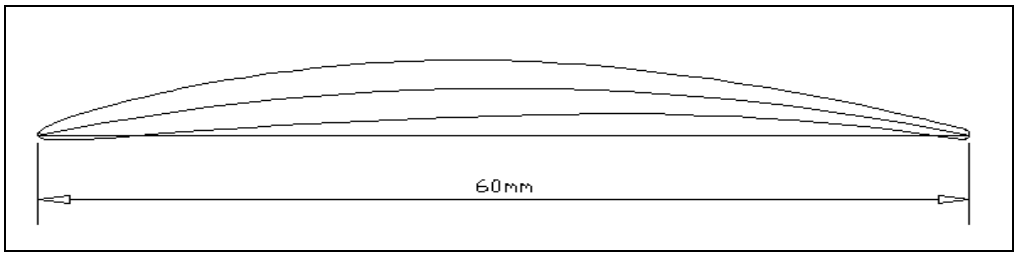

Figure 4–10: NACA 65 thickened profile.

The designing parameters of these blades and the new test rig are illustrated in table 2.

Table 2: Cascade test rig design parameters.

Blade section (width-height) mm	241.659 x 180
Blade number	9
Chord length (mm)	60
Design point incidence (deg)	0
Stagger angle (deg)	36
Pitch / chord	0.8
Thickness/chord ratio (t/c)	0.08
Passage width (mm)	48
Reynolds number based on the chord	$3.8*10^5$
Camber angle (deg)	30

The selection of the particular number of blades has been done under consideration of the wall boundary layer effects. In a compressor cascade the increase in pressure across the blades causes wall boundary layer thickening and contraction of the flow (see figure 4-11).

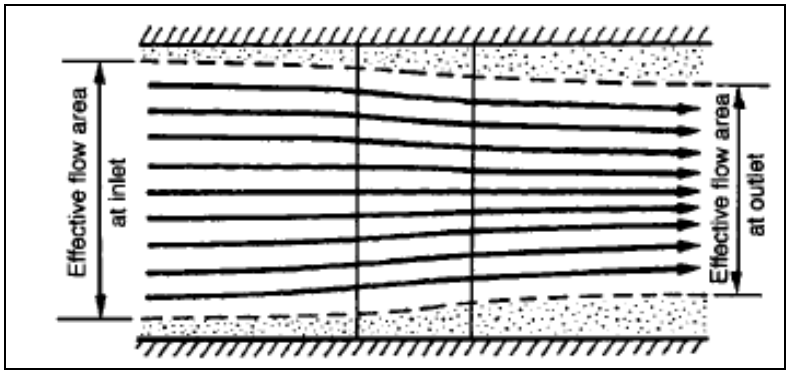

Figure 4–11: Streamline contraction due to boundary layer thickening (Dixon, 1998).

Due to the contraction of the flow the fluid accelerates and this is a fact that comes in conflict with the diffusing action of the compressor cascade and hence reduces the static pressure increase that theoretically would be achieved.
In order to reduce these effects Dixon (1998) refers that it is customary to incorporate at least seven blades for compressor cascade testing and each blade having a minimum aspect ratio (span/chord) of three. Following the authors statements the appropriate test rig selections have been done in terms of blade number and aspect ratio.
Pollard and Gostelow (1967) run some experiments with two low speed compressor cascade tunnels, one having an aspect ratio less than 3 and applying sidewall boundary layer suction and one with solid walls having a high blade aspect ratio greater than 3. The authors state that if porous sidewalls are used to control the sidewall boundary layer, a low aspect ratio will give good two-dimensional results, while for the case of solid side walls two-dimensionality of the flow can be obtained using aspect ratios equal or greater than 3.

4.4 Step calculations for the test rig design

The designing of the cascade test rig involved several calculations and parameters that were taken into account. Initially, the values of pitch over chord ratio, camber angle and nominal deviation had to be established. The nominal deviation δ^* is the deviation related to the nominal deflection ε^* that is the deflection at 80% of maximum deflection. In order to calculate the nominal deviation, the parameter m had to be extracted from the graph of figure 4-12 that gives a relation between this parameter and the blade stagger angle.

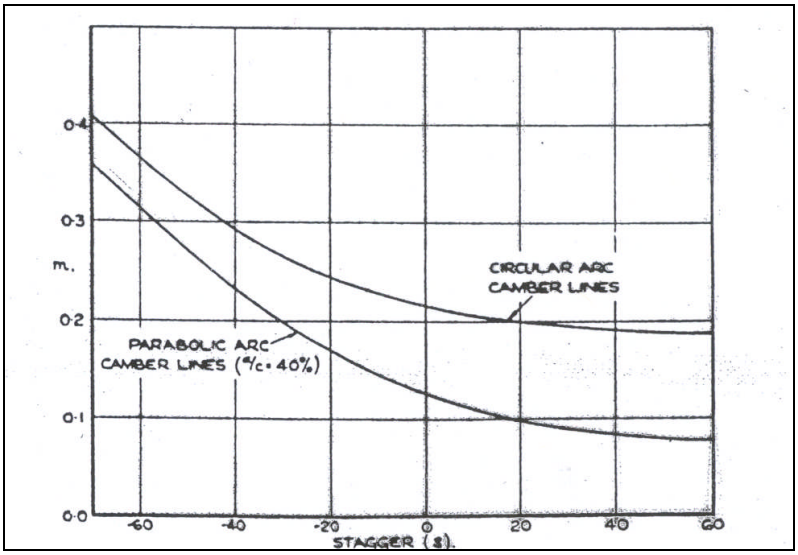

Figure 4–12: Parameter m versus stagger angle (Ramsden, 2002).

The nominal deviation was estimated using the following formula according to Horlock (1973):

$$\delta^* = m\theta\sqrt{\frac{s}{l}} \quad (155)$$

m : parameter m
θ : camber angle
$\frac{s}{l}$: space / chord ratio

Obtaining the value of nominal deviation and knowing the blade metal outlet angle for fixed blade incidence, the nominal outflow angle β_2^* was calculated as follows:

$$\beta_2^* = \delta^* + \beta_2^{'} \quad (156)$$

$\beta_2^{'}$: outlet blade metal angle ($a_2^{'}$ figure 2-17)

The value of nominal outlet angle β_2^* was used in order to calculate the outlet area A_2 of one blade passage and to compare it with the inlet area A_1 of the same passage where the incidence was chosen to be zero degrees and to obtain the De haller number c_2/c_1 (see figure 4-13). This important value had to be checked if it is greater than the value of 0.7 in order for the design to be judged as acceptable.

DeHaller number = $A_1/A_2 = c_2/c_1$ (157)

A_1: Inlet passage area

A_2: Outlet passage area

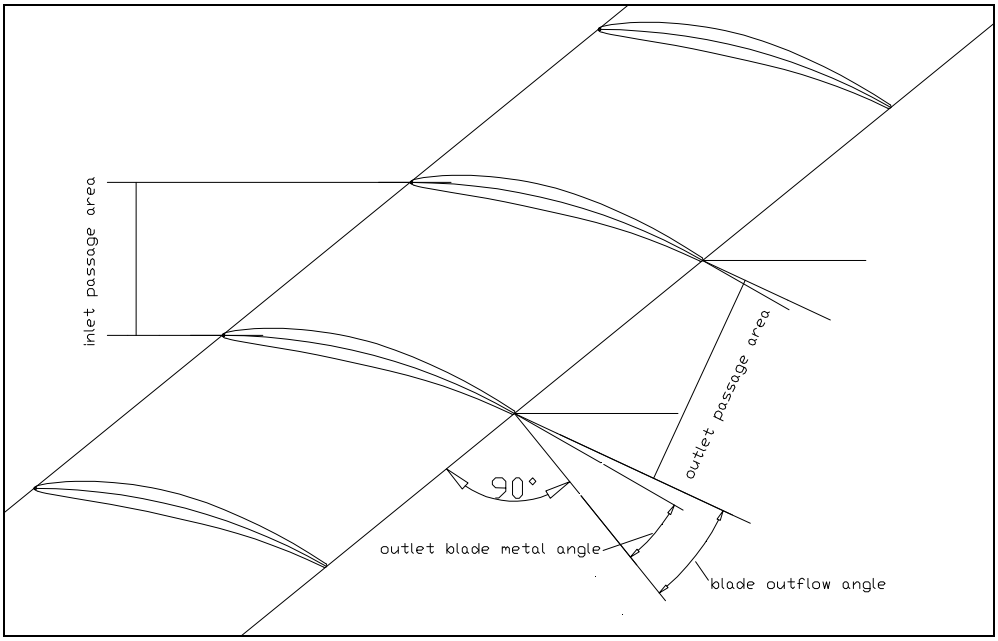

Figure 4–13: Example of blade passage inflow and outflow areas.

4.4.1 Blade passage calculations

Having established the number of blades, the chord length (60mm), the blade aspect ratio (3) and the space/chord ratio (0.8) of the blade passage, the rig test section was designed by having the nine blades inclined in a plane diverging from the vertical plane test section at 51 degrees (see figure 4-14).

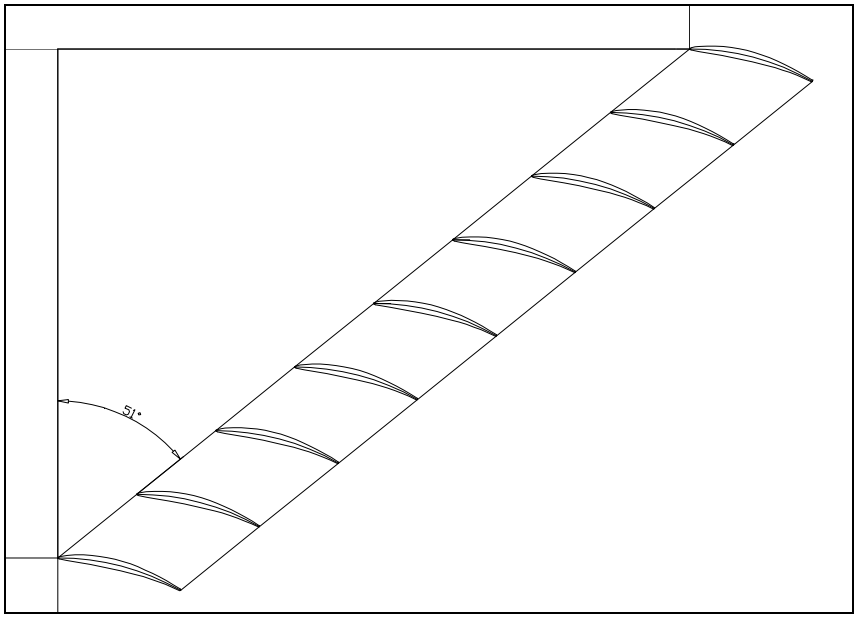

Figure 4–14: 51 degrees blade section inclination.

This plane inclination took place in increments of one degree clockwise up to the time the pressure rise along the blades corresponded to an acceptable De Haller number greater than 0.7. At 51 degrees the De Haller number was found to be 0.7 which was

an acceptable value for the cascade blading which was set at zero incidence (see figure 4-15).

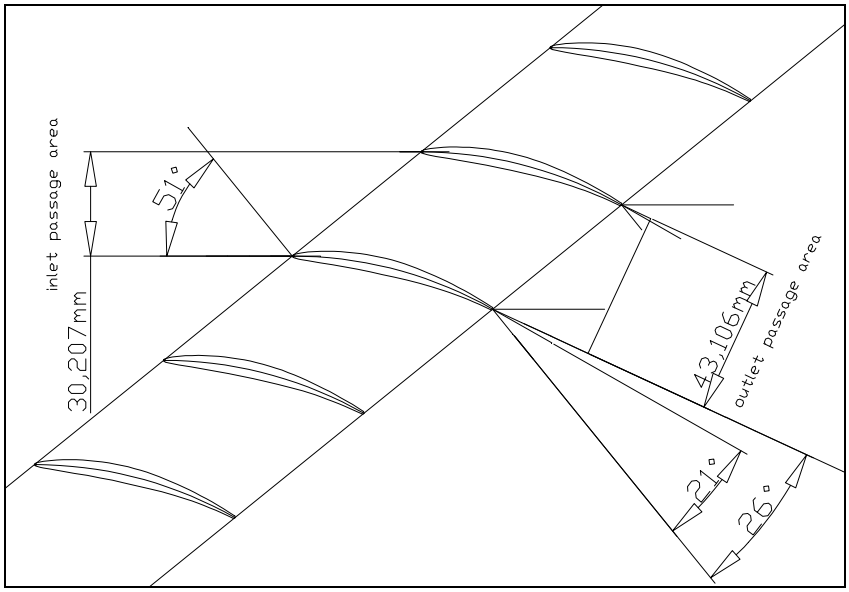

Figure 4–15: Dehaller number indication (passage inlet / passage outlet area).

In order to achieve the De Haller number for zero blade incidence the passage inlet and outlet areas were estimated. The inlet passage area was estimated by just taking the vertical distance between two horizontal streamlines entering the passage and bumping on the leading edges of two opposite blades. The outlet area was estimated by taking the vertical distance between two outlet streamlines from the same blades.
The next step in terms of calculations was to determine the air mass flow through the rig by establishing a test section inlet Mach number value of 0.3. Then from compressible flow tables (see Appendix table 9) the 1000Q value was found to be 19.861 and the mass flow rate through the rig was estimated to be 5.1 kg/s according to the following formula:

$$1000Q = 19.861 \Rightarrow 1000\frac{w\sqrt{T_1}}{P_1 A_1} = 19.861 \Rightarrow w = \frac{19.861 P_1 A_1}{1000\sqrt{T_1}} \qquad (158)$$

w: test section mass flow rate

T_1 : test section inlet total temperature (293.15 K)

P_1 : test section inlet total pressure (100576 Pa)

A_1 : test section inlet cross sectional area (241.659 mm x 180mm)

The total pressure and total temperature at the test section entrance was calculated by assuming that:

- Total pressure loss along the intake 1%
- Total temperature constant along the rig (adiabatic flow)

The total pressure and temperature at the intake flare of the test rig was established to be at the levels of ambient values where the test rig suction fan was tested to. Then checking the characteristic curve of the fan (see Appendix figure A3 and table 10) followed in order to see if the fan can handle the calculated mass flow of 5.1 kg/s and the value was found to be acceptable.

4.4.2 Test rig intake flare

The intake of the compressor cascade rig has been designed according to the specifications of McKenzie's (1966) intake flare (see figure 4-16).

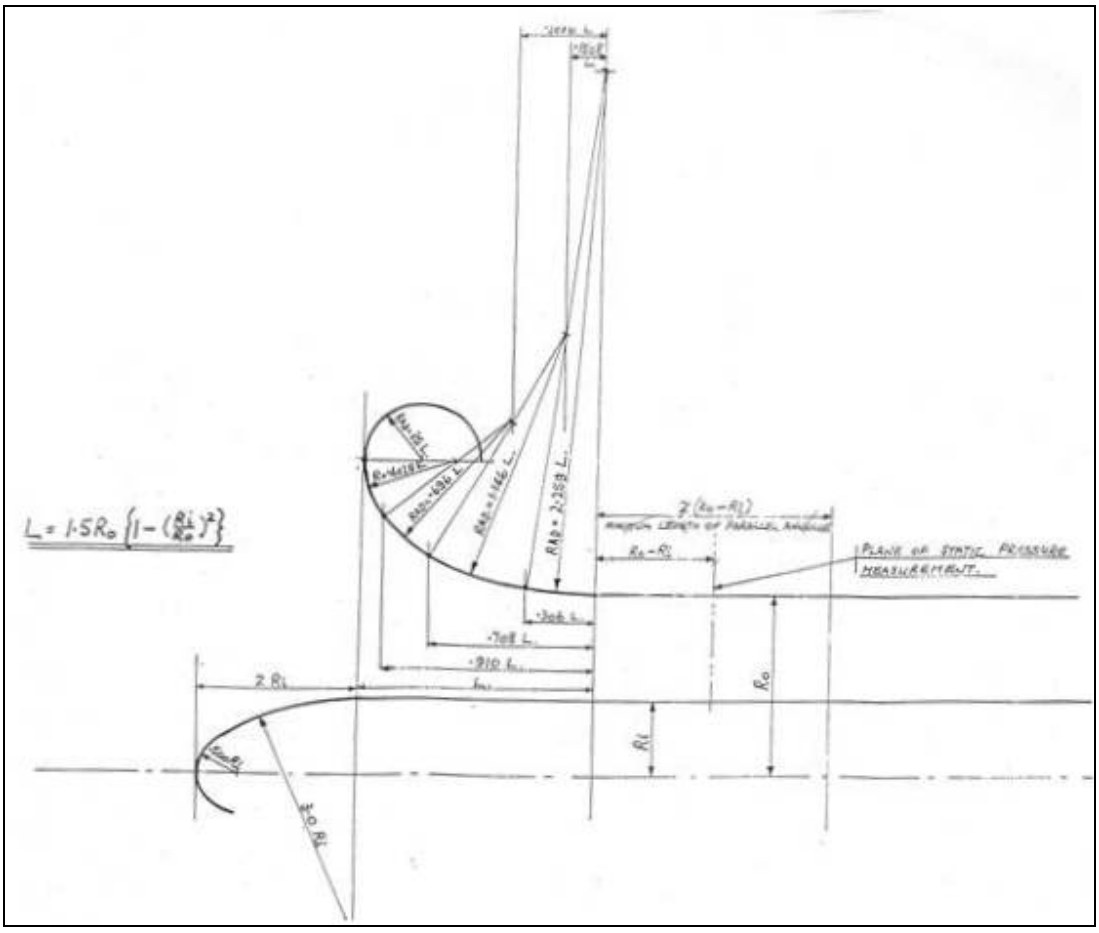

Figure 4–16: McKenzie's intake flare specification dimensions (McKenzie, 1966).

4.4.3 Test rig plenum chamber and exit cone

A plenum chamber (see figure 4-17) was installed at the back end of the blade test section. The ideal cascade experiment would discharge the airflow from the blading into an infinite space (atmosphere e.g.). In the case concerning the current project, since the facility employs a suction pump (fan) this is not possible. Accordingly, the blading discharges into the largest volume feasible. It is important however, that the

effect of the plenum chamber does not distort the cascade discharge streamtube substantially.

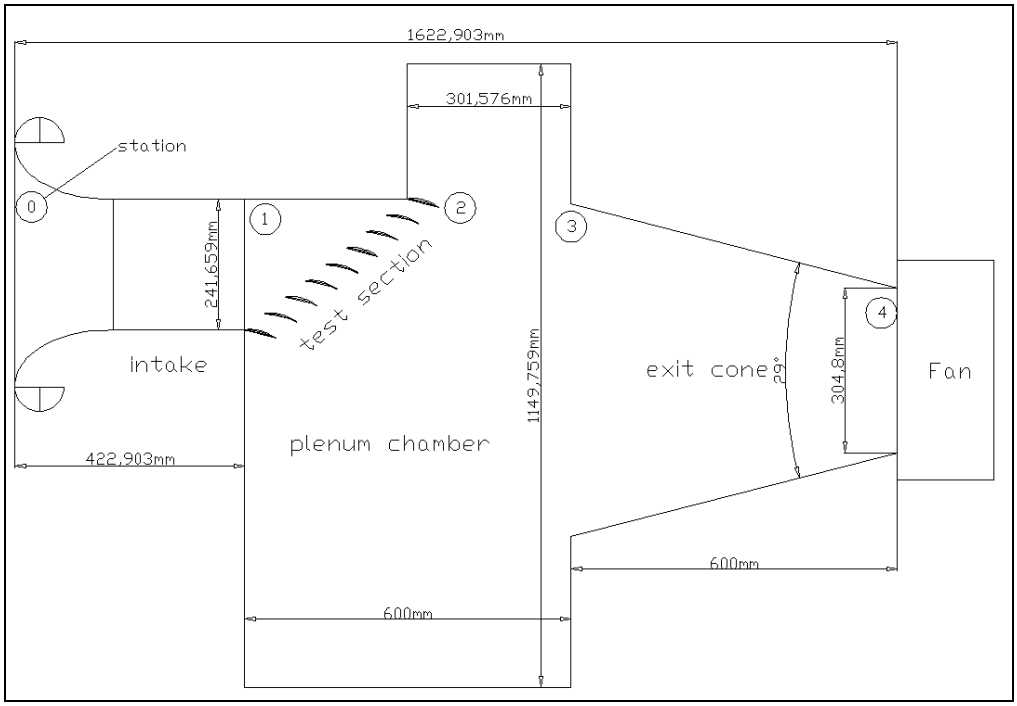

Figure 4–17: Test rig with plenum chamber configuration (zero incidence).

The dimensions of the plenum chamber were not calculated arbitrarily. First the nominal deviation of the blades set at zero degrees incidence was calculated (see table 3).

Table 3: Nominal deviation and outflow angle data.

camber angle θ degrees	space/chord ratio (s/c)	inlet flow angle α_1 degrees				
30	0.8	51				
incidence i degrees	stagger angle ζ degrees	m	nominal deviation $\delta^*=m\theta(s/c)^{0.5}$ degrees	blade metal angle α_2' degrees	nominal flow outlet angle α_2^* degrees	nominal deflection $\varepsilon^*= \alpha_1-\alpha_2^*$ degrees
0	36	0.19	5.098	21	26.1	24.9

The outflow angle for zero blade incidence was estimated and the outflow streamlines corresponding to these angles were drawn behind the blade trailing edges (see figure 4-18).

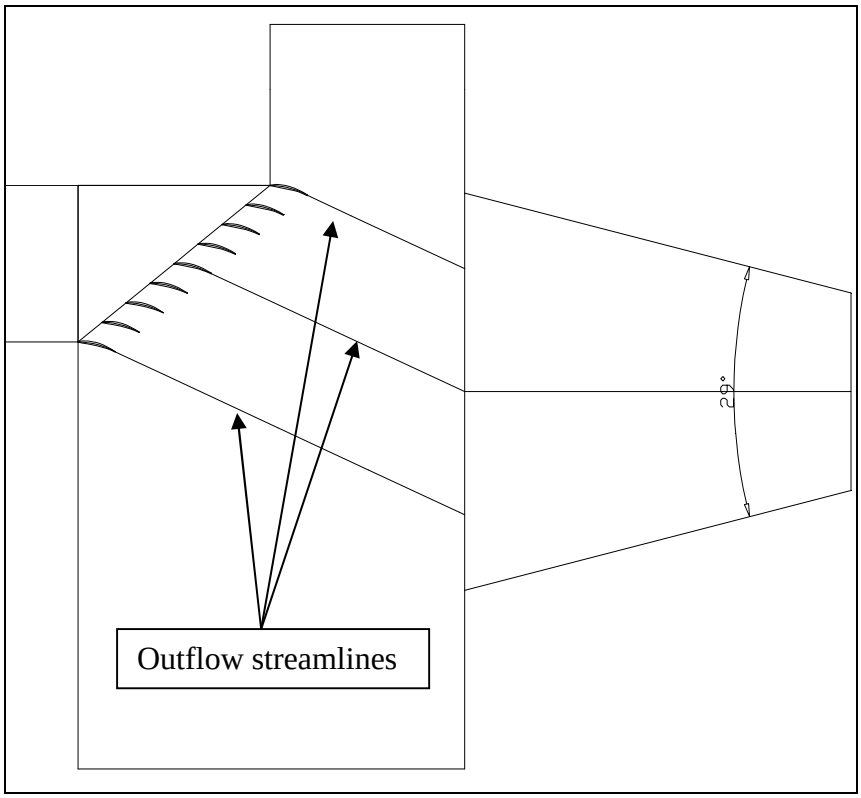

Figure 4–18: Zero incidence cascade blade exit streamtube.

The plenum chamber designed was a metallic box of 600 mm length in order to accommodate enough space for the positioning of a yaw meter behind the blades at least one chord in order to obtain measurements of pressures, velocities and outflow angles. The height of the plenum chamber was chosen to be approximately 1150 mm.
The exit of the plenum chamber was determined by taking into account the nominal exit flow angle corresponding to the zero degrees nominal incidence giving to it an extra distance corresponding between two exit streamlines on both ends so that the plenum exit cone shape duct to accommodate comfortably the cascade exit flow streamtube.
The length of the exit cone was 600 mm with cone angle of 29 degrees in order to accommodate comfortably the cascade exit streamtube. 29 degrees is a satisfactory value since according to Munson (1998) it gives a low loss coefficient K_L of around 0.02 determined from the following formula:

$$K_L = \frac{\Delta p}{\frac{1}{2}\rho V^2} \qquad (159)$$

Δp : pressure drop along the duct
V : duct velocity inlet
ρ : fluid density

4.5 Test rig measurements

Experiments have to be done with the compressor cascade test rig of the current project under certain blade inlet Mach number and nominal blade incidence angle of zero degrees. The parameters that are going to be measured are the following:

- Static and total pressures one chord upstream of the cascade blades
- Static and total pressures one chord downstream of the cascade blades
- Exit flow angles one chord downstream of the blades
- Velocity of the flow one chord downstream of the blades

Using this data the total pressure loss coefficient $\Delta p_0 / (\frac{1}{2} \rho c_1^2)$ can be calculated.

The inlet axial cascade velocity c_1 can be calculated by applying continuity.

$$c_1 = \dot{m} / \rho A_1 \quad (160)$$

$\dot{m}$: mass flow rate

ρ : air density

A_1 : inlet cascade area

4.6 Test rig 3-D representations

Initially, the test rig was about to be built in terms of variable incidence cascade blades moving on a turntable (see figure 4-19).

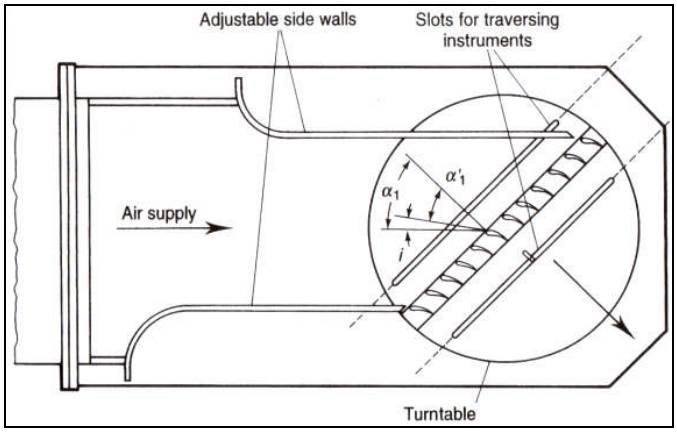

Figure 4–19: Cascade test rig with turntable (Saravanamuttoo, 2001).

In order to accommodate cascade tests over a wide incidence range, the horizontal position of the plenum chamber exit to the fan could be moved vertically. This would minimise the effect of the plenum exit ducting position on the cascade exit streamtube

shape as far as incidence was changing (see figure 4-20) in order for the streamtube to be accommodated as comfortably as possible from the exit cone.

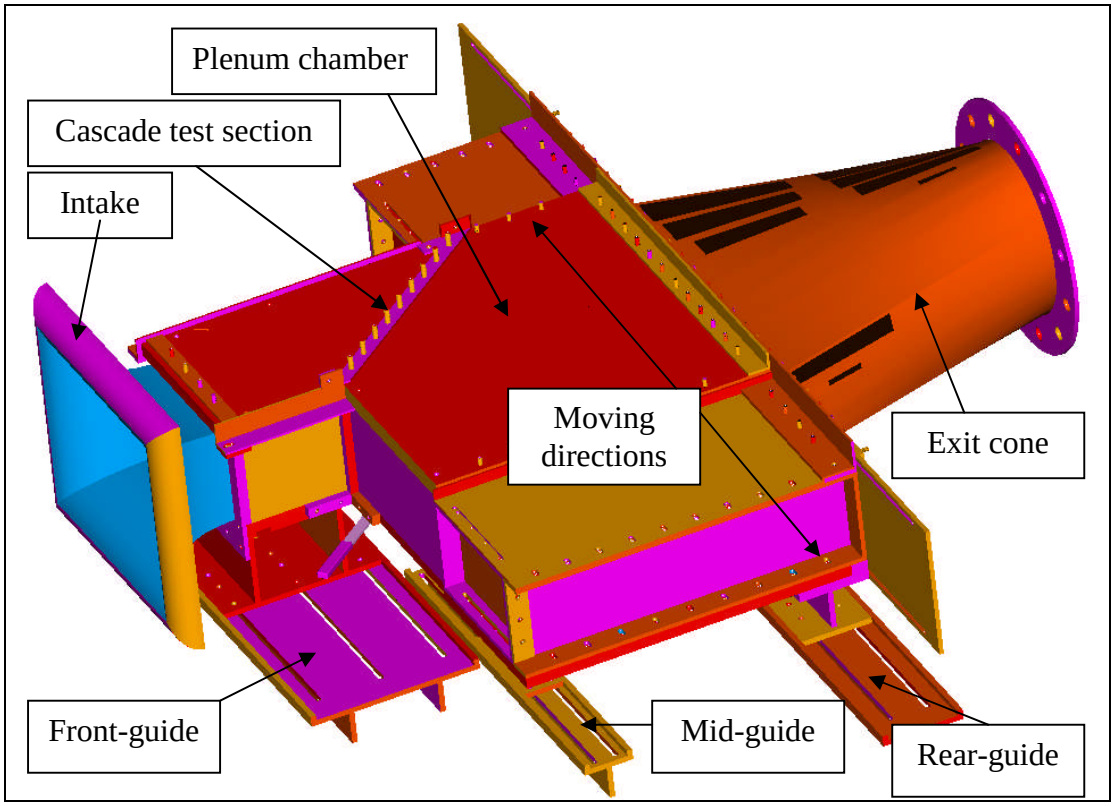

Figure 4–20: Initial cascade rig right isoview.

In figure 4-20 one can see the front, mid and rear guides along which the whole test rig could slide on, always vertically with respect to the axial direction. The exit cone of the rig is stationary and bolted on the centrifugal fan that runs the test rig. This stationary exit cone could be welded on a transfer plate (see figure 4-21) that would be the medium connecting the moving part with the stationary part of the test rig. This transfer plate had slots along which the moving part of the rig could slide on.

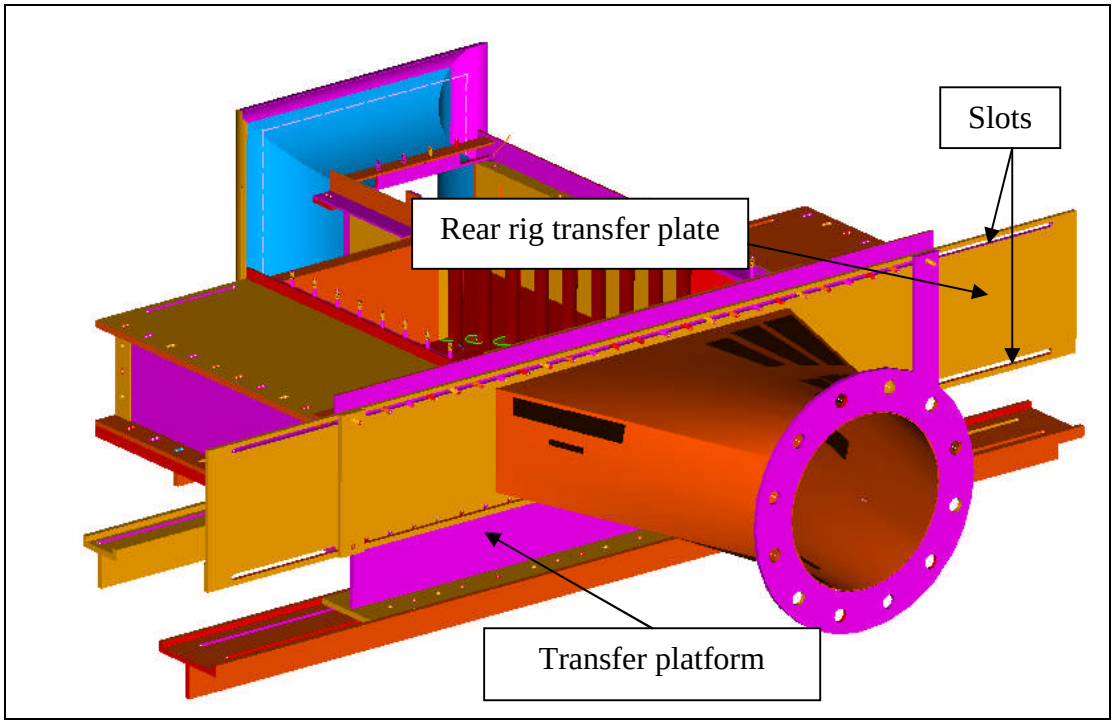

Figure 4–21: Initial cascade rig rear view.

However, it was decided that the rig will be of constant incidence which was chosen to be the nominal blade incidence of zero degrees and for this reason there was no need of using transfer guides, platforms and transfer plate, fixing so the exit cone at a particular position with respect to the remaining part of the test rig (see figure 4-22).

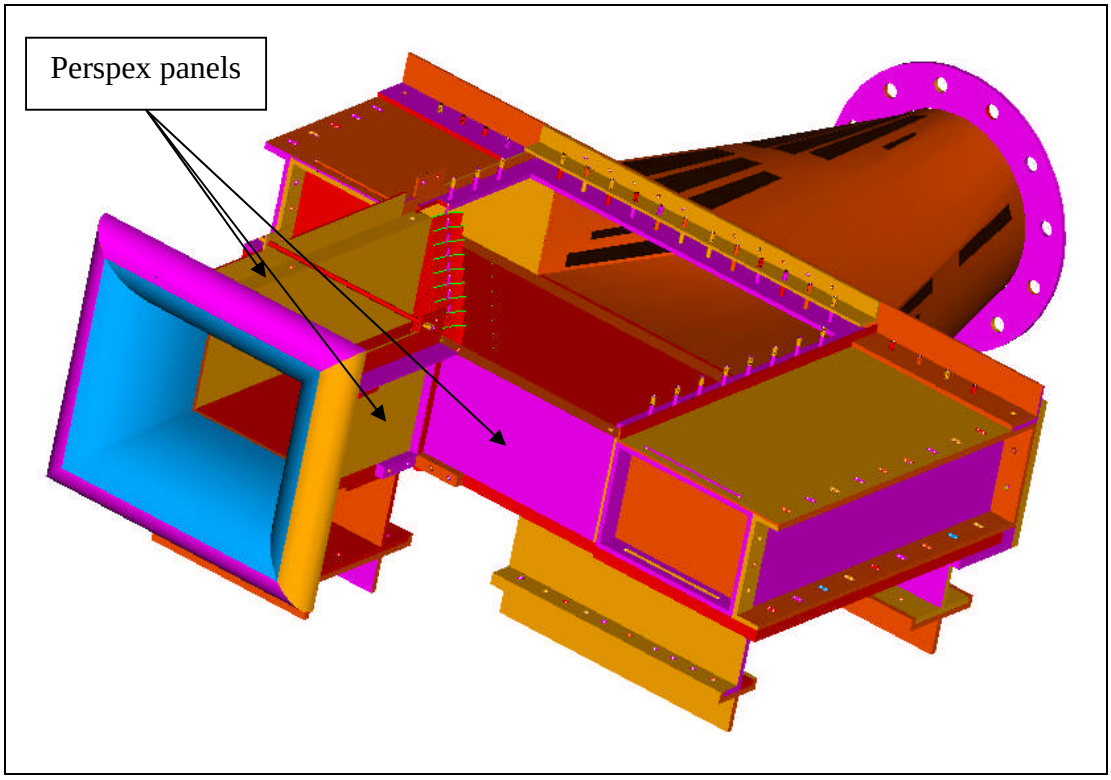

Figure 4–22: Actual cascade rig isoview.

From figure 4-22 one can see that the whole rig arrangement involves three side transparent panels made from perspex with 30mm thickness. Two of these panels are positioned on the left and the right side of the rig in order to provide visibility in front of the test section of the rig. Another one panel is positioned at the left side of the plenum chamber and the biggest one is the panel that covers the roof of the rig illustrated on figure 4-23. On this perspex roof a slot will be drilled in order to accommodate the yaw meter that will take measurements of the cascade blade exit flow angles.

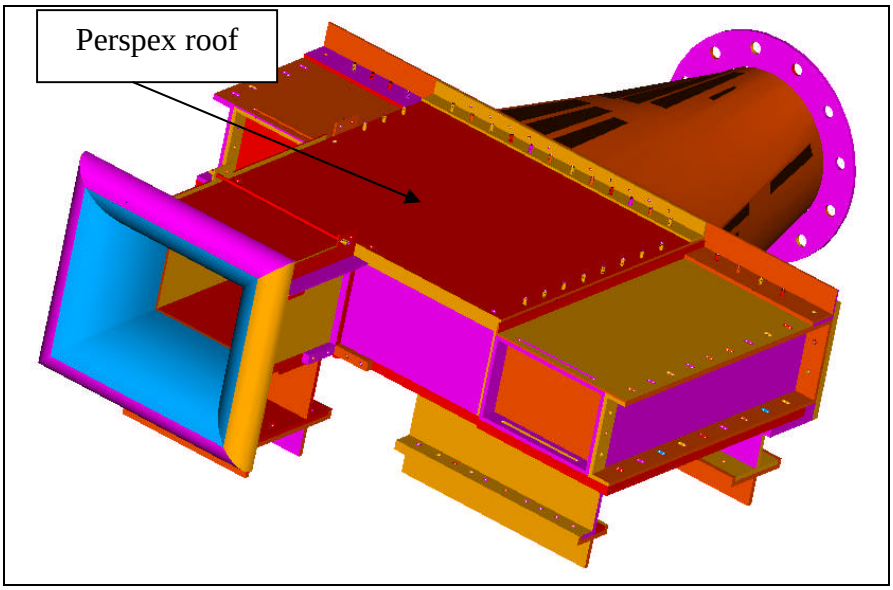

Figure 4–23: Actual cascade rig upper Perspex illustration.

The upper and side view of the test rig is illustrated by figures 4-24 and 4-25 respectively. From these figures one can see more clearly where the cascade blades (see figure 4-26) are positioned on the rig floor.

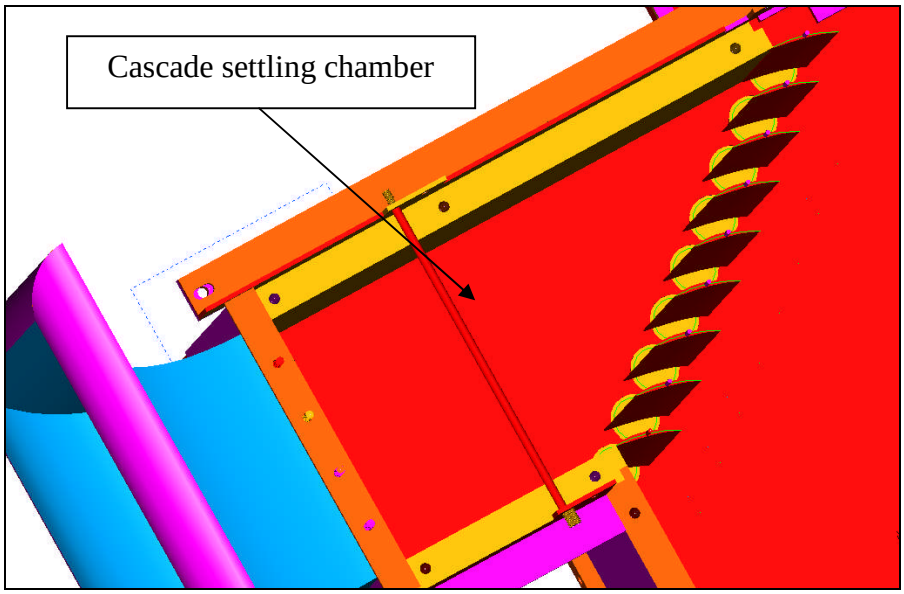

Figure 4–24: Actual cascade rig test section.

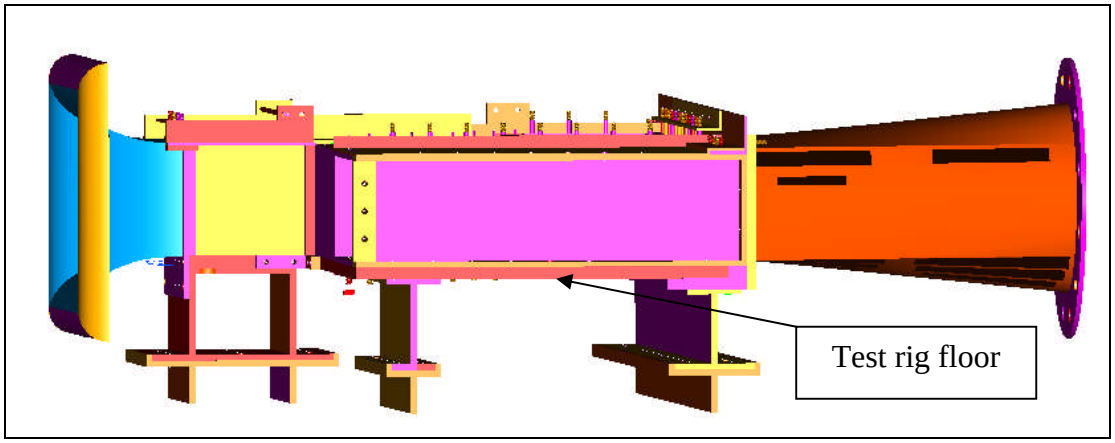

Figure 4–25: Cascade rig side view.

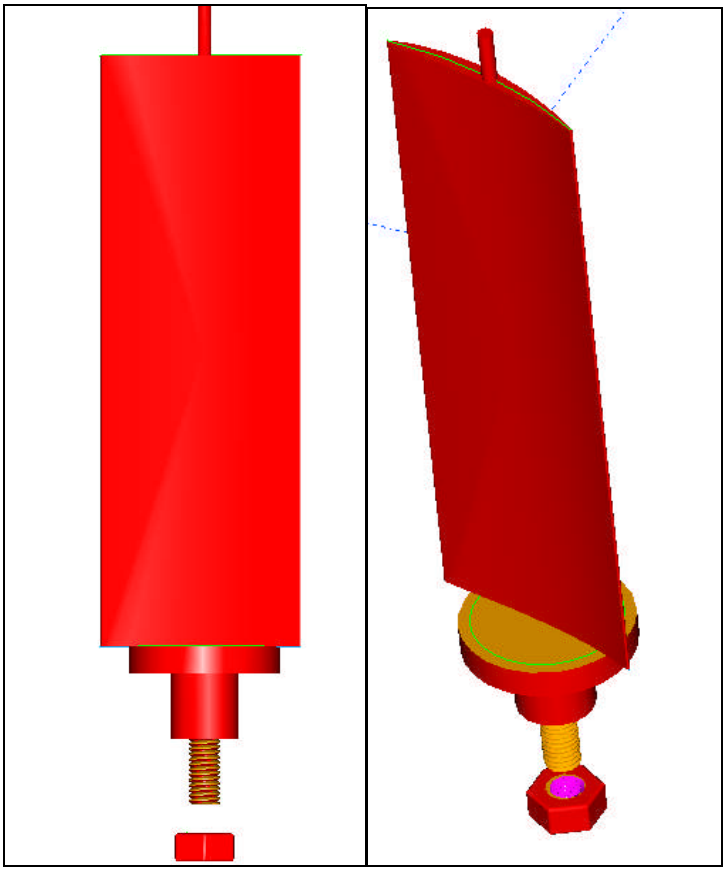

Figure 4–26: 2-D and 3-D blade illustration.

The last part of the test rig comprises a centrifugal fan with a butterfly valve arrangement positioned between the fan and the cascade test rig exit cone (see figure 4-27) in order to control the mass flow rate through the rig. The fan is driven by an electric motor of 45 kW power running at 2955 maximum rpm.

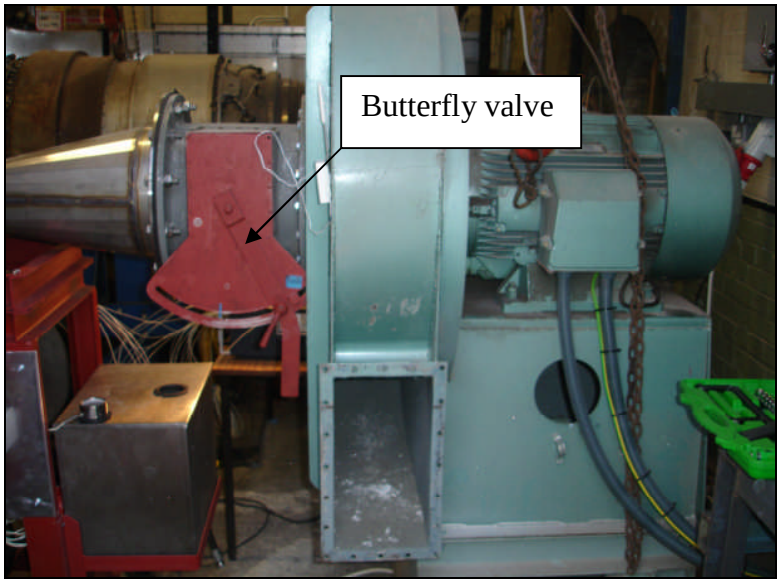

Figure 4–27: Centrifugal fan illustration.

4.7 Test rig instrumentation

The test rig is constructed to involve a set of different kind of measurements taken from various instrumentation available.

4.7.1 Pitot

Pressure measurements in a traverse set at one chord distance in front of the blade leading edges were taken by an L-shaped pitot static tube (see figure 4-28) with an outer diameter of 2.3 mm from the head up to a distance of 123 mm after it's bend. After this distance the diameter was 4 mm. The total length of the tube is 270 mm and it's inner diameter is 0.85 mm.

Figure 4–28: Pitot-static tube.

The total and static pressure measurements taken from this tube were used for the calculation of the inner cascade velocity as follows:

$$M = \sqrt{\frac{2}{\gamma - 1}\left[\left(\frac{P_t}{p_s}\right)^{\frac{\gamma-1}{\gamma}} - 1\right]} \qquad (161)$$

M : Mach number
P_t : total pressure
p_s : static pressure
γ =0.4

$$v_i = M\sqrt{\gamma R T_s} \qquad (162)$$

v_i : local velocity

R=287 J/kgK

T_s : static temperature

where

$$T_s = \frac{T}{1+\frac{\gamma-1}{2}M^2} \qquad (163)$$

T : total pressure

Calculating the value of velocity in front of the cascade blades the mass flow rate $\dot{m}$ can be achieved as follows:

$$\dot{m} = \rho A U \qquad (164)$$

ρ : air density

$$\rho = p_s / RT_s \qquad (165)$$

A : cascade inlet cross sectional area (settling chamber cross sectional area)

In order to calculate the air mass flow rate of the cascade tunnel, first the discharge velocity had to be determined in front of the cascade test section using the same pitot static probe traversing it in a cross sectional plane perpendicular to the flow in the area of the settling chamber half width distance from the first blade (see figure 4-29). This distance was chosen according to the preliminary test rig design CFD results showing a uniform velocity distribution there.

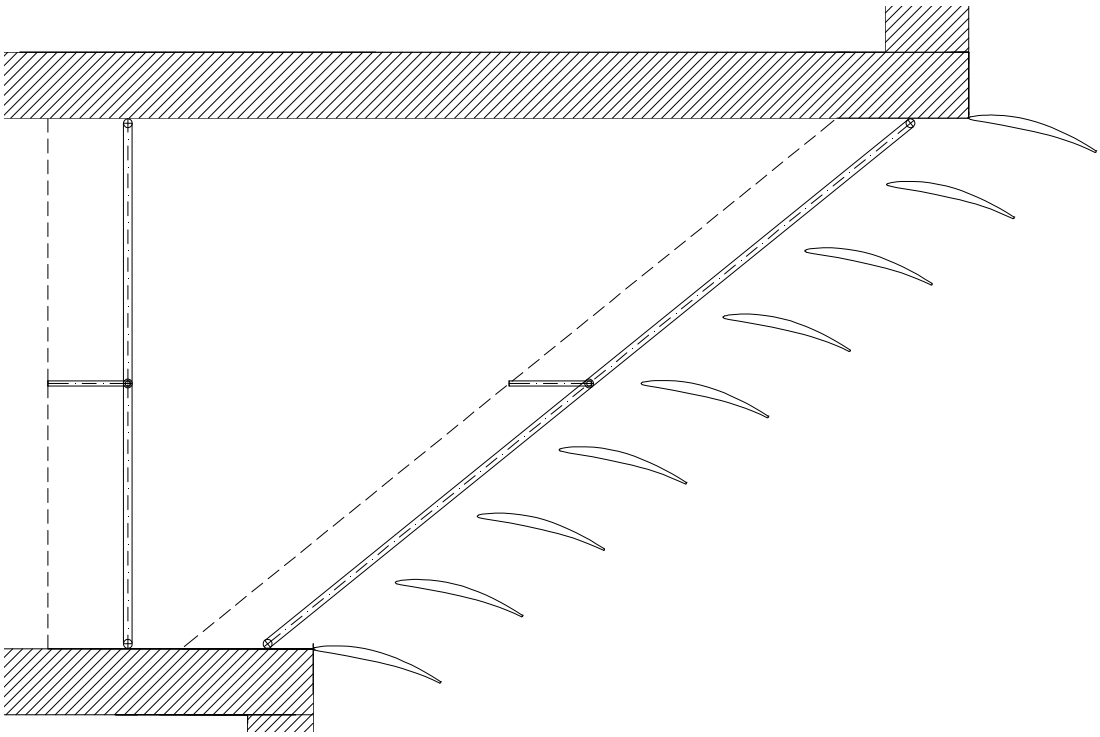

Figure 4–29: Actual positions of pitot-static tube in the cascade rig.

In order to calculate the velocity an arithmetical method was used. According to Bristish Standard 1042, the measuring cross-section is divided into a smaller number of section elements. The measuring locations are predetermined for each section element from an assumption of the mathematical form of the velocity distribution law in the element under consideration and from a choice of the weighting coefficients. According to the BS 1042, in the peripheral zone, a logarithmic law is assumed for velocity distribution with respect to the distance from the wall. The arithmetical method used at the current case was the Log-linear method where according to the BS 1042 by hypothesis the mathematical form of the velocity distribution law for each element is:

$$v = A \log y + By + C \quad (166)$$

y: distance to the wall
A,B,C: any three constants

This British standard in order to apply the log-linear method in a rectangular cross-section uses 26 measuring points whose locations are given in figure 4-30 accompanied with a table of weighted coefficients for each measured local velocity corresponding to each point.

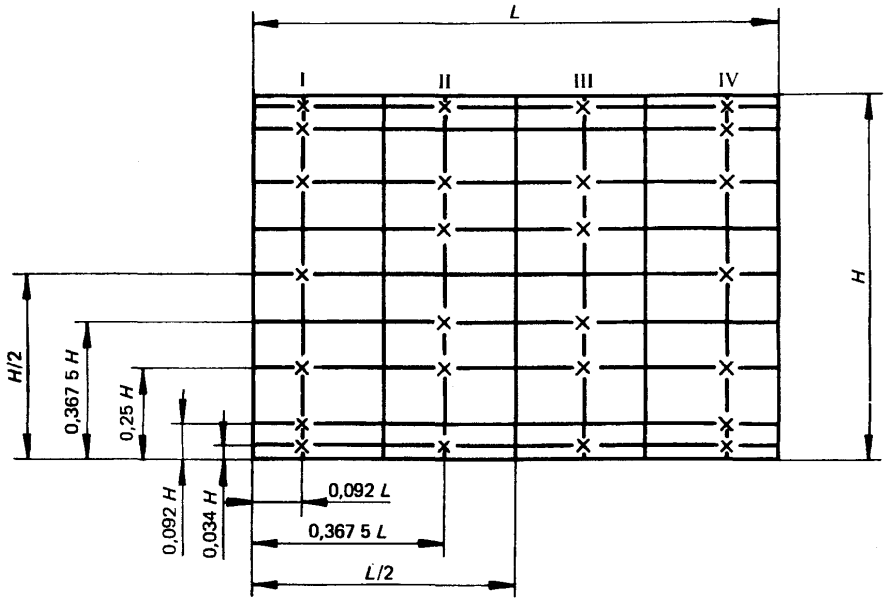

h/H \ l/L	I 0,092	II 0,367 5	III 0,632 5	IV 0,908
0,034	2	3	3	2
0,092	2	–	–	2
0,250	5	3	3	5
0,367 5	–	6	6	–
0,500	6	–	–	6
0,632 5	–	6	6	–
0,750	5	3	3	5
0,908	2	–	–	2
0,966	2	3	3	2

Figure 4–30: Location of measuring points in a rectangular cross-section conduit in the case of the log-linear method using 26 points (BS 1042, 1983).

The discharge velocity U is equal to the weighted mean of the measured local velocities:

$$U = \frac{\Sigma k_i' v_i}{\Sigma k_i} \qquad (167)$$

k_i': local weighted coefficient

v_i: local velocity

4.7.2 Yawmeter

One three-hole cobra probe (see figure 4-31) was used for the downstream traverses (see figure 4-32) at a distance of one chord length from the blade trailing edge towards the calculated exit cascade streamtube flow angle. At this distance most of the mixing has taken place and pitchwise flow angle variation will be only small (Gostelow, 1984).
The width of the probe head is 2.4 mm, the height is 0.8 mm and the total length is 500 mm. The three holes of the probe are located in the same plane parallel to the probe axis and their diameter is 0.5 mm. The distance between the two lateral holes is 1.7 mm. The head of the probe is trapezoidal with a characteristic wedge angle $\delta=45^{o}$.

Figure 4–31: Three-hole cobra probe.

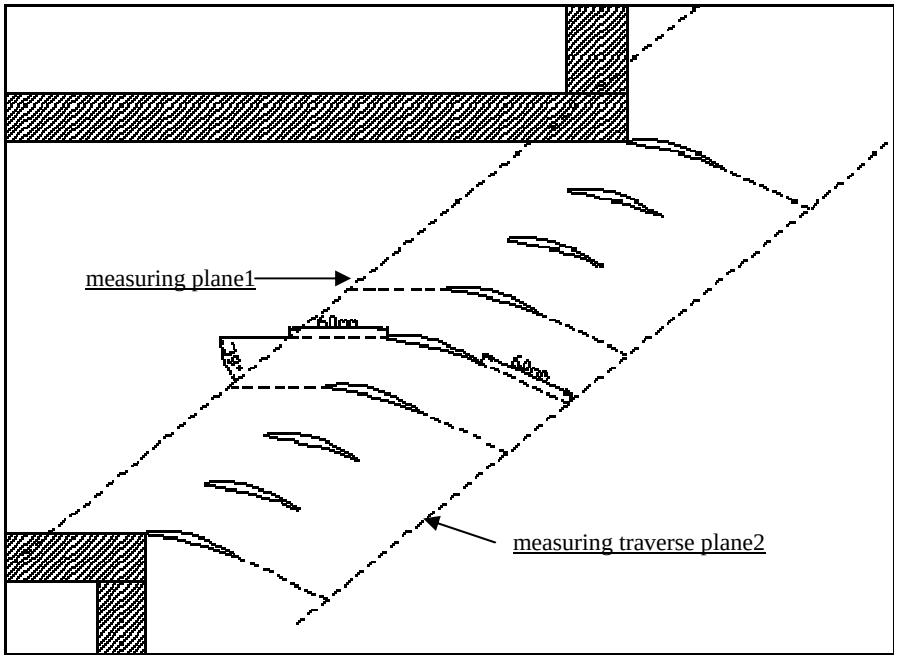

Figure 4–32: Cascade traverse planes.

The pressure readings extracted from the yaw meter were combined in order to provide particular coefficient values that were related to the yaw meter calibration chart so as to extract the flow exit flow angles from the cascade blades. Also, the blade exit flow velocity was calculated using coefficients of this chart.

4.7.2.1 Experimental calibration

The calibration of the three hole yaw probe has been carried out at the laboratory of Cranfield University. The main equipment for the calibration involves a suction wind tunnel, the three hole yaw probe, a pitot static probe and three pressure transducers (see figures 4-33 and 4-34).

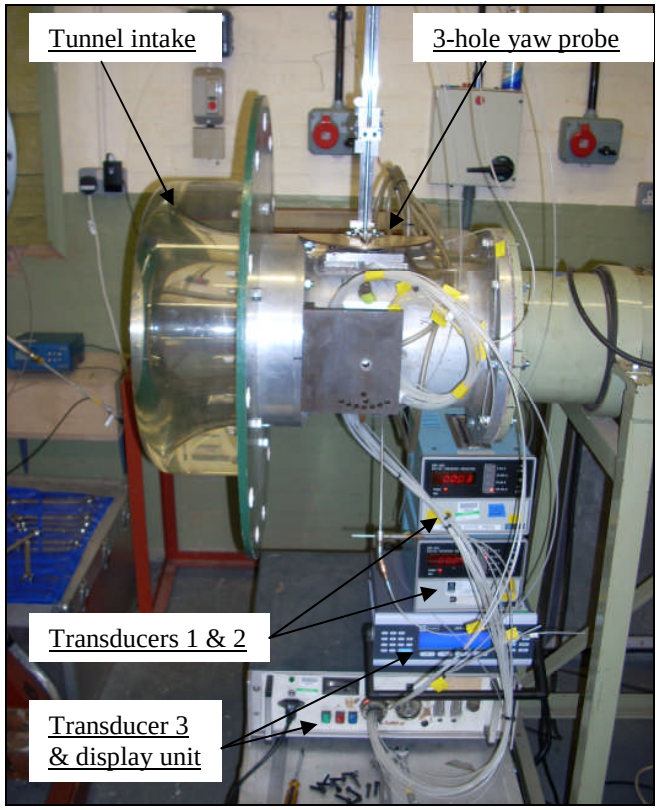

Figure 4–33: Wind tunnel arrangement.

In figure 4-32 the position of the three hole yaw probe and the pitot static probe can be seen. The yaw probe is positioned in the middle of the tunnel and the pitot static probe is positioned 50 mm away from the centreline of the tunnel.

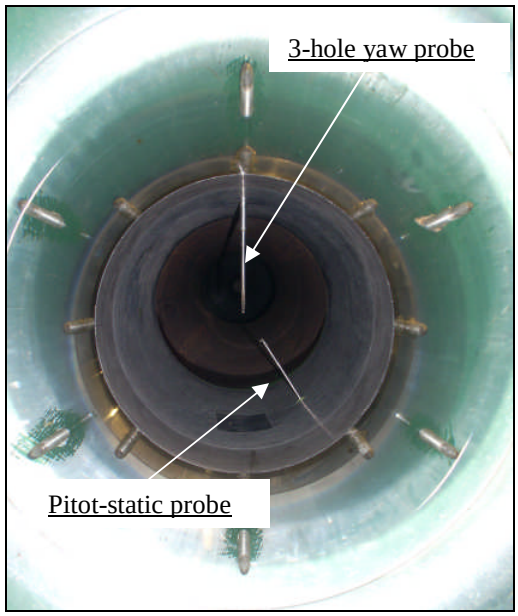

Figure 4–34: Probe location.

The flow field velocity was adjusted manually using a speed control transmission which actuates a 86 KW DC motor. A centrifugal blower is driven by the motor

supplying an airflow of 6.6 m^3/s at 4000 rpm. The throat diameter of the tunnel intake convergent nozzle is 212 mm and the probe is positioned at a distance of one throat diameter downstream of the throat. Inside the tunnel four static ports exist for the measure of tunnel static pressure. The total pressure was obtained via the pitot-static probe. The pressure reading associated to the static ports of this probe was averaged with the pressure readings associated with the tunnel static pressure ports. A barometer and a thermometer were positioned outside the tunnel in order to provide readings of ambient pressure and temperature respectively.
Three pressure transducers were used in order to convert the pressure signals into electrical signals. Transducers number 1 and 2 equipped with electronic displays were used to receive the signals from the right (port 2) and left port (port 3) of the three-hole yaw probe. Transducer number 3 was used for receive of the remaining pressure signals for the calibration and it was connected to a separate electronic display.
The calibration results in terms of the direction, total pressure and static pressure coefficient are given in the following figures 4-35, 4-36 and 4-37.

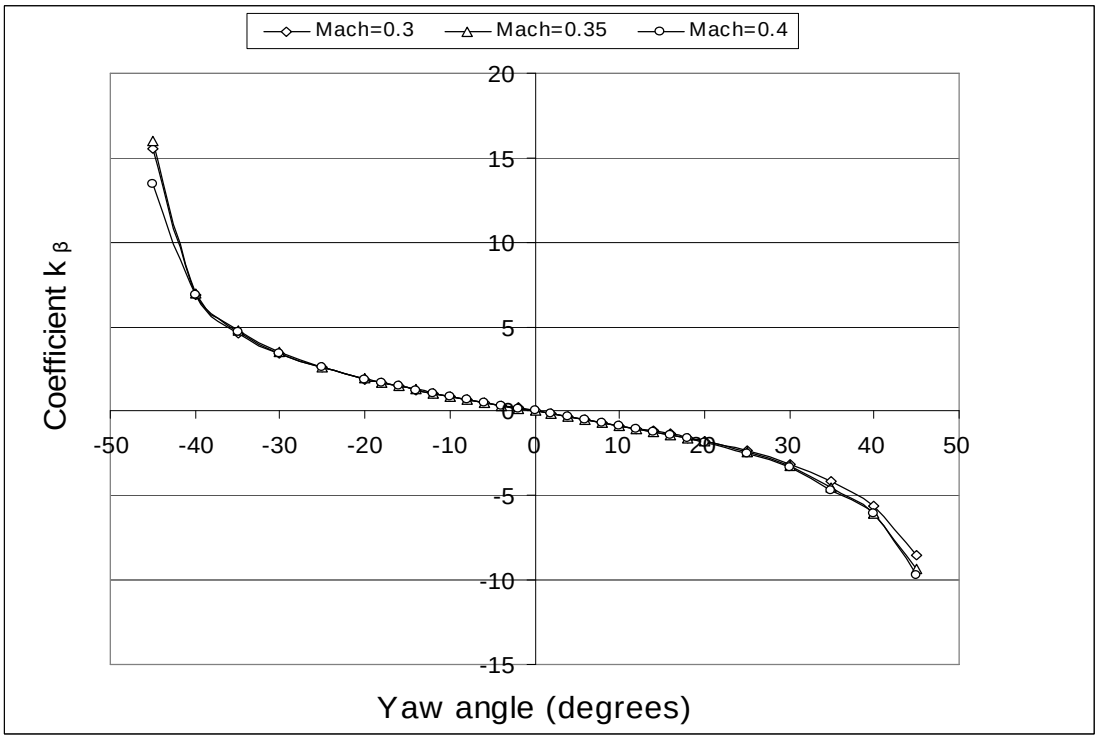

Figure 4–35: Coefficient k_β versus yaw angle.

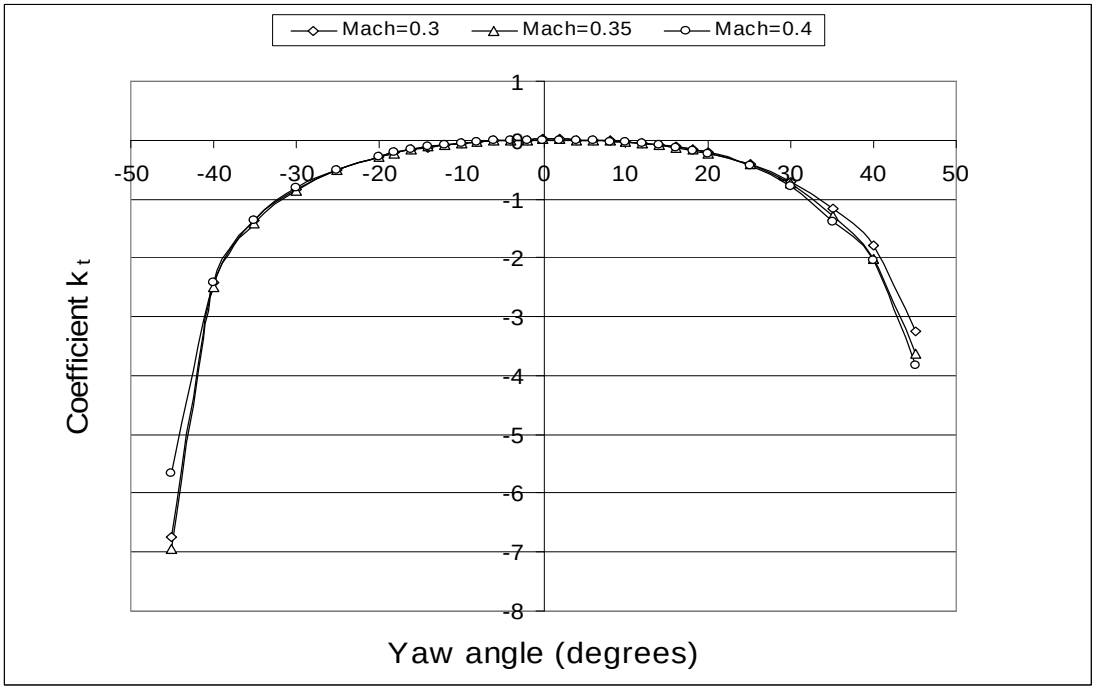

Figure 4–36: Coefficient k_t versus yaw angle.

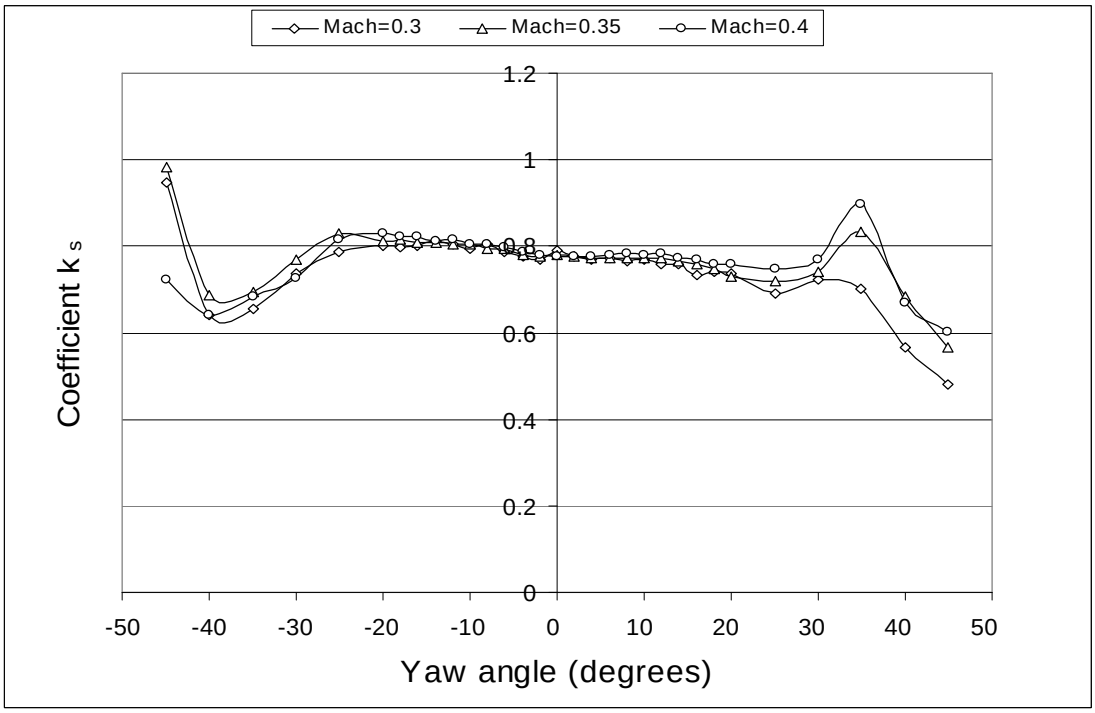

Figure 4–37: Coefficient k_s versus yaw angle.

4.7.3 Chell blocks

In order to convert pressure signal from the spherical pitot probe holes or pitot static ports into an analog electrical signal, a pressure transducer was used (see figure 4-38).

Figure 4–38: Chell 9000 Intelligent Pressure scanners rated at 30 psi.

The scanners receive the pressure signals from the pitot and yaw probe and the data is digitised and transferred to a computer via a serial connection.

4.7.4 Ambient temperature and pressure instrumentation

Ambient temperature and pressure were taken from a Digi Tech thermometer graduated in degrees Celcius and a barometer graduated in millibars respectively (see figures 4-39 and 4-40).

Figure 4–39: Thermometer.

Figure 4–40: Barometer.

4.7.5 Roughness measuring device working explanation

Roughness is the term that includes the finest irregularities of a surface (see figure 4-41).

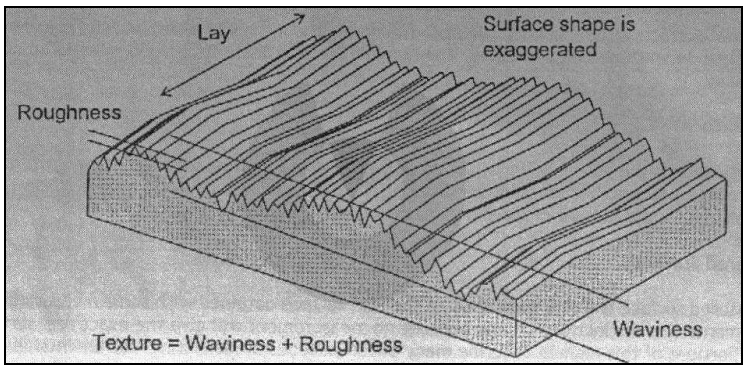

Figure 4–41: Surface texture parameters (Surface metrology guide, 1998).

The parameter used to measure the roughness of a surface is the roughness parameter Ra which is the arithmetic mean of the absolute departures of the roughness profile from the mean line of the profile and is expressed as follows:

$$Ra = \frac{1}{l}\int_0^l |z(x)|\ dx \qquad (168)$$

l : sampling length

Mean line (see figure 4-42) is a reference line from which profile deviations are measured. It is the zero level for a total modified profile. For the case of this surface roughness measuring devise the areas of the profile above and below this line are equal (Taylor Hobson brochure 2004).

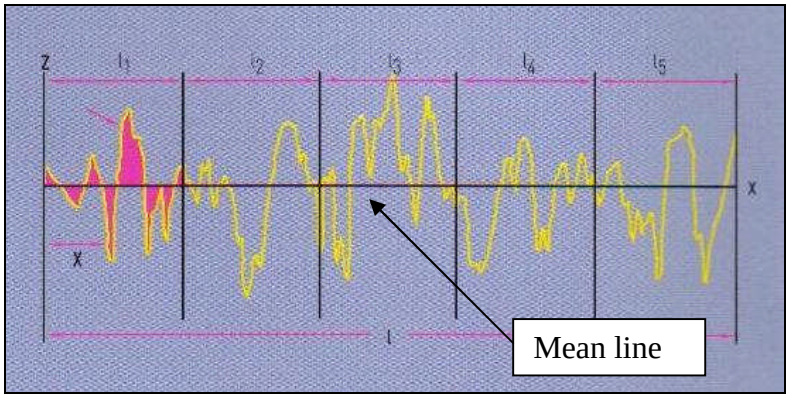

Figure 4–42: Mean line profile departures (Taylor Hobson brochure, 2004).

The instruments that are used to measure surface roughness comprise a pick up unit that follows the profile of the surface under measurement (see figure 4-43).

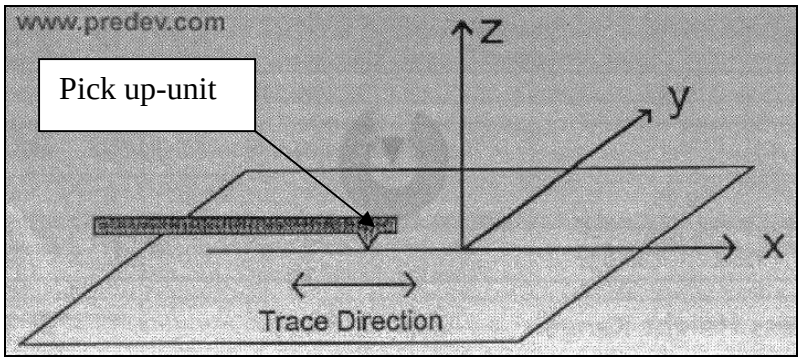

Figure 4–43: Surface profiling coordinate system (www.predev.com).

The pick-up unit traverses along the profile traverse length which is the total distance travelled by the unit.
Evaluation length L is the entire length of a profile over which data has been collected (see figure 4-44) and a standard roughness evaluation length comprises five sample lengths.

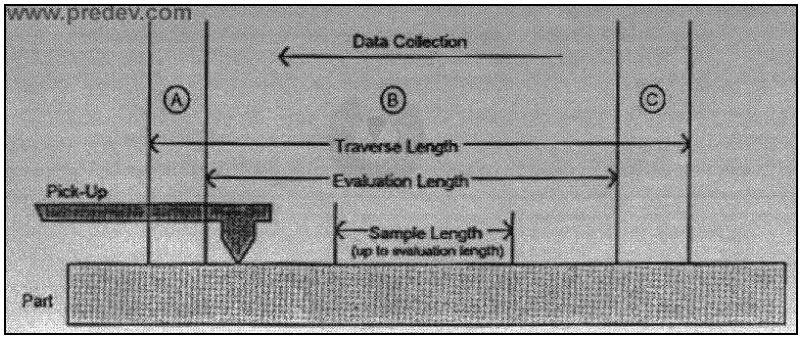

Figure 4–44: Evaluation length illustration (www.predev.com).

The roughness measuring device (Surtronic S25) which was used to measure the current project's blade cascade surface roughness is illustrated at figure 4-45.

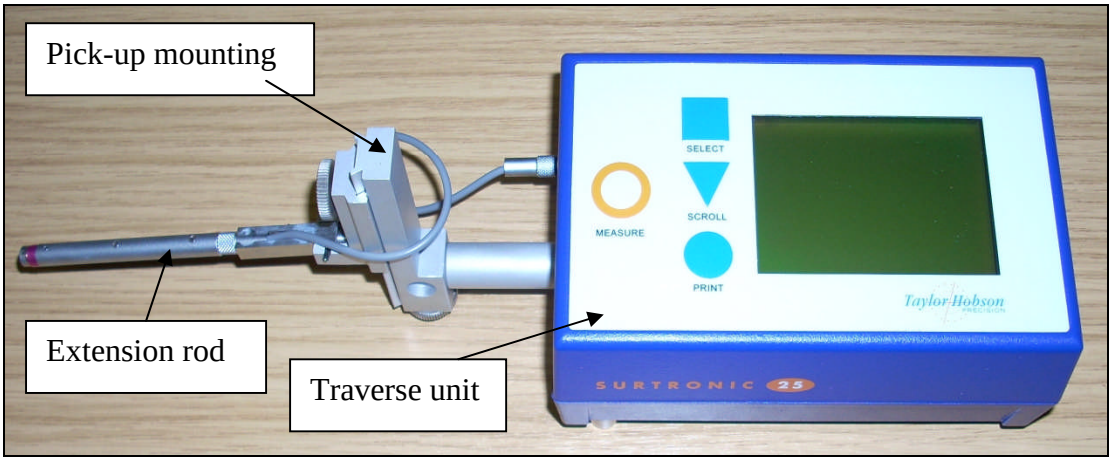

Figure 4–45: Roughness measuring device.

The devise comprises two parts, the pick up mounting and the traverse unit. The pick up mounting part involves a stylus and a skid that follow the surface under measurement profile and they are both followed by an extension rod. As the pick up traverses along the surface the movements of the stylus (see figure 4-46) relative to the skid are detected and converted into a proportional electrical signal which at the end is translated in the traverse unit in terms of roughness determination parameters.

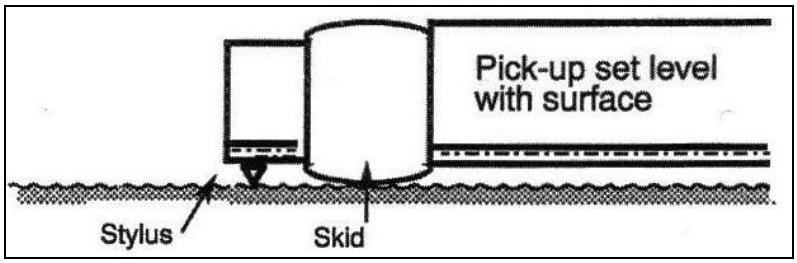

Figure 4–46: Pick up arrangement (Sutronic 25 user's guide, 2004).

4.7.6 Constant temperature hot wire anemometer

4.7.6.1 Main Components

The present hot wire anemometer equipment includes several units. The signal receiver is a single-sensor hot wire 55P11 probe (see figure 4-47) accompanied with a probe support and cable that connects the probe to the hot wire anemometer.

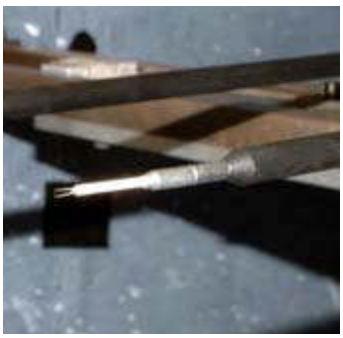

Figure 4–47: 55P11 single sensor miniature wire probe.

The actual hot-wire anemometer (see figure 4-48) is a research type (multi-channel) constant temperature hot-wire anemometer including bridge, servo loop and signal conditioner for high-pass, low-pass filtering and for signal amplification. A voltmeter is connected to the anemometer for bridge balancing purposes. An oscilloscope is included as well in to provide the time value for calculating the cut-off frequency of the probe/anemometer system. The analog signal coming out from the anemometer is then transformed into digital via an A/D card and it is then received by a computer. The data transferred to the computer were collected using Visual basic software and post-processed by using Matlab.

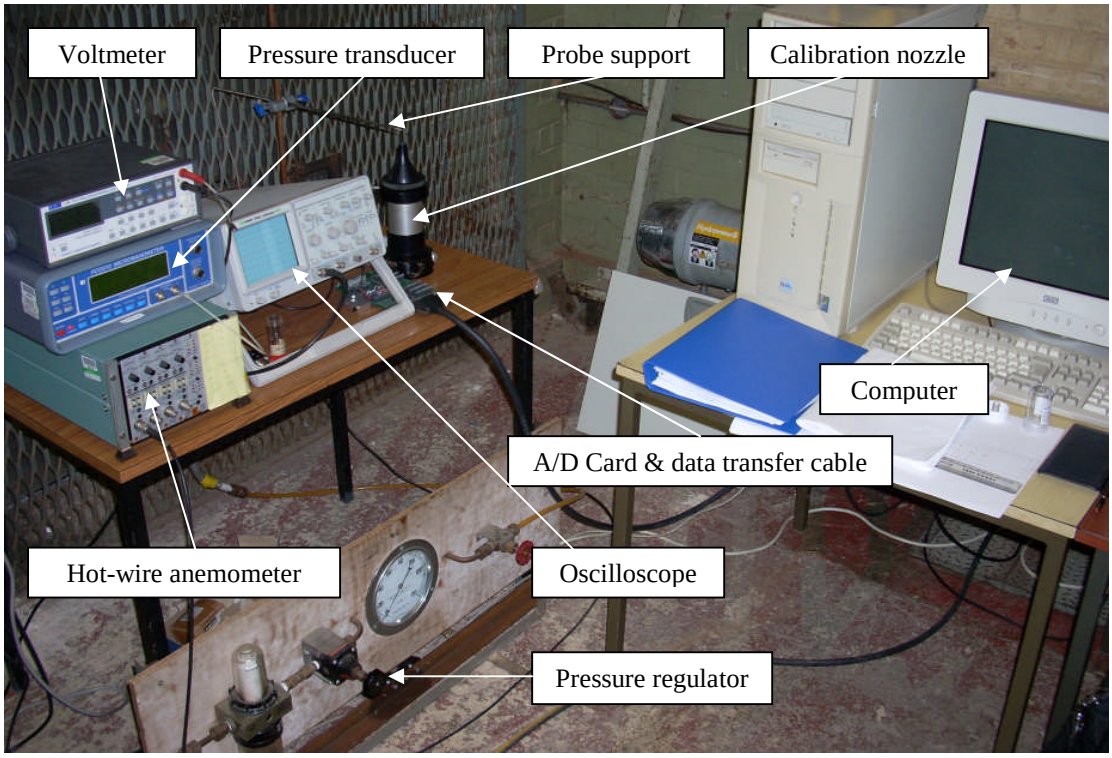

Figure 4–48: Constant temperature hot-wire components.

4.7.6.2 Hot-wire calibration

The calibration of the hot-wire is very important for the accuracy of the experiment under consideration. It involves a calibration nozzle supplied with air from a compressor via a pressure regulator, producing a low-turbulent free jet whose velocity is calculated on the basis of pressure drop at it's exit (see figure 4-48). A pressure transducer is connected to the nozzle regulated to provide the velocity readings associated to the pressure drop. For different jet velocities a voltmeter provides the related voltages for each particular range of velocities examined. In order to create the calibration curve (see figure 4-49) the square power of the voltages versus jet velocities(40-60 m/s) to the power of 0.41, 0.43 and 0.45 were plotted and the best fit curve was determined in order to provide the empirical constants A and B according to King's law (1914).

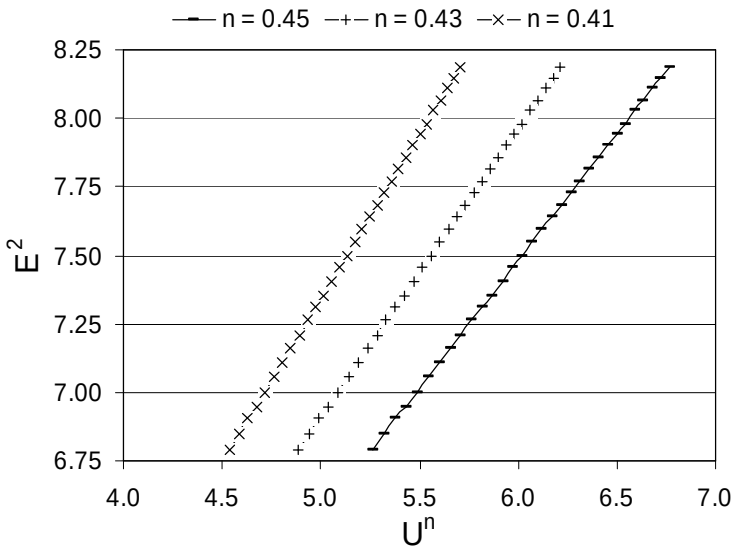

Figure 4–49: Actual hot-wire calibration curves.

Chapter 5 - Test rig computational fluid dynamics simulation

5.1 Test rig geometry set up

A computational solution using a commercial CFD package (Fluent 6.3) was developed for the compressor cascade geometry of the current project. The simulation was three-dimensional and steady-state. For the simulation of the cascade test rig, the inlet, test section, plenum chamber and outlet part of the rig before the air regulator valve were involved excluding the flow through the air regulator valve and the air suction pump (see figures 5-1).

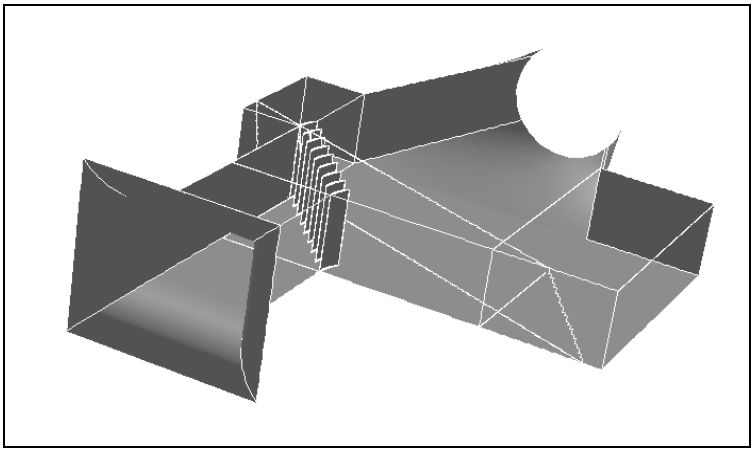

Figure 5–1 : Cascade rig perimetric illustration.

For this three-dimensional simulation most of the parameters were analysed on a mid-plane (see figure 5-2) that was created in Fluent exactly horizontally at the middle of the cascade test rig volume.

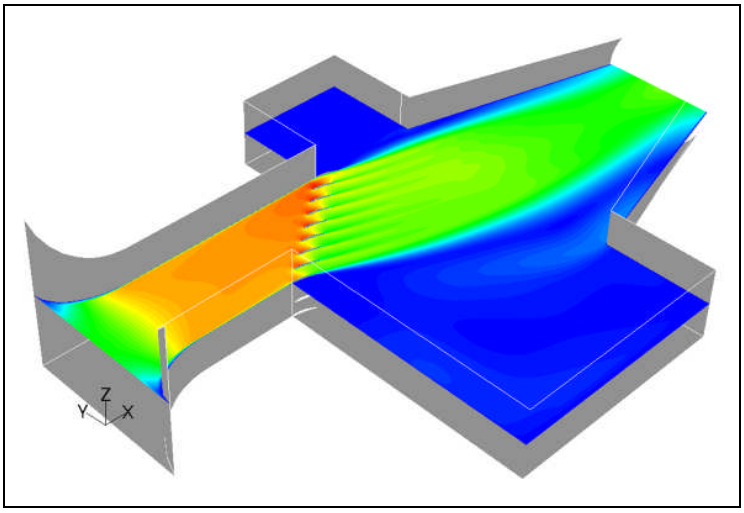

Figure 5–2: Cascade rig midplane illustration.

On the midplane, front and rear blade traverse lines were used at distances of 5, 30 and 60 mm in front of the blades and at distances of 5, 30 and 60 mm behind the blades towards the exit flow streamtube in order to examine the pressure and velocity distributions (see figure 5-3).

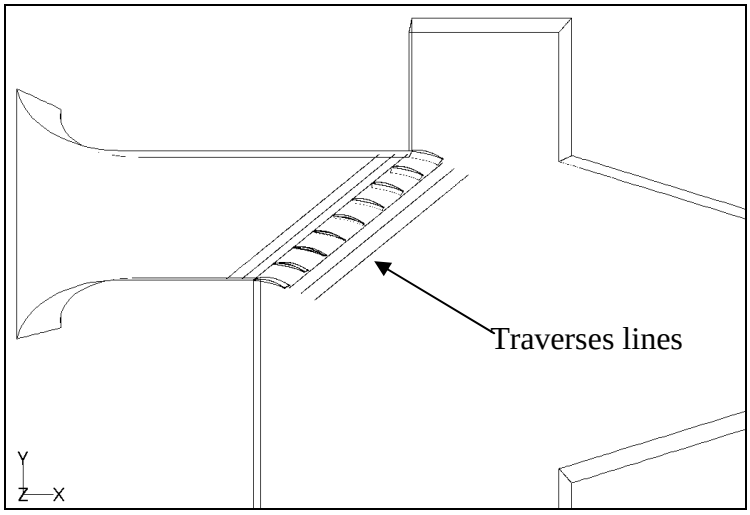

Figure 5–3: Front and rear blade traverses illustration.

5.2 Grid generation

The whole cascade tunnel fluid volume was meshed with a combination of structured and unstructured grid which was created using the preprocessor Gambit 2.4. The internal passage grid of the cascade geometry is illustrated in figure 5-4 and figure 5-5. It consists of an H-grid with an extra O-grid around the cascade blades containing the boundary layer region. The O-grid around the cascade blades contains 176 x 50 grid points. The grid in the tunnel exit cone and in the area (settling chamber) between the inlet and the test section was unstructured.

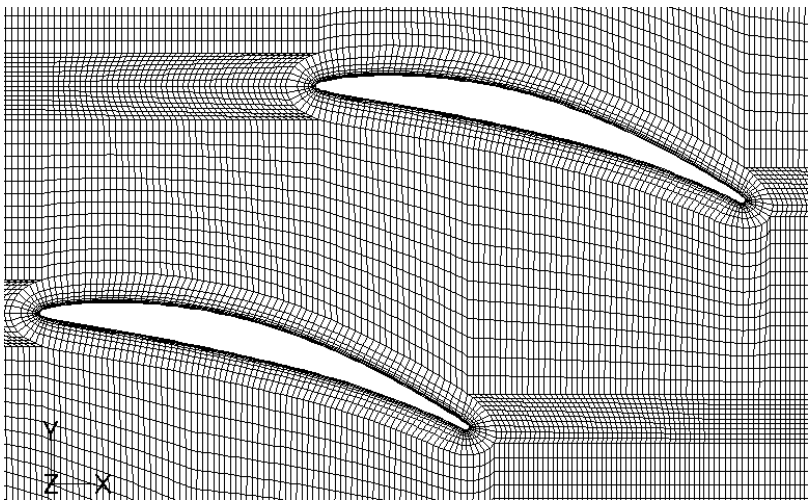

Figure 5–4: Cascade passage structured grid illustration.

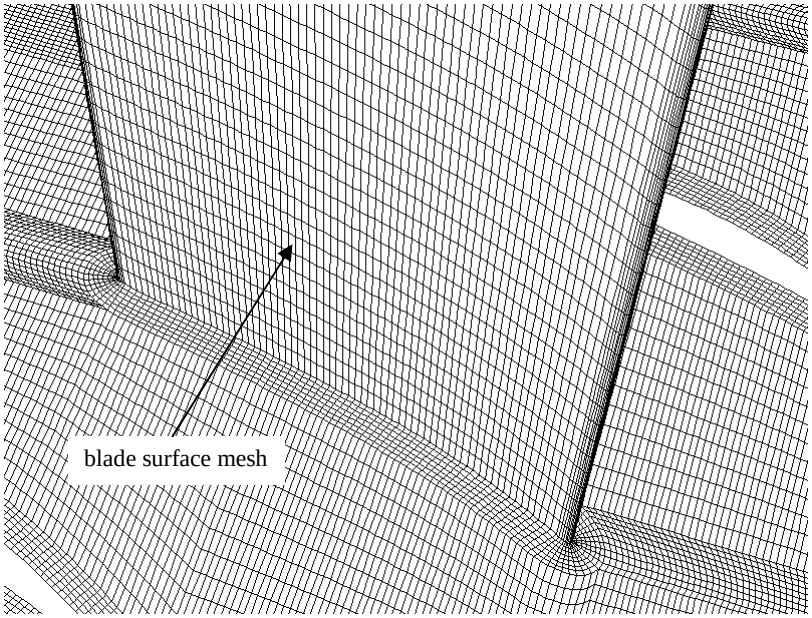

Figure 5–5: Blade surface meshing.

The grid was finer at cascade test section at the regions close to the blade surfaces where adverse pressure gradients may interact with blade surface boundary layers causing separation, in order for a more accurate simulation to take place for these regions. The volumes far away from the important volume that is the cascade test section were constructed from unstructured grid.
The O-grid around the cascade blades except those located close to the side walls of the cascade rig, contains 176 x 50 grid points. The distribution of points in the near blade wall region was denser in order to resolve the boundary layer in the viscous sublayer region and y^+ values below 5 along the blade pressure and suction surfaces were detected. The first grid point from the blade surface was located at 2 μm from the blade wall surface. The y^+ plus parameter is compute from:

$$y^+ = \frac{\rho u_\tau y_P}{\mu} \quad (169)$$

u_τ : friction velocity
y_P : distance from point to the wall
μ : dynamic viscosity

For this simulation enhanced wall treatment was used in Fluent 6.3 (2007) which is a near-wall modelling method employing enhanced wall functions with the presupposition that the near wall mesh is fine enough to be able to resolve the laminar sublayer (y^+ <5). These wall functions are a collection of semi-empirical formulas and functions that link the solution variables at the near-wall cells and the corresponding quantities on the wall.
Different meshes were examined and grid independency was achieved after 9 million cells by checking the total pressure loss coefficient between one chord distance upstream of the cascade blades and one chord distance downstream of the blades towards the cascade outflow vector (see figure 5-6). The final grid involving

10140777 cells was finally used for further analysis of the cascade flow in terms of the k-ε model.

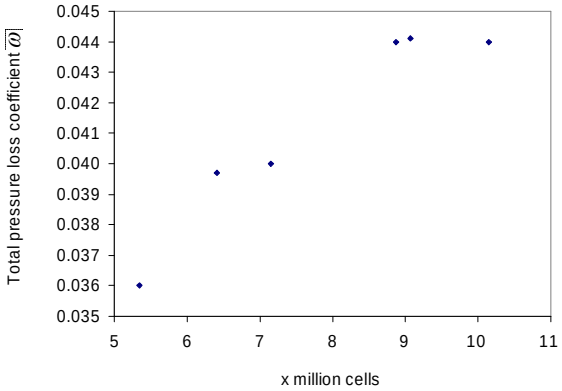

Figure 5–6: Grid independency plot.

5.3 Turbulence model and solver selection

Two-equation models are the models where the turbulence velocity and length scales can be determined by solving two separate transport equations. The standard k-ε model is a two-equation turbulence model and it is widely used for engineering flow calculations since it was introduced by Launder and Spalding (1972). It's robustness, economy and reasonable accuracy in terms of turbulence flows made it applicable in many industrial flow and heat transfer simulations. The standard k-ε model is based on model transport equations for the turbulence kinetic energy k and its dissipation rate ε.

The turbulence models used for the simulation related to the cascade test rig were the standard k-ε and the k-ω SST (Shear Stress Transport) models. The k-ε model focuses on the mechanics that affect the turbulence kinetic energy and for the simulation enhanced wall treatment was involved.

The k-ω SST (Shear Stress Transport) is a two equation turbulence model which solves for the turbulence kinetic energy k and the rate of dissipation of turbulence per unit energy ω (specific dissipation rate). This model was chosen as well, since it performs better for adverse pressure gradient flows (F.R. Menter 1991) compared to the k-ε model that produces unacceptably high shear-stress levels in such cases leading to prediction of delayed flow separation. Another one reason for using the k-ω model was that it performs better in integrating through the viscous sublayer (low Reynolds number turbulent near wall region) of the boundary layer than the k-ε model which involves significant inaccuracy in integrating through this region (Kandula et al 1995). When using the k-ω model, equations are solved inside the boundary layers and the standard k-ε model is utilised elsewhere (Menter 1993) because the k-ω model is harmfully sensitive to the free stream turbulence, whereas the k-ε model does not share this level of sensitivity (Hellsten 1998). The SST version of the k-ω model introduces an upper limit for the principal turbulent shear stress in boundary layers in order to avoid excessive shear-stress levels typically predicted with Boussinesq eddy-viscosity concept (Hellsten 1998) on which most turbulence models are based. In terms of the Boussinesq approach related to the k-ω SST model, the turbulent shear stress τ is given by the following relation:

$$\tau = \mu_t \Omega = \sqrt{\frac{production \quad of \quad k}{dissipation \quad of \quad k}} \rho \alpha_r k \qquad (170)$$

where

a_r : ratio of Reynolds shear stress to turbulent kinetic energy

ρ : density

μ_t : turbulent viscocity

Ω : vorticity tensor

k : turbulence kinetic energy

For a boundary layer in zero or favourable pressure gradient the production of turbulence kinetic energy is approximately equal to the dissipation of turbulence energy in the outer region of the boundary layer and the Boussinesq approach comes into agreement with the relation used from Bradshaw (1965), that states the shear stress in a boundary layer is analogous to the turbulent kinetic energy k according to the formula:

$$\tau = 0.3\rho k = \rho \alpha_1 k \qquad (171)$$

However, in cases of adverse pressure gradient flows the two formulations of shear stress diverge significantly since the ratio of production of turbulent kinetic energy is much larger than the dissipation of energy. So, in order to overcome this problem Menter (1993) proposed the turbulence viscosity ν_t as

$$\nu_t = \min\left(\frac{k}{\omega}, \frac{a_1 k}{\Omega}\right) = \frac{a_1 k}{\max(\alpha_1 \omega, \Omega)} \qquad (172)$$

ω: turbulence energy dissipation

which applies the Bradshaw's relation for the outer region of the boundary layer and retains the Boussinesq relation for the rest of it. This approach in terms of the turbulence viscosity considered as eddy viscosity adjustment, is what characterizes the Shear Stress Transport (SST) version of the k-ω model and in parallel improves the model's predictions for separated flows.

In addition, the blending between the inner and the outer region of the boundary layer is achieved incorporating a particular function called blending function that gradually changes from value one in the inner region of the boundary layer to zero near the edge of it.

However, for further simulations the k-ω model was not used since convergency problems existed by increasing the convergence criteria in terms of continuity, x, y, z velocity, energy, turbulence kinetic energy k and specific dissipation rate ω.

A second order discretization scheme was used for all the solved quantities of the simulation including the turbulence parameters and the pressure based solver was implemented since the flow was initially assumed to be middly compressible. Extra information regarding the numerical solver can be found in the Fluent user's guide.

5.4 3-D CFD boundary settings and results analysis

In order to run the simulation the boundary condition values were calculated at the cascade inlet (station 0) and at the outlet of the exit cone (station 4) (see figure 5-7).

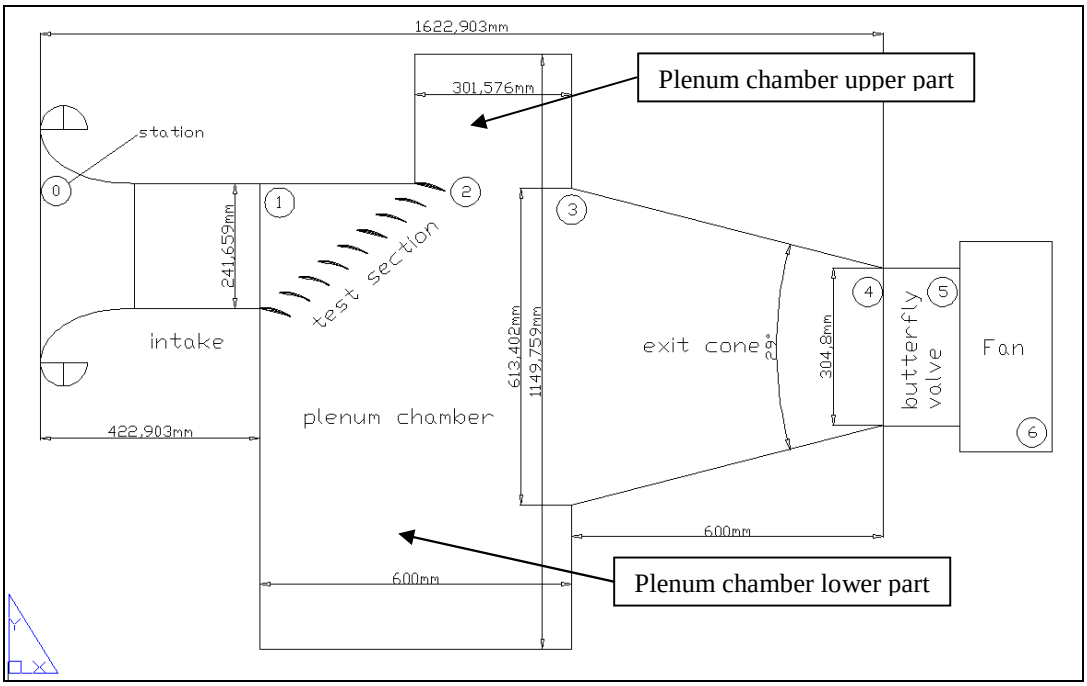

Figure 5–7: Rig stations illustration.

The total pressure (101592 Pa) and temperature (293.15 K) at the intake of the rig was set to be the ambient operating pressure and temperature respectively at which the characteristic curve of the fan was obtained so, the first boundary for the simulation had already been determined. At this boundary the turbulence intensity was set to 1%, while the length scale was set to 1.765 mm.

The second boundary to be determined was the outlet of the exit cone. At this point it must be referred that for the simulation it was assumed that no pressure drop takes place along the butterfly valve when it is fully open for the case of zero blade incidence, so the pressure at station 4 of the rig was set to be equal to the pressure of station 5 at the inlet of the fan.

Knowing the mass flow, the air density and the cross sectional area of the fan inlet, the velocity V_5 at the inlet of the fan was calculated (58 m/s equal to the velocity at station 4 since station 4 and 5 have the same cross sectional area).

Then assuming that the flow through the rig is adiabatic and the total temperature at the inlet equals that at the outlet the ratio of $V_5 / \sqrt{T_5}$ was calculated to be equal to 3.382. Interpolating for this value from the compressible flow tables (table 9 Appendix) the ratio of total pressure P_5 over static pressure p_5 at station 5 was found to be 1.020. In order to calculate p_5 the total pressure P_5 had to be calculated first.

Knowing the mass flow, the air density and the exit mass flow area of the fan the exit velocity V_6 at the exit of the fan was calculated (60 m/s). Then at the exit of the fan applying Bernoulli the total pressure of station 6 (P_6) was found to be 103772 Pa. In order to find the total pressure at station 5 (P_5) which is equal to the total pressure of station 4 P_4 assuming that the losses at the butterfly valve are negligible when it is

fully opened, data were extracted from the characteristic curve of the fan (see table 5 appendix).
According to these data the total pressure increase along the fan was 6277 Pa and the total pressure at the fan inlet was calculated to be 97495 Pa. Then using the ratio of P_5/p_5 the static pressure p_5 was found to be 95583 Pa which composed the outlet boundary condition of the three dimensional rig simulation.
According to the 3-dimensional CFD analysis the static pressure distribution along the cascade test rig was predicted to be almost at the same levels for both turbulence models used k-ε and k-ω (see figures 5-8, 5-9 & 5-10). A cascade test section pressure increase from approximately 89500 Pa to 94500 Pa was predicted from both models giving a ratio of cascade static pressure inlet over outlet p_1/p_2 of 0.95.

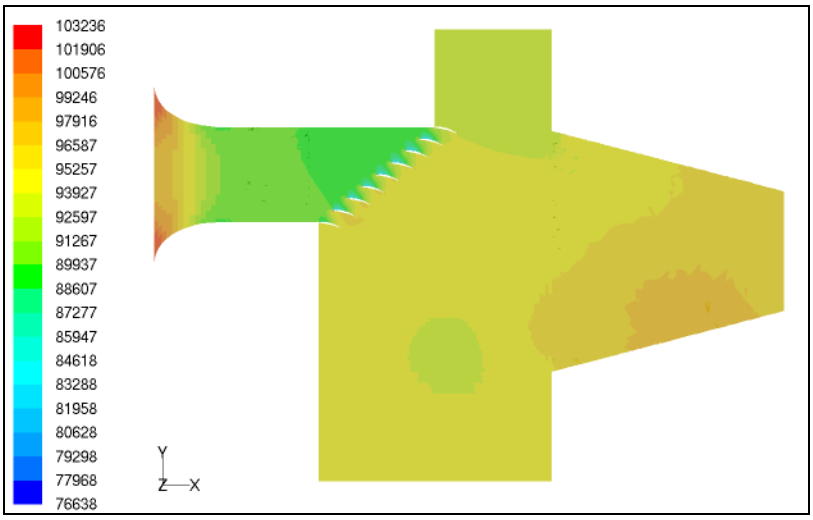

Figure 5–8: Static pressure contours (model k-ε).

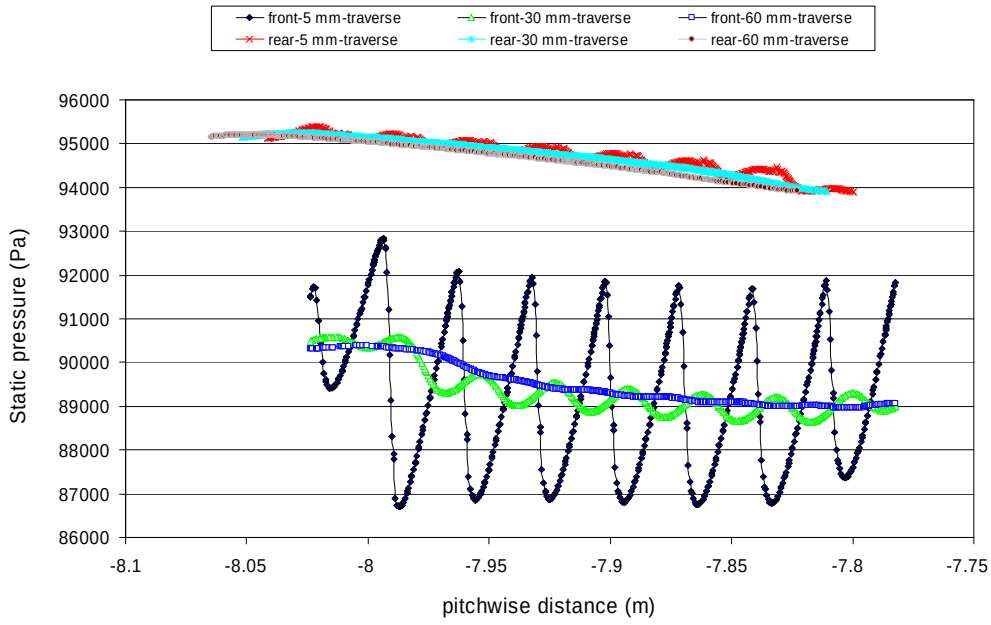

Figure 5–9: Static pressure distribution along the traverses (model k- ε).

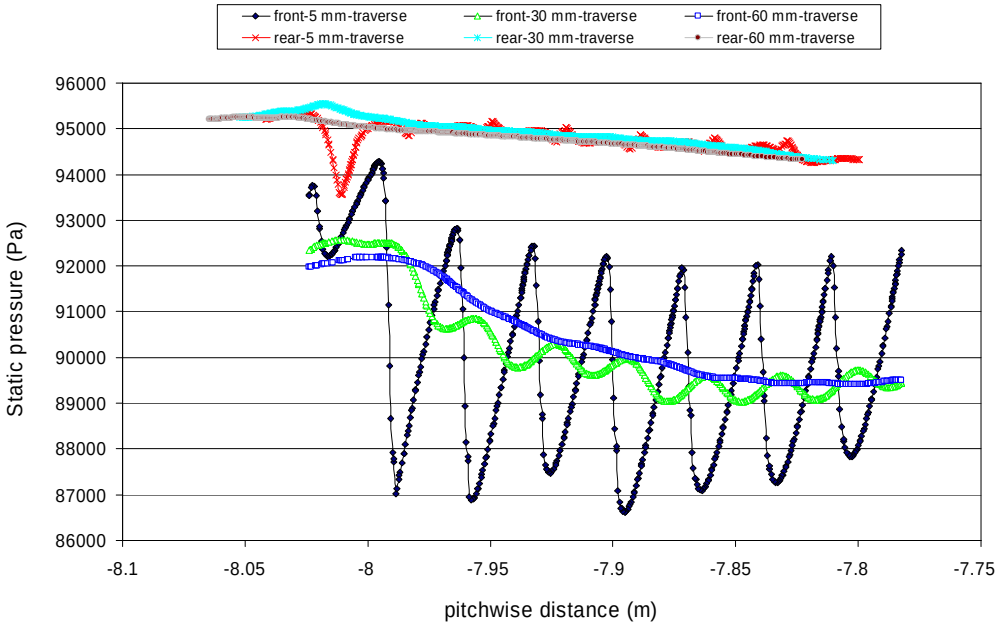

Figure 5–10: Static pressure distribution along the traverses (model k-ω).

Checking velocity distributions both turbulence models predicted almost the same velocity decrease from about 145 m/s to 105 m/s as the flow propagates from the test section blade inlet towards the exit of the blade section (see figures 5-11, 5-12 & 5-13), declaring a DeHaller number of approximately 0.72 which is very close to the value of 0.702 found from calculations. However, the cascade inlet velocity value of 145 m/s is not satisfactorily predicted by Fluent since the value there should be around 100 m/s declaring a Mach number of 0.3 according to the assumption made at the beginning for the designing of the test rig.

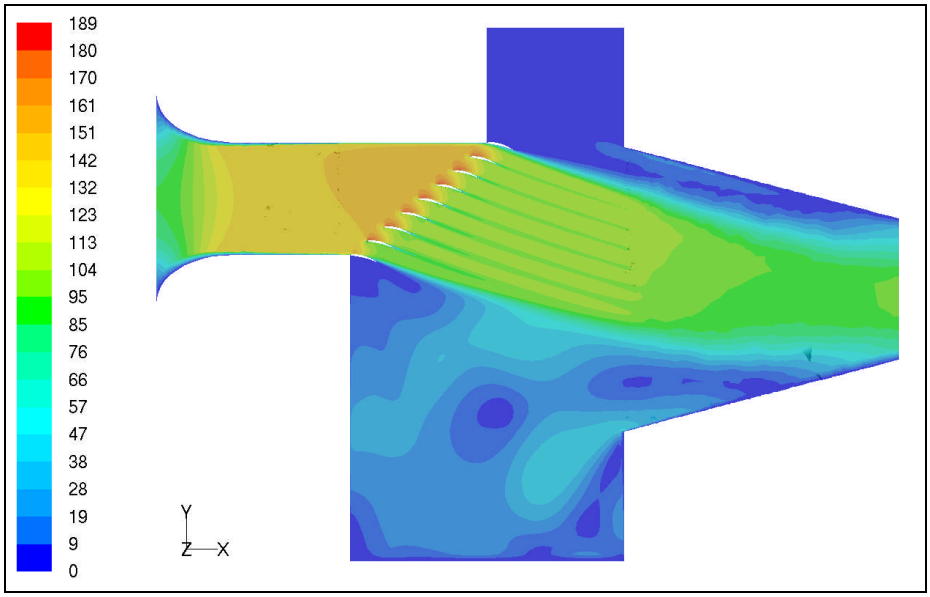

Figure 5–11: Velocity contours (model k-ε).

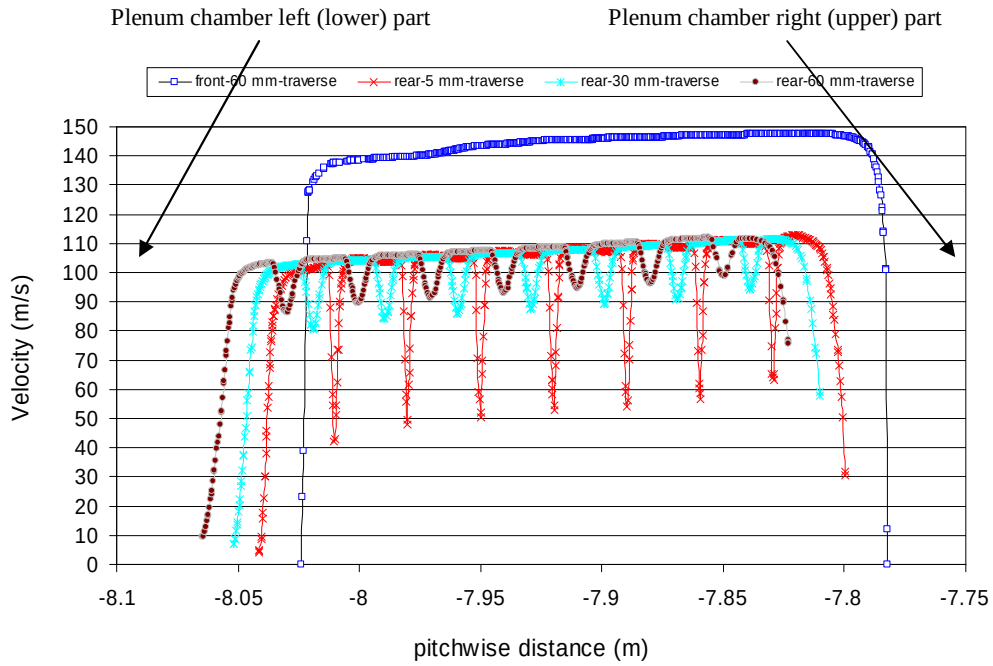

Figure 5–12: Velocity distribution along the traverses (model k-ε).

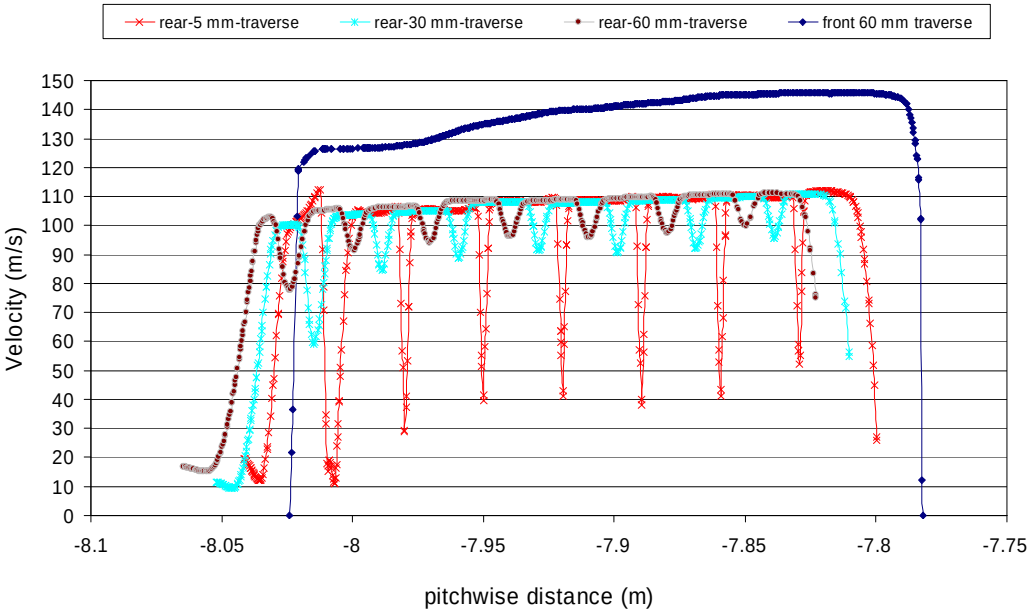

Figure 5–13: Velocity distribution along the traverses (model k-ω).

Checking the velocity distributions behind the blades it can be seen that the velocities at the right part of the cascade are higher than these at the left part of the cascade and this is related straight forward to the lower pressures existing at the right part compared to those of the left. This velocity increase and decrease towards the right and left part of the cascade respectively can be attributed to the vortices existing at

these areas enhancing and retarding the flow (see figures 5-14 & 5-15). However, the same scheme exists in terms of the velocities predicted one blade chord distance in front of the cascade.

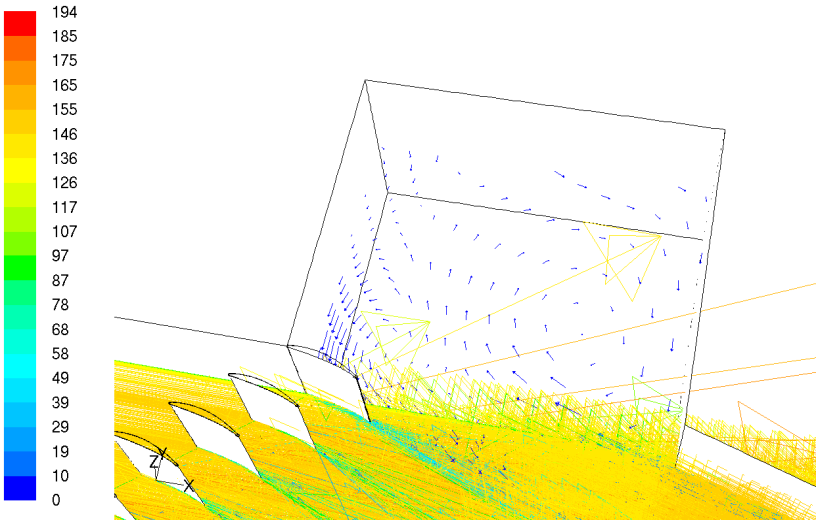

Figure 5–14: Upper plenum chamber vectors coloured by velocity magnitude (model k-ε).

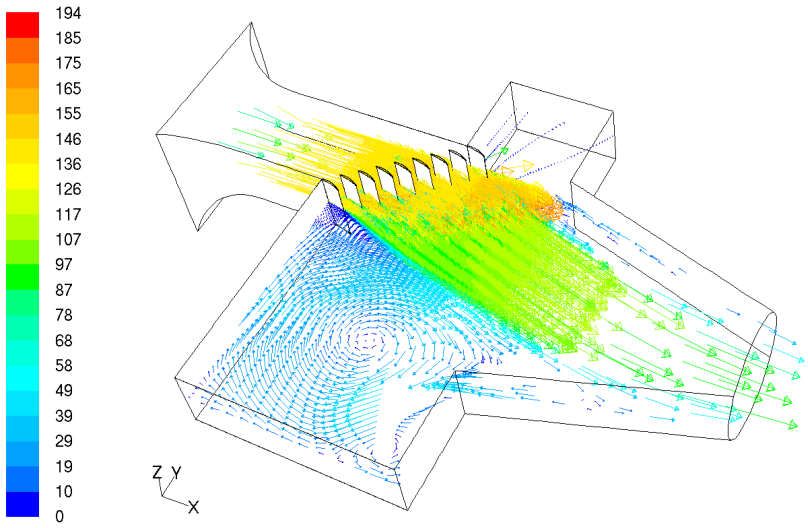

Figure 5–15: Upper and lower plenum chamber velocity vectors (model k-ε).

5.5 Plenum chamber size increase effects

A bigger plenum chamber was simulated having top, bottom and side walls extended by 1 meter (see figure 5-16).

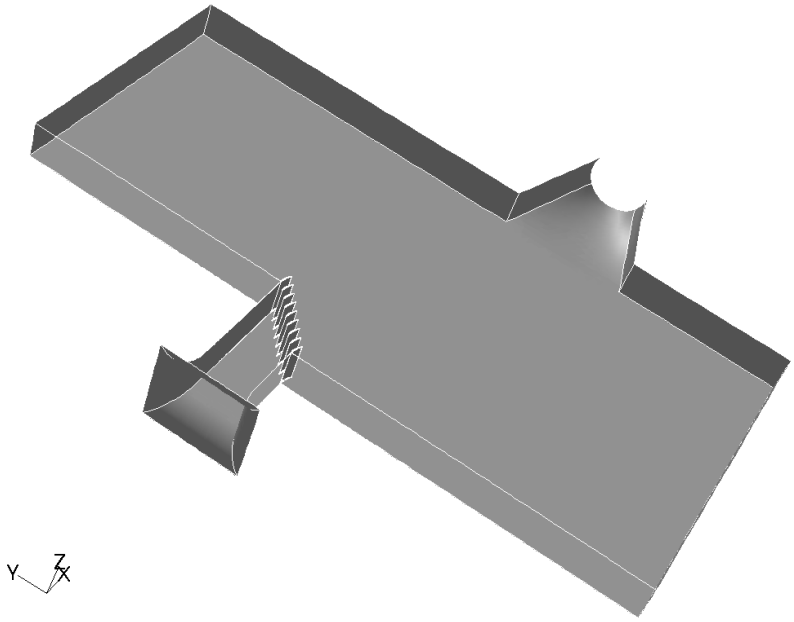

Figure 5–16: Extended plenum chamber.

The simulation run using the standard k-ε turbulence model and keeping the grid in the cascade test section area the same as it was for the simulation of the current project cascade test rig simulation. Again at this case vortices were predicted in the left and right part of the extended plenum chamber (see figure 5-17), however the pressure and velocity distributions in front and rear of the blades were smoother (see figures 5-18 and 5-19). Especially at the rear traverses the velocity distribution was predicted to be very uniform holding an almost constant value of 100 m/s and not disturbed from the plenum chamber side vortices. This extended plenum chamber arrangement seem to provide better cascade flow results but the space limitations associated prevented it from construction.

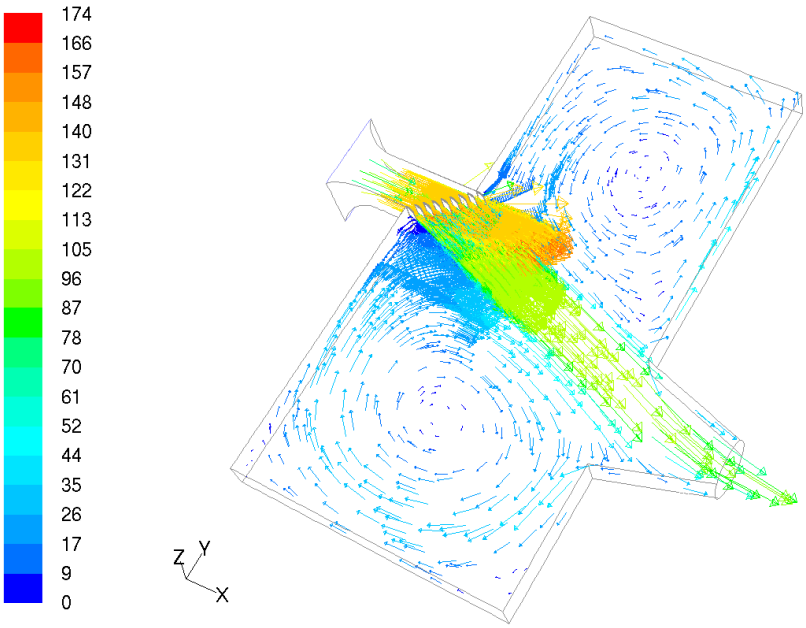

Figure 5–17: Extended plenum chamber velocity vectors coloured by velocity magnitude.

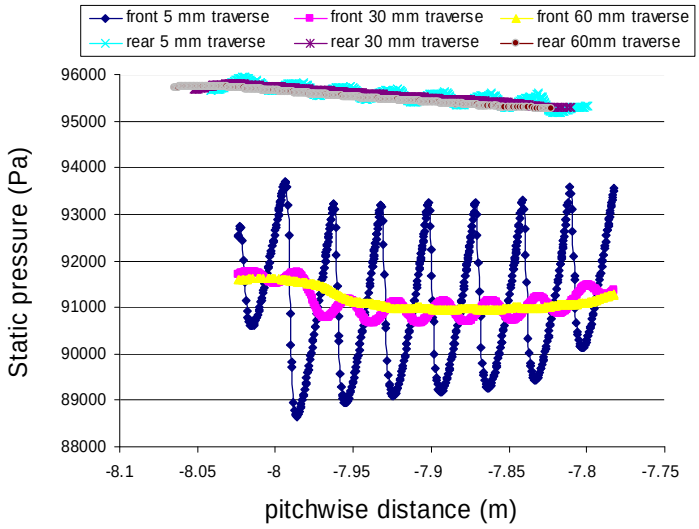

Figure 5–18: Extended cascade rig static pressure distribution.

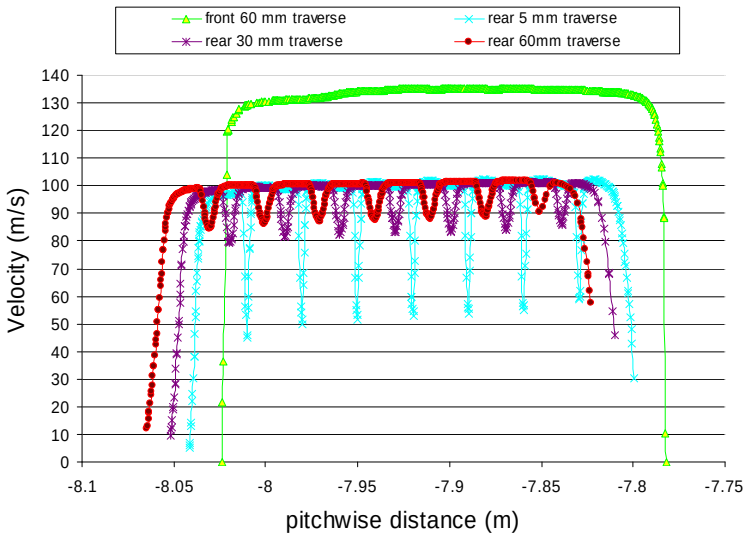

Figure 5–19: Extended cascade rig velocity distribution.

5.6 Blowing type cascade test rig

The same cascade arrangement was simulated under conditions of blowing type test rig with the air flow passing through the cascade blades exiting straight at the ambient air, keeping the ambient pressure and temperature at the same levels of 101592 Pa and 293.15 K respectively. The results obtained in terms of pressure and velocity distributions are shown in figures 5-20 and 5-21. Both distributions seem to be quite uniform in front and rear of the cascade blades.

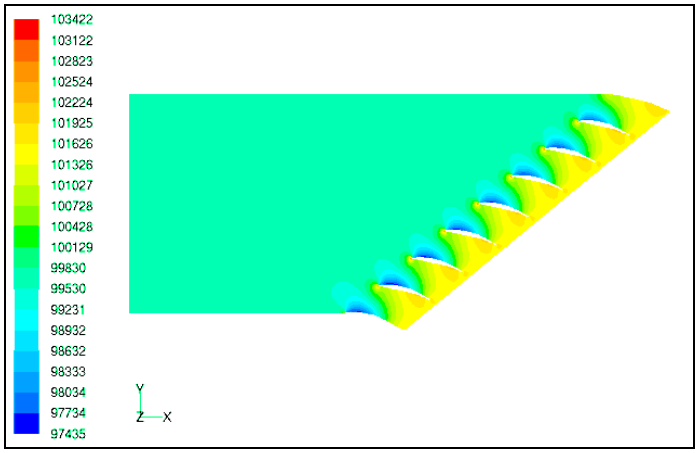

Figure 5–20: Blowing type cascade rig static pressure contours (Pa).

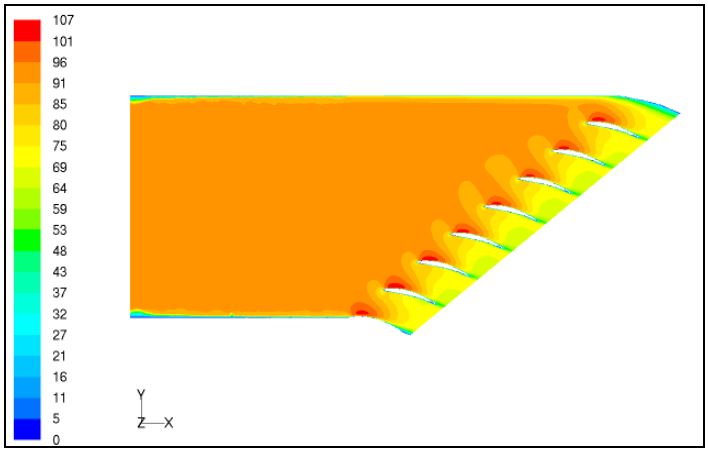

Figure 5–21: Blowing type cascade rig velocity contours (m/s).

Setting traverse lines at a height of mid-blade span, 20, 40 and 60 mm in front of the cascade blade leading edges and 5 mm behind the blade trailing edges, one can see from the results obtained (see figures 5-22 and 5-23) that the static pressure and velocity distribution is very uniform even at the right and left sides of the blowing type cascade compared to the distribution of the suction type rig with the plenum chamber on the back. This can be attributed to the fact that this blowing type arrangement does not involve any vortices on the left and right hand side of the rig like in the case of the plenum chamber arrangement, which can distort the flow.

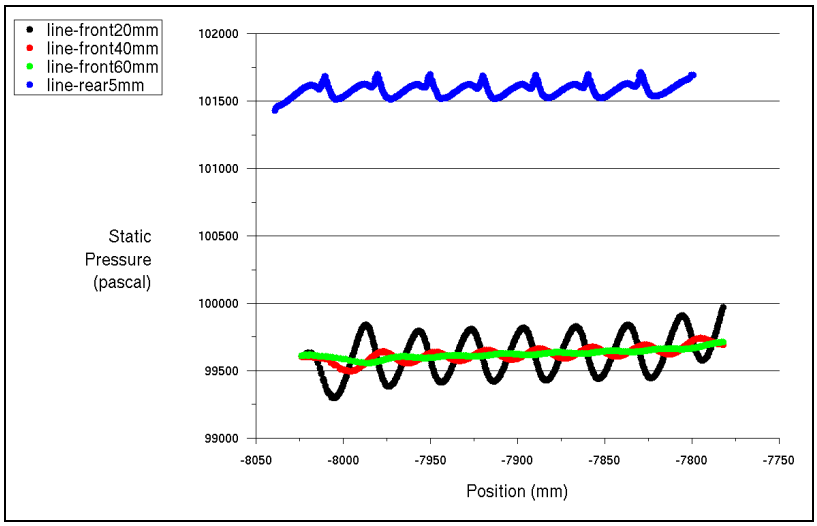

Figure 5–22: Blowing type cascade rig static pressure distribution along front and rear traverses.

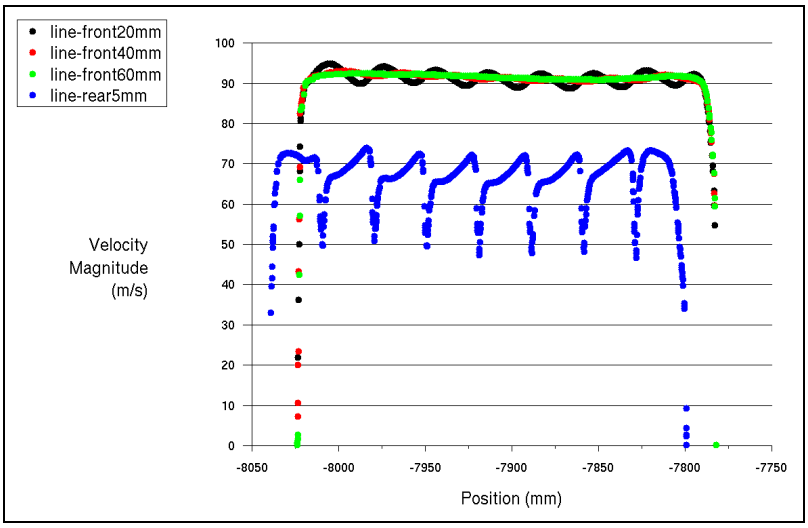

Figure 5–23: Blowing type cascade rig velocity distribution along front and rear traverses.

Chapter 6 - Simulating roughness

6.1 Roughness and measuring parameters

The cascade middle blade profiles were roughened by covering the surfaces of the blade with very thin double-sided sticky tape in order not to increase significantly the thickness of the profile and applying on them carborundum in such a way so as the blade surface roughness distribution to be uniform. The carborundum grain sizes are defined with emery grade numbers which represent different sieve sizes via which the grains pass through. The grit numbers involved are 60, 120, 180 and 220 meaning grain sizes of 254, 102, 76 and 63 microns which correspond to K_s/c values of 0.0042, 0.0017, 0.0013 and 0.0010, respectively. K_s is the physical roughness height and according to Fluent 6.3, for a uniform sand-rain roughness this parameter can get the value of the height of the sand-grain. For a non-uniform sand-grain the roughness height can be equal to the mean diameter of the grains. For the particular simulation the fouling grains were assumed to be uniformly distributed on the blade surfaces and the mean diameter (average size) of them was used as the roughness height input for the simulation.
CFD measurements of blade total pressure loss ω and blade outflow angle α_2 in the area of the wake took place for the case of absolutely smooth blades and for the cases related to the roughened three middle passage blades with different carborundum grit sizes.
Experimentally, a pitot-static probe is going to be used for the front traverses at a distance of one blade chord from the blade leading edges in order to enhance the calculation of inlet cascade velocity. One three-hole cobra probe is going to be used for the downstream traverses at a distance of one chord length from the blade trailing edge towards the calculated exit cascade streamtube flow angle. At this distance most of the mixing has taken place and pitchwise flow angle variation will be only small (Gostelow J., 1984). According to these, traverse lines and planes were created in Fluent Inc. one chord in front of the blades and one chord behind them towards the streamtube vector to monitor predicted velocities and pressures. The blade profile total pressure loss coefficient

$$\omega = \frac{P_1 - P_2}{P_1 - p_1} \qquad (173)$$

has been obtained via analysis of the pressure data from the front and downstream blade traverses.
The effect of thickness due to roughness has not been taken into account in the current study. Gbadebo et al (2004) in order to separate the effect of thickness from the effect of roughness, performed tests by covering the leading edge / peak suction region with thin cardboard strips of similar thickness to that of the emery paper used for applying roughness. Comparing contours of stage pressure rise coefficient for thickened blades with these of smooth and roughened blades they found that the thickness has

negligible contribution to wake thickening. According to Saravanamuttoo (2001) test results for subsonic compressor blade sections over a range of Mach numbers shows that at low Mach numbers, the losses for zero angle of incidence are very low compared to those at higher incidence and higher Mach number. The current cascade runs at a Mach number of 0.4 and at a nominal incidence of zero degrees. The corresponding losses are expected to be low and depend only secondarily on blade thickness. However, at high Mach number and incidence far away from nominal, as expected the losses increase dramatically. In this case, blade thickening due to roughness significantly increases the pressure losses.

6.2 CFD modelling

A computational solution using Fluent was developed for the cascade geometry of the current project. The simulation involved a combination of structured and unstructured grid and the standard version of the k-ε turbulence model. In order to simulate roughness effects the finest grid (10140777 cells) of the previous simulations related to smooth blades was used, but it was modified in order the centroids of the cell nodes close to the walls to be at a distance higher than the roughness height which was assumed to be the size of the particles uniformly spread along the blade surfaces.
For the cases of applying roughness on the blade surfaces standard wall functions were used. Wall functions comprise laws-of-the-wall for mean velocity and temperature and formulas for near-wall turbulent quantities. According to Fluent 6.3, the wall roughness effects can be included through the law-of-the-wall modified for roughness which has the following form:

$$\frac{u_P u^*}{\tau_w / \rho} = \frac{1}{\kappa}\ln(E\frac{\rho u^* y_P}{\mu}) - \Delta B \qquad (174)$$

u_P : Mean fluid velocity at point P
τ_w : Wall shear stress
κ : Von Karman constant (=0.4187)
E : Empirical constant (=9.793)
y_P : Distance from point P to the wall

$$u^* = C_\mu^{1/4} k^{1/2} \qquad (3)$$

C_μ : Empirical constant (=0.09)
k : Turbulent kinetic energy

$$\Delta B = \frac{1}{\kappa}\ln f_r \qquad (175)$$

f_r : Roughness function

For a sand-grain roughness and similar types of uniform roughness elements ΔB has been found to be well-correlated with the non-dimensional roughness height K_s^+.

$$K_s^+ = \rho K_s u^* / \mu \qquad (176)$$

K_s: Roughness height

According to Fluent 6.3 (2007), it has been observed that there three distinct regimes:

- hydrodynamically smooth ($K_s^+ \le 2.25$)
- transitional ($2.25 < K_s^+ \le 90$)
- fully rough ($K_s^+ > 90$)

Roughness effects are negligible in the hydrodynamically smooth regime, but become increasingly important in the transitional regime and especially in the fully rough regime. In Fluent 6.3 for the hydrodynamically smooth regime $K_s^+ \le 2.25$:

$$\Delta B = 0 \qquad (177)$$

For the transitional regime $2.25 < K_s^+ \le 90$:

$$\Delta B = \frac{1}{\kappa}\ln\left[\frac{K_s^+ - 2.25}{87.75} + C_s K_s^+\right] \times \sin\{0.4258(\ln K_s^+ - 0.811)\} \qquad (178)$$

C_s: Roughness constant

In the fully rough regime $K_s^+ > 90$:

$$\Delta B = \frac{1}{\kappa}\ln(1 + C_s K_s^+) \qquad (179)$$

The inlet of the cascade geometry was set as pressure inlet boundary with a total pressure of 101592 Pa and total temperature 293.15 K.The turbulence intensity was set to 1%, while the length scale was set to 1.765 mm.
The outlet of the cascade was treated as pressure outlet boundary with a static pressure of 95583 Pa, assuming that the flow between the inlet and the outlet of the cascade is adiabatic.
A second order discretization scheme was used for the simulation and the pressure based solver was implemented since the flow was initially assumed to be middly compressible. The SIMPLE algorithm for pressure-velocity coupling was used, as well.

6.2.1 CFD Velocity analysis

Applying roughness at the middle passages of the blade cascade one can see from figure 6-1 and 6-2 the results coming out from a 60 mm traverse line towards the exit cascade streamtube taken at a midspan height. As the particle size and hence the roughness size increases the wake velocity behind the roughened blades drops continuously but not linearly.

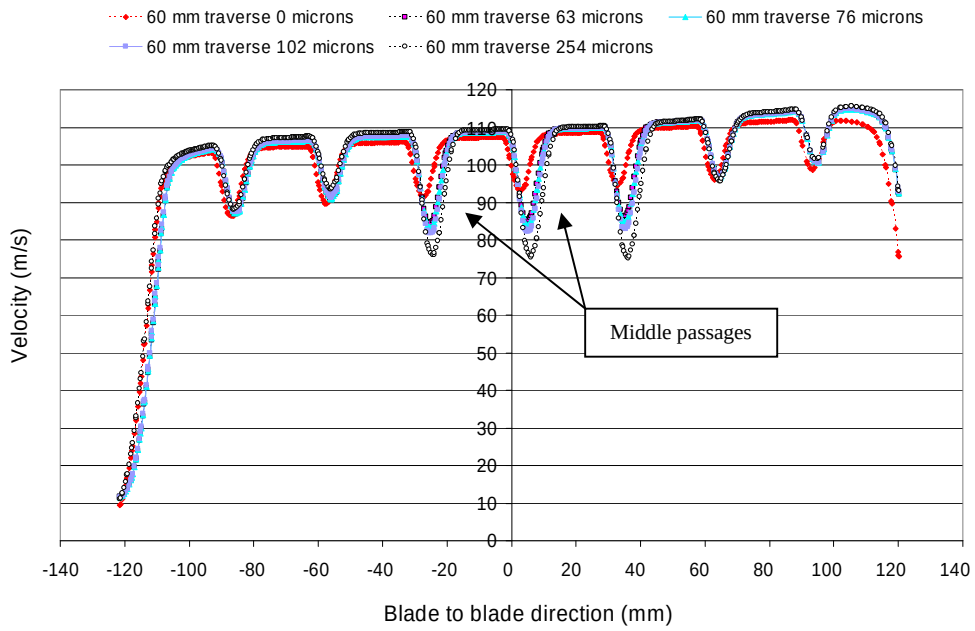

Figure 6–1: Velocity distribution at 60 mm traverse.

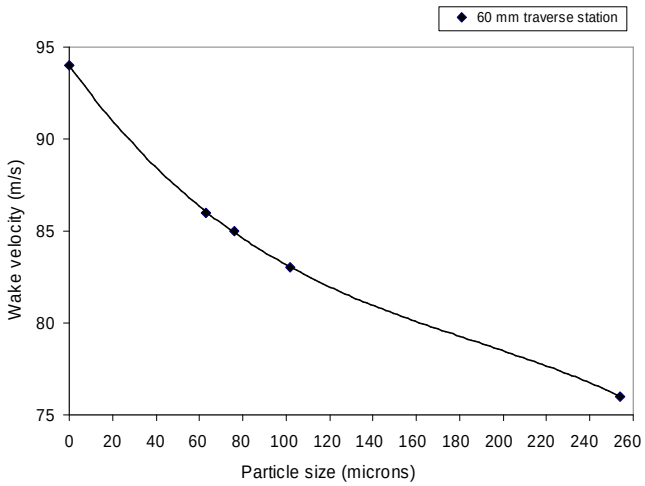

Figure 6–2: Wake velocity deterioration.

As the diameter of the particles increases gradually from 63 to 254 μm the wakes behind the three cascade middle blades widen and the air velocity magnitude decreases significantly behind these blades compared to the passage existing

velocities. For smooth blades the wake velocity comes out to drop to about 94 m/s from the passage velocity of 108 m/s.
As the size of the particles applied on the middle blades and the roughness increases, the velocity magnitude in these passages increases as a result of the reduction of the passage flow area trying to maintain continuity. At the worst case of 254 μm the velocity in the wake falls to about 76 m/s from a value of 110 in the passage. In fact, when comparing smooth blades of zero roughness to blades of 254 microns roughness height, the velocity increase in the potential core flow is significantly less than the velocity decrease of the wake. Furthermore, this difference increases with increasing roughness.
For smooth blades at the trailing edge the boundary layer thickness is bigger on the suction surface than it is on the pressure surface. Accordingly, the total wake thickness at the trailing edge is biased to the suction surface side. For this reason the wakes of the roughened blades seem to move more and more to the right behind the blades (towards the trailing edge) as the roughness increases.
Comparing results coming out from 5 and 30 mm traverses behind the blades with those of 60 mm traverse, it can be seen from figures 6-3 and 6-4 that the wake velocity increases as the flow moves rearwards while the passage velocity decreases. Also, proceeding further downstream the measuring station, the broader and shallower is the wake and this was also reported by Pollard and Gostelow (1967).

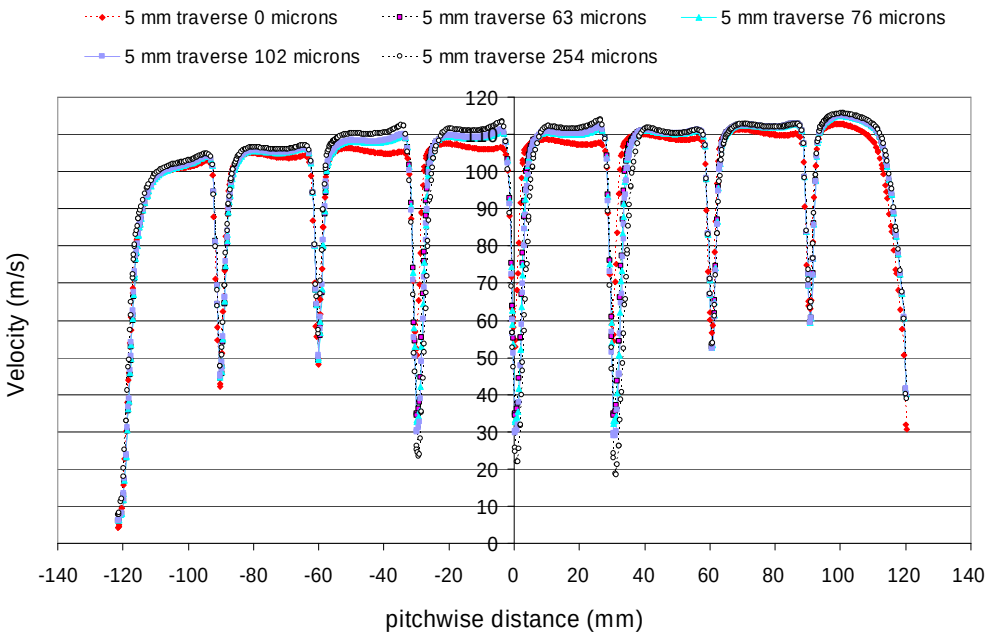

Figure 6–3: Velocity distribution at 5 mm traverse.

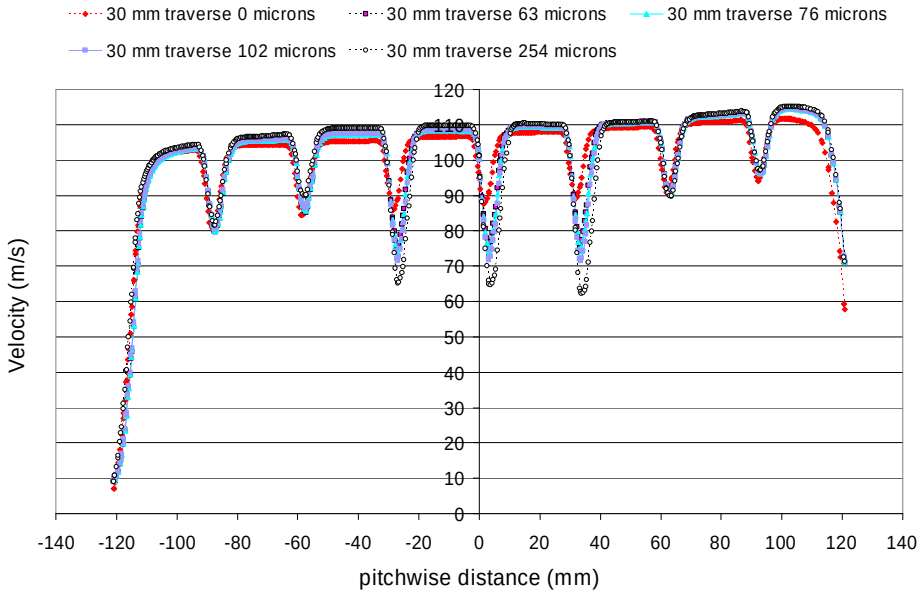

Figure 6–4: Velocity distribution at 30 mm traverse.

Increasing the surface roughness height to 254 microns the wake velocity magnitude reaches values of 23, 65 and 76 m/s towards the 5, 30 and 60 mm traverse line stations. These values are quite lower than these found for the smooth blades which are 53, 87 and 94 m/s towards the same traverse stations and represent reduction of about 57, 25 and 19 % respectively. CFD results indicate a non-linear velocity distribution towards the exit of the middle blade passage streamtube (see figure 6-5). The velocities along this direction seem to increase by different amounts between smooth and roughened blades. However, the velocities associated with the roughened blades only are of a lower level of magnitude than those related to the smooth blades and they seem to increase proportionally after the station of 30 mm behind the blade trailing edge.

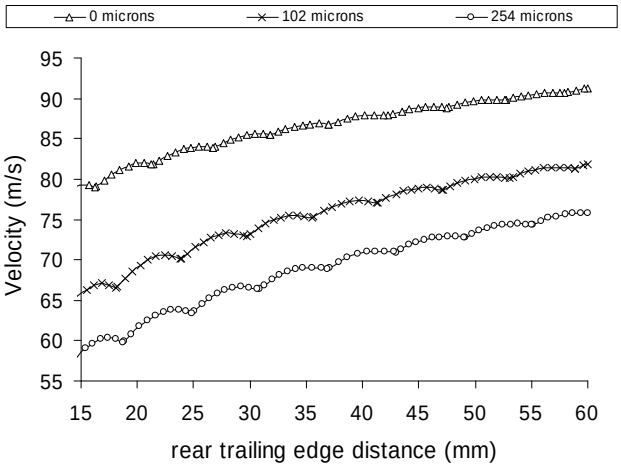

Figure 6–5: Wake velocity distribution.

Passing from smooth to roughened blades the gradient of the velocity distribution in the wake becomes steeper. This happens because the mixing process of kinetic energy

transfer from the potential flow into the wake flow increases as surface roughness increases. As surface roughness increases, turbulence intensity in the wake increases encouraging more energy transfer from the potential flow into the wake flow so, as you proceed from the blade trailing edge downstream in the wake the kinetic energy of the wake flow increases, increasing therefore the average velocity of the wake flow.

6.2.2 Losses

The Fluent model is unable to accurately predict the total pressure in the potential flow at the cascade exit. In fact the model predicts a small total pressure rise in the potential flow between blade rows. This cannot be the case and at the time of writing the reason for this case has not been established. Accordingly the zero line in figure 6-6 has been adjusted to correspond to zero total pressure change in the potential region across the cascade blade row (in effect the flow in this region is assumed isentropic). From this figure it is obvious that the total pressure loss coefficient ω increases as the particle size and therefore, blade roughness increases. In addition, loss increases were reported by Kind et al (1998) as a function of increasing roughness height over chord (k/c) ratios of 0.0021, 0.0045 and 0.0063 for design incidence and spacing parameter λ_s (area of roughened blade surface / total frontal area of roughness elements) near 10. In figure 6-6, passing from smooth blades to fully roughened blades with particle sizes of 254 microns, the loss increases from 0.17 to about 0.36. The losses associated with 63, 76 and 102 microns show no significant difference. In addition, the loss increase in the passage area is not significantly different between smooth blades and fully roughened blades as well.

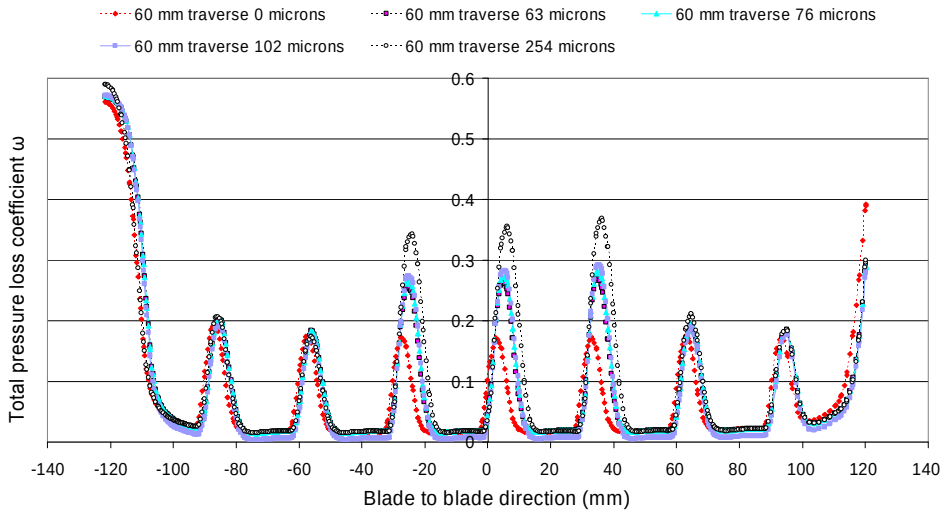

Figure 6–6: Loss distribution at 60 mm traverse.

Comparing figure 6-6 with figures 6-7 and 6-8, it can be seen that as the traverses move rearwards (5, 30 and 60 mm distance) the losses reduce for constant roughness height. For the biggest particle sizes of 254 microns the loss reaches a value of 0.67 to 0.44 and then to 0.36 following the results of the traverses rearwards. The total pressure loss for the smooth blades reaches values of 0.45, 0.22 and 0.17 following

the traverses in the same rearward direction. Hence, the losses increase by 48.9, 100 and 112 % respectively, for the different traverse stations as the roughness increases from 0 to 254 microns.

Following the traverses behind the blades in an axial sense towards the streamtube vector, the total pressure losses in the wake area decrease as the flow propagates far away from the trailing edge. This is similar behaviour to that detected in terms of velocity. For smooth blades, taking as a datum value the level of loss at a distance of 5 mm behind the blade trailing edge, the loss decreases by 51 % at a distance of one half chord and by 62 % at a distance of one chord. In the case of the highest roughness considered, namely 254 microns, the corresponding losses decrease by 34 % and 46 % respectively. This loss dissipation pattern is due to increasing the turbulent mixing between the blade wakes and the free stream potential flow.

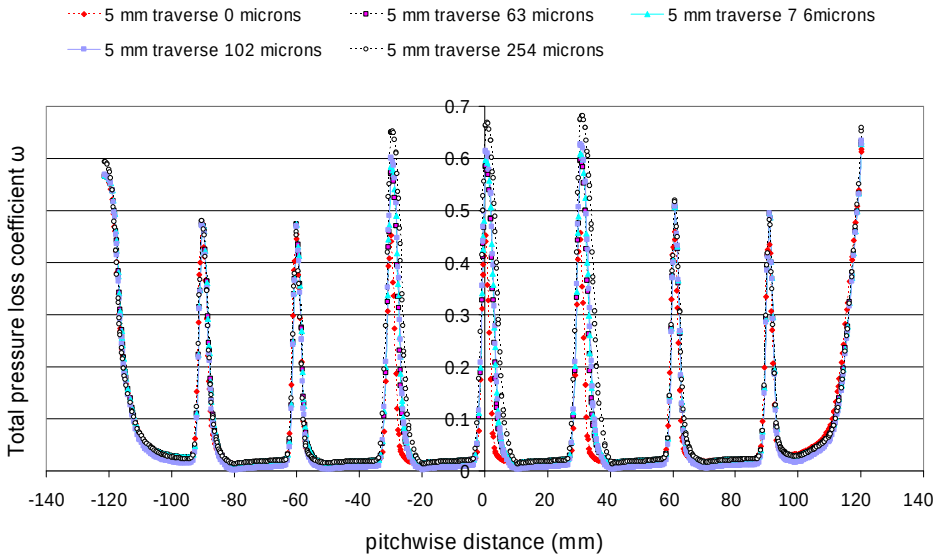

Figure 6–7: Loss distribution at 5 mm traverse.

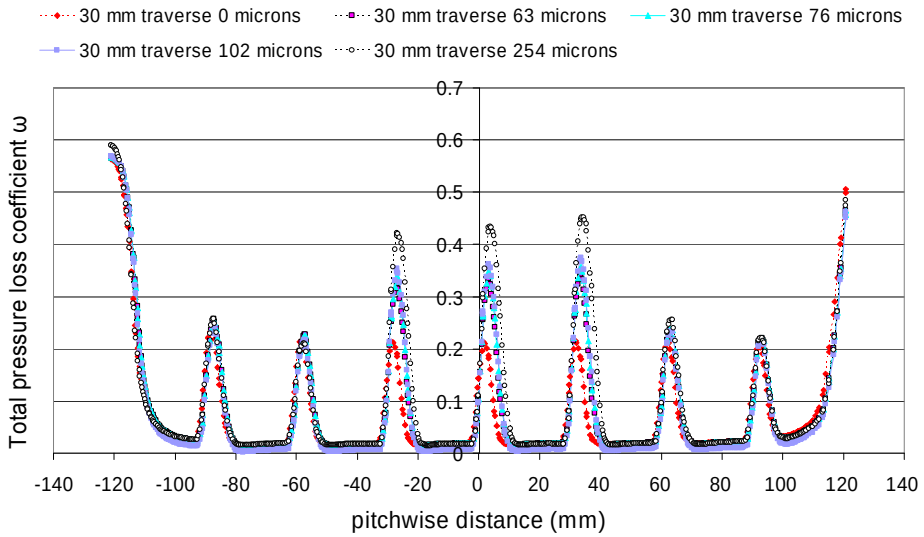

Figure 6–8: Loss distribution at 30 mm traverse.

6.2.3 Exit flow angle analysis

Investigating the exit flow angles α_2 behind the blade trailing edges, from the CFD results obtained (figure 6-9), it is seen that as the particle size and therefore roughness height increases, the exit flow angle increases. For smooth blades the passage exit flow angle at a distance of one chord behind the blades towards the cascade stream tube vector is 30.5 degrees. The distribution of exit flow angle along the traverse seems to be uniform with some disturbances in the wake region. However, when increasing the roughness size, the distribution ceases to be uniform. Correspondingly, very high peak values of exit flow angle exist in the wake areas reaching 33.5 degrees for the highest roughness values examined. As the particle size increases by approximately 100 microns the exit flow angle increases by almost 2 degrees. Above this as the roughness size reaches 2.5 times larger (254 microns) the exit flow angle increases by a further 1 degree. Therefore, the reduction in the exit flow angle seems to be eliminated by half as the particle size roughening the blades exceeds 40% of the highest value (254 microns). The fact is that at cascade exit, there is a pitch wise reduction in static pressure as shown in figure 6-10. This will cause the upstream flow to deviate towards the lower static pressure region and progressively increase the values of α_2 at exit from the blades in a pitch wise direction.
As surface roughness increases the passage blockage increases to accelerate the flow towards the lower static pressure region downstream. This effect increases in magnitude as pitch wise distance away from the centre blade increases. This increasing blockage progressively reduces the deviation and therefore the α_2 in the pitch wise direction. This effect is further illustrated with a cross plot of figure 6-9 along the zero pitch line. This is shown in figure 6-11. The final outcome is that at low surface roughness levels, the effect of roughness on α_2 is much stronger than at high levels of roughness.

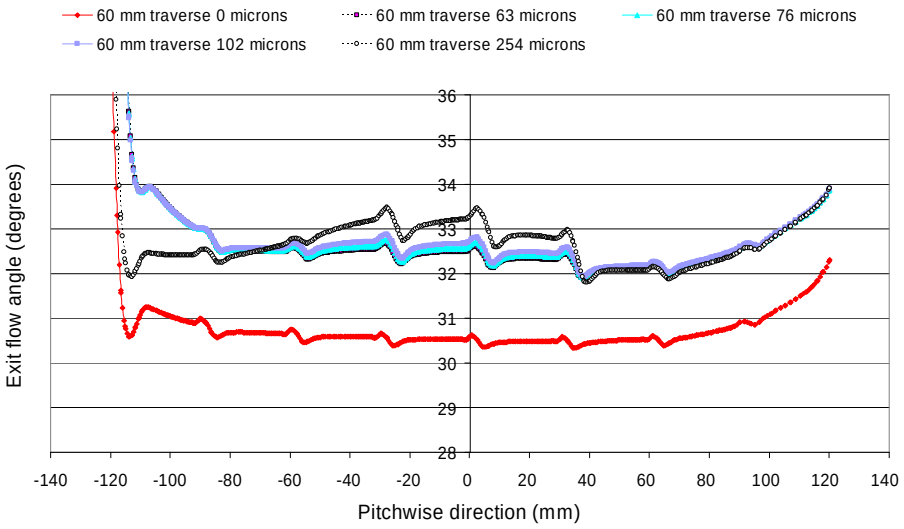

Figure 6–9: Exit flow angle distribution at 60 mm traverse.

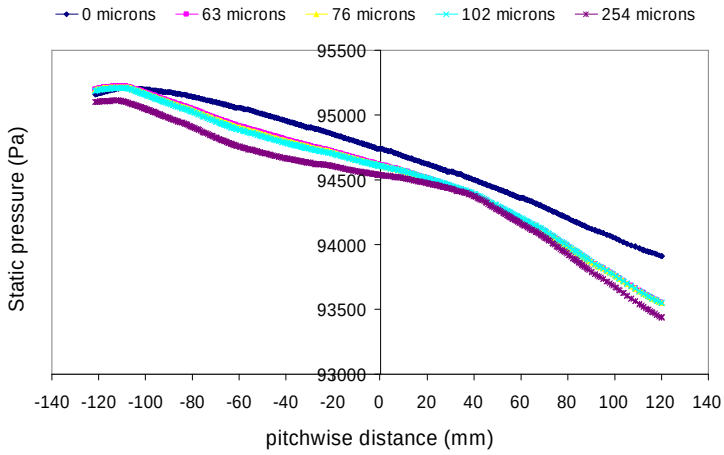

Figure 6–10: Rear pressure distribution at 60 mm traverse.

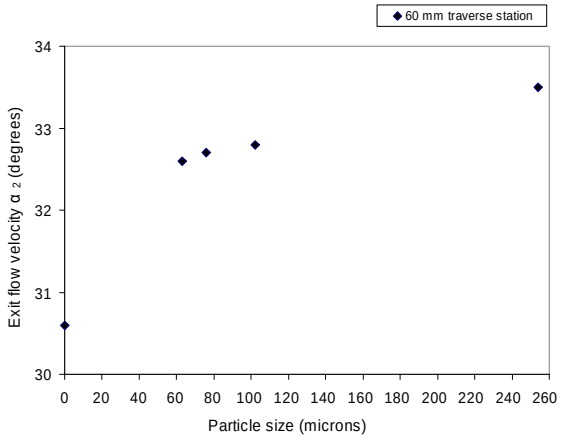

Figure 6–11: CFD prediction of exit flow angle change with roughness size.

All these CFD results are in good agreement with the experimental data of Kind et al (1998). He showed that roughness has little effect on the flow deviation angle δ (blade exit flow angle minus blade metal angle). In fact, he showed that deviation increased by no more than one degree for any roughness case investigated. He concluded that this is consistent with the small effect of roughness on static pressure distribution around the blades since flow deflection is directly dependent on blade loading.
In the mean time as figure 6-9 illustrates the exit flow angles of the outer passages that are not roughened seem to be affected from the middle roughened passages. Comparing figure 6-9 with figures 6-12 and 6-13, it can be seen that the wake exit flow angle decreases as the mixing process develops downstream of the blade trailing edges.

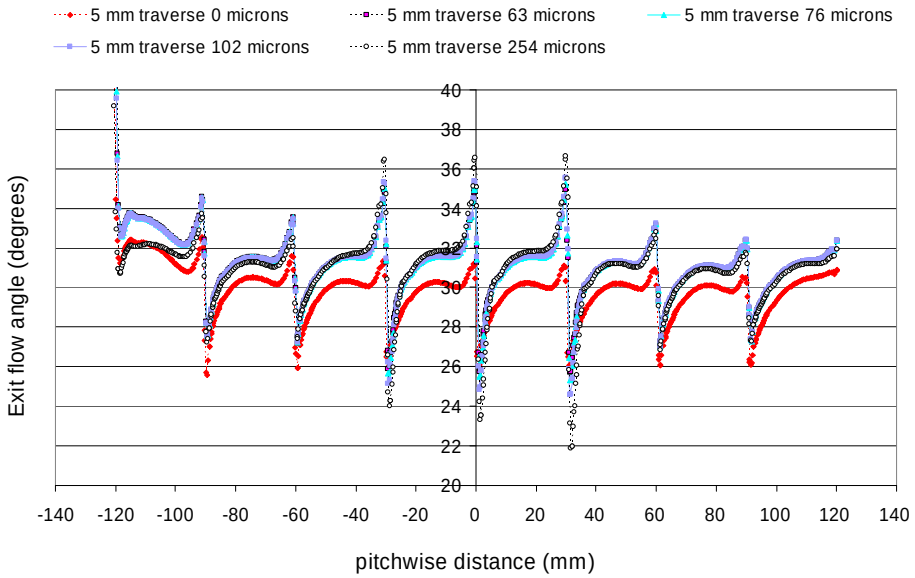

Figure 6–12: Exit flow angle distribution at 5 mm traverse.

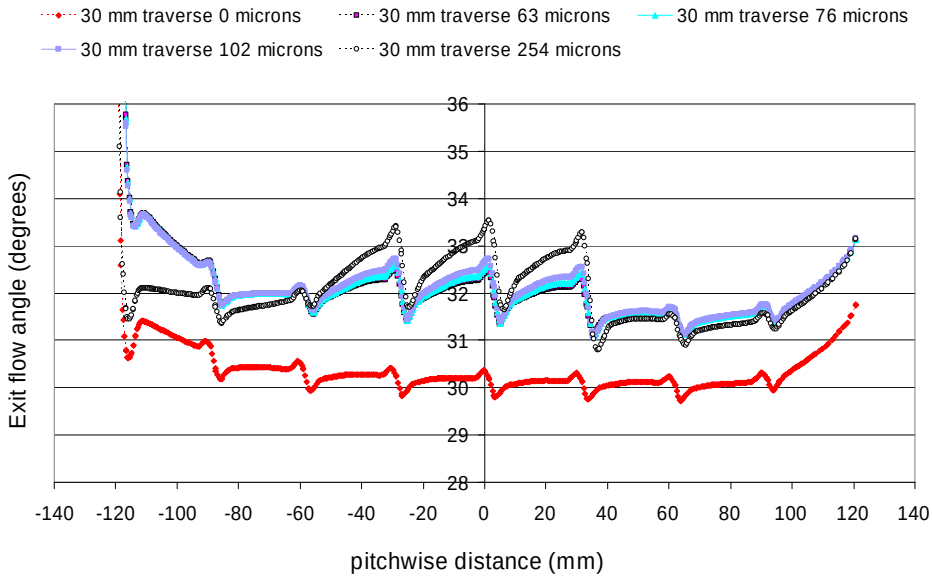

Figure 6–13: Exit flow angle distribution at 30 mm traverse.

6.3 Gas turbine performance degradation due to fouling

The cascade rig CFD results were analysed according to Howell (1945) in order to relate the cascade with an actual stage (see Appendix: Preliminary cascade CFD results related to performance deterioration). From the CFD results the blade profile loss coefficient was calculated and then the overall drag coefficient was estimated. Calculating the lift coefficient and the mean cascade flow angle α_m the polytropic

efficiency η_p related to an actual stage was calculated. The actual stage polytropic efficiency calculated was then compared to the polytropic efficiency of an ABB GT13 E2 industrial gas turbine. Running CFD simulations for different levels of fouling, different values of actual stage polytropic efficiency were calculated and for each case the percentage deterioration in polytropic efficiency was calculated. These percentages of polytropic efficiency deterioration were the input in the performance simulation tool Turbomatch examining the performance of an ABB GT13 E2 engine. Hence, it was considered that the percentage deterioration in polytropic efficiency of this engine is equal to percentage deterioration of the polytropic efficiency derived from the cascade related to stage CFD results.
The input in the performance simulation tool was percentage deterioration in polytropic efficiency and not in compressor isentropic efficiency since the ratio of compressor polytropic over isentropic efficiency is close to unity for higher levels of pressure ratio and therefore both quantities are almost equal (see figure 6-14).

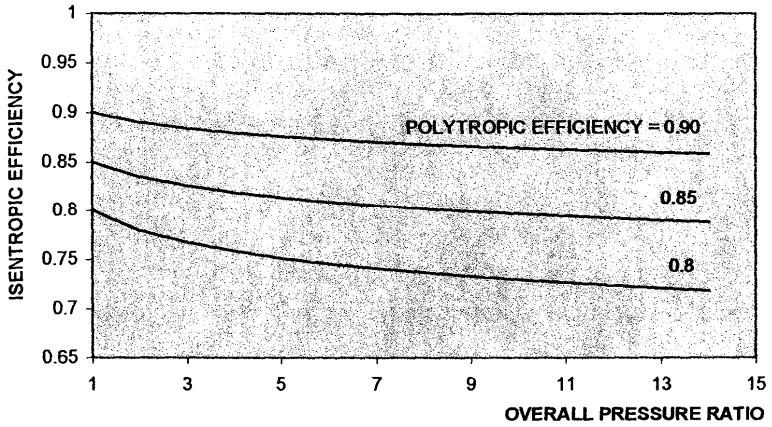

Figure 6–14: Variation of isentropic efficiency with compressor pressure ratio (Ramsden, 2002).

The variation in polytropic efficiency η_p resulting from the cascade-stage correlation data is illustrated in figure 6-15 for the different fouling particle sizes. As the fouling particle size increases the polytropic efficiency decreases. This happens because the overall blade drag to lift coefficient ratio increases upon which the polytropic efficiency depends (see formula 55). This ratio is dominated by the blade profile drag coefficient which increases because of the increase of pressure loss along the blades as the fouling particle size increases and the blade boundary layer thickens.

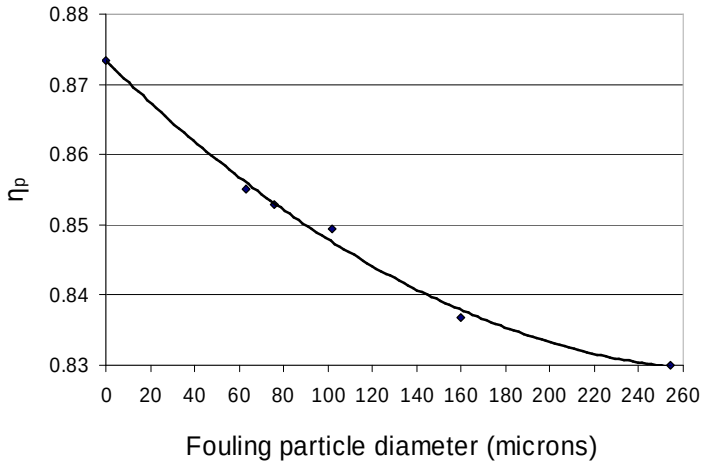

Figure 6–15: Polytropic efficiency versus fouling particle diameter.

From figure 6-16, it can be seen that the rate of deterioration in polytropic efficiency, ΔI % reduces as particle size increases. In particular, above 160 microns, the deterioration in flow deflection ε (see figure 6-17) reduces as a result of increasing blockage. At the same time, static pressure rise, Δpstatic, reduces (see figure 6-18) whilst total pressure loss, Δpo, increases (see figure 6-19). This loss is the main factor that controls the profile drag of the blading and has a large effect on the polytropic efficiency. This is due to boundary layer thickness increasing with increasing surface roughness. This is explained in full in the literature part of the thesis.

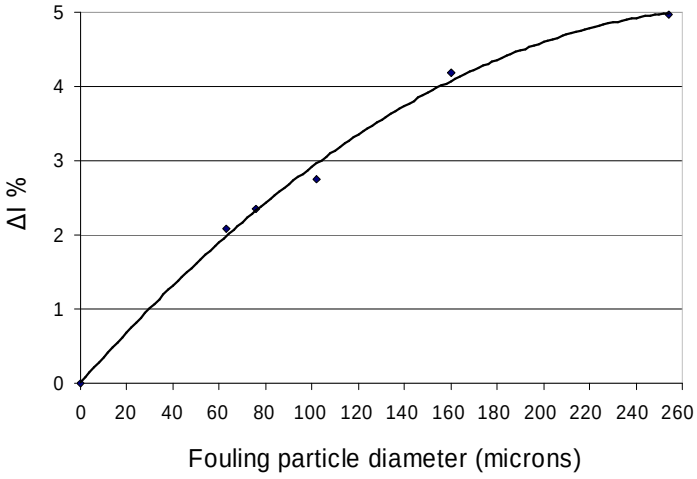

Figure 6–16: Percentage deterioration in polytropic efficiency due to fouling.

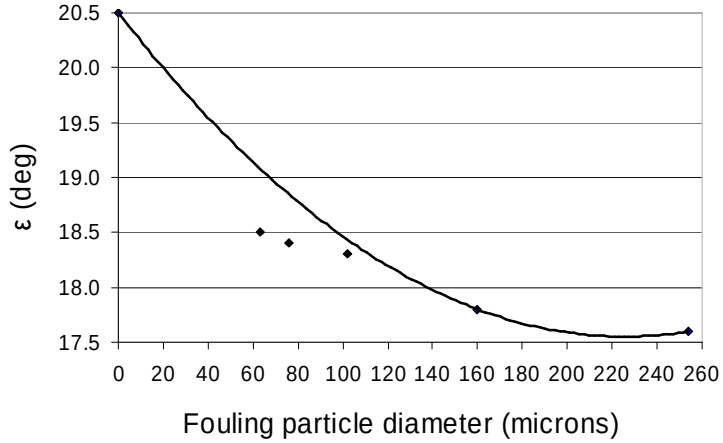

Figure 6–17: Blade flow deflection versus fouling particle diameter.

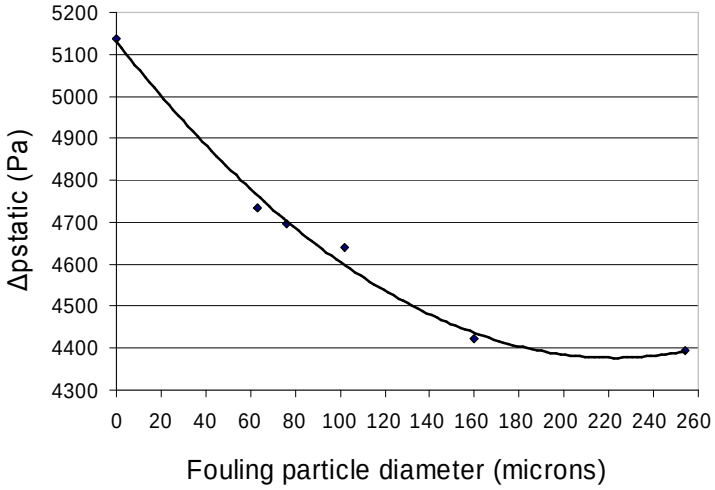

Figure 6–18: Cascade static pressure increase variation with respect to particle size.

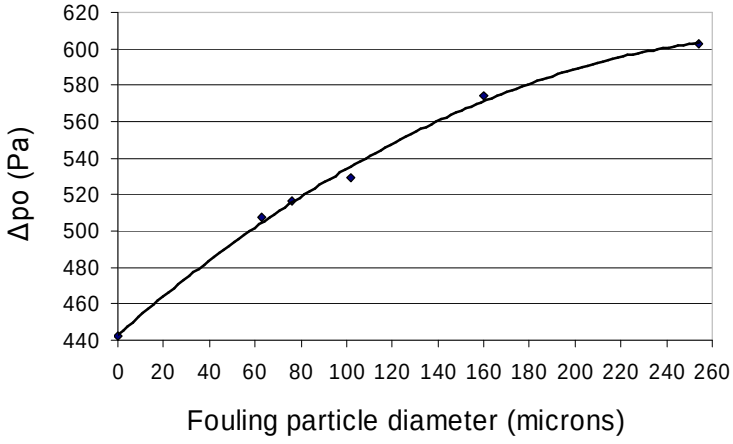

Figure 6–19: Cascade total pressure loss versus fouling particle diameter.

Another parameter used as input in the Turbomatch performance simulation tool is the percentage deterioration in non-dimensional mass flow obtained from the CFD results. This is assumed to be equal to the percentage reduction in non-dimensional mass flow $\Delta(W_1T_1^{0.5}/P_1)$ of the industrial ABB GT13 E2 gas turbine engine.
Figure 6-20 shows that this deterioration does not increase significantly above a particle size of 102 microns. This is thought to be due to the fact that below 100 microns, roughness elements lie inside the boundary layer and, therefore, cannot influence the mainstream flow. However, above 100 microns in size, passage blockage increases due to protrusion of the roughness elements above the boundary layer. At this level, the mainstream flow is more significantly prone to increasing blockage. In the limit, at the largest roughness sizes, increase production of turbulence gives rise to substantial passage blockage.

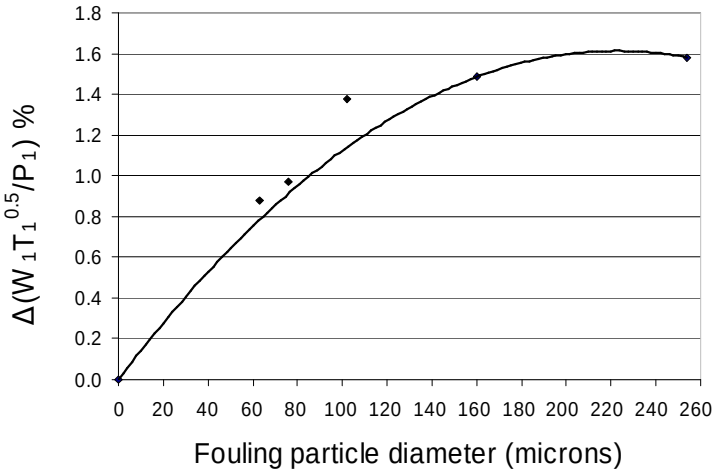

Figure 6–20: Cascade percentage deterioration in non-dimensional mass flow due to fouling.

Plotting the thermal efficiency η_{th} against the turbine entry temperature (TET), it can be seen from figure 6-21 that the thermal efficiency increases as the TET increases. This can be attributed to the increase of the compressor pressure ratio as the TET increases (see figure 6-22) since the thermal efficiency is a function of the pressure ratio (see formula 180).

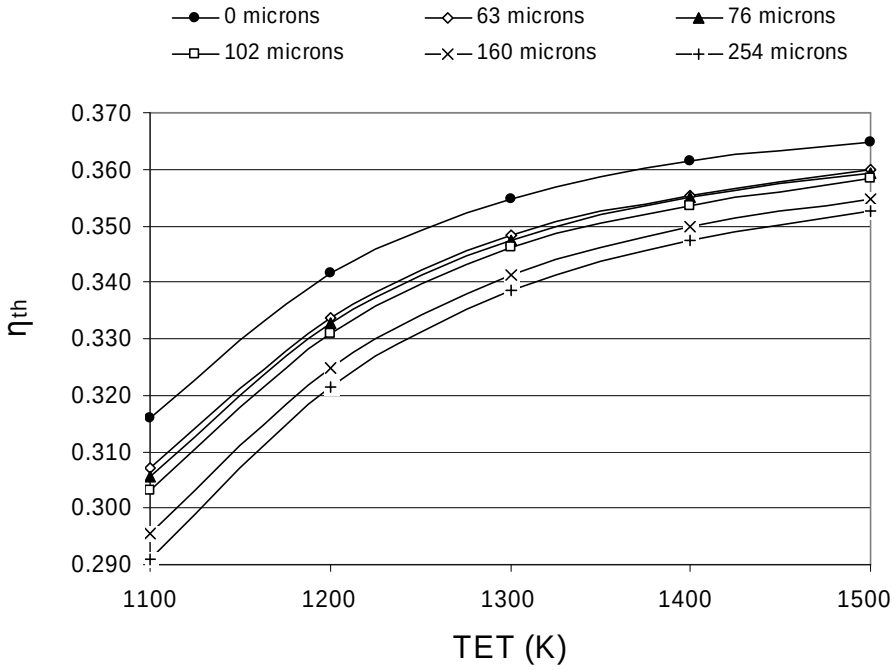

Figure 6–21: Thermal efficiency versus TET (preliminary results).

$$\eta_{th} = 1 - \frac{1}{PR^{\frac{\gamma-1}{\gamma}}} \qquad (180)$$

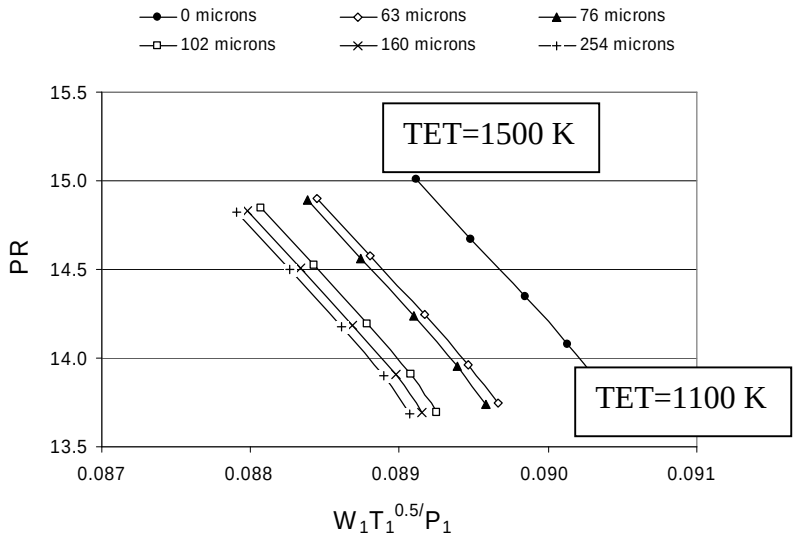

Figure 6–22: Pressure ratio versus non-dimensional mass flow.

As the fouling deteriorates the pressure ratio drops and the efficiency decreases referring to values of constant TET. Considering the case of smooth blades (0 microns) the TET increases from 1100 K to 1500 K and the thermal efficiency increases by 15%. Taking into account the case of the highest fouling of 254 microns

for the range of the same TET increase, the thermal efficiency increases by 21% up to 1500 K. Therefore as the fouling particle size increases, the percentage thermal efficiency gain in the same level of TET increase gets higher.

As a result of the diverging constant pressure lines in the temperature-entropy diagram (see figure 6-23), the useful power (UW, see figure 6-24) progressively increases with increasing turbine entry temperature. As a result of compressor fouling the compressor efficiency reduces and the compressor work increases. As TET increases the effect of increasing compressor work with increasing fouling reduces. Finally, the outcome is that the engine performance measured by the thermal efficiency is less sensitive to component inefficiency as TET increases. This fact is illustrated by the reducing range of thermal efficiency change with increasing TET shown in figure 6-25. In conclusion the engine performance deterioration due to fouling is highest at low TET.

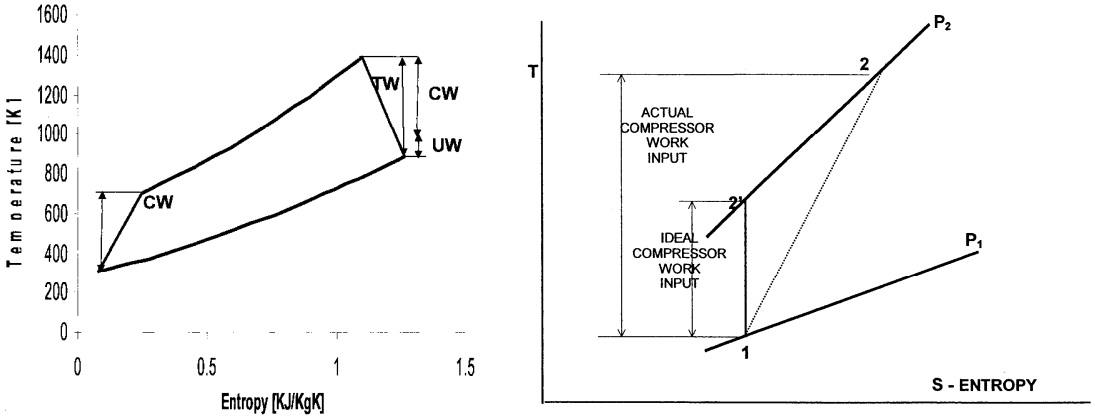

Figure 6–23: Temperature versus entropy (Pilidis, 2002).

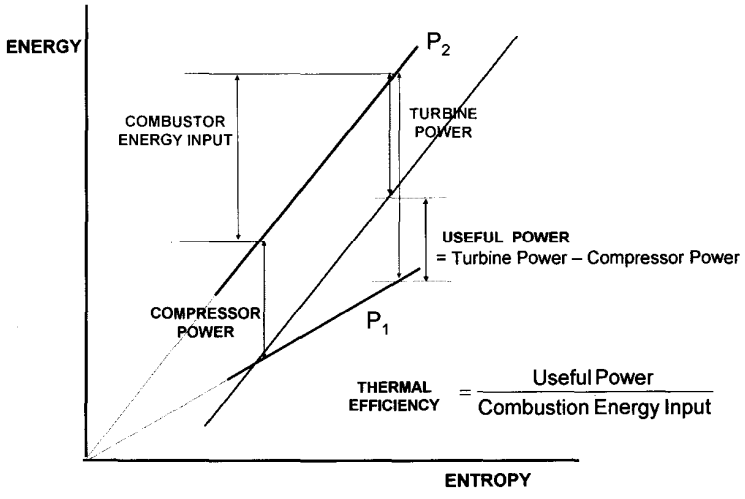

Figure 6–24: Energy versus entropy (Ramsden, 2006).

All the above analysis can also be illustrated with figure 6-25 which shows that as the TET increases the thermal efficiency of the industrial gas turbine is affected less by the parameter fouling. This can be seen from the fact that the slopes of the curves of thermal efficiency versus fouling particle diameter reduce continuously as the TET increases gradually from 1100 K to 1500 K. For the same fouling particle diameter

increase from 0 to 254 microns as the TET increases from 1100 K to 1500 K hence by 36.4% the drop in thermal efficiency reduces from a value of 8.2% to 3.3%, respectively.

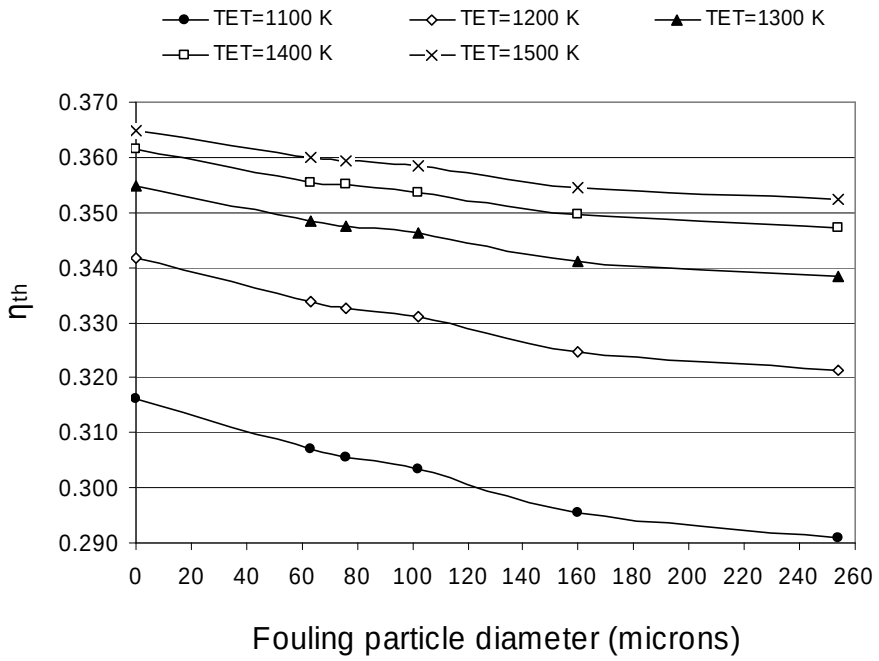

Figure 6–25: Thermal efficiency against fouling particle diameter.

The distribution of useful power (shaft power) the difference between turbine power and compressor power with respect to the TET increase (see figure 6-26) was found to be linear and for higher levels of fouling particle size the useful power drop was increased. Comparing smooth clean blades to heavily fouled ones (254 microns) for TETs of 1100 K and 1500 K, the useful power drop is 11.4 and 7.6 % respectively. Therefore, at lower TETs the useful power decrease due to fouling (0 to 254 microns) is higher when compared with higher TETs. This can be attributed to the shape of the Temperature-entropy diagram (see figure 6-23) whose constant pressure lines diverge for higher TETs producing an increasing divergence between compressor and useful power with the useful power always increasing. Therefore, the industrial gas turbine engine is more prone to fouling in terms of performance, at lower TETs.

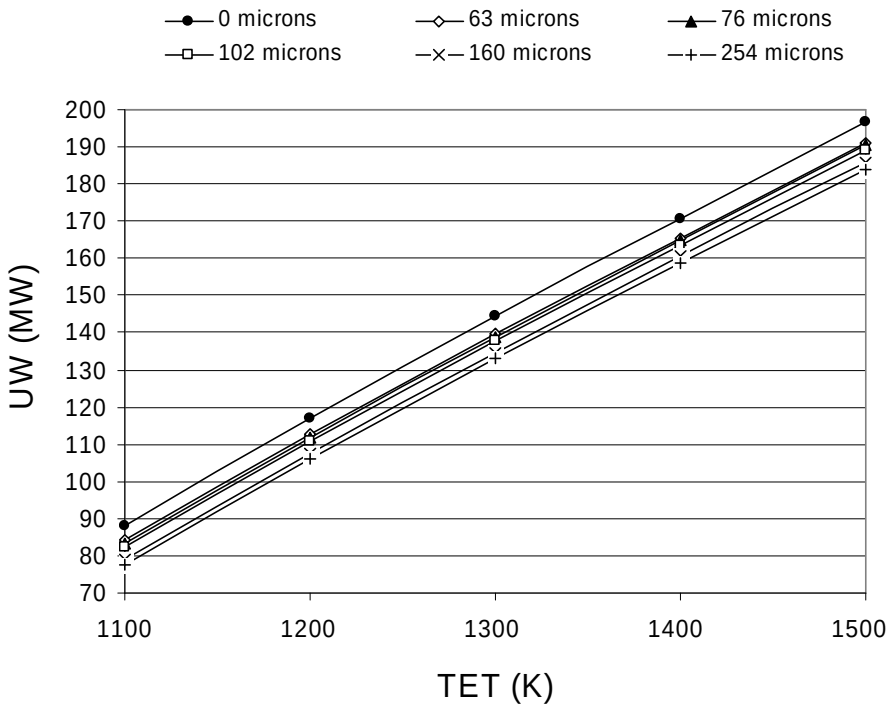

Figure 6–26: Useful power versus TET (preliminary results).

The decrease in useful power as the fouling level increases is due to the mass flow reduction caused. Figure 6-27 shows the decrease in the non-dimensional mass flow $W_1T_1^{0.5}/P_1$ of the ABB GT13 E2 gas turbine compressor as the size of the fouling material increases. After the size of 102 microns the non-dimensional mass flow seems to stabilize and not to be affected significantly from the fouling level. This happens due to the fact that the input file in Turbomatch involves the calculated percentage deterioration in mass flow capacity (non-dimensional mass flow) of the cascade test rig after the level of 102 microns (see figure 6-20).

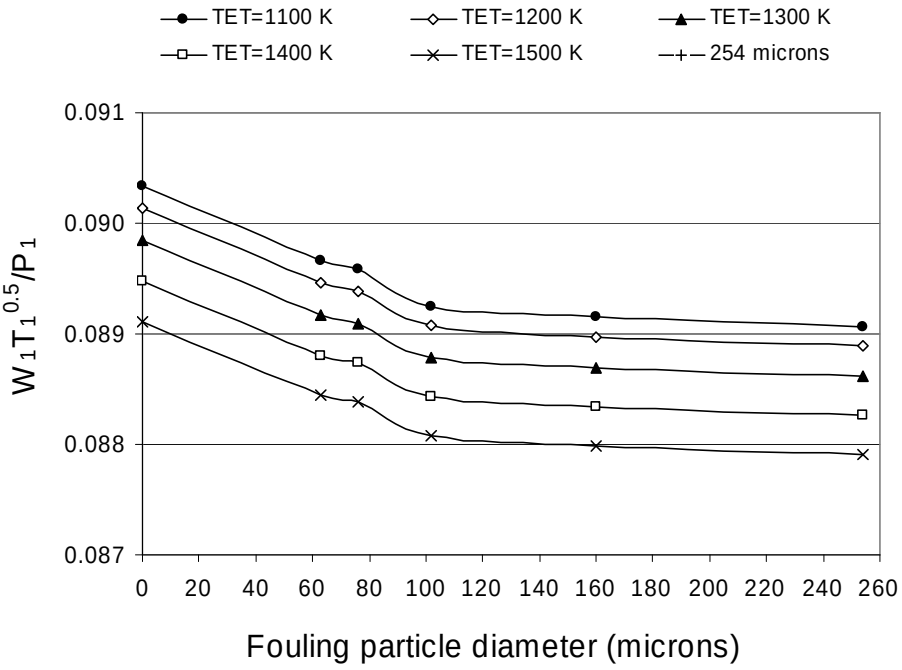

Figure 6–27: ABB GT13 E2 mass flow capacity versus fouling particle diameter.

In figure 6-28 the effect of particle size hence the fouling level on the compressor pressure ratio is illustrated. It can be seen that as the size of the particles increases from 0 up to 102 microns the pressure ratio decreases by almost 1.3 % for all the cases corresponding to different TETs. However, after the size of 102 microns the pressure ratio does not seem to decrease further much and this is a result of the compressor mass flow capacity after this point.

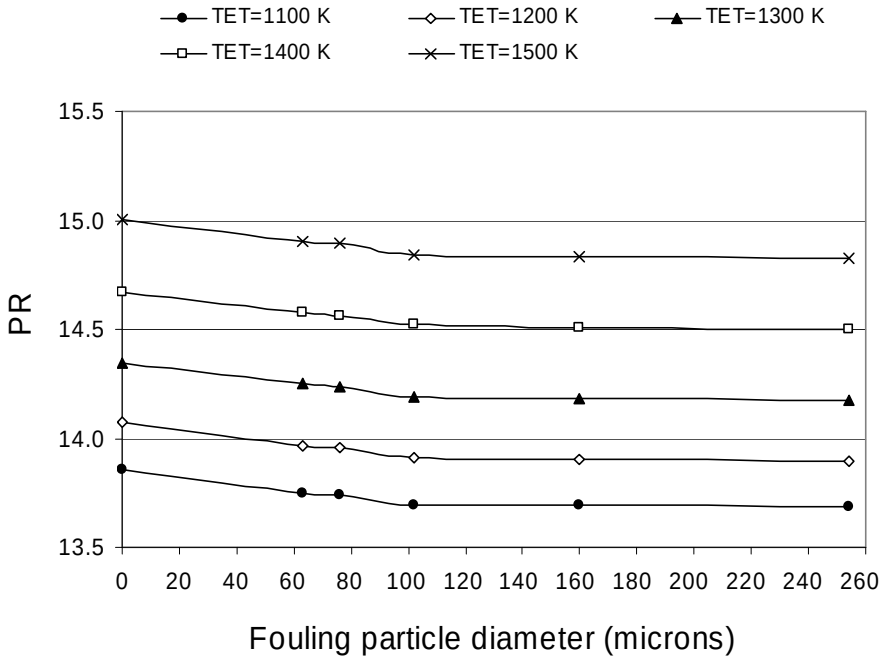

Figure 6–28: Preliminary pressure ratio deterioration due to fouling.

Checking the thermal efficiency variation with respect to the useful power, it can be seen from figure 6-29 that for increasing TET values both terms increase in value. Comparing the gain in thermal efficiency and in useful power due to TET increase from 1100 K to 1500 K for the cases of zero and 254 microns, the gain in thermal efficiency for 254 microns fouling is 41% higher than this corresponding to zero microns and the gain in useful power is 11.4 % higher as well. Therefore, for the same range of TET considered, the higher the level of fouling then the higher the gain in thermal efficiency and in useful power.

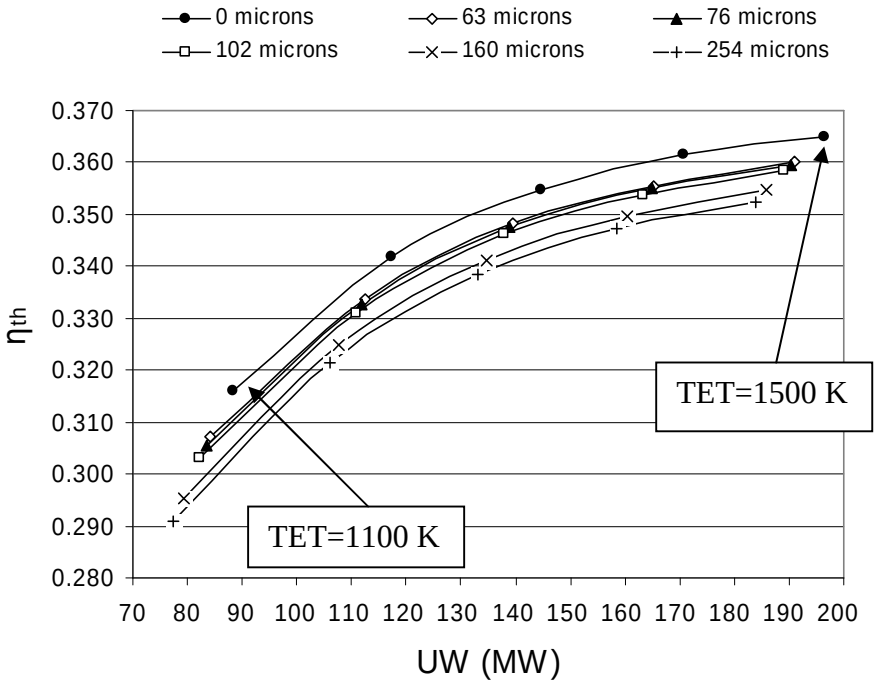

Figure 6–29: Thermal efficiency versus useful power (preliminary results).

It is easily shown that compressor overall (adiabatic) efficiency is a function of pressure ratio through equation 181 below.

$$\eta_c = \frac{Ideal\ compressor\ work}{Actual\ compressor\ work} = \frac{\left(\frac{P_2}{P_1}\right)^{\frac{\gamma-1}{\gamma}} - 1}{\frac{T_2}{T_1} - 1} \qquad (181)$$

P_2 / P_1: compressor pressure ratio

Using predicted data (see Appendix, Preliminary performance deterioration by applying 254 microns particles), from the Turbomatch code, figure 6-30 shows that for an engine whose design point is at a TET of 1378 K, the rate of reduction of compressor efficiency with roughness element size increase is independent of TET. This leads to a single graph for the effect of roughness shown in figure 6-31 where the loss of efficiency is plotted as a percentage of the corresponding value at the design TET.

Figure 6-30 also shows that compressor efficiency at the design TET reduces as roughness size increases. This is because the losses due to roughness are increasing and polytropic efficiency is, therefore, falling. This effect is shown graphically in figure 6-32.

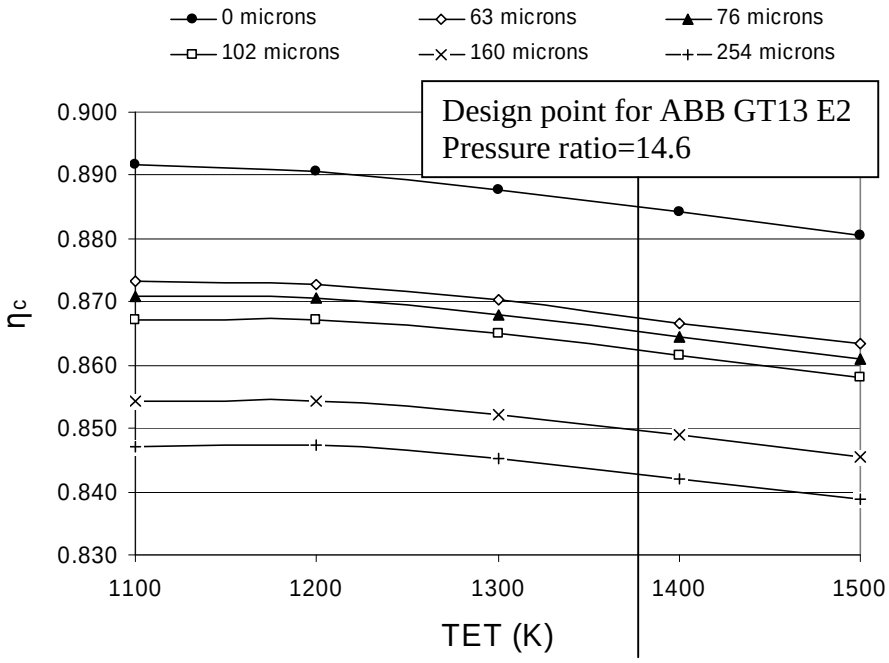

Figure 6–30: Compressor efficiency versus TET (preliminary results).

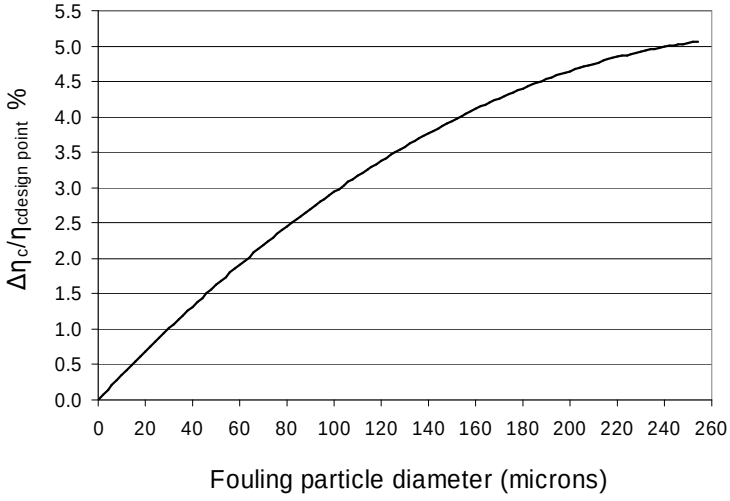

Figure 6–31: Percentage deterioration in compressor efficiency versus particle size increase.

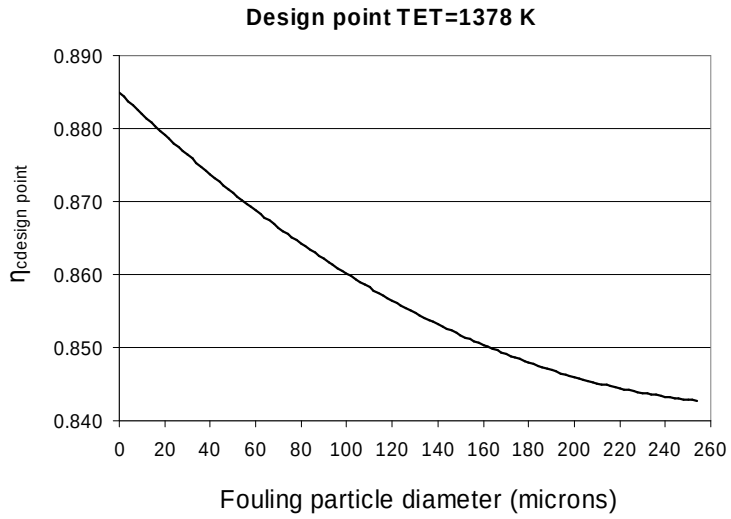

Figure 6–32: Design point compressor efficiency deterioration due to fouling.

The turbine isentropic efficiency η_t was almost unaffected from the increase in turbine entry temperature and from the increase of fouling level (see figure 6-33).

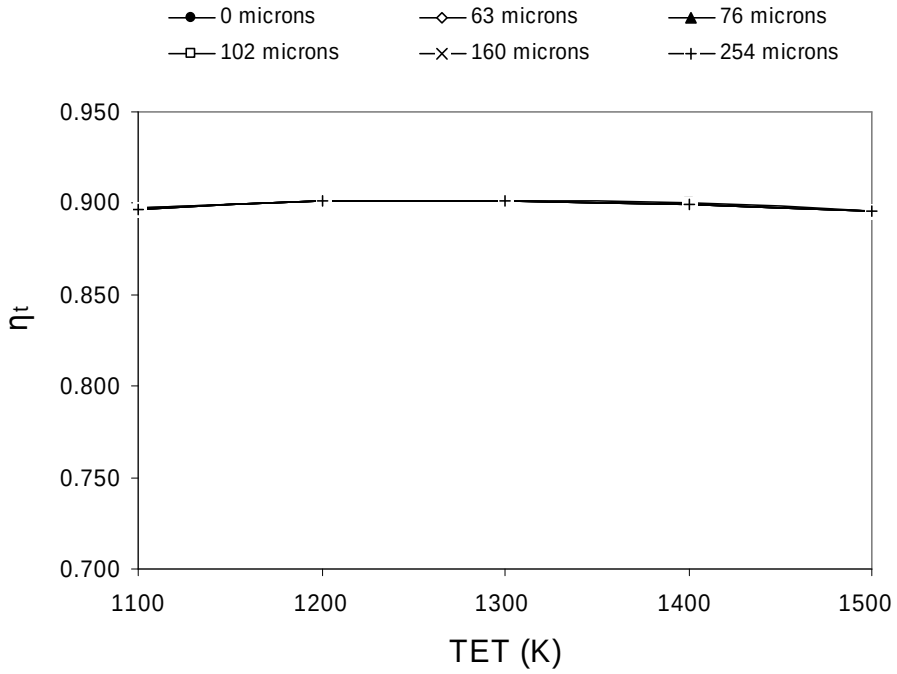

Figure 6–33: Turbine efficiency versus TET (preliminary results).

Chapter 7 - Experimental and CFD analysis results

7.1 Experimental results – Un-roughened blades

Experimental measurements concerning blade fouling took place in the test house 12 of Cranfield University using the current project compressor cascade test rig (see figure 7-1).

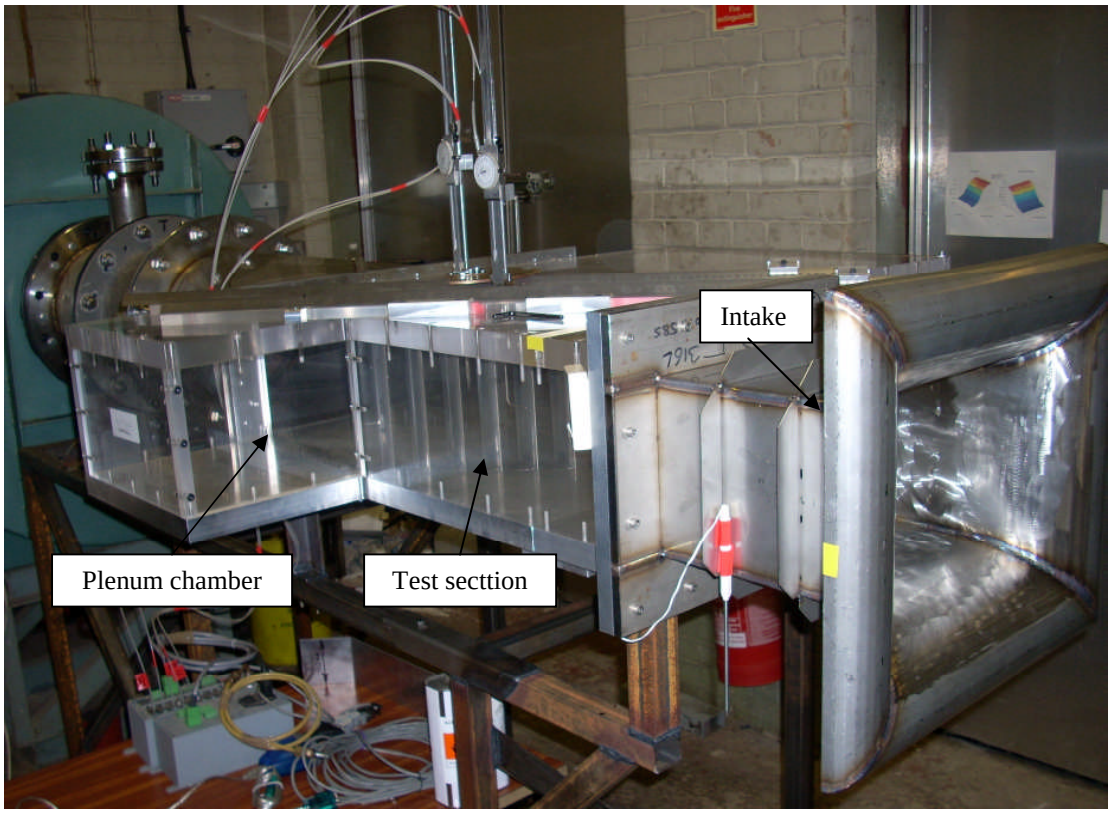

Figure 7–1: Compressor cascade rig.

Before running experiments concerning fouling of the three middle cascade blades, hot wire anemometer runnings took place in order to measure the turbulence intensity and the mean velocity at the entrance of the cascade tunnel intake. The turbulence intensity and intake mean velocity were found to be 2.245% and 52.6 m/s respectively.
Measurements were taken also at the exit of the conical part of the cascade tunnel intake hence at the beginning of the cascade flow settling chamber, by traversing the hot wire probe from the central position (see figure 7-2). The traverses were taken at mid height of the tunnel and at increments of 20 mm from the central position both ways. The maximum length covered each time traversing either right or left was 100 mm. The average turbulence intensity value obtained from all these traverses was 1.7%. The average mean velocity was found to be 92 m/s. All these measurements were taken under ambient atmospheric pressure of 99962 Pa and ambient temperature of 13 ^{o}C.

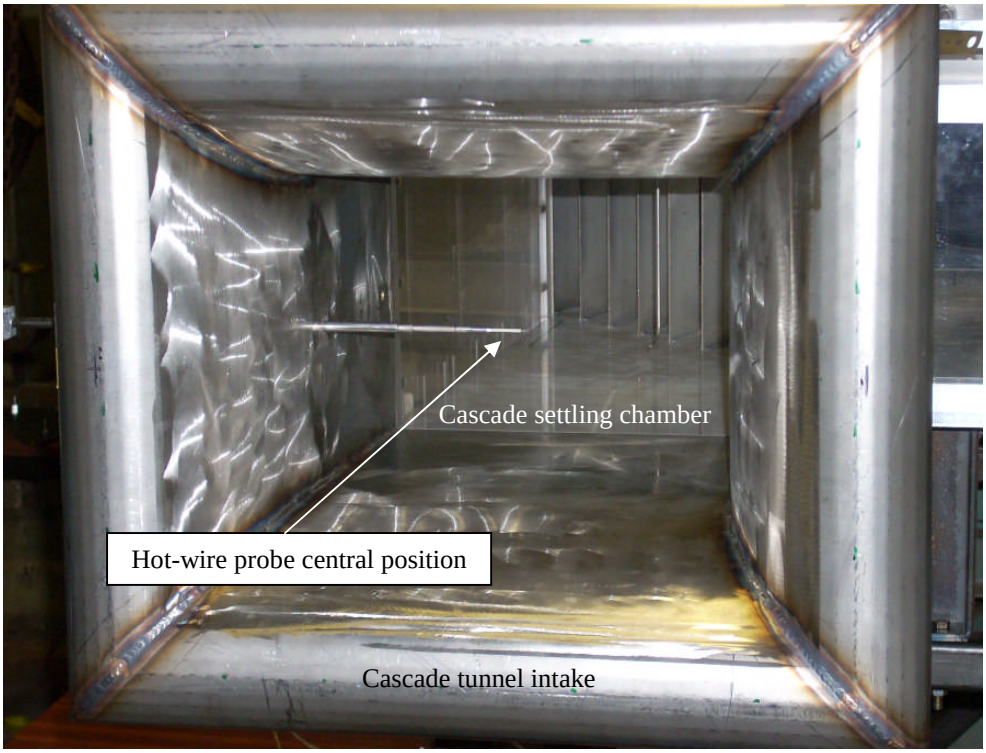

Figure 7–2: Actual hot-wire positioning illustration.

Pressure readings were obtained one chord in front and at the rear of the blades towards the cascade stream tube direction at a mid-span blade height. The actual positioning of the pitot-static probe and the three-hole yaw probe assemblies is illustrated in figure 7-3.

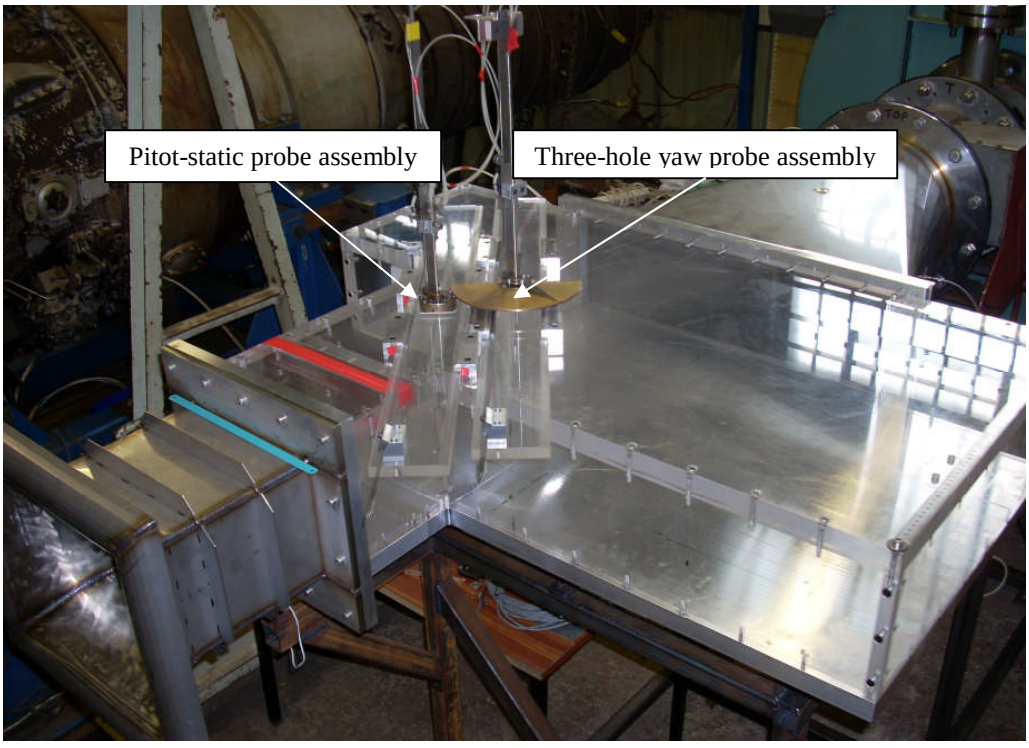

Figure 7–3: Probe assembly illustration.

The traversing slots where the probes slide in are illustrated in figure 7-4.

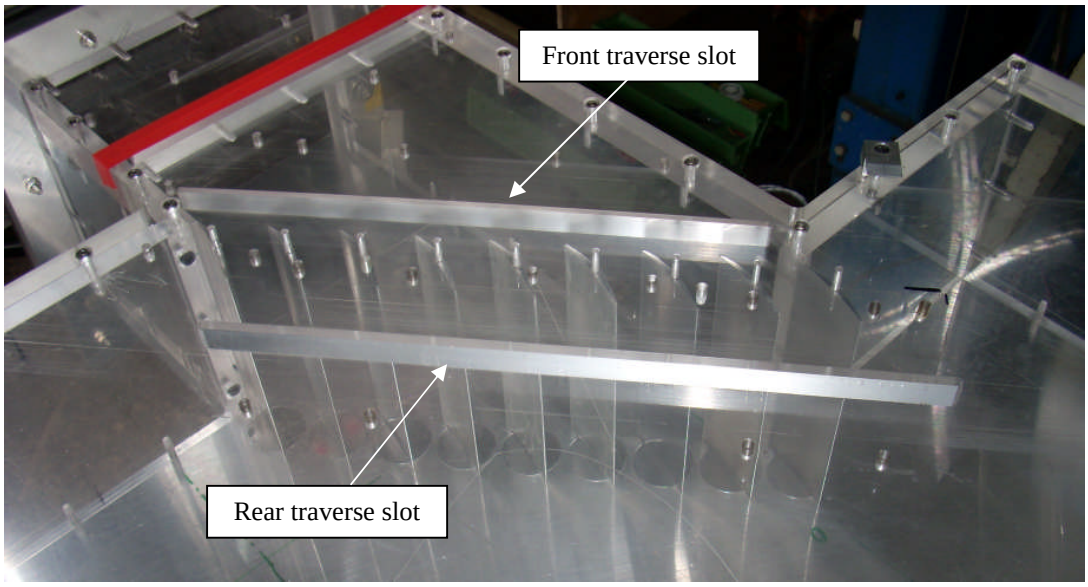

Figure 7–4: Probe slots illustration.

The velocity distributions at one chord downstream of the cascade towards the cascade stream-tube exit vector were investigated experimentally at a mid-span height for clean blades. The results are shown in figure 7-5. This shows cascade exit flow velocity at different ambient conditions. The passage and wake velocity scatter for all these experiments was about 2% and therefore, it can be stated that the parameter velocity is not affected much from the parameter ambient condition.

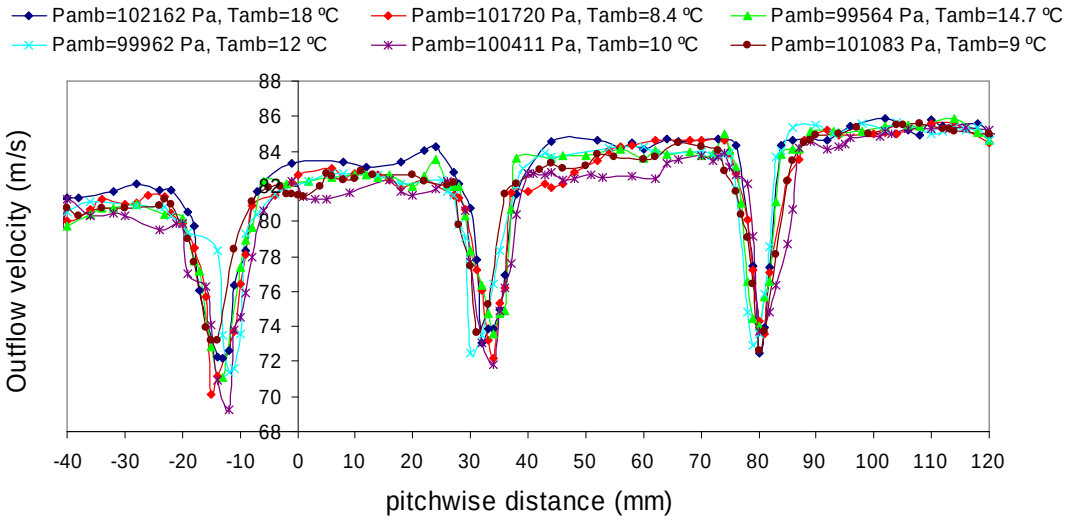

Figure 7–5: Velocity distribution at 60 mm traverse.

A statistical average of all the results has been plotted in figure 7-6 and it can be seen that the passage velocity increases very slightly from 81 m/s to 85 m/s towards the right side of the cascade. This variation occurs because at the cascade exit there is a pitch-wise gradient in static pressure (see figure 7-7) of 0.2 %. This causes the upstream flow to deviate towards the lower static pressure region and progressively

increase the values of α_2 at the exit of the cascade blades in a pitch-wise direction. The wakes are all about 10 mm thick and the wake velocity decreases in the centre passage from 83 m/s to 73.5 m/s.

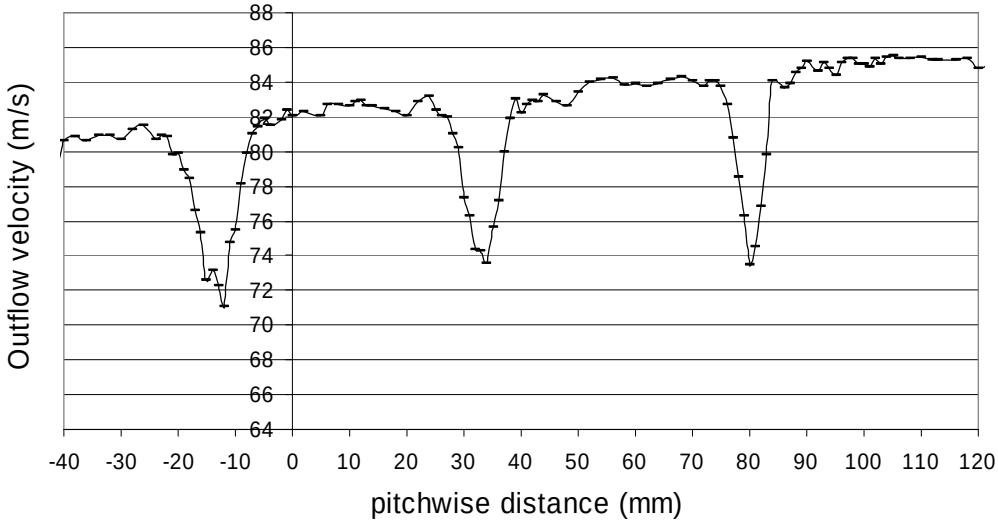

Figure 7–6: Statistical average velocity distribution at 60 mm traverse.

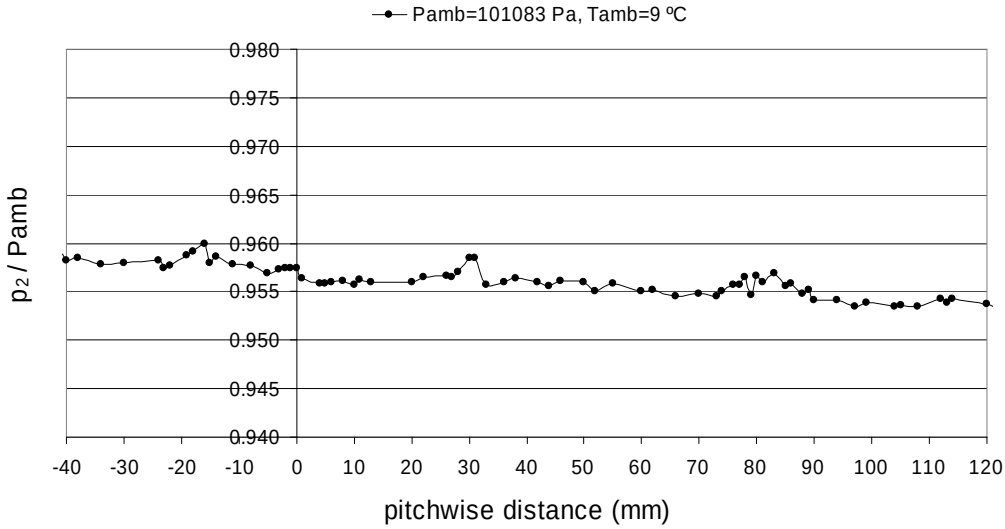

Figure 7–7: Normalised rear static pressure distribution at 60 mm traverse.

The pressure losses concerning all the three middle passages of the cascade test rig were investigated experimentally as well (see figure 7-8).

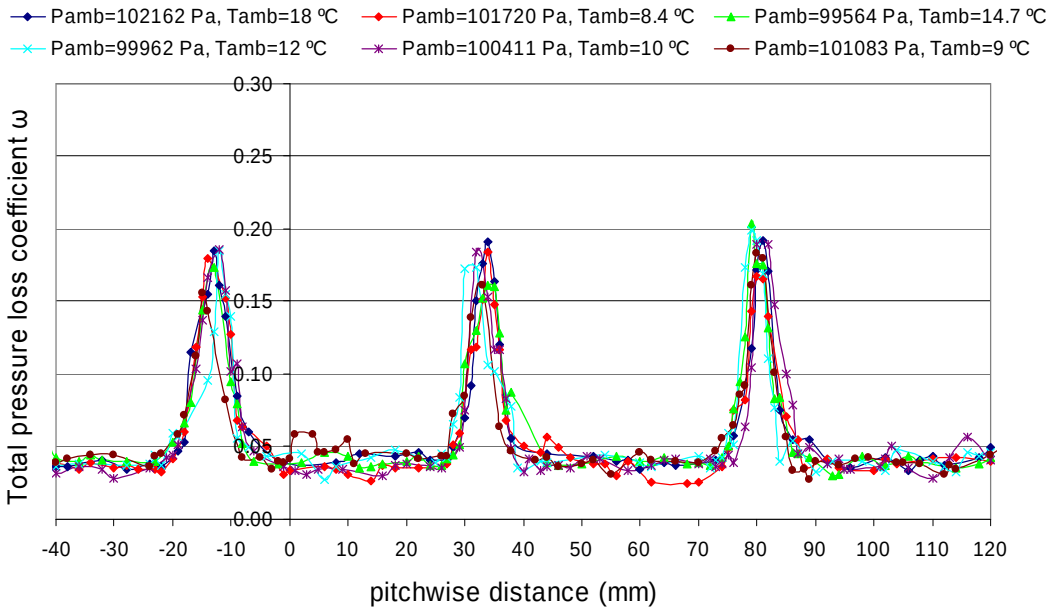

Figure 7–8: Loss distribution at 60 mm traverse (at pseudo constant Mach number, M_1=0.3).

Figure 7-9 illustrates a statistical average of pressure loss coefficient values calculated at different ambient conditions. The wake loss coefficient of the middle blade gets a maximum value of 0.16 and the left and right blade loss coefficients reach a value of 0.18. The loss coefficient corresponding to the three passages investigated is almost constant at a value of 0.04.

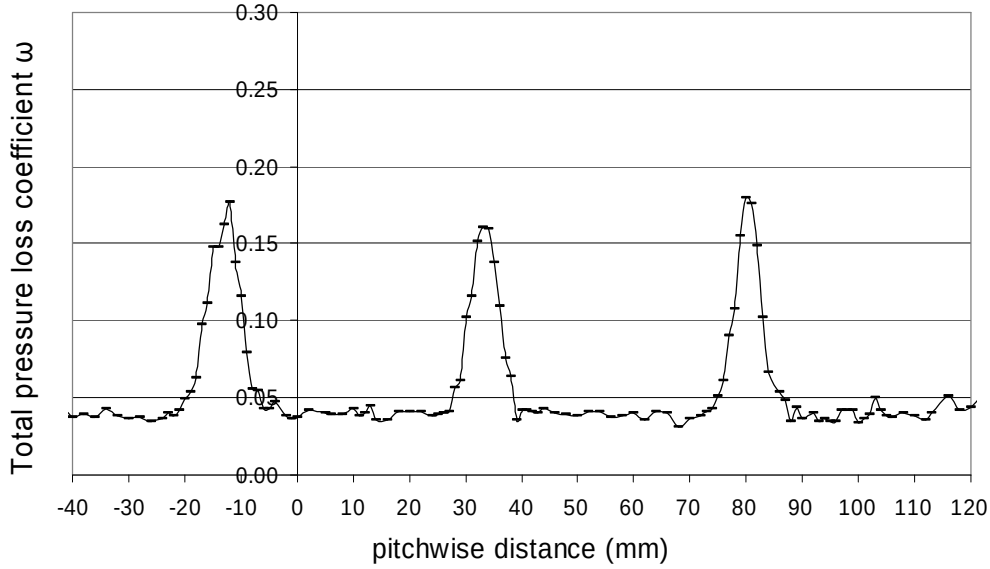

Figure 7–9: Statistical average loss distribution at 60 mm traverse.

It is important to note that all the cascade experiments have been undertaken at a nominal inlet Mach number of 0.3. In fact the range of Mach number varies from Mach 0.297 to Mach 0.31. Typical variation of losses with Mach number over a range of incidences is shown in figure 7-10.

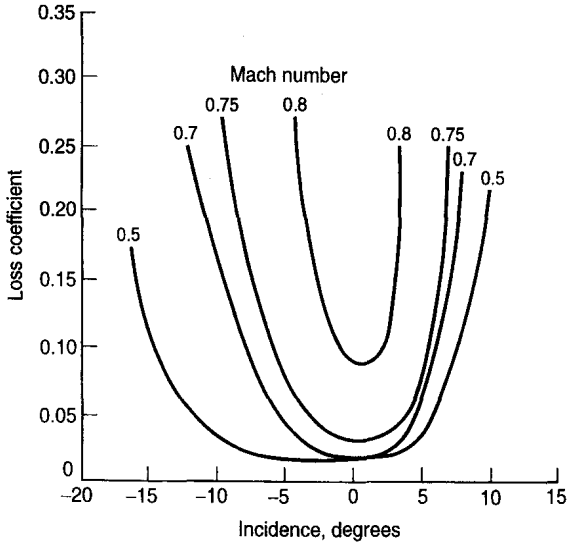

Figure 7–10: Effect of Mach number on losses (Saravanamuttoo, 2001).

The above data and many similar examples, (NASA SP36) show that for Mach number less than 0.5, looses are independent of Mach number.
Therefore, for the test cases considered here, experimental examination of losses at Mach numbers less than 0.3 has not been undertaken. The fan capacity did not allow experimentation at Mach number 0.5.
The exit flow angle α_2 distribution one chord distance behind the blade trailing edges was investigated as well for different ambient conditions (see figure 7-11). The results show that the exit flow angle distribution is not affected much of the parameter ambient condition.

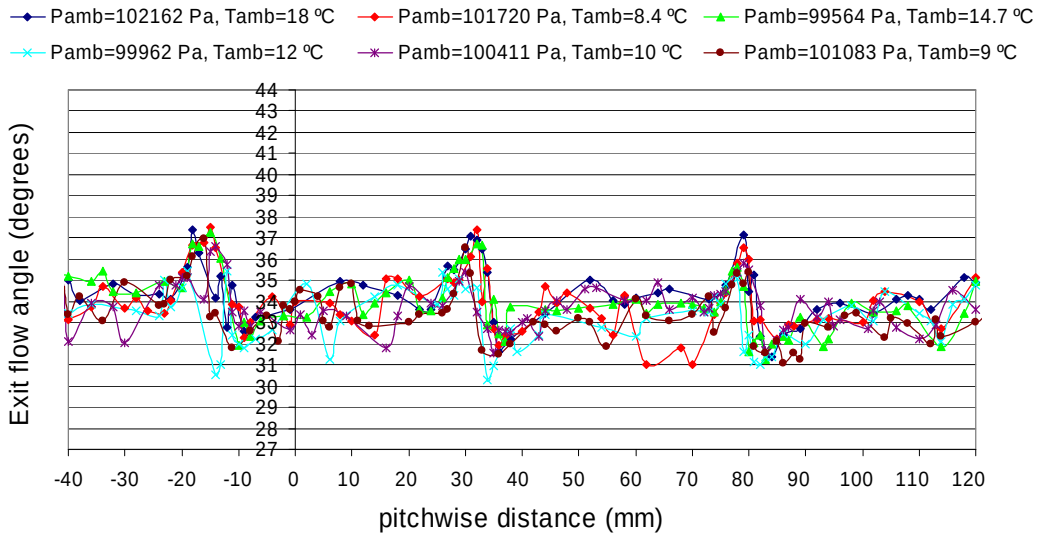

Figure 7–11: Exit flow angle distribution at 60 mm traverse.

A statistical representation of the exit flow angle distribution is illustrated in figure 7-12. It can be seen that the middle blade wake exit flow angle is 36 degrees whilst in the passage the exit flow falls to 34 degrees. In addition, there is a small (one degree)

decrease in the maximum value of the wake exit flow angle, alpha 2, from one side of the cascade to the other. This is within the limits of experimental error.
It should also be noted that the static pressure downstream of the cascade varies slightly along the pitch line. This is due to the fact that the settling chamber is too small to allow the cascade to discharge to uniform static pressure. When employing suction driven cascade experimentation, exit conditions in terms of static pressure are always greatly influenced by the near and far downstream discharge conditions. In cases like those reported here, uniform exit static pressure could only be achieved with an infinite (or very large) cascade exit volume.

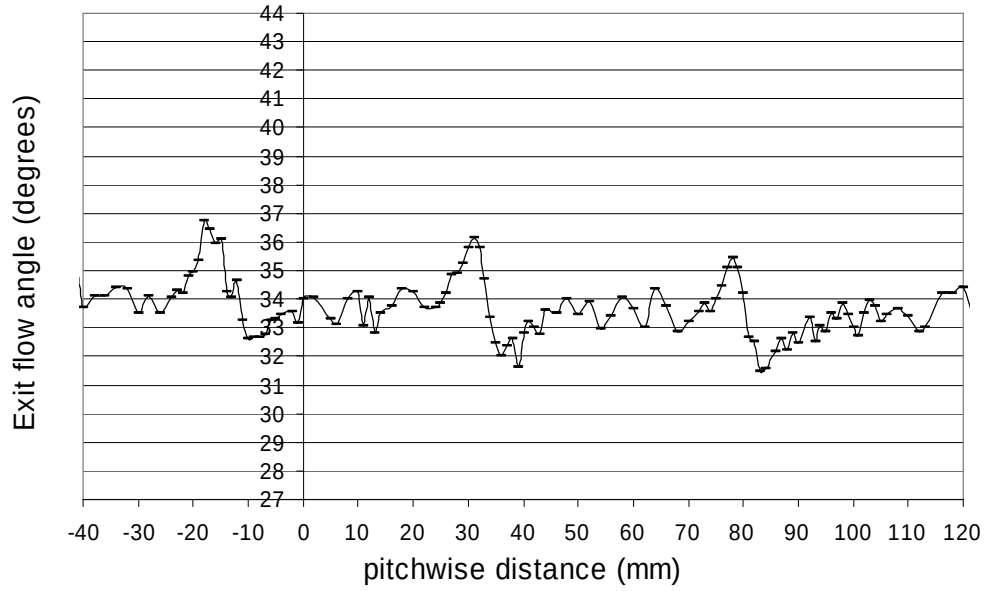

Figure 7–12: Statistical average exit flow angle distribution at 60 mm traverse.

7.2 Experimental results –Roughened blades

Roughness was applied uniformly on the blades and investigated experimentally. The particles used were carborundum particles of 63, 76, 102 and 254 microns average size (see figure 7-13) stuck with very thin double sided sticky tape on the blade. In sampling lengths of 4 mm, the roughness parameter Ra on different positions of the blade surfaces along the blade span and chord was measured using the Sutronic 25 roughness measuring devise (see Appendix tables 11, 12, 13 and 14).

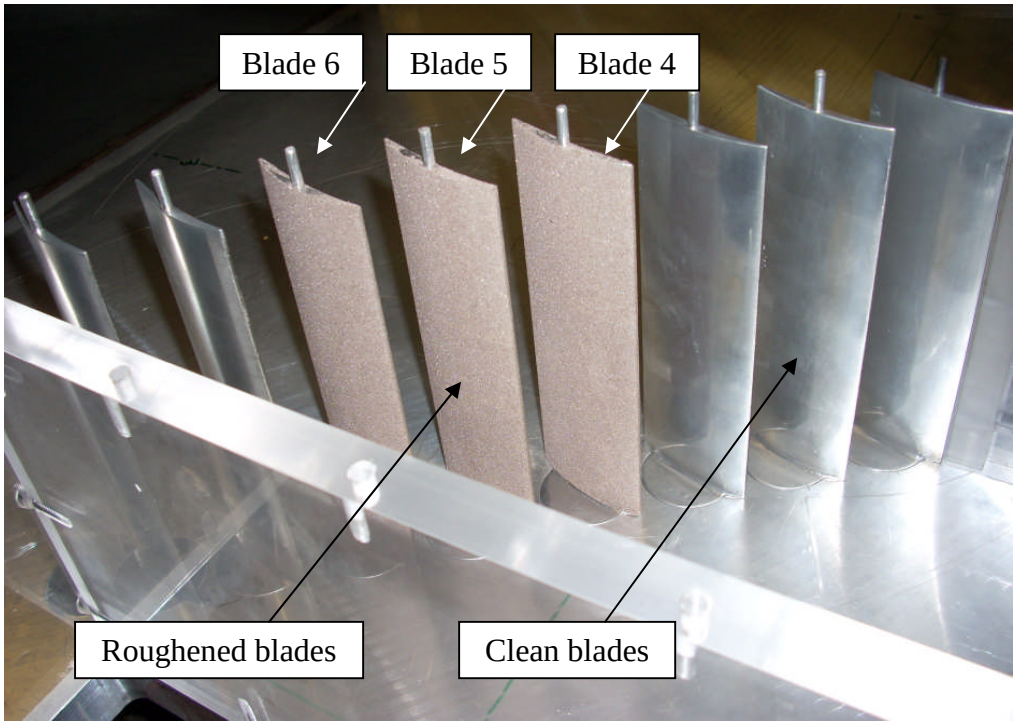

Figure 7–13: Roughened blades illustration.

For every fouling level two cascade rig runnings took place every time at different days with different ambient conditions and not big changes were recorded in terms of velocity and pressure losses. This can be seen from figures 7-14 up to 7-21.
It can be seen that for the heavily fouled blade cases of 102 microns and 254 microns the scatters of velocity and pressure loss match better. In the absence of further results, it is assumed that the higher the fouling level on the blades the lower is the scatter. The exit flow angle results seem to compare quite well for the case of 254 microns (see figure 7-22).

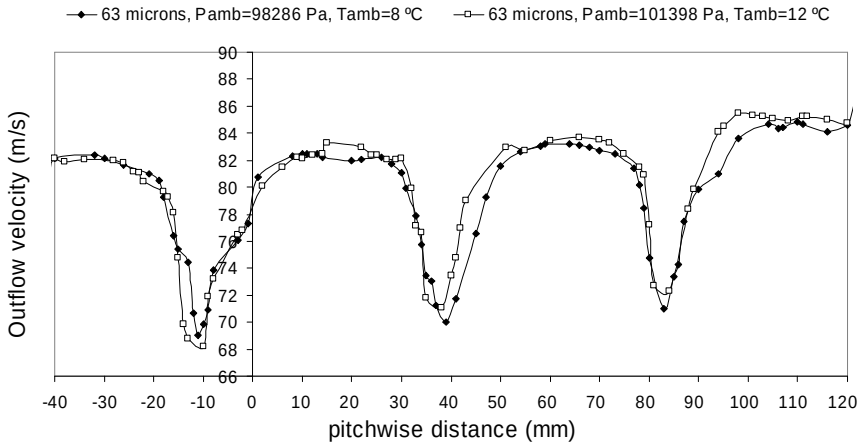

Figure 7–14: 63 microns velocity distribution at 60 mm traverse.

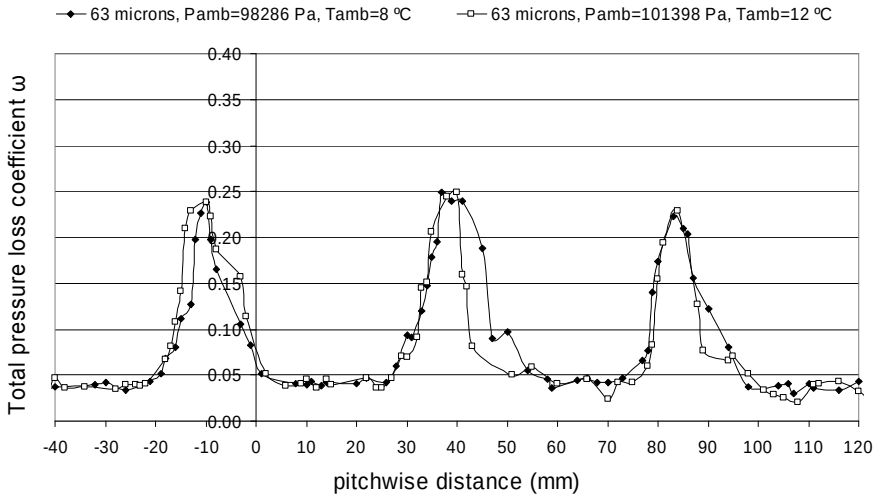

Figure 7–15: 63 microns loss distribution at 60 mm traverse.

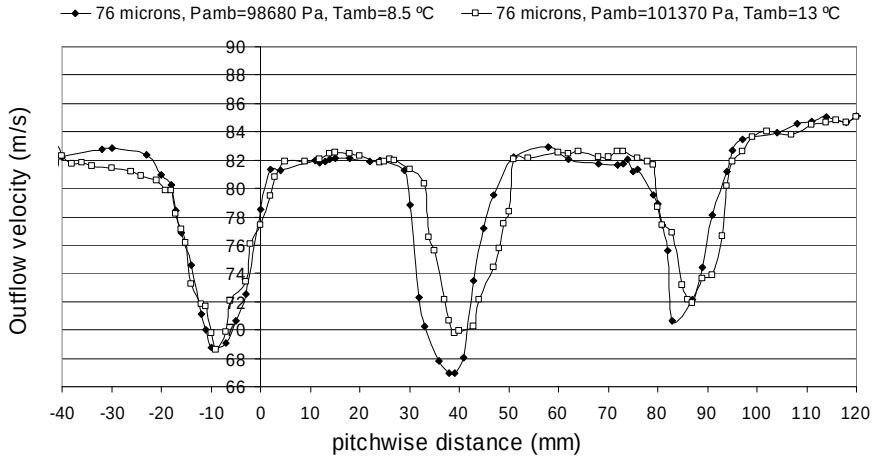

Figure 7–16: 76 microns velocity distribution at 60 mm traverse.

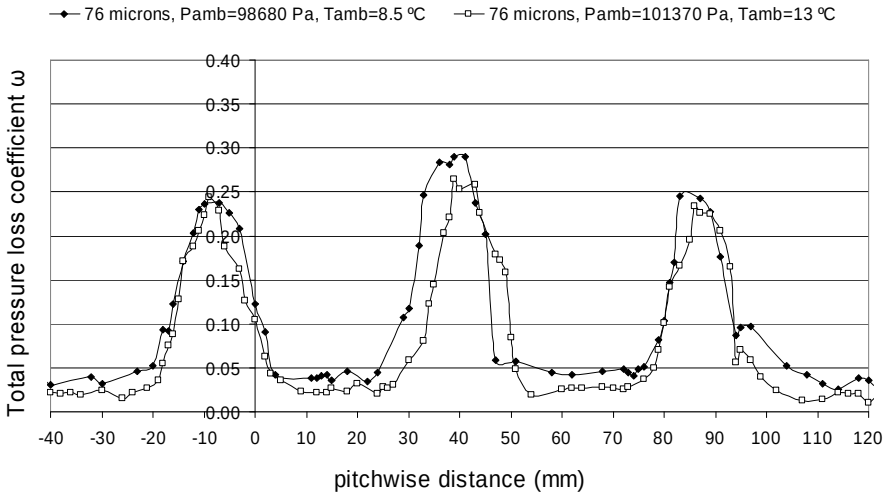

Figure 7–17: 76 microns loss distribution at 60 mm traverse.

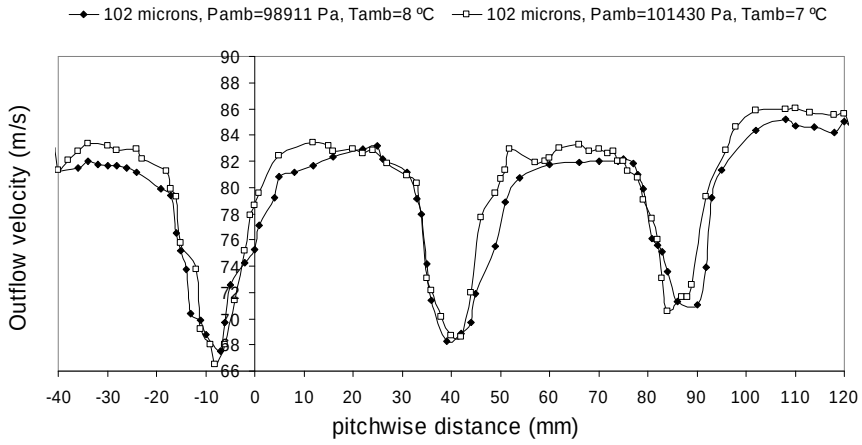

Figure 7–18: 102 microns velocity distribution at 60 mm traverse.

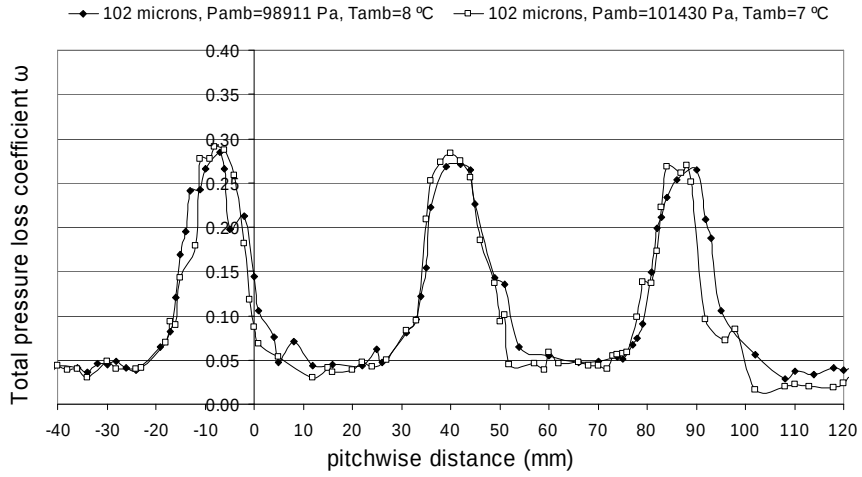

Figure 7–19: 102 microns loss distribution at 60 mm traverse.

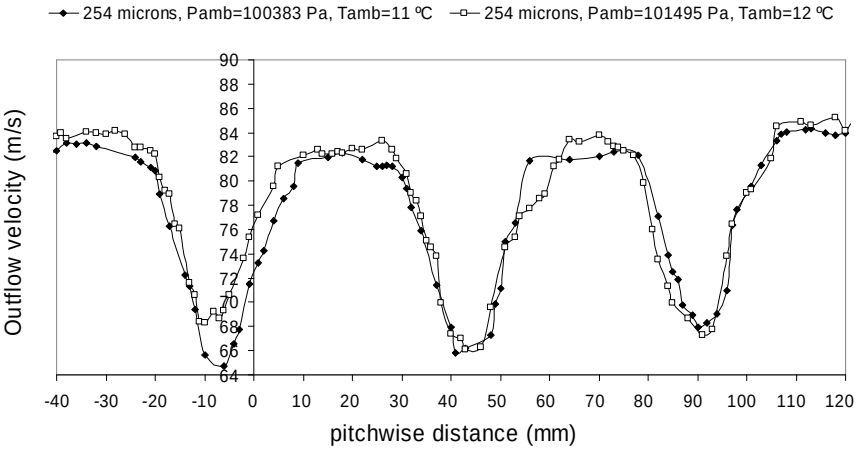

Figure 7–20: 254 microns velocity distribution at 60 mm traverse.

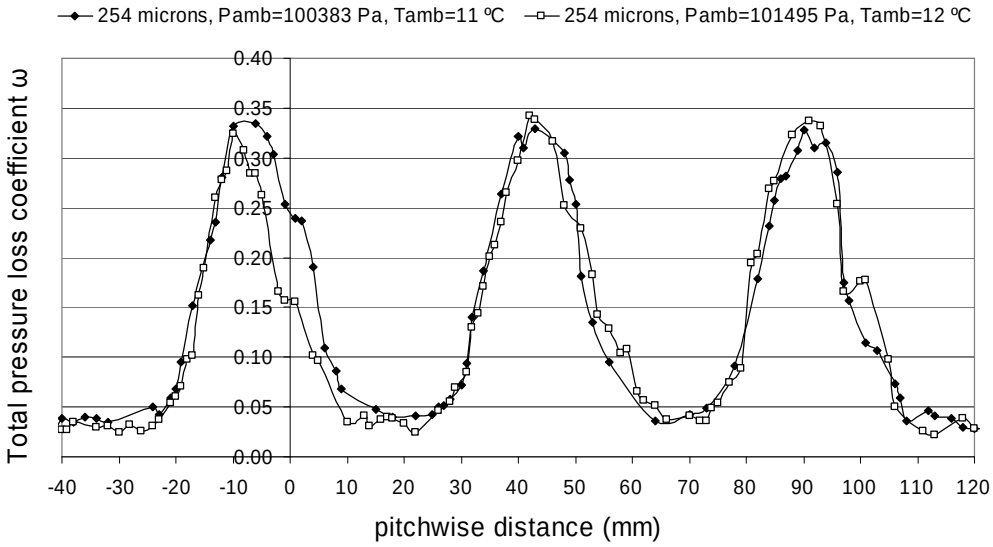

Figure 7–21: 254 microns loss distribution at 60 mm traverse.

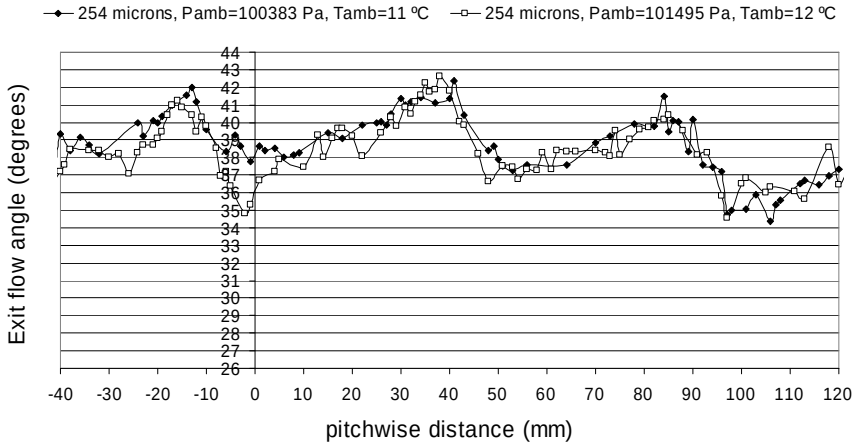

Figure 7–22: 254 microns exit flow angle distribution at 60 mm traverse.

Comparisons between roughened blades with various levels of roughness and clean blades took place as well and the ambient conditions under which these fouling cases were run are referred in the following table.

Table 4: Roughness cases ambient conditions

	Pamb (Pa)	Tamb (^{o}C)
0 microns	101083	9
63 microns	101398	12
76 microns	101370	13
102 microns	101430	7
254 microns	101495	12

The effect of fouling on the velocity distribution spanwise one chord distance towards the cascade streamtube behind the blades was investigated. From figure 7-23, it can be seen that the middle passage velocity remains almost constant at 83 m/s. However, as the fouling level increases the wake velocity undergoes significant changes. Increasing the particle size from 0 microns for clean blades to 63, 76, 102 and 254 microns the wake velocity drops from 74 to 71, 70, 68.5 and 66 m/s respectively. These values correspond to percentage falls of 10.8, 14.5, 15.7, 17.5 and 20.5 %. This shows that the percentage drop in the wake velocity has been almost increased by half passing from a level of 0 microns (smooth clean blades) to 76 microns and almost doubled passing from a level of 0 microns to a level of 254 microns. This indicates that the wake velocity behind the roughened blades drops continuously but not linearly.

Also, the wake widens as the fouling level increases. For clean blades the wake is 10 mm thick. However, for fouling levels of 63, 76 and 102 microns the wake thickness seems to be kept almost constant at 24 mm. Fouling the blades with particles of 254 microns the wake increases dramatically to 39 mm.

From figure 7-23, it can also be seen that all the wakes are moving towards the right with respect to the 0 microns wake by increasing the fouling level. This happens due to the higher boundary layer growth of the upper surface of the blades compared to the lower surface boundary layer. The effect of the pitchwise static pressure increment towards the right side of the cascade (see figure 7-24) behind the blades is assumed not to be so important causing this wake shift towards the right side of the cascade since the flow Mach number there is very low below 0.3 and for such cases probable incidence changes do not cause significant change on the blade drag coefficient which is related to the thickness of the boundary layer which affects the blade wake. Also, the big wakes towards the right for the severely fouled blades with 254 microns particles can be attributed to upper blade surface boundary layer separation.

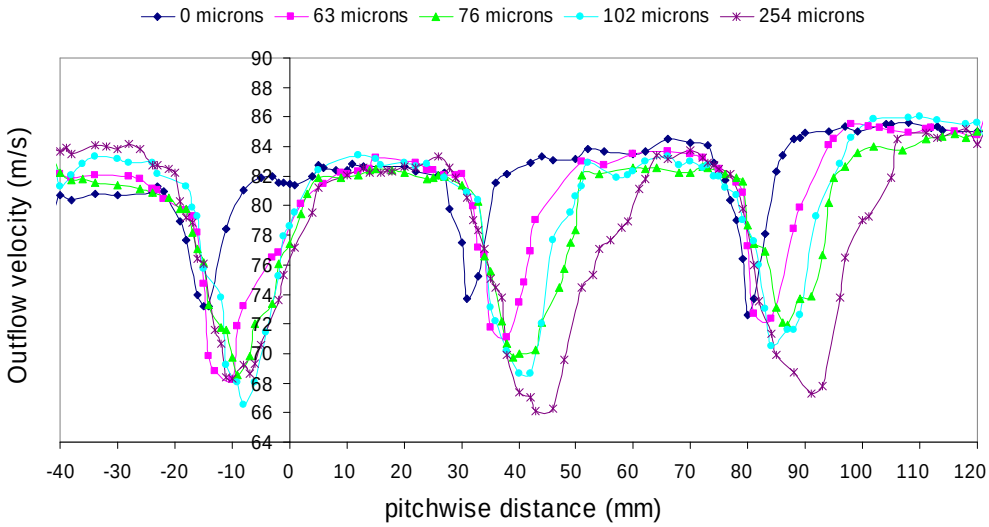

Figure 7–23: Roughness cases velocity distribution at 60 mm traverse.

By applying fouling on the blades it was found that the existing static pressure gradient towards the right side of the cascade vanishes (see figure 7-24).

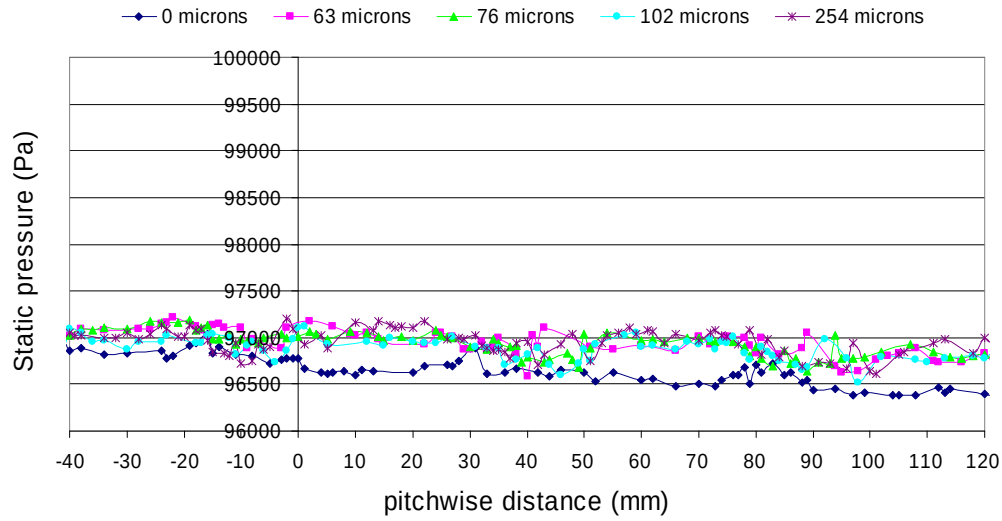

Figure 7–24: Roughness cases rear pressure distribution at 60 mm traverse.

The pressure losses concerning the all three middle passages behind the blades were investigated and figure 7-25 illustrates the pressure loss distribution one chord distance behind the blades towards the cascade exit streamtube. Taking into account the middle passage, as fouling level applied on the blade surface increases from 0 microns (smooth blades) to 63, 76, 102 and 254 microns the total pressure loss coefficient increases from 0.16 to 0.25, 0.27, 0.285 and 0.35 respectively. The passage loss varies smoothly around the value of 0.04 and it seems that the fouling does not affect this area significantly.

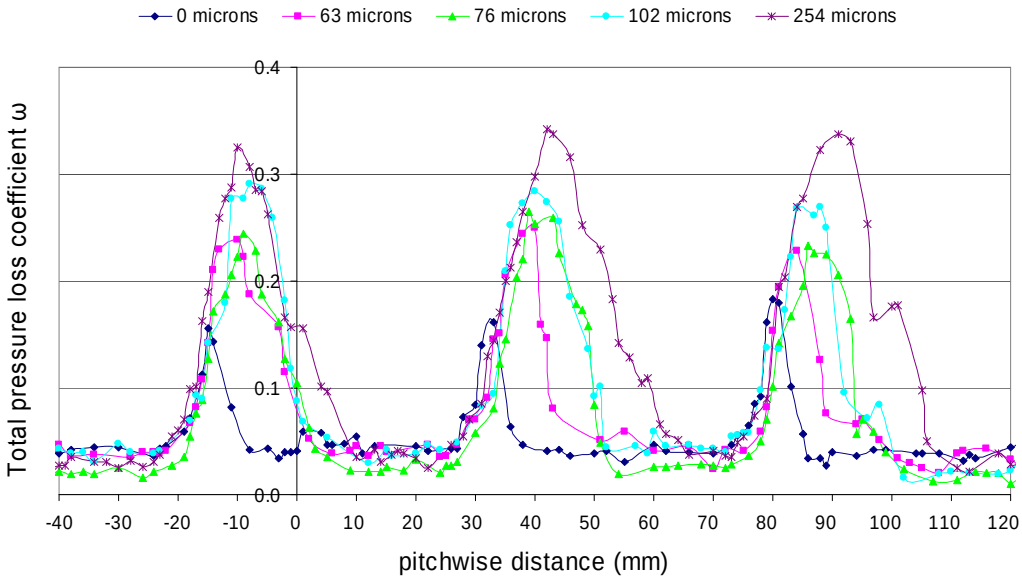

Figure 7–25: Roughness cases loss distribution at 60 mm traverse.

The total pressure losses associated to each passage separately are illustrated in table 5.

Table 5: Passage losses associated to the fouling cases.

	Δpo (Pa)	$[(\Delta po_{rough}-\Delta po_{clean})/\Delta po_{clean}]\%$
0 microns	150	0.0
63 microns	177	18.2
76 microns	188	25.3
102 microns	209	39.5
254 microns	241	61.0

During the experiments it was recorded that as the fouling level increases from 0 to 76 microns the middle passage exit flow angle corresponding to the nulling point in the passage between blade 4 and 5 increases from 34 degrees to 37 degrees. Increasing the fouling level further to 102 and 254 microns the passage exit flow angle at the same point gets values of 38 and 39.5 degrees (see figure 7-26). Hence, the passage exit flow angle seems to decrease in a lower proportion as the roughness increases more than 102 microns. Up to the 102 microns the increase in exit flow angle is 4 degrees and from 102 microns to 254 microns the increase is eliminated to 1.5 degrees only. This can be attributed to the increase of the passage blockage which progressively reduces the deviation and therefore the exit flow angle.

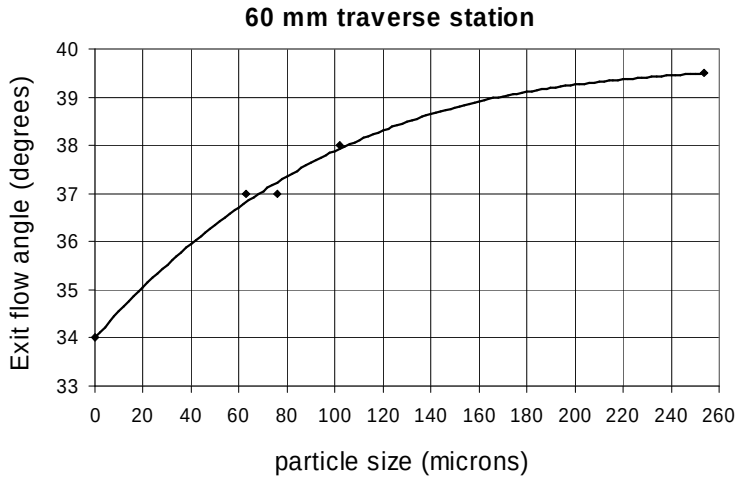

Figure 7–26: Blade 4-5 passage exit flow angle versus particle size.

Checking figure 7-27, it can be seen that the middle passage wake exit flow angle gets values of 36.5, 39.5, 40.5, 40.7 and 42.7 as the particle size increases from 0 to 63, 76, 102 and 254 microns respectively.

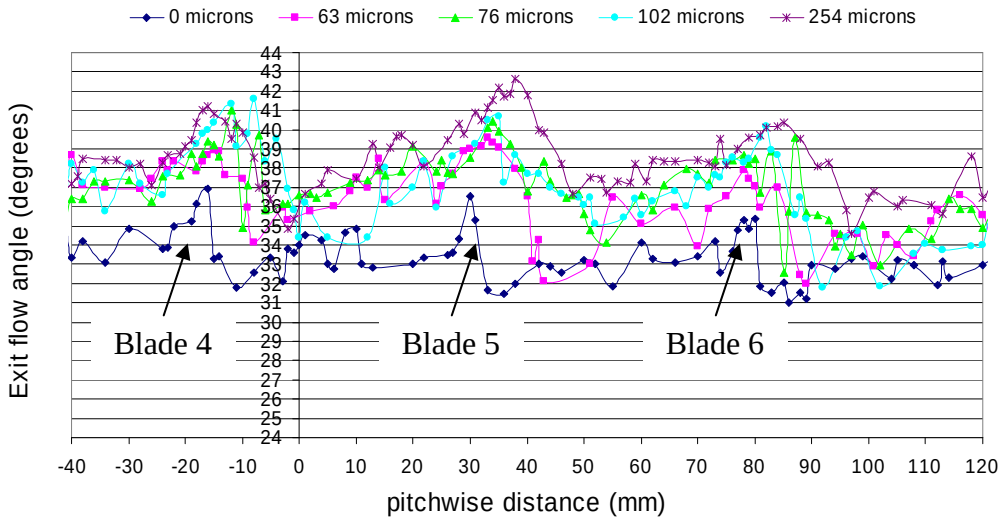

Figure 7–27: Roughness cases exit flow angle distribution at 60 mm traverse.

7.3 Comparison between CFD and experimental data

Three-dimensional CFD simulations based on the preliminary cascade simulations using the k-ε turbulence model of Fluent 6.3 took place again for the fouling cases of 0 microns and 102 microns corresponding to different boundary conditions of experimental results taken at different dates.

Comparing the experimental results taken at a particular date using smooth blades with the simulation results one chord distance downstream of the blades towards the cascade streamtube flow direction, it can be seen from figure 7-28 that the mildly compressible simulation underpredicts the middle passage velocity by 10 %, however the middle cascade blade minimum wake velocity is well predicted at 74 m/s. Also, the simulation predicts thicker wakes for all the passages. The incompressible simulation gives better results in terms of passage velocities but it predicts deeper wakes a bit displaced towards the lower surface side of the blades (left side of the pitchwise direction).

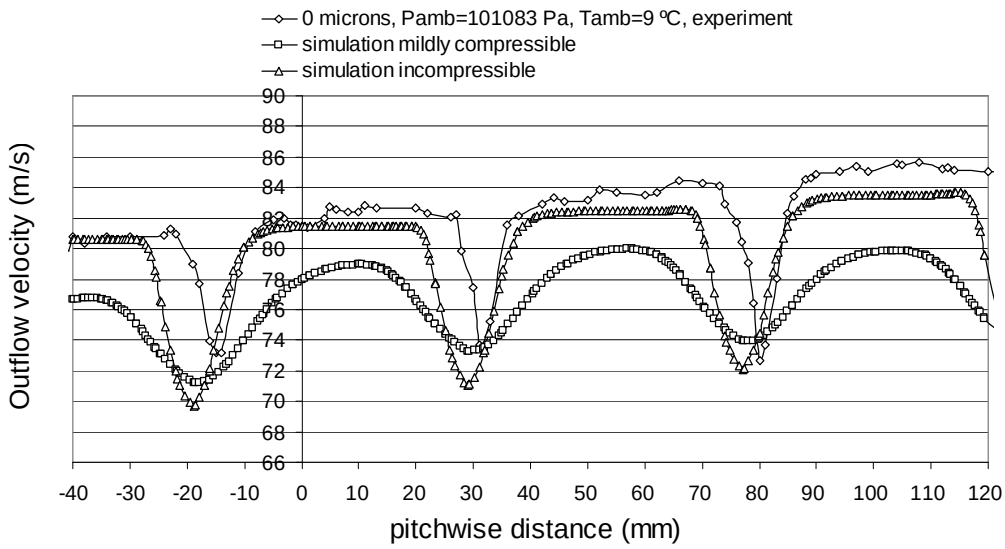

Figure 7–28: Smooth blades experimental and CFD velocity distributions at 60 mm traverse.

Contours of velocity for smooth blades at a cross-sectional midplane of the rig volume are illustrated in figure 7-29. The flow enters the cascade test section with a velocity close to 100 m/s corresponding to a Mach number of 0.3 and this is well predicted according to the velocities found experimentally in this region.

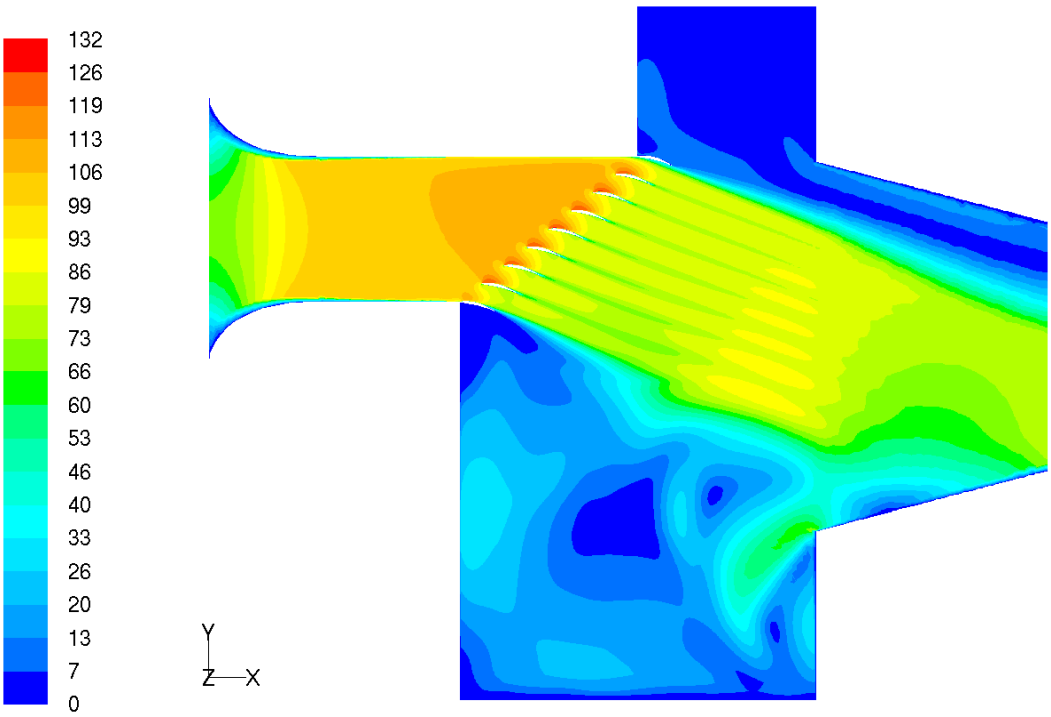

Figure 7–29: Incompressible flow velocity contours, k-ε model.

The Fluent model predicts a very small total pressure rise in the potential flow between the blade rows and this cannot be the case. Accordingly the passage total pressure loss coefficient level for the simulation in figure 7-30 has been adjusted to correspond to the relevant experimental level that is 0.04. According to Fluent the actual wake total pressure loss was underpredicted treating the flow as mildly

compressible. Running the flow incompressible the results in terms of the loss were better closer to the experimental ones (see figure 7-30).

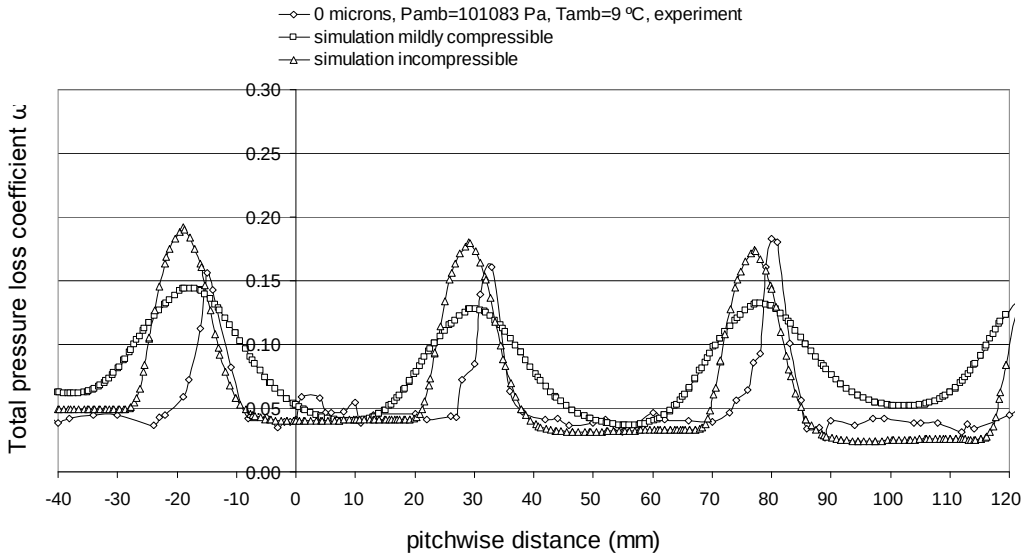

Figure 7–30: Smooth blades experimental and CFD loss distribution at 60 mm traverse.

The case of 102 microns fouling level is illustrated in figure 7-31, in terms of velocities behind the cascade middle blades. The middly compressible CFD simulation predicted a passage velocity of 81 m/s which is less by 2.5 % from the actual experimental value. The wake thickness was well predicted at almost 18 mm, but the predicted wakes are deeper and shifted towards the left of the cascade by 10 mm. Treating the flow as incompressible, the simulation gave better results by predicting the middle passage velocity at 83 m/s which is very close to the experimental value. The depth and the width of the wakes were well predicted compared to the experimental. However, both simulations predicted wakes shifted towards the left hence different flow deflection compared to the actual. This effect is thought to be associated with the fact that the Fluent code is less able to predict the flow field in the mildly compressible and incompressible flow regime. Other researchers have experienced Fluent predictions with similar outcome. Also, the code uses the exact particle diameter set without accounting for probable changes in the blade contour of the blades due to possible improper particle distribution increasing the roughness height more than the set one.

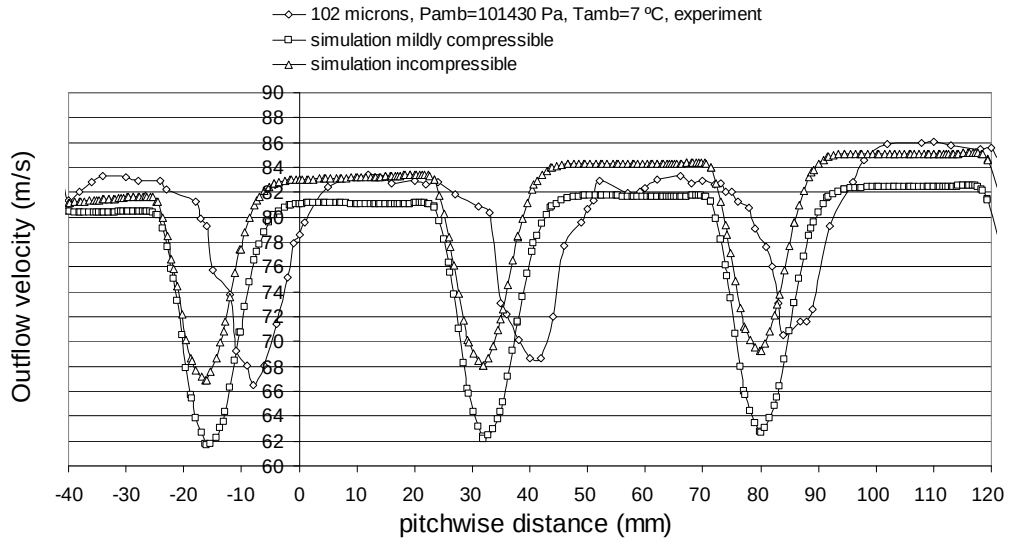

Figure 7–31: 102 microns experimental and CFD velocity distribution at 60 mm traverse.

Checking figure 7-32, it can be seen that for the 102 microns roughness level the wake and losses were well predicted.

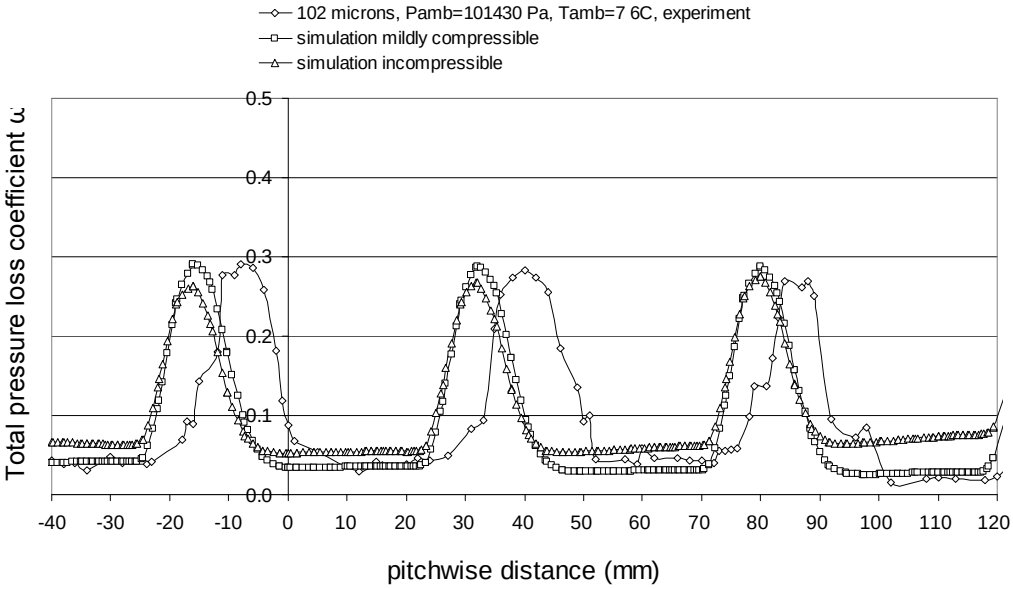

Figure 7–32: 102 microns experimental and CFD loss distribution at 60 mm traverse.

7.4 Experimental performance simulation results

Using Howell's correlation (1945), the cascade experimental results were correlated to a real stage. This time a real stage polytropic efficiency was calculated from the cascade results and using the following formula related to the pressure ratio the compressor overall efficiency was calculated.

$$\eta_c = \frac{(PR)^{\frac{\gamma-1}{\gamma}} - 1}{(PR)^{\frac{\gamma-1}{\gamma\eta_P}} - 1} \quad (182)$$

The total pressure loss coefficient per passage is illustrated in figure 7-33 with respect to the level of roughness applied on the cascade blades.

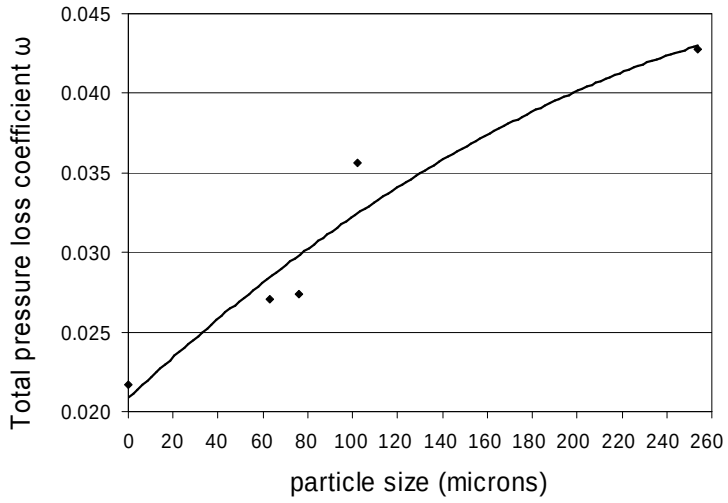

Figure 7–33: Total pressure loss coefficient per passage versus fouling particle size.

The compressor overall efficiency was calculated for smooth and fouled blades as well and the percentage deterioration in terms of polytropic and compressor overall efficiency was established. Figures 7-34 and 7-35 illustrate that for fouling levels of 63, 76, 102 and 254 microns examined experimentally, the percentage deterioration in polytropic efficiency gets values of 2.2, 2.9, 4.4 and 7.4 % and in compressor overall efficiency, assuming that the compressor is fouled uniformly all the way through, gets values of 3.2, 4.3, 6.6 and 11 % respectively.

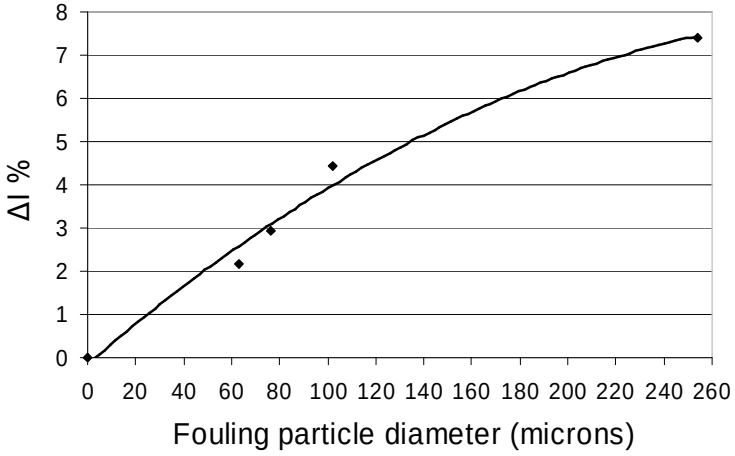

Figure 7–34: Experimental percentage deterioration in polytropic efficiency due to fouling.

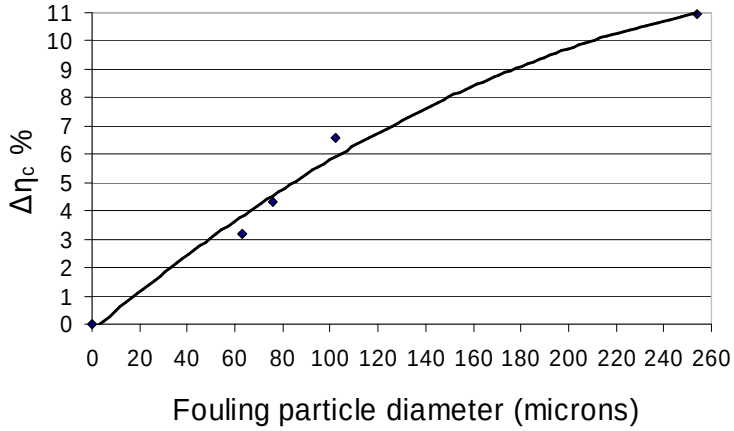

Figure 7–35: Percentage deterioration in calculated compressor efficiency due to fouling.

The following tables 6 and 7 illustrate all the necessary calculations taken place in order to correlate cascade data with real stage data for the cases of smooth clean and fouled blades.

Table 6: Smooth blades experimental results

Cascade experimental results	smooth blades					
α_1 (deg)	51	51	51	51	51	51
α_2 (deg)	34	34	34	34	34	34
$\varepsilon=\alpha_1-\alpha_2$	17	17	17	17	17	17
P_1 (Pa)	102157	101718	99573	99983	100420	101119
p_1 (Pa)	95657	95124	93244	93629	93936	94578
P_2 (Pa)	101677	101259	99133	99532	99979	100693
p_2 (Pa)	97775	97294	95292	95655	96153	96735
$\Delta po=P_1-P_2$ (Pa) per passage	160	153	147	150	147	142
$\Delta pstatic=p_2-p_1$ (Pa)	2117	2170	2048	2026	2217	2157
$M_1=[(2/(\gamma-1))((P_1/p_1)^{((\gamma-1)/\gamma)}-1)]^{0.5}$	0.308	0.311	0.308	0.308	0.310	0.311
T_1 (K)	291.15	281.55	287.9	285.2	283.15	282.15
$t_1=T_1/[1+((\gamma-1)/2)M_1^2]$ (K)	285.73	276.21	282.50	279.85	277.80	276.81
$\rho=p_1/Rt_1$	1.166	1.200	1.150	1.166	1.178	1.190
A (m^2)	0.043	0.043	0.043	0.043	0.043	0.043
$c_1=M_1(\gamma Rt_1)^{0.5}$	104.32	103.57	103.67	103.18	103.66	103.57
$m_{inlet\ experimental}=W_1$	4.909	5.060	4.870	4.899	4.875	4.986
$W_1T_1^{0.5}/P_1$	0.0008	0.0008	0.0008	0.0008	0.0008	0.0008
$\alpha_m=atan((tan\alpha_1+tan\alpha_2)/2)$	43.67	43.67	43.67	43.67	43.67	43.67
$C_L=2(s/l)cos\alpha_m(tan\alpha_1-tan\alpha_2)$	0.649	0.649	0.649	0.649	0.649	0.649
$C_{Dp}=(s/l)(\Delta po/0.5\rho c_1^2)(cos^3\alpha_m/cos^2\alpha_1)$	0.019	0.018	0.018	0.019	0.018	0.017
$C_{Da}=0.02(s/l)(l/H)$	0.0053	0.0053	0.0053	0.0053	0.0053	0.0053
$C_{Ds}=0.018C_L^2$	0.0076	0.0076	0.0076	0.0076	0.0076	0.0076
$C_D=C_{Dp}+C_{Da}+C_{Ds}$	0.032	0.031	0.031	0.031	0.031	0.030
$\eta_s=1-(2/sin2\alpha_m)(C_D/C_L)=\eta_p$	0.901	0.904	0.904	0.903	0.905	0.908
$\Phi=c_x/U=1/(tan\alpha_1+tan\alpha_2)$	0.524	0.524	0.524	0.524	0.524	0.524
λ	0.84	0.84	0.84	0.84	0.84	0.84
$\psi=\Delta H/U^2=\lambda\Phi(tan\alpha_1-tan\alpha_2)$	0.247	0.247	0.247	0.247	0.247	0.247
$c_p\Delta T_s/0.5U^2=2\lambda(c_x/U)(tan\alpha_1-tan\alpha_2)$	0.493	0.493	0.493	0.493	0.493	0.493
$\Delta P_s/0.5\rho U^2=\eta_s c_p\Delta T_s/0.5U^2$	0.444	0.446	0.446	0.445	0.446	0.448
Average η_p	0.904					
Δl%	0.000					
$\eta_{pcleanABBGT13E2}=[(\gamma-1)/\gamma][log(P_2/P_1)]_{DP}/[log(T_2/T_1)]_{DP}$	0.919					
$\eta_{pfouledABBGT13E2}=\eta_{pcleanABBGT13E2}-\Delta l$						
R	14.6					
Average η_c	0.864					
$\Delta\eta_c=\eta_{c\ clean}-\eta_{c\ fouled}$						
$\Delta\eta_c$%	0.000					
$\eta_{c\ cleanABBGT13E2}$	0.885					
Reynolds number	$3.8*10^5$					

Table 7: Roughened blades experimental results.

Cascade experimental results	63 μm	63 μm	76 μm	76 μm	102 μm	102 μm	254 μm	254 μm
α_1 (deg)	51	51	51	51	51	51	51	51
α_2 (deg)	36.5	37	37	37	38	38	39.5	39.5
$\varepsilon=\alpha_1-\alpha_2$	14.5	14	14	14	13	13	11.5	11.5
P_1 (Pa)	98301	101408	98698	101265	98936	101458	100374	101484
p_1 (Pa)	92145	95144	92578	95192	92861	95330	94419	95462
P_2 (Pa)	97747	100900	98071	100766	98286	100854	99610	100801
p_2 (Pa)	94008	97009	94362	96984	94570	96937	95930	96976
$\Delta po=P_1-P_2$ (Pa) per passage	185	169	209	166	217	201	255	228
$\Delta pstatic=p_2-p_1$ (Pa)	1863	1865	1784	1791	1710	1607	1511	1515
$M_1=[(2/(\gamma-1))((P_1/p_1)^{((\gamma-1)/\gamma)}-1)]^{0.5}$	0.305	0.303	0.304	0.299	0.302	0.300	0.297	0.297
T_1 (K)	281.15	285.15	281.65	286.15	281.15	280.15	284.15	285.15
$t_1=T_1/[1+((\gamma-1)/2)M_1^2]$ (K)	276.00	280.00	276.55	281.14	276.11	275.21	279.23	280.21
$\rho=p_1/Rt_1$	1.163	1.184	1.166	1.180	1.172	1.207	1.178	1.187
A (m^2)	0.043	0.043	0.043	0.043	0.043	0.043	0.043	0.043
$c_1=M_1(\gamma Rt_1)^{0.5}$	101.69	101.70	101.26	100.34	100.67	99.65	99.44	99.63
$m_{inlet\ experimental}=W_1$	4.860	4.927	4.856	4.521	4.906	4.608	4.901	4.938
$W_1T_1^{0.5}/P_1$	0.0008	0.0008	0.0008	0.0008	0.0008	0.0008	0.0008	0.0008
$\alpha_m=atan((tan\alpha_1+tan\alpha_2)/2)$	44.64	44.83	44.83	44.83	45.23	45.23	45.84	45.84
$C_L=2(s/l)cos\alpha_m(tan\alpha_1-tan\alpha_2)$	0.563	0.546	0.546	0.546	0.511	0.511	0.458	0.458
$C_{Dp}=(s/l)(\Delta po/0.5\rho c_1^2)(cos^3\alpha_m/cos^2\alpha_1)$	0.022	0.020	0.025	0.020	0.026	0.024	0.030	0.026
$C_{Da}=0.02(s/l)(l/H)$	0.0053	0.0053	0.0053	0.0053	0.0053	0.0053	0.0053	0.0053
$C_{Ds}=0.018C_L^2$	0.0057	0.0054	0.0054	0.0054	0.0047	0.0047	0.0038	0.0038
$C_D=C_{Dp}+C_{Da}+C_{Ds}$	0.033	0.031	0.036	0.031	0.036	0.034	0.039	0.035
$\eta_s=1-(2/sin2\alpha_m)(C_D/C_L)=\eta_p$	0.881	0.888	0.869	0.887	0.860	0.868	0.830	0.845
$\Phi=c_x/U=1/(tan\alpha_1+tan\alpha_2)$	0.506	0.503	0.503	0.503	0.496	0.496	0.486	0.486
λ	0.84	0.84	0.84	0.84	0.84	0.84	0.84	0.84
$\psi=\Delta H/U^2=\lambda\Phi(tan\alpha_1-tan\alpha_2)$	0.211	0.203	0.203	0.203	0.189	0.189	0.167	0.167
$c_p\Delta T_s/0.5U^2=2\lambda(c_x/U)(tan\alpha_1-tan\alpha_2)$	0.421	0.407	0.407	0.407	0.378	0.378	0.335	0.335
$\Delta P_s/0.5\rho U^2=\eta_s c_p\Delta T_s/0.5U^2$	0.371	0.361	0.353	0.361	0.325	0.328	0.278	0.283
Average η_p	0.885		0.878		0.864		0.837	
$\Delta l=\eta_{pclean}-\eta_{pfouled}$	0.020		0.026		0.040		0.067	
Δl%	2.162		2.918		4.445		7.408	
$\eta_{pfouledABBGT13E2}=\eta_{pcleanABBGT13E2}-\Delta l$	0.899		0.893		0.879		0.852	
Average η_c	0.836		0.826		0.807		0.769	
$\Delta\eta_c=\eta_{c\ clean}-\eta_{c\ fouled}$	0.028		0.037		0.057		0.094	
$\Delta\eta_c$%	3.202		4.319		6.572		10.932	
$\eta_{c\ fouledABBGT13E2}=\eta_{c\ cleanABBGT13E2}-\Delta\eta_c$	0.857		0.848		0.828		0.791	

The percentage deteriorations in overall compressor efficiency for the various fouling cases examined experimentally were incorporated in the performance simulation tool Turbomatch file of an ABB GT13 E2 industrial gas turbine by scaling appropriately the compressor map of the engine under consideration of these percentage changes.
Performance simulation runs were done in terms of increasing the TET combined with the effect of fouling. The thermal efficiency of the engine was examined first. The thermal efficiency η_{th} increases as the turbine entry temperature increases and this can be attributed to the parallel increase of the compressor pressure ratio by increasing the TET (see figure 7-36).

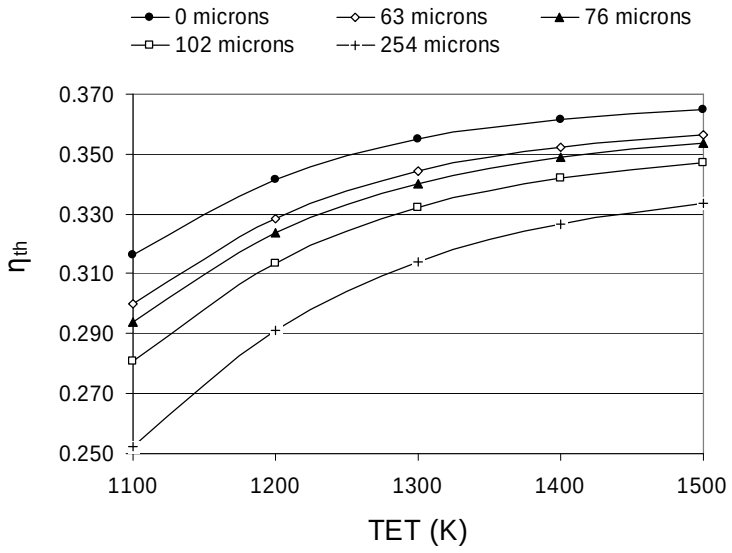

Figure 7–36: Thermal efficiency versus TET (experimentally correlated results).

Keeping the TET constant, as the fouling level (particle size) on the blades increases, the pressure ratio of the compressor drops and the thermal efficiency decreases as well since it's a function of pressure ratio (see formula 180). Considering the case of smooth blades as the TET increases from 1100 K to 1500 K, the thermal efficiency increases by 15.5 %. However, for the worst fouling case of 254 microns the same increase in TET corresponds to an increase in thermal efficiency of 32 %. This indicates that the higher the fouling level on the blades is then the higher the gain in thermal efficiency for the same range of TET increase. The higher gain in thermal efficiency as the fouling level increases in the same range of TET increase, it was attributed to the fact that the gas turbine is less sensitive to component inefficiency as the TET increases and the useful power continuously increases as a result of the diverging constant pressure lines in the Temperature-entropy diagram (see figures 6-23 and 6-24).
From the Turbomatch results obtained it was shown that as the fouling level increases the useful power of the gas turbine decreases but increasing the TET this drawback could be handled (see figure 7-37). Taking into account the case of 0 microns (smooth blades), incorporating a fouling level of 254 microns on the blades at the same TET of 1100 K the useful power drops by 27 % and only by 13 % for the level of 1500 K. In order the engine to recover the original useful power at 0 microns after suffering from fouling level of 254 microns at the TET of 1100 K, it has to increase it's TET by almost 100 K. For the case of 102 microns passing to 254 microns, the TET should

increase by half hence 50 K in order to recover the original useful clean engine output.
Also, for constant values of fouling level the useful power was increased linearly with respect to the TET increase. The decrease in useful power as the fouling level (particle size) on the blades increases is caused due to reduction of the engine mass flow capacity (see figure 7-38).

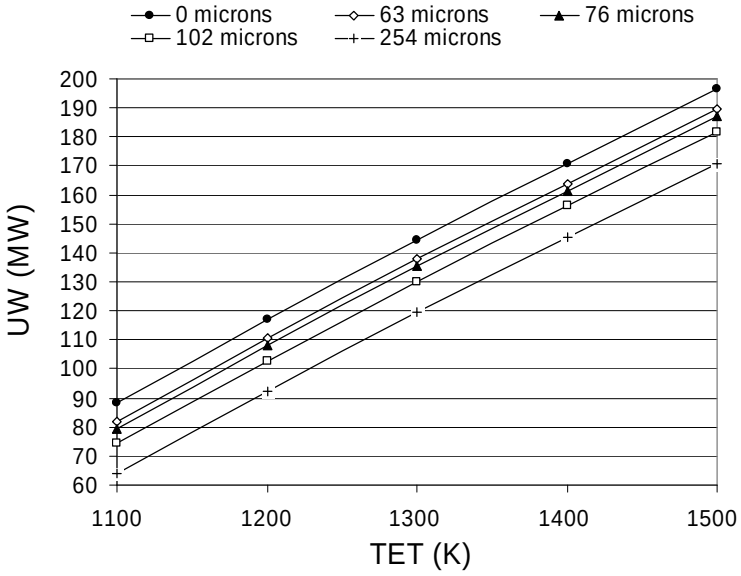

Figure 7–37: Useful power versus TET (experimentally correlated results).

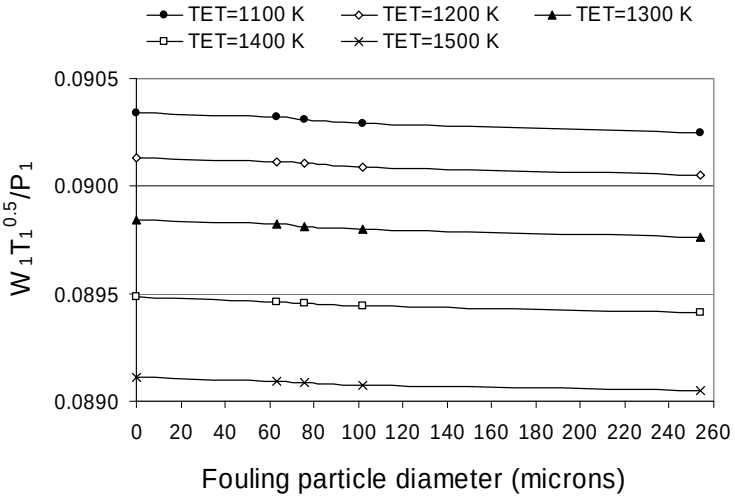

Figure 7–38: ABB GT13 E2 non-dimensional mass flow versus fouling particle size (experimental approach).

Checking the trend of thermal efficiency with respect to the useful power, it can be seen from figure 7-39 that both terms increase as the TET increases but the gain they achieve by increasing the TET in the same interval between 1100 K and 1500 K is higher as the roughness level increases. In this temperature range the gain in thermal

efficiency for 102 microns fouling is 51 % higher than this corresponding to 0 microns and the gain in useful power is 17 % higher as well.

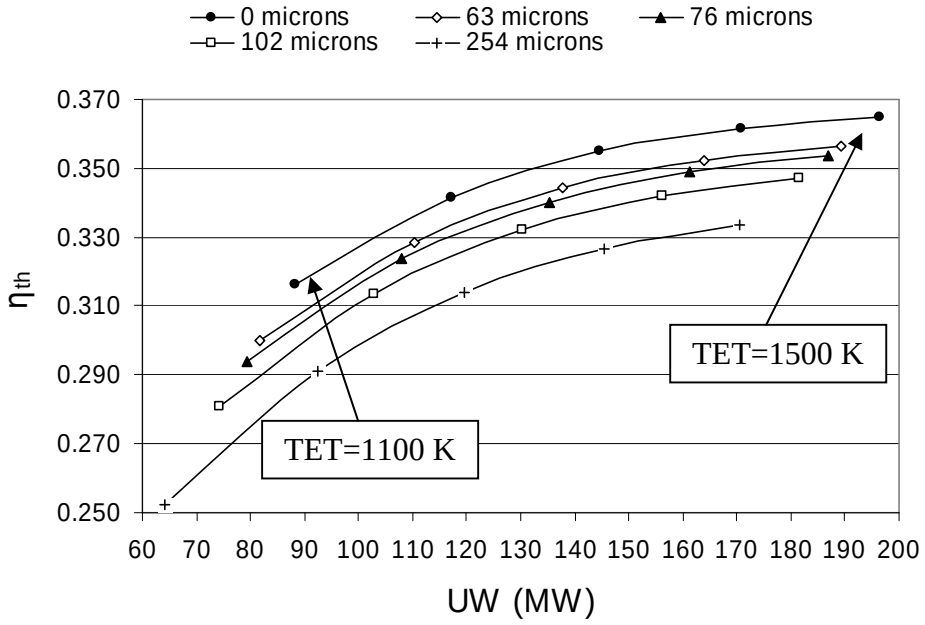

Figure 7–39: Thermal efficiency versus useful power (experimentally correlated results).

Using predicted data (see Appendix, Experimental related performance deterioration by applying 102 microns particles), from the Turbomatch code, figure 7-40 shows that increasing the TET from 1100 K to 1500 K the compressor efficiency η_c keeps falling by almost 1.2 % for all the fouling cases examined. Hence, figure 7-40 shows that for an engine whose design point is at a TET of 1378 K, the rate of reduction of compressor efficiency with roughness particle size increase is independent of TET. This leads to a single plot for the effect of roughness shown in figure 7-41 where the loss of efficiency is plotted as a percentage of the corresponding value at the design TET.

As the compressor efficiency drops the actual compressor work increases and therefore the useful engine power decreases since this is the difference between turbine and compressor power. In order the engine to retrieve this loss in useful power the turbine power must increase by increasing the turbine entry temperature.

Figure 7-40 also shows that compressor efficiency at the design TET reduces as roughness size increases. This is because the losses due to roughness are increasing and polytropic efficiency is, therefore, falling. This effect is shown graphically in figure 7-42.

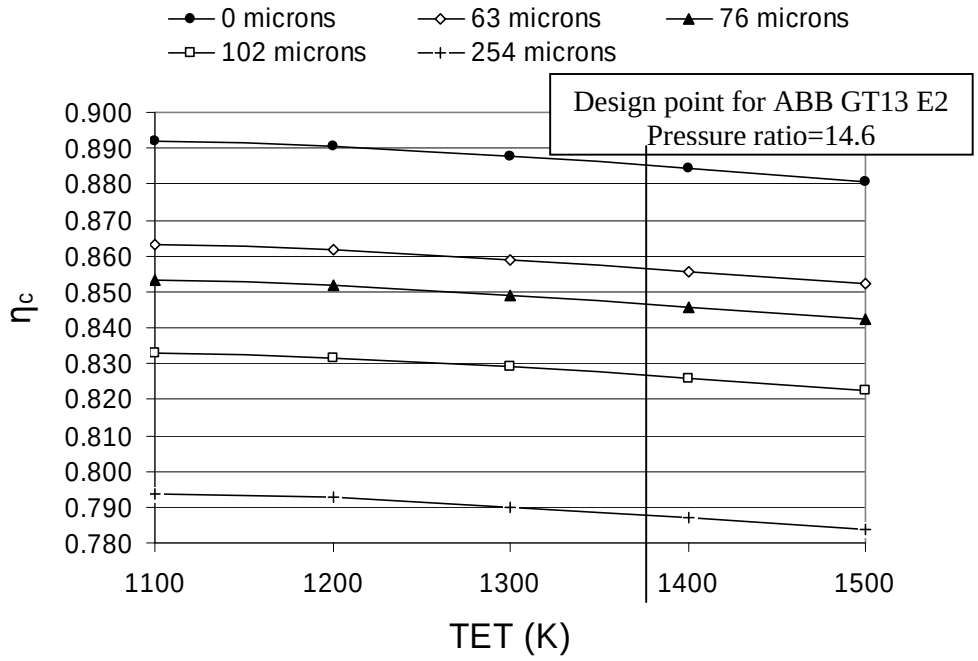

Figure 7–40: Compressor efficiency versus TET (experimentally correlated results).

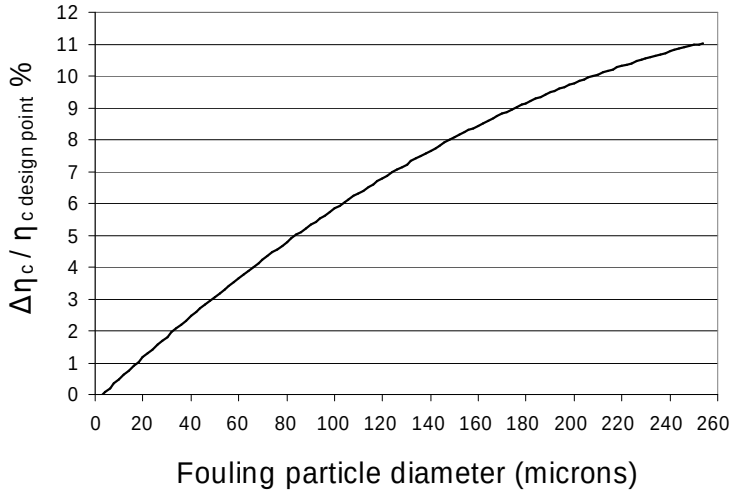

Figure 7–41: Percentage deterioration in compressor efficiency versus particle size increase (experimental approach).

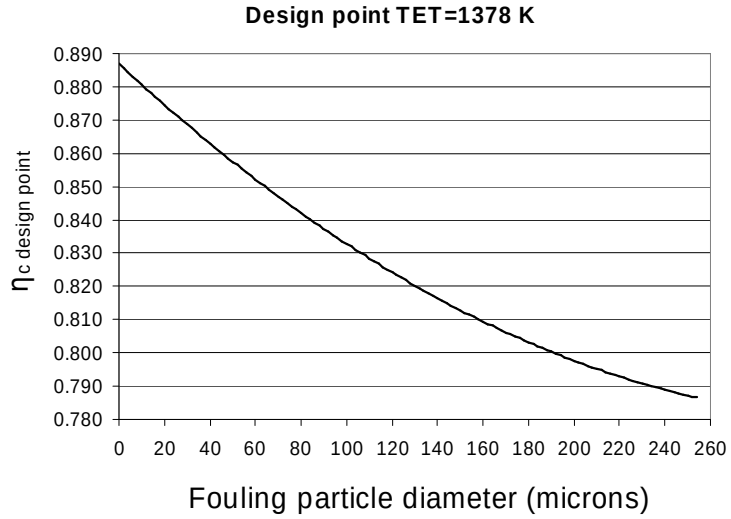

Figure 7–42: Design point compressor efficiency deterioration due to fouling (experimental approach).

The turbine isentropic efficiency η_t was almost unaffected from the increase in TET and from the increase of fouling particle size on the compressor blades (see figure 7-43).

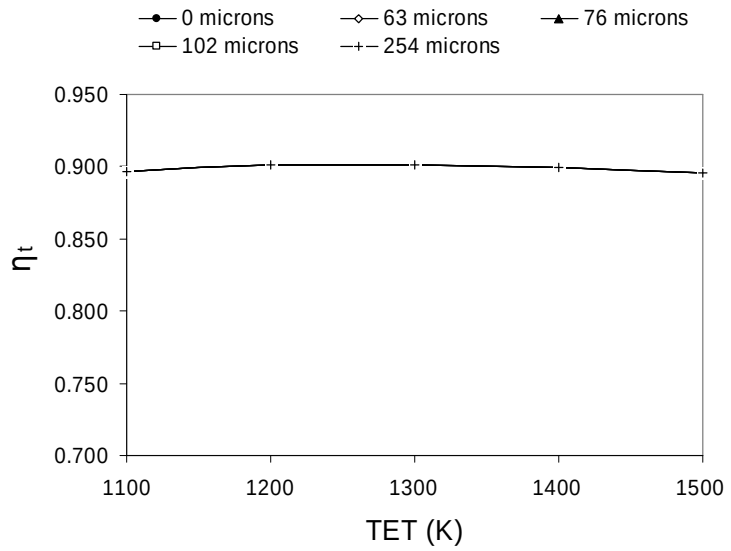

Figure 7–43: Turbine efficiency versus TET (experimental approach).

Keeping the TET constant and increasing the fouling level gradually, the performance drawbacks in terms of percentage compressor efficiency, thermal efficiency and useful power deterioration are illustrated in table 8. From the experimental cascade results correlated to the real uniformly roughened fouled engine via Howell's theory, it was found that increasing the roughness up to a level of 254 microns the drawbacks in compressor efficiency can be as high as 11 %. Taking into account these deterioration percentages in terms of compressor efficiency, increasing the fouling towards the level of 254 microns at 1100 K turbine entry temperature, the percentage deterioration in the useful power produced by the engine was found to be 27.4 %.

This percentage deterioration was eliminated by 51.8 %, hence almost by half, as the TET was increased to 1500 K (36.4 % increase in TET). For the same TET increase and fouling particle size of 254 microns, the percentage deterioration in thermal efficiency was eliminated by 57.4 %. For lower levels of fouling increasing the TET in the same range similar trends in terms of useful power and thermal efficiency were found. Therefore it can be stated that one performance deterioration inhibitor when fouling presents, is the parameter TET which must be increased properly.

Table 8: Percentage efficiency and useful work drawbacks due to fouling (ABB GT13 E2).

	0 microns	63 microns	76 microns	102 microns	254 microns
$\Delta\eta_c$ %	0	3.2	4.3	6.6	10.9
$UW_{(1100\ K)}$ MW	88.2	81.7	79.4	74.4	64.1
$\Delta UW_{(1100\ K)}$ %	0.0	7.4	10.1	15.7	27.4
$UW_{(1500\ K)}$ MW	196.5	189.4	186.9	181.5	170.5
$\Delta UW_{(1500\ K)}$ %	0.0	3.6	4.9	7.6	13.2
η_{th} (1100 K)	0.316	0.300	0.294	0.281	0.252
$\Delta\eta_{th\ (1100\ K)}$ %	0.0	5.1	7.0	11.1	20.2
η_{th} (1500 K)	0.365	0.357	0.354	0.347	0.333
$\Delta\eta_{th\ (1500\ K)}$ %	0.0	2.3	3.1	4.9	8.6

Chapter 8 Conclusions and recommendations

8.1 Conclusions

In the current project the parameters that affect the water injection for compressor cleaning of industrial gas turbines were examined via CFD tools and the effects of fouling were investigated using a compressor cascade test rig.
Increasing the droplet diameter a better IGV coverage was achieved. A compromise between intake wall water spillage and blade erosion caused by big droplets and insufficient IGV coverage due to small droplets took place by suggesting the use of 300 microns diameter droplets. Examining the intake of an ABB GT13 D2 industrial gas turbine, the CFD results showed that pointing the upper water injection nozzles parallel to the centreline of the engine and all the rest towards the midspan of the blades, better IGV coverage can be obtained. Using even or odd number of water nozzles the results were similar. Increasing the injection velocity gave much better results in terms of IGV coverage but some extra water spillage on the walls of the intake was unavoidable. High wall water spillage was also detected by increasing the angle of the injection cones from 40 to 80 degrees.
In terms of all cases examined IGV coverage above the engine shaft cone region was not achieved perfectly and the simulations taken place gave a better approach in solving the problem as much as possible.
CFD simulations were also run in order to examine any possible swirl effect in the intake flow imparted from the rotational flow field of the first stage rotor of the ABB GT13 D2 engine. The results showed that there isn't any swirl component in front of the IGV region and the flow enters the engine axially. It was shown as well that as the water droplets pass the IGVs entering the rotor region, the droplets lift up in the upper part of the engine hub area obtaining better cleaning of the blades spanwise. Lift of the droplets was detected in the lower part of the engine hub as well.
The CFD simulation predicted a Mach number value in front of the IGVs of 0.5 which is quite representative of the Mach numbers existing in this area for many industrial gas turbine engines.
Experiments examining possible swirl effects in the intake of a Rolls Royce Avon jet engine took place by injecting smoke in the intake bellmouth of it. A small swirl increment was detected only in the 12 and 6 o'clock position of the intake and it was disappeared elsewhere along the perimeter of the intake. If there was indeed swirl in the engine intake imparted from the rotation of the rotor, this would affect the whole perimeter of the engine intake flow. So, since this is not the case, the author assumes that the small swirl imparted into the flow in the positions referred previously is due to possible vortices coming into the engine intake flow from the testing room area.

A two-dimensional compressor cascade rig was designed and constructed in order to investigate the effect of fouling in gas turbine engines. The test rig involved a plenum chamber behind the blade test section in order to simulate unrestricted diffusion of the flow behind the blades. Preliminary results were obtained with the rig running in the mildly compressible flow regime of Mach number close to 0.4. The preliminary results showed that using a suction type facility for cascade testing imparts a small pressure gradient pitchwise behind the blades causing a sort of non uniformity in

terms of velocity distributions there. This was caused due to vortices existing in the lower and upper part of the plenum chamber. In order to eliminate this undesirable pressure gradient a very large plenum chamber geometry was attached behind the blade test section and this phenomenon was eliminated quite satisfactory. However, the geometrical plenum volume supposed to be attached could not be constructed in practise due to space limitations of the testing house room where the cascade tunnel facility had to be placed in.
A major outcome of this experimental work is to demonstrate that ideally, suck down facilities cannot achieve the most realistic environment for cascade data acquisition and then accurately predict results which are directly applicable to real compressor. In an ideal case, only blow down facilities can obtain this. However, the results presented in the current thesis are based on the most carefully designed settling chamber so as to minimise the effects of non-uniform exit static pressure. That was, in fact, achieved through exhausting CFD predictions in which the settling chamber volume was the major variable.

Preliminary three-dimensional CFD predictions have been undertaken which relate velocities, profile losses and exit flow angles as a function of surface roughness uniformly applied on the cascade blade surfaces. In particular, the preliminary CFD work on roughness reports the results of the CFD predictions for a range of roughness levels up to 254 microns with the cascade rig running close to an inlet Mach number of 0.4. Within that roughness range, the wake velocity is predicted to decrease from 94 m/s to 76 m/s at a distance of one chord downstream. Furthermore, it is predicted simultaneously that the wake becomes wider as roughness is increased. However, between the blade wakes, passage velocity increases slightly whereas inside the wake, the velocity increases non-linearly as roughness increases. A non-linear distribution of wake velocity for constant roughness values is also predicted within successive stations downstream of the cascade. In fact, as the flow moves downstream, the wake velocity increases at all values of constant roughness. This increase is found to be non-linear for all roughness cases considered.
It is also demonstrated that at one chord downstream of the blades, the loss coefficient increases with increasing roughness. For example, at that position, the loss coefficient increases from 0.16 for smooth blades to 0.36 for a roughness 254 microns. That is the loss is more than doubled. As the flow proceeds further away from the trailing edge in the wake, it is predicted that the losses decrease. This decrease appears to be lower for the roughened blades than for smooth ones. This is thought to be due to the increasing wake energy acquired through turbulent mixing increasing with position downstream.
In the cases examined, CFD predicts that increasing roughness has a small effect on the blade exit flow angle. For example, for low values of roughness a 2 degree increase occurs when compared with smooth blades. This corresponds to the small effect of roughness on blade static pressure distributions shown in the other research work reported. However, in cascade predictions, the effect of roughness on exit flow angle for centre passage roughened blades can effect neighbouring un-roughened blades. This is due to the corresponding lower static pressure levels to which the smooth blades are discharging downstream.
Finally, when roughness levels increase from smooth to102 microns, exit flow angle increases by 2 degrees. However, further increases in roughness to 254 microns, causes a further increase of only one degree. This is attributed to the exit flow blockage experienced as a result of wake size increase.

Preliminary performance results were obtained via applying Howell's theory on the preliminary design cascade CFD data. The results showed that increasing the fouling level on the cascade from 63 microns to 254 microns, the percentage deterioration in polytropic efficiency increases from 2.1 % to 5 %, respectively. These preliminary results also illustrated that increasing the fouling level the thermal efficiency of the engine and the useful work decrease as a result of pressure ratio and mass flow capacity deterioration, respectively.

The constructed cascade tunnel of the current project was used in order to examine the effect of fouling on two-dimensional compressor blades. The experimental runnings took place at an inlet Mach number one chord in front of the cascade blades of 0.3 and at a Reynolds number based on blade chord of $3.8*10^5$ for smooth blades. Using hot wire anemometer the cascade tunnel turbulence intensity was found to be very low in the order of 2 % and this value was very close to the original value of 1 % assumed for the preliminary CFD investigation of the rig before its construction.
The velocity, pressure loss and exit flow angle distributions examined at a distance of one chord downstream of the three middle cascade blades illustrated that the results are independent of the total ambient conditions and this holds even for the case of the roughened blade experiments.
Comparing the fouling results with the smooth clean blade results it was found that the low value static pressure gradient towards the right part of the rig was almost vanished by applying fouling on the blades. Increasing the fouling level the width and the depth of the wakes increased significantly, but in all cases the wakes due to fouling were shifted towards the right side of the cascade rig due to the higher boundary layer growth on the upper surfaces of the blades. Increasing the roughness towards the level of 254 microns the total pressure loss coefficient one chord downstream of the blades corresponding to all three middle passages increases from 0.16 to 0.35 and this represents a loss more than doubled. This was predicted from the preliminary CFD results as well.
From the experimental and the preliminary CFD results it can be concluded that the middle passage exit flow angle increase from 0 microns to 102 microns was eliminated by half passing from the fouling level of 102 microns to the level of 254 microns This is due to the resulted increased exit flow blockage related to the increase of the wake size as the roughness increases.

Further CFD simulations taken place by using the actual experimental boundary conditions of the cascade test rig gave satisfactory results in terms of passage and wake velocities and losses especially for the cases where the flow was treated as incompressible compared to the cases where it was treated as mildly compressible. However, both approaches predicted higher deflection and hence lower exit flow angles and as a result the wakes were shifted towards the left part of the passages compared to the experimental ones.

Trying to correlate the compressor cascade of the current project with a real compressor stage and to investigate the relevant engine performance via applying Howell's theory combined with the performance simulation tool Turbomatch for the different fouling cases examined, the results showed that increasing the fouling level the deterioration in polytropic and compressor efficiency increases continuously.

Increasing severely the fouling level at 254 microns the percentage deterioration in polytropic and compressor efficiency compared to smooth clean blades reached values of 7.4 and 10.9 % respectively.
As the turbine entry temperature increases the thermal efficiency of the engine increases as well as a result of the increase in pressure ratio. Also, for the same range of TET increase, the higher the level of fouling on the blades, the higher the gain in thermal efficiency is compared to clean blades. Keeping the TET constant and increasing the fouling level, the pressure ratio drops and the thermal efficiency decreases.
The useful power increases linearly with the TET and for constant TET by increasing the fouling level the power reduces due to the reduction in the mass flow capacity of the engine. At lower TETs the decrease in useful power due to fouling (0 to 254 microns) is higher than this corresponding to higher TETs as a result of the extra margin in useful power incorporated as the diverging lines of the Temperature-Entropy diagram show.
The compressor efficiency falls by increasing the fouling level on the compressor blades due to the pressure ratio degradation caused. However, by increasing the TET from 1100 K to 1500 K, the compressor efficiency falls by 1.2 % no matter how severely fouled the compressor is. However, in order the engine to recover the loss in useful power due to the increasing compressor power input caused by the fouled and non-efficient compressor the TET must increase.
Increasing the TET by 36.4 % (from 1100 to 1500 K) and keeping the fouling level constant, the engine percentage performance deterioration in terms of useful power and thermal efficiency was eliminated almost by half.
The turbine efficiency remains unaffected from the increase in the TET and the fouling level of the engine compressor.

8.2 Recommendations

In terms of further work that has to be done, experiments with fouling distributed partially on the cascade blades can be suggested. Purely spherical particles can also be used to roughen the blades in order the blade samples to give clear geometrical data of the roughened blade surfaces after examined by microscope so as equivalent sand grain roughness values to be obtained.

Blade cleaning of the current fouled compressor cascade test rig can be applied as well and the results in terms of velocity, pressure loss and exit flow angle distribution one chord behind the blades can be examined. This can be done by using the current available washing kit provided by the R-MC Recovery company after applying the appropriate water-air ratios into the cascade tunnel flow.

Further work can also take place by investigating the effect of double sided sticky tape applied on the blades in terms of velocity distribution, pressure losses and exit flow angle behind the blades. This investigation will illustrate if the increase of blade thickness due to the addition of sticky tape of the blades plays significant role or not in terms of the parameters mentioned. For the work done up to the present time this effect has been assumed to be negligible.

One further suggestion for future work is to modify the test rig to facilitate variable incidence. This can be achieved by attaching the blades to a turntable. This turntable can be constructed carefully and rotated in the test section area without problems since the test rig has been designed under movable plenum chamber configurations. This will accommodate various cascade streamtube directions at different incidences. Following this path, a map of compressor cascade characteristics like that obtained by Howell (1942) can be obtained (see figure 8-1).

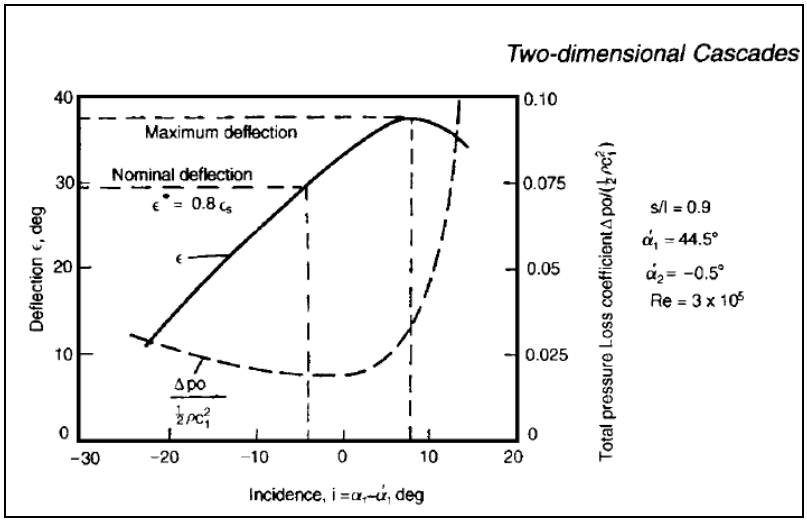

Figure 8–1: Compressor cascade characteristic curve (Howell, 1942).

Also, correlation of the cascade results can be obtained with a real compressor stage according to Howell's (1945) theory and the effect of blade roughness at various blade incidences in terms of engine performance can be examined as well.

For the present compressor cascade test rig, laser diffraction instrumentation can be used in order to measure droplet diameters of water injected to clean the cascade blades. Using this equipment, light from a laser is shone into a cloud of particles which are suspended in a transparent gas such as air. Then light is scattered from the particles and it is measured by a series of photodetectors placed at different angles (see figure 8-2). This is called the diffraction pattern for the sample which is used to measure the size of the particles.

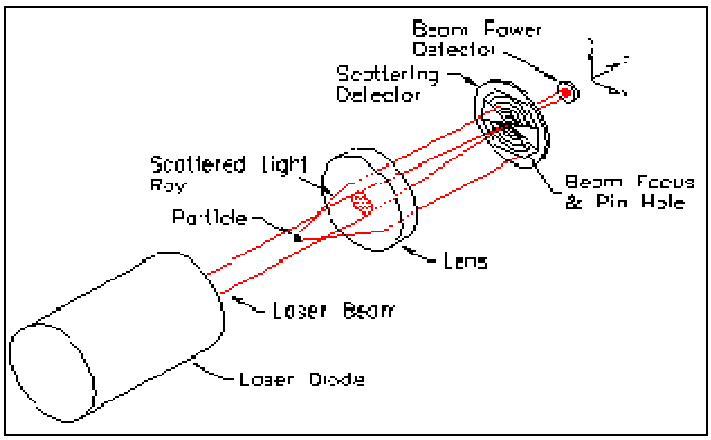

Figure 8–2: Laser diffraction instrumentation (www.malvern.com).

Particle image velocimetry (PIV) can be used in order to measure the velocity of injected droplets that are going to clean the current project cascade blades from fouling material. Particle image velocimetry is an optical method used to measure velocities (Khan et all 2000) and related properties in fluids. The fluid is seeded with particles whose motion is used to calculate velocity information. Typical PIV apparatus consists of a digital camera, a high power laser, an optical arrangement (cylindrical lens) to convert the laser output light to a light sheet and the fluid/gas under investigation (see figure 8-3).

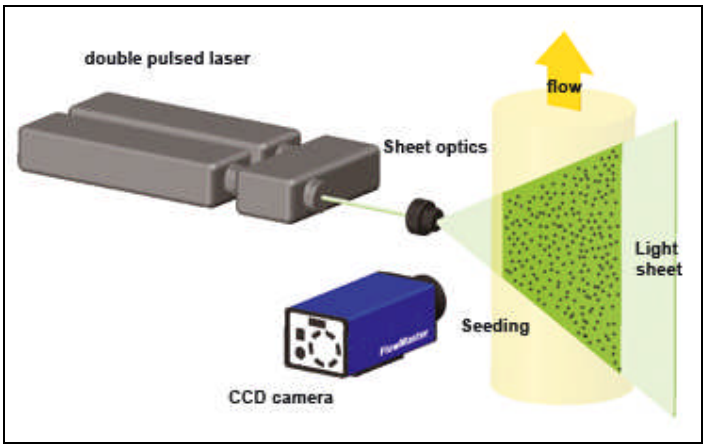

Figure 8–3: Particle image velocimetry illustration (www.lavision.de).

A fibre optic cable often connects the laser to the cylindrical lens setup. The laser acts as a photographic flash for the digital camera and the particles in the fluid scatter the light which is detected by the camera.
In order to measure whole velocity fields particle image velocimetry takes two images shortly after each other and calculates the distance that the individual particles travelled within this time. From the known time difference and the measured displacement the velocity is calculated.

References

Al-Hassani J. (1982). Turbine rotor blade erosion control with film cooling. PhD Thesis, Cranfield University, UK.

Anonymous (2007). FLUENT 6.3 User's Guide. Fluent Inc.

Bammert K. and Sandstede H. (1980). Measurements of the boundary layer development along a turbine blade with rough surfaces. ASME Transactions. Journal of. Engineering for Power, 102, pp. 978-983.

Bammert K. and Milsch R. (1972). Boundary Layers on rough compressor blades. ASME Paper No. 72-GT-48.

Biesinger T. and Lepel M. (2002). Flow field Investigations in intake manifolds of industrial gas turbines including CFD matching. 5th European Turbomachinery Conference, Prague.

British Standard BS 1042 (1983). Measurements of fluid flow in closed conduits. Part 2. Velocity area methods. Section 2.1. Method using pitot static tubes.

Bradshaw P., Ferris D.H. and Atwell N.P. (1965). Calculation of boundary-layer development using the turbulent energy equation. J. Fluid Mechanics, Vol.28, 1965, pp.593-616, ARC-32401.

Bromley Andrew F. and Meher-Homji Cyrus B. (2004). Gain a competitive edge with a better understanding of GT compressor fouling, washing. Combined Cycle Journal, Fourth Quarter 2004.

Bruun H. (1995). Hot-wire anemometry: principles and signal analysis. Oxford university press, New York.

Carl Hjerpe (2004). Maintaining turbine efficiency. Earthscan COSPP Technologies.

Day, I., Freeman, C., Williams, J. (2005). Rain ingestion in axial flow compressors at part speed. Paper No GT2005-68582, ASME Turbo Expo 2005, Power of land, sea and air, June 6-9, 2005, Reno-Tahoe, Nevada, Usa.

Diego Lerena Diaz. (2003). Experimental calibration of three-hole pressure probes with different head geometries. Diploma Thesis. Vienna University of Technology.

Dixon, S.L. (1998). Fluid mechanics and thermodynamics of turbomachinery. Butterworth-Heinemann.

Gbadebo S., Hynes T. and Cumpsty N. (2004). Influence of surface roughness on three-dimensional separation in axial compressors. Journal of Turbomachinery, Vol. 126, pp. 455-463.

Gostelow J., 1984, Cascade aerodynamics, first edition, Pergamon Press, Oxford.

Hayward, J., Winson, G., Raatrae, A. (1999). Wash system for gas turbine compressors. European Patent EP0933502A2.

Hellsten A. (1998). Some improvements in Menter's k-ω SST turbulence model. 29th AIAA Fluid Dynamics Conference, Albuquerque, New Mexico, June 15-18, 1998, AIAA 98-2554.

Horlock J. H. (1973). Axial flow compressors. Butterworth.

Howell A. R. (1942). The present basis of axial flow compressor design: Part I, Cascade theory and performance. ARC R and M. 2095.

Howell A. R. (1945). Design of axial compressors. Proc. Instn. Mech. Engrs., 153.

Howell A. R. (1945). Fluid dynamics of axial compressors. Proc. Instn. Mech. Engrs., 153.

Howell A. R. and Bonham R. P. (1950). Overall and stage characteristics of axial-flow compressors. Proc. Instn. Mech. Engrs., 163.

Jorgensen F. E. (2002). How to measure turbulence with hot-wire anemometers. A practical guide, Dantec Dynamics.

Kandula M., Wilcox D.C. (1995). An examination of k-ω turbulence model for boundary layers, free shear layers and separated flows. AIAA 26th Fluid Dynamics Conference, San Diego, CA, June 19-22, 1995, AIAA 95-2317.

Khan A., Leport D., Hyde M. and Jasuja A. (2000). Investigation into the behaviour of a fan spray using LSI / PDPA / PIV techniques. ILASS-Europe.

Kind R., Serjak P. and Abbott M. (1998). Measurements and prediction of the effects of surface roughness on profile losses and deviation in a turbine cascade. ASME Transactions, Journal of Turbomachinery, 120, pp. 20-27.

King L.V. (1914). On the convection of heat from small cylinders in a stream of fluid: Determination of the convection constants of small platinum wires with applications to hot-wire anemometry. Phil. Trans. Roy. Soc. A214, pp. 373-432.

Lee J.C. and Ash J. E. (1956). A three-dimensional spherical pitot probe. Trans. A.S.M.E. 78, 603-8.

Leipold R., Boese M. and Fottner L. (2000). The influence of technical surface roughness caused by precision forging on the flow around a highly loaded compressor cascade. ASME Transactions, Journal of Turbomachinery, 122, pp. 416-424.

Lenschow D. H. and Stankov B. B. (1986). Length scales in the convective boundary layer. Journal of the Atmospheric Sciences, Vol. 43, No. 12, pp. 1198-1209.

Lomas C. (1986). Fundamentals of hot wire anemometry. Cambridge university press, Cambridge.

McKenzie A.B. (1966). An investigation of flare dimensions for standard and annular air meters. Rolls-Royce report RCP 90087.
Menter F.R. (1991). Performance of popular turbulence models for attached and separated adverse pressure gradient flows. AIAA 22nd Fluid Dynamics, Plasma Dynamics & Lasers Conference, Honolulu, Hawaii, June 24-26, 1991, AIAA-91-1784.

Menter, F. (1993). Zonal two equation k-ω turbulence models for aerodynamic flows. AIAA 24th Fluid Dynamics Conference, Orlando, July, 1993, AIAA 93-2906.

Milne-Thomson L. M. (1950). Theoretical hydrodynamics. The MacMillan Company, New York, N. Y., second edition.

MorsiS. A.and Alexander A.J.(1972). An Investigation of Particle Trajectories in Two-Phase Flow Systems. *J. Fluid Mech.*, 55(2):193-208, September 26 1972.

Mund, F.C. (2006). Coordinated application of CFD and gas turbine performance methods. PhD thesis, Cranfield University, UK.

Mund, F.C. and Pilidis, P. (2005). Online compressor washing: a numerical survey of influencing parameters. J. Power and Energy. Proc. IMechE Vol.219 Part A.

Mund, F.C., Pilidis, P. (2004). Effects of spray parameters and operating conditions on an industrial gas turbine washing system. Paper No GT2004-53551, ASME Turbo expo 2004, Power for land, sea and air, June 14-17, 2004, Vienna, Austria.

Munson B., Young D., Okiishi T. (1998). Fundamentals of fluid mechanics. Wiley, 3rd edition.

Mustafa, Z. (2005). Aerodynamic investigation of fluid injection in axial compressor. PhD thesis, Cranfield University, UK.

NASA SP-36 (1965). Aerodynamic design of axial-flow compressors. Scientidic and Technical Information Division, National Aeronautics and Space Administration, Washington, D.C.

Nikuradse J. (1933). Laws of flow in rough pipes. NACA TM 1292, National Advisory Committee on Aeronautics.

Nowack, C. F. R. (1970). Improved calibration method for a five-hole spherical pitot probe. Journal of Physics. E: Sci. Instrum. 3, 21-26. Delft University of Technology, Netherlands.

Panofsky H. A. and Dutton J. A. (1984). Atmospheric turbulence. Wiley and Sons, 97pp.
Pilidis P. (2002). Gas turbine theory and performance, course notes, Cranfield University, UK.

Perry A. E. (1982). Hot-wire anemometry. Clarendon Press, Oxford.

Pollard D. and Gostelow J. (1967). Some experiments at low speed on compressor cascades. ASME Transactions, Journal of Engineering for Power, 88-89, pp. 427-436.

Rafel Giralt I Cubi (2008). Investigation on the effect of Reynolds number on phneumatic three-hole pressure probe calibration. Diploma Thesis. Vienna University of Technology.

Ramsden, K. W. (2002). Axial turbine design and performance - Axial turbine design manual, course notes, Cranfield University, UK.

Ramsden, K. W. (2006). Axial compressor design and performance, course notes, Cranfield University, UK.

Ramsden, K. W. (2008). Gas turbine fundamentals and turbomachinery, short course notes, Cranfield University, UK.

Saravanamuttoo H.IH., Rogers G.F.C., Cohen H. (2001). Gas turbine theory, fifth edition, Prentice Hall, Essex.

Schlichting H. (1936). Experimental investigation of the problem of surface roughness. NACA TM-832, National Advisory Committee on Aeronautics.

Shukry A. (1949). Flow around bends in an open flume. Proc. Am. Soc. Civ. Engrs, Vol 75, 715-9.

Surface metrology guide (1998). Surfaces and profiles.

Springer J. (1934). Aerodynamic theory. Berlin, p. 213.

Launder B. E. and Spalding D. B. (1972). Lectures in mathematical models of turbulence. Academic Press, London, England.

Stalder J. P. (2001). Gas turbine compressor washing state of the art: field experiences.
Journal of Engineering for Gas Turbines and Power, Vol. 123, pp. 363-369.

Syverud, E., Bakken E.L. (2005). Online water wash tests of GE J85-13. Paper No GT2005-68702, ASME Turbo expo 2005, Power for land, sea and air, June 6-9, 2005, Reno-Tahoe, Nevada, Usa.

Suder K., Chima R., Strazisar A. and Roberts W. (1995). The effect of adding roughness and thickness to a transonic axial compressor rotor. ASME Transactions, Journal of Turbomachinery, 117, pp. 491-505.

Taylor G. I. (1938). The spectrum of turbulence. Proc. Roy. Soc. London, A132, pp. 476-490.
Taylor Hobson. (2004). Surtronic 25 User's guide. Taylor Hobson Ltd.

Taylor Hobson. (2004). A guide to surface texture parameters. Taylor Hobson precision brochure.

Treaster A. L. and Yocum A. M., (1979). The calibration and application of five-hole probes. ISA Transactions, Vol. 18: 23-34.
Wright M. A. (1970). The evaluation of a simplified form of presentation for five-hole spherical and hemispherical pitotmeter calibration data. Journal of Physics E. Scientific instruments, Vol. 3.

Zhang Q., Lee S. and Ligrani P. (2004). Effects of surface roughness and turbulence intensity on the aerodynamic losses produced by the suction surface of a simulated turbine airfoil. ASME Transactions, Journal of Fluids Engineering, 126, pp. 257-265.

Zuniga O. (2007). Analysis of gas turbine compressor fouling and washing on line. PhD thesis, Cranfield University, UK.

Appendix

Table 9: Compressible flow tables.

GAMMA =	1.4	GAS CONSTANT =	287			
Mach No	**T / t**	**P / p**	**V / Root.T**	**1000 Q**	**1000 q**	**A / A***
0.000	1.0000	1.0000	0.000	0.000	0.000	infinity
0.005	1.0000	1.0000	0.100	0.349	0.349	115.7425
0.010	1.0000	1.0001	0.200	0.698	0.698	57.8738
0.015	1.0000	1.0002	0.301	1.048	1.048	38.5855
0.020	1.0001	1.0003	0.401	1.397	1.397	28.9421
0.025	1.0001	1.0004	0.501	1.745	1.746	23.1568
0.030	1.0002	1.0006	0.601	2.094	2.095	19.3005
0.035	1.0002	1.0009	0.701	2.443	2.445	16.5465
0.040	1.0003	1.0011	0.802	2.791	2.794	14.4815
0.045	1.0004	1.0014	0.902	3.139	3.144	12.8757
0.050	1.0005	1.0018	1.002	3.487	3.493	11.5914
0.055	1.0006	1.0021	1.102	3.834	3.843	10.5410
0.060	1.0007	1.0025	1.202	4.182	4.192	9.6659
0.065	1.0008	1.0030	1.302	4.528	4.542	8.9257
0.070	1.0010	1.0034	1.402	4.875	4.891	8.2915
0.075	1.0011	1.0039	1.503	5.221	5.241	7.7421
0.080	1.0013	1.0045	1.603	5.566	5.591	7.2616
0.085	1.0014	1.0051	1.703	5.911	5.941	6.8378
0.090	1.0016	1.0057	1.803	6.255	6.291	6.4613
0.095	1.0018	1.0063	1.903	6.599	6.641	6.1247
0.100	1.0020	1.0070	2.002	6.943	6.991	5.8218
0.105	1.0022	1.0077	2.102	7.285	7.342	5.5480
0.110	1.0024	1.0085	2.202	7.627	7.692	5.2992
0.115	1.0026	1.0093	2.302	7.969	8.043	5.0722
0.120	1.0029	1.0101	2.402	8.309	8.393	4.8643
0.125	1.0031	1.0110	2.502	8.649	8.744	4.6732
0.130	1.0034	1.0119	2.601	8.988	9.095	4.4969
0.135	1.0036	1.0128	2.701	9.326	9.446	4.3337
0.140	1.0039	1.0138	2.801	9.664	9.797	4.1824
0.145	1.0042	1.0148	2.900	10.001	10.149	4.0416
0.150	1.0045	1.0158	3.000	10.336	10.500	3.9103
0.155	1.0048	1.0169	3.100	10.671	10.852	3.7877
0.160	1.0051	1.0180	3.199	11.005	11.203	3.6727
0.165	1.0054	1.0192	3.298	11.338	11.555	3.5649
0.170	1.0058	1.0204	3.398	11.670	11.908	3.4635
0.175	1.0061	1.0216	3.497	12.001	12.260	3.3680
0.180	1.0065	1.0229	3.596	12.330	12.612	3.2779
0.185	1.0068	1.0242	3.696	12.659	12.965	3.1928
0.190	1.0072	1.0255	3.795	12.987	13.318	3.1123
0.195	1.0076	1.0269	3.894	13.313	13.671	3.0359
0.200	1.0080	1.0283	3.993	13.639	14.024	2.9635
0.205	1.0084	1.0297	4.092	13.963	14.378	2.8947
0.210	1.0088	1.0312	4.191	14.286	14.732	2.8293
0.215	1.0092	1.0327	4.290	14.607	15.086	2.7670
0.220	1.0097	1.0343	4.389	14.928	15.440	2.7076
0.225	1.0101	1.0359	4.487	15.247	15.794	2.6509
0.230	1.0106	1.0375	4.586	15.565	16.149	2.5968
0.235	1.0110	1.0392	4.685	15.881	16.504	2.5451
0.240	1.0115	1.0409	4.783	16.196	16.859	2.4956
0.245	1.0120	1.0427	4.882	16.510	17.214	2.4482
0.250	1.0125	1.0444	4.980	16.822	17.570	2.4027

GAMMA =	1.4	GAS CONSTANT =	287			
Mach No	**T / t**	**P / p**	**V / Root.T**	**1000 Q**	**1000 q**	**A / A***
0.255	1.0130	1.0463	5.079	17.133	17.925	2.3591
0.260	1.0135	1.0481	5.177	17.442	18.282	2.3173
0.265	1.0140	1.0500	5.275	17.750	18.638	2.2771
0.270	1.0146	1.0520	5.373	18.056	18.995	2.2385
0.275	1.0151	1.0539	5.471	18.361	19.352	2.2013
0.280	1.0157	1.0560	5.569	18.664	19.709	2.1656
0.285	1.0162	1.0580	5.667	18.966	20.066	2.1311
0.290	1.0168	1.0601	5.765	19.266	20.424	2.0979
0.295	1.0174	1.0623	5.862	19.564	20.782	2.0659
0.300	1.0180	1.0644	5.96	19.861	21.141	2.0351
0.305	1.0186	1.0666	6.058	20.156	21.499	2.0053
0.310	1.0192	1.0689	6.155	20.449	21.858	1.9765
0.315	1.0198	1.0712	6.252	20.741	22.218	1.9487
0.320	1.0205	1.0735	6.35	21.031	22.577	1.9219
0.325	1.0211	1.0759	6.447	21.319	22.937	1.8959
0.330	1.0218	1.0783	6.544	21.606	23.298	1.8707
0.335	1.0224	1.0808	6.641	21.890	23.659	1.8464
0.340	1.0231	1.0833	6.738	22.173	24.020	1.8229
0.345	1.0238	1.0858	6.835	22.454	24.381	1.8001
0.350	1.0245	1.0884	6.931	22.733	24.743	1.7780
0.355	1.0252	1.0910	7.028	23.010	25.105	1.7565
0.360	1.0259	1.0937	7.124	23.285	25.467	1.7358
0.365	1.0266	1.0964	7.221	23.559	25.830	1.7156
0.370	1.0274	1.0992	7.317	23.830	26.193	1.6961
0.375	1.0281	1.1019	7.413	24.100	26.557	1.6771
0.380	1.0289	1.1048	7.509	24.368	26.921	1.6587
0.385	1.0296	1.1077	7.605	24.633	27.285	1.6408
0.390	1.0304	1.1106	7.701	24.897	27.650	1.6234
0.395	1.0312	1.1135	7.797	25.159	28.015	1.6065
0.400	1.0320	1.1166	7.893	25.418	28.381	1.5901
0.405	1.0328	1.1196	7.988	25.676	28.747	1.5742
0.410	1.0336	1.1227	8.084	25.931	29.113	1.5587
0.415	1.0344	1.1258	8.179	26.185	29.480	1.5436
0.420	1.0353	1.1290	8.274	26.436	29.847	1.5289
0.425	1.0361	1.1323	8.369	26.686	30.215	1.5146
0.430	1.0370	1.1355	8.464	26.933	30.583	1.5007
0.435	1.0378	1.1388	8.559	27.178	30.951	1.4872
0.440	1.0387	1.1422	8.654	27.421	31.320	1.4740
0.445	1.0396	1.1456	8.748	27.662	31.690	1.4612
0.450	1.0405	1.1491	8.843	27.900	32.059	1.4487
0.455	1.0414	1.1526	8.937	28.137	32.430	1.4365
0.460	1.0423	1.1561	9.032	28.371	32.801	1.4246
0.465	1.0432	1.1597	9.126	28.603	33.172	1.4131
0.470	1.0442	1.1634	9.22	28.833	33.544	1.4018
0.475	1.0451	1.1670	9.314	29.061	33.916	1.3908
0.480	1.0461	1.1708	9.407	29.287	34.288	1.3801
0.485	1.0470	1.1746	9.501	29.510	34.662	1.3697
0.490	1.0480	1.1784	9.594	29.731	35.035	1.3595
0.495	1.0490	1.1823	9.688	29.950	35.409	1.3495
0.500	1.0500	1.1862	9.781	30.167	35.784	1.3398

Table 10 : Fan characteristic curve extracted data.

mass flow lb/s	mass flow kg/s	dynamic pressure inches W.G.	dynamic pressure Pa	total pressure rise inches W.G.	total pressure rise Pa	HP	HP electric Watt
0.60	0.272	0.8	199.271	46.0	11458.090	15.6	11637.6
1.25	0.567	1.0	249.089	46.4	11557.725	19.6	14621.6
1.85	0.839	1.2	298.907	46.6	11607.543	22.8	17008.8
2.50	1.134	1.6	398.542	46.8	11657.361	26.4	19694.4
3.10	1.406	2.0	498.178	46.4	11557.725	28.2	21037.2
3.75	1.701	2.6	647.631	46.2	11507.908	32.4	24170.4
4.35	1.973	3.0	747.267	46.0	11458.090	35.6	26557.6
5.00	2.268	3.4	846.902	45.6	11358.454	38.4	28646.4
5.60	2.540	4.0	996.356	44.6	11109.365	40.8	30436.8
6.25	2.835	4.2	1046.173	43.2	10760.641	43.2	32227.2
6.85	3.107	4.6	1145.809	41.6	10362.099	45.6	34017.6
7.50	3.402	5.4	1345.080	40.0	9963.556	48.0	35808.0
8.10	3.674	5.6	1394.898	38.2	9515.196	49.0	36554.0
8.75	3.969	5.8	1444.716	36.0	8967.201	50.4	37598.4
9.35	4.241	6.4	1594.169	33.6	8369.387	51.2	38195.2
10.00	4.536	6.8	1693.805	30.8	7671.938	52.0	38792.0
10.60	4.808	7.0	1743.622	28.0	6974.489	51.8	38642.8
11.25	5.103	7.4	1843.258	25.2	6277.041	51.0	38046.0
11.85	5.375	7.8	1942.893	22.4	5579.592	48.8	36404.8
12.50	5.670	8.4	2092.347	19.4	4832.325	45.2	33719.2

Table 11: Upper surface spanwise roughness Ra in µm.

0 microns	25% chord	50% chord	75% chord
75% span	0.6	0.4	0.4
50% span	0.4	0.4	0.4
25% span	0.4	0.4	0.5
63 microns	25% chord	50% chord	75% chord
75% span	7.6	7.3	6.9
50% span	6.4	8.2	7.3
25% span	7.1	6.6	6.8
76 microns	25% chord	50% chord	75% chord
75% span	10.9	8.8	8.7
50% span	11.9	8.8	7.6
25% span	7.5	10.7	8.7
102 microns	25% chord	50% chord	75% chord
75% span	14.5	12.4	13.2
50% span	13	13.7	13.2
25% span	14.3	14.2	12.4
254 microns	25% chord	50% chord	75% chord
75% span	23.7	24.9	27.5
50% span	25.3	24.4	27.8
25% span	25.7	25.8	20.9

Table 12: Lower surface spanwise roughness Ra in µm.

0 microns	25% chord	50% chord	75% chord
75% span	0.6	0.4	0.4
50% span	0.4	0.4	0.4
25% span	0.4	0.4	0.4
63 microns	25% chord	50% chord	75% chord
75% span	7.6	7.4	8.7
50% span	7	7.1	7.9
25% span	7.9	7.1	7.2
76 microns	25% chord	50% chord	75% chord
75% span	11.9	8.6	10.6
50% span	9.6	10.5	7.9
25% span	11	10.4	8.5
102 microns	25% chord	50% chord	75% chord
75% span	14.3	14.1	13.1
50% span	14.3	11.9	12.7
25% chord	16	12.9	12.8
254 microns	25% chord	50% chord	75% chord
75% span	26.4	21.1	20.8
50% span	28.2	25	25.9
25% span	24.2	24.7	26.9

Table 13: Upper surface streamwise roughness Ra in µm.

0 microns	25% chord	50% chord	75% chord
75% span	0.6	0.6	0.4
50% span	0.4	0.6	0.4
25% span	0.4	0.6	0.4
63 microns	25% chord	50% chord	75% chord
75% span	7.1	7.2	7.4
50% span	6.9	6.4	7.2
25% span	7.1	6.1	6.3
76 microns	25% chord	50% chord	75% chord
75% span	9.8	9.2	9.3
50% span	9.1	8.7	10.4
25% span	8.4	9	9.5
102 microns	25% chord	50% chord	75% chord
75% span	13.1	12.4	13.5
50% span	15.2	15.3	11.5
25% span	15.5	12.8	13.1
254 microns	25% chord	50% chord	75% chord
75% span	22.8	26.6	23.3
50% span	21	25	25.3
25% span	23.2	25	19.2

Table 14: Lower surface streamwise roughness Ra in µm.

0 microns	25% chord	50% chord	75% chord
75% span	0.4	0.4	0.6
50% span	0.4	0.4	0.4
25% span	0.4	0.4	0.4
63 microns	25% chord	50% chord	75% chord
75% span	8.4	6.7	8.1
50% span	7.4	7.1	7.1
25% span	8.2	6.9	6.9
76 microns	25% chord	50% chord	75% chord
75% span	11.2	9.1	8.7
50% span	9.3	10	11.7
25% span	10.7	10	10.8
102 microns	25% chord	50% chord	75% chord
75% span	13.6	14.4	14.3
50% span	14.3	11.4	12.9
25% span	13	15.3	15.5
254 microns	25% chord	50% chord	75% chord
75% span	25.1	20	25
50% span	22.5	20.5	25.7
25% span	22	20.9	23.7

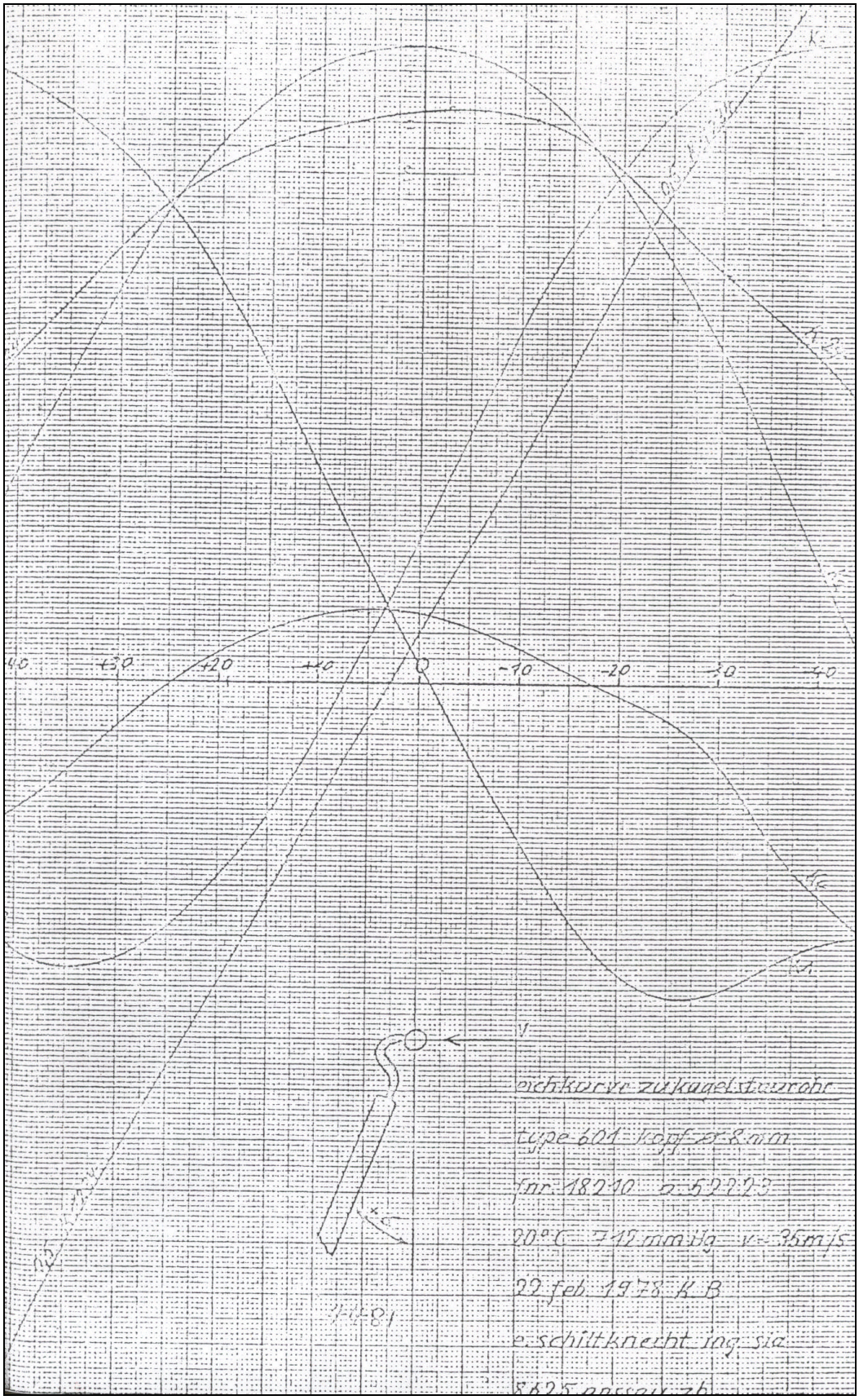

Figure A 1: Yaw meter exit flow angle curves.

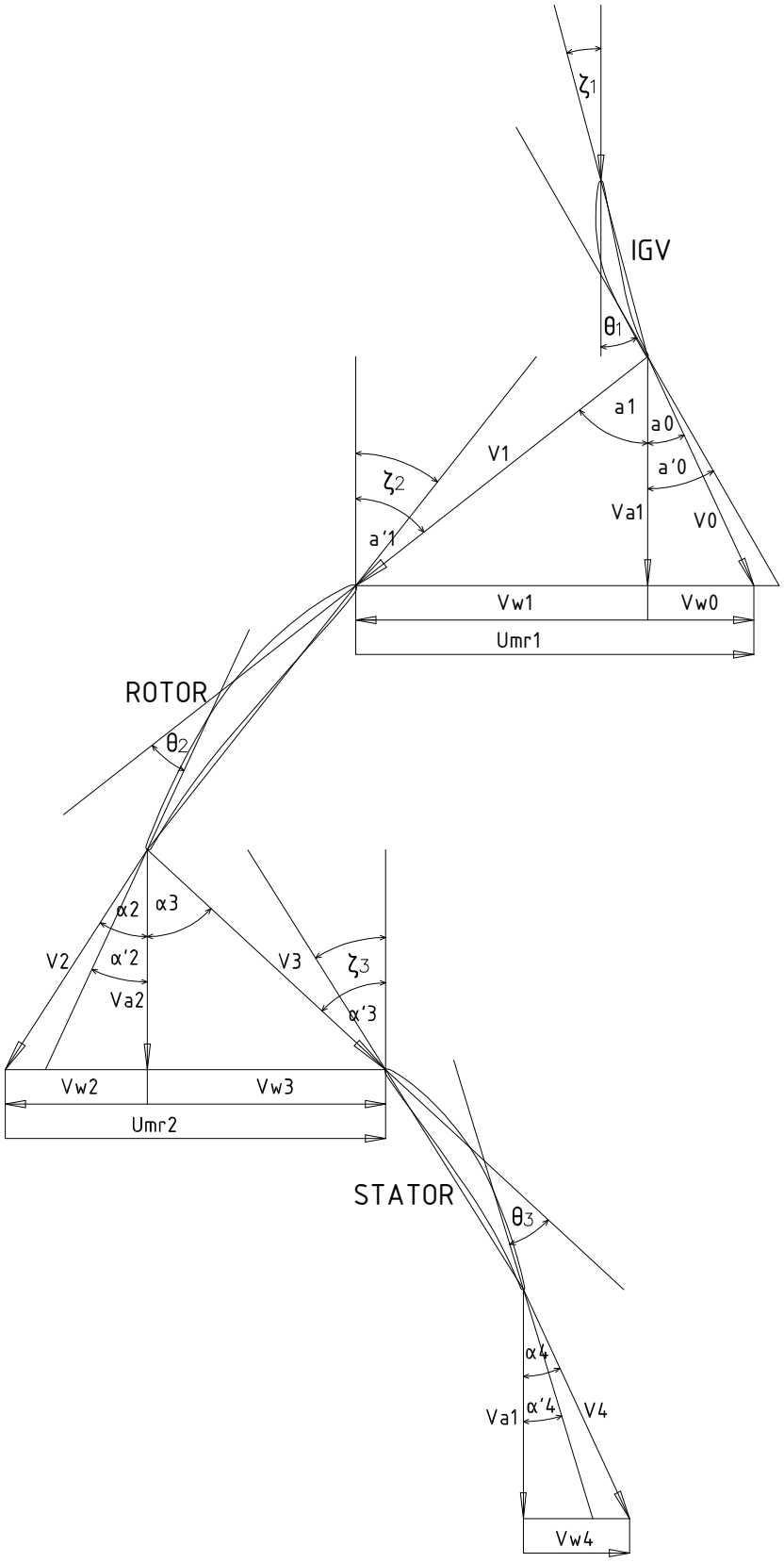

Figure A 2: ABB GT13 D2 first compressor stage velocity triangles.

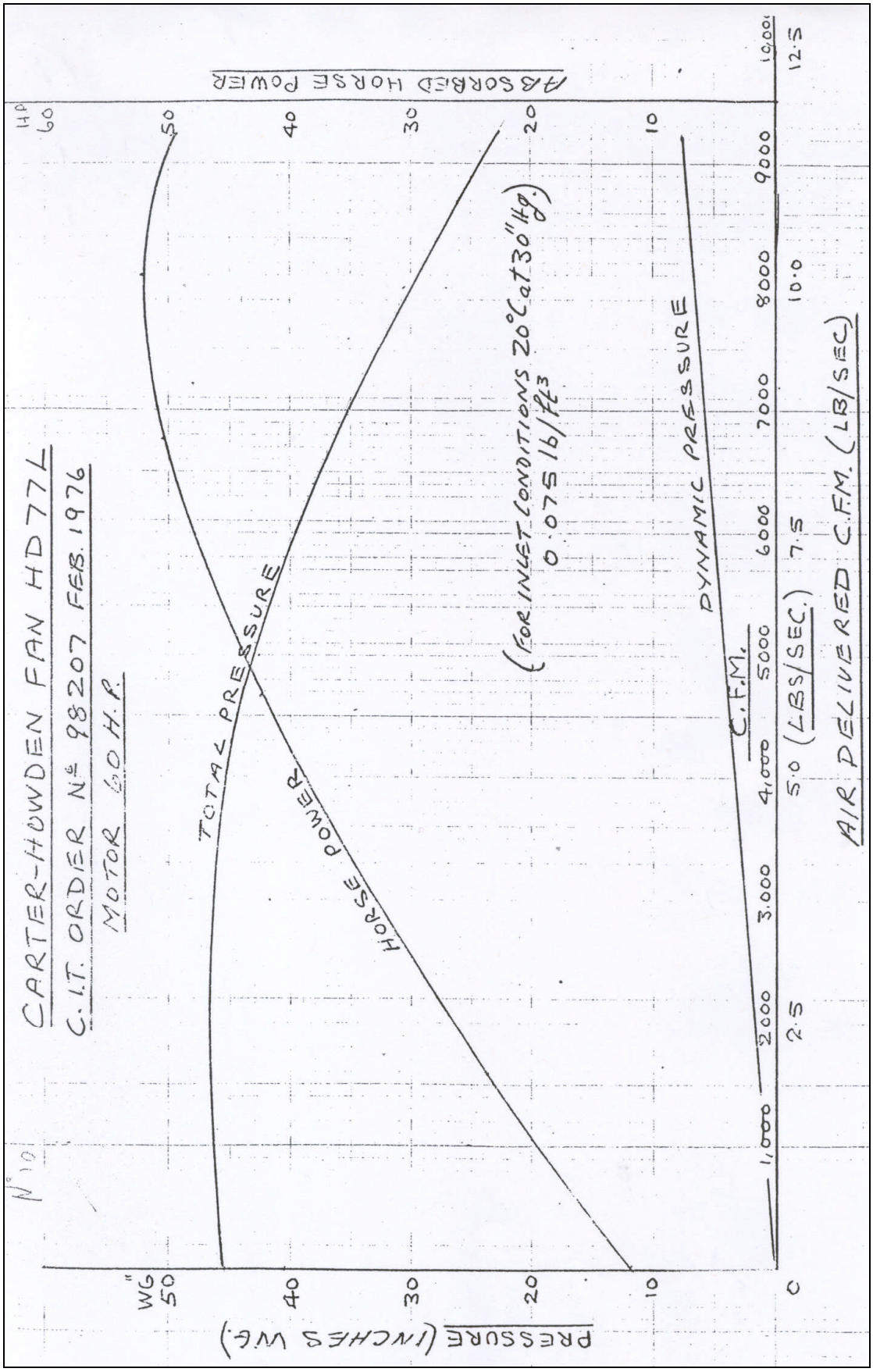

Figure A 3: Fan characteristic curves.

Preliminary axial compressor design — ABB GT13 D2

Type		ABB GT13 D2
Power output (MW)		98
Single shaft		
Ambient temperature (K)		300.15
Ambient pressure (Pa)		98300
Fuel Natural gas		
Blade axial velocity contant throughout the stage		

Compressor Specifications

number of stages		14
Overall pressure ratio Rc		12.109
Polytropic efficiency n_p (K. Ramsden 2002)		0.88
Mass flow W (kg/s)		370
Inlet total pressure P1 (Pa)		97450
Inlet total temperature T1 (K)		300.15
Ratio of specific heats γ		1.4
1st stage Blockage factor K_{B1}		0.99
Shaft speed N (rpm)		2970
1st rotor tip diameter Dt1 (mm)		2128.736
Blade height 1st rotor B1 (mm)		354.782
Tip clearance (mm)		7
Ideal gas constant R (J/KgK)		287
1st rotor hub diameter Dhr1 (mm)		1419.172
1st rotor medium diameter Dmr1 (mm)		1773.954
Gas turbine operating frequency f (Hz)		49.5
Angular velocity w (rad/s)	$2*\pi*f$	311.018
1st rotor inlet mean blade speed Umr1 (m/s)	w*(Dmr1/2)	275.866
Absolute air angle at inlet to the first stage α0 (degrees)	assumption	25
IGV tip diameter Dt_{IGV} (mm)		2224.648
IGV hub diameter $Dhub_{IGV}$ (mm)		1419.172
Inlet guide vane annulus area A_{IGV} (m^2)	$\pi[(Dt_{IGV}^2)-(Dhub_{IGV}^2)]/4$	2.305
Qo	$(W*\sqrt{T1})/(P1*A_{IGV})$	0.0285
IGV axial Mach number Ma	from tables	0.464
IGV face static temperature t_{IGV} (K)	$T1/[1+((\gamma-1)/2)*Ma^2)]$	287.759
Rotor inlet mean axial velocity Va1 (m/s)	$Ma*\sqrt{(\gamma*R*t_{IGV})}$	157.775
Inlet hub / tip ratio Dhr1/Dt1		0.667
Temperature rise per stage		constant
Annulus configuration		constant hub diameter

Rotor inlet

Absolute rotor inlet whirl velocity Vw0 (m/s)	Va1*tanα0	73.572
Relative rotor inlet whirl velocity Vw1(m/s)	Umr1-Vw0	202.294
Relative rotor inlet air angle α1 (degrees)	atan(Vw1/Va1)	52.05
Relative rotor inlet velocity V1 (m/s)	Va1/cosa1	256.546
Compressor overall efficiency n_c	[(Rc^(γ-1/γ))-1]/[(Rc^(γ-1/γn_p))-1]	0.833
Compressor temperature rise ΔTc (K)	(T1/n_c)*[(Rc^(γ-1/γ)) -1]	374.373
Stage temperature rise ΔTstage (K)	ΔTc/number of stages	26.741
Va1/√T1		9.107
Qo1	from tables	0.0285
Rotor inlet axial Mach number Ma		0.464
1st rotor inlet cross sectional area A1 (m^2)	design data	2.3050
1st rotor inlet cross sectional area A1 calculated (m^2)	(W√T1)/(Qo1*P1*K_{B1})	2.3314

Rotor outlet

1st rotor exit hub diameter Dhr2 (mm)	design data	1419.172
1st rotor exit tip diameter Dt2 (mm)	design data	2109.58
1st rotor exit medium diameter Dmr2 (mm)	design data	1764.376
1st rotor outlet mean blade speed Umr2 (m/s)	π*Dmr2*N/60	274.376
Specific heat at constant pressure Cp (J/KgK)	(γ/(γ-1))*R	1004.500
1st rotor absolute whirl velocity Vw3 (m/s)	((Cp*ΔTstage)+ (Umr1*Vw0))/Umr2	171.870
1st stage pressure ratio Rstage1	[(np*(ΔTstage/T1))+1]^(γ/(γ-1))	1.302
1st stage exit total pressure P2 (Pa)	Rstage1*P1	126914.920
1st rotor absolute exit velocity V3 (m/s)	((Vw3^2)+(Va1^2))^0.5	233.307
1st rotor relative exit whirl velocity Vw2 (m/s)	Umr2-Vw3	102.506
1st rotor relative exit flow angle α2 (degrees)	atan(Vw2/Va1)	33.01
1st rotor relative exit velocity V2 (m/s)	Va1/cosα2	188.150
1st rotor DeHaller number calculated	V2/V1	0.733
1st rotor absolute exit flow angle α3 (degrees)	atan(Vw3/Va1)	47.45
Stage loading coefficient ΔH/$(Umr2)^2$	((Vw3*Umr2)-(Vw0*Umr1))/Umr2^2	0.357
Stage flow coefficient	Va1/Umr2	0.575
1st stator exit flow angle α4 (degrees)	assumption	25
1st stator exit flow absolute velocity V4 (m/s)	Va1/cosα4	174.085
1st stator DeHaller number	V4/V3	0.746
1st stage exit total temperature T2 (K)	T1+ Δtstage	326.891
V3/√T2		12.904
1st rotor absolute exit Mach number M3	from tables	0.672
Va1/√T2		8.726
P2/pstatic2	from tables	1.1448
1st stage outlet static pressure pstatic2		110862.090
Qo2		0.0276
1st stage exit Blockage factor K_{B2}		0.95
First stage exit annulus area A2 (m^2)	design data	1.9134
First stage exit annulus area calculated A2 (m^2)	(W√T2)/(Qo2*P2*K_{B2})	2.0103

Axial Velocity Calculation Iterative Process

Estimation of rotor axial velocity		
1st stage rotor exit total temperature T3 (K)	T2	326.891
1st stage rotor exit blockage factor K_{B1}		0.99
1st stage rotor exit total pressure P3 (Pa)	P2	126914.920
1st rotor exit annulus area Aann (m^2)	$\pi[(Dt2^2)-(Dhr2^2)]/4$	1.9134
A3*V3=Aann*Va1 or A3=Aann*cosα3		
Q3	$(W\sqrt{T3})/(K_{B1}*A3*P3)$	
Q3*cosα3	$(W\sqrt{T3})/(K_{B1}*Aann*P3)$	0.0278
First approximation to rotor exit axial velocity		
Va1=Va2 (m/s)		157.775
1st rotor absolute exit velocity V3 (m/s)	((Vw3^2)+(Va1^2))^0.5	233.307
V3/√T3		12.904
Q3	from tables	0.0362
Q3*cosα3		0.0278
α3 (degrees)	$\cos^{-1}$(0.0278/Q3)	39.77
1st rotor exit axial velocity Va2 (m/s)	Vw3/tanα3	206.527
Second approximation to rotor exit axial velocity		
Va2 (m/s)	(157.775+206.527)/2	182.151
1st rotor absolute exit velocity V3 (m/s)	((Vw3^2)+(Va2^2))^0.5	250.437
V3/√T3		13.851
Q3	from tables	0.0375
Q3*cosα3		0.0278
α3 (degrees)	$\cos^{-1}$(0.0278/Q3)	42.10
1st rotor exit axial velocity Va2 (m/s)	Vw3/tanα3	190.230
Third approximation to rotor exit axial velocity		
Va2 (m/s)	(182.151+190.230)/2	186.190
1st rotor absolute exit velocity V3 (m/s)	((Vw3^2)+(Va2^2))^0.5	253.390
V3/√T3		14.015
Q3	from tables	0.0377
Q3*cosα3		0.0278
α3 (degrees)	$\cos^{-1}$(0.0278/Q3)	42.43
1st rotor exit axial velocity Va2 (m/s)	Vw3/tanα3	188.006
Fourth approximation to rotor exit axial velocity		
Va2 (m/s)		187.098
1st rotor absolute exit velocity V3 (m/s)	((Vw3^2)+(Va2^2))^0.5	254.057
V3/√T3		14.052
Q3	from tables	0.0378
Q3*cosα3		0.0278
α3 (degrees)	$\cos^{-1}$(0.0278/Q3)	42.60
1st rotor exit axial velocity Va2 (m/s)	Vw3/tanα3	186.919
1st rotor DeHaller number V2/V1	(Va2/cosα2)*(cosα1/Va1)	0.869
1st stator DeHaller number V4/V3	(Va1/cosα4)*(cosα3/Va2)	0.630
Vo/√T1	(Va1/cosα1)/√T1	14.808
Rotor inlet absolute Mach number Mo	from tables	0.783
Rotor inlet relative Mach number M1	Mocosα0/cosα1	1.154
V3	Va2/cosα3	276.403
V3/√T3		15.288
Rotor exit absolute Mach number M3	from tables	0.811

Compressor exit

Compressor exit total temperature Texit (K)	T1+ ΔTc	674.523
Va1/√Texit		6.075
Qoexit	from tables	0.0202
K_{Bexit}		0.880

Blade design data

IGV T6 blade

T6 profile		
blade inlet metal angle γ'0(degrees)		0
blade inlet flow angle γ0 (degrees)		0
blade incidence i (degrees)	γ0-γ'0	0
outflow absolute blade angle α0 (degrees)	assumption	25
blade deviation δ1 (degrees)	assumption	5
outlet blade metal angle α'0 (degrees)	α0+ δ1	30
stagger angle ζ1 (degrees)	(γ'0+α'0)/2	15
camber angle θ1 (degrees)	γ'0-α'0	-30

Rotor blade

NACA65 thickened profile		
blade inlet flow angle α1 (degrees)		52.05
blade inlet metal angle α'1(degrees)		52.05
blade incidence i (degrees)	α1-α'1	0
outflow relative blade angle α2 (degrees)		33.01
blade deviation δ2 (degrees)	assumption	8
outlet blade metal angle α'2 (degrees)	α2- δ2	25.01
outflow absolute blade angle α3 (degrees)		47.45
stagger angle ζ2 (degrees)	(α'1+α'2)/2	38.53
camber angle θ2 (degrees)	α'1-α'2	27.04

Stator blade

NACA65 thickened profile		
blade inlet metal angle α'3(degrees)		47.45
blade inlet flow angle α3 (degrees)		47.45
blade incidence i (degrees)	α3-α'3	0
outflow relative blade angle α4 (degrees)	assumption	25
blade deviation δ3 (degrees)	assumption	8
outlet blade metal angle α'4 (degrees)	α4- δ3	17
stagger angle ζ3 (degrees)	(α'3+α'4)/2	32.23
camber angle θ3 (degrees)	α'3-α'4	30.45

Preliminary cascade CFD results related to performance deterioration

	clean blades	fouling 1	fouling 2	fouling 3	fouling 4	fouling 5
Cascade inlet conditions **P_{inlet}=101591.6 Pa** **T_{inlet}=293.15 K**		**63** microns	**76** microns	**102** microns	**160** microns	**254** microns
α_1 (deg)	51	51	51	51	51	51
α_2 (deg)	30.5	32.5	32.6	32.7	33.2	33.4
P_1 (Pa)	101181	101224	101225	101228	101205	101227
p_1 (Pa)	89509	89758	89793	89847	89986	90013
P_2 (Pa)	100738	100716	100709	100699	100630	100624
p_2 (Pa)	94647	94493	94490	94486	94410	94407
$\Delta po=P_1-P_2$ (Pa)	442.6	507.7	516.2	529.3	574.6	602.9
$M_1=[(2/(\gamma-1))((P_1/p_1)^{((\gamma-1)/\gamma)}-1)]^{0.5}$	0.422	0.418	0.417	0.416	0.413	0.413
T_1 (K)	293.15	293.15	293.15	293.15	293.15	293.15
$t_1=T_1/[1+((\gamma-1)/2)M_1^2]$ (K)	283.061	283.252	283.282	283.329	283.473	283.480
$\rho=p_1/Rt_1$	1.102	1.104	1.104	1.105	1.106	1.106
A (m^2)	0.043	0.043	0.043	0.043	0.043	0.043
$c_1=M_1(\gamma Rt_1)^{0.5}$	142.366	141.011	140.800	140.464	139.433	139.384
$m_{inlet}=\rho Ac_1$ calculated results	6.823	6.773	6.764	6.751	6.708	6.708
$m_{outletFLUENT}=m_{inletFLUENT}=W_1$	6.705	6.649	6.643	6.616	6.607	6.602
$m_{deterioration}/m_{clean}$		0.992	0.991	0.987	0.985	0.985
Δm%	0	0.835	0.925	1.327	1.462	1.536
$W_1T_1^{0.5}/P_1$	0.001135	0.001125	0.001124	0.001119	0.001118	0.001117
$\Delta(W_1T_1^{0.5}/P_1)$%	0.000	0.877	0.968	1.373	1.485	1.581
$\Phi=c_x/U=1/(\tan\alpha_1+\tan\alpha_2)$	0.548	0.534	0.533	0.533	0.529	0.528
λ	0.84	0.84	0.84	0.84	0.84	0.84
$\psi=\Delta H/U^2=\lambda\Phi(\tan\alpha_1-\tan\alpha_2)$	0.297	0.268	0.267	0.265	0.258	0.255
$\alpha_m=\text{atan}((\tan\alpha_1+\tan\alpha_2)/2)$	42.36	43.11	43.14	43.18	43.37	43.44
$C_L=2(s/l)\cos\alpha_m(\tan\alpha_1-\tan\alpha_2)$	0.764	0.698	0.695	0.692	0.675	0.669
$C_{Dp}=(s/l)(\Delta po/0.5\rho c_1^2)(\cos^3\alpha_m/\cos^2\alpha_1)$	0.032	0.036	0.037	0.038	0.041	0.043
$C_{Da}=0.02(s/l)(l/H)$	0.0053	0.0053	0.0053	0.0053	0.0053	0.0053
$C_{Ds}=0.018C_L^2$	0.0105	0.0088	0.0087	0.0086	0.0082	0.0080
$C_D=C_{Dp}+C_{Da}+C_{Ds}$	0.048	0.050	0.051	0.052	0.055	0.057
C_D/C_L	0.0628	0.0716	0.0734	0.0751	0.0815	0.0852
$c_p\Delta T_s/0.5U^2=2\lambda(c_x/U)(\tan\alpha_1-\tan\alpha_2)$	0.595	0.537	0.534	0.531	0.516	0.510
$\eta_s=1-(2/\sin2\alpha_m)(C_D/C_L)=\eta_p$	0.873	0.855	0.853	0.849	0.837	0.830
$\Delta P_s/0.5\rho U^2=\eta_s c_p\Delta T_s/0.5U^2$	0.520	0.459	0.455	0.451	0.432	0.424
R	14.6	14.6	14.6	14.6	14.6	14.6
$\Delta l=\eta_{pclean}-\eta_{pfouled}$	0.000	0.018	0.021	0.024	0.037	0.043
Δl%	0.000	2.090	2.352	2.746	4.191	4.970
$\eta_{pcleanABBGT13E2}=[(\gamma-1)/\gamma][\log(P_2/P_1)]_{DP}/[\log(T_2/T_1)]_{DP}$	0.919					
$\eta_{pfouledABBGT13E2}=\eta_{pcleanABBGT13E2}-\Delta l$	0.919	0.901	0.898	0.895	0.882	0.876

Preliminary performance deterioration by applying 254 microns particles (TET=1100 K)

```
TURBOMATCH SCHEME - Windows NT version (October 1999)

 LIMITS:100 Codewords, 800 Brick Data Items, 50 Station Vector
 15 BD Items printable by any call of:-
 OUTPUT, OUTPBD, OUTPSV, PLOTIT, PLOTBD or PLOTSV

  Input "Program" follows

 ! INDUSTRIAL GAS TURBINE:

 ABB GT13E2 POWER GENERATION

 50 Hz SIMPLE CYCLE

 MODELLED BY P.SCHWABE / SME / AUGUST 1997


 OD SI KE CT XP
  -1
  -1
 INTAKE S1-2        D1-4               R300
 ARITHY             D310-317
 ARITHY             D320-327
 COMPRE S2-3        D5-11              R301      V5   V6
 PREMAS S3,4,9      D12-15
 BURNER S4-5        D16-18             R303
 MIXEES S5,9,6
 TURBIN S6-7        D19-26,301,27                V19  V20
 NOZCON S7-8,1      D28                R305
 PERFOR S1,0,0      D19,29-31,305,300,303,0,0,0,0,0,0,0
 CODEND



 BRICK DATA ITEMS
 ! INTAKE
 1 0.0           ! ALTITUDE
 2 0.0           ! ISA DEVIATION:Tamb=288.15 K, Pamb=1.01325 bar
 3 0.0           ! MACH NUMBER
 4 0.9951        ! PRESSURE RECOVERY
 ! COMPRESSOR
 5 -1.0          ! SURGE MARGIN
 6 0.6           ! DESIGN SPEED
 7 14.6          ! DESIGN PRESSURE RATIO
 8 0.885         ! ISENTRIOPIC EFFICIENCY
 9 1.0           ! ERROR SELECTION
 10 3.0          ! COMPRESSOR MAP NUMBER
 11 0.0          ! RELATIV TO DP VARIABLE STATOR ANGLE
 ! SPLITTER
 12 0.96         ! LAMBDA (W)
 13 0.0          ! DELTA (W)
 14 1.0          ! LAMBDA (P)
 15 0.0          ! DELTA (P)
 ! BURNER
 16 0.07         ! PRESSURE LOSS 0%
 17 0.998        ! EFFICIENCY
 18 -1.0         ! FUEL FLOW (-1 = TET SPECIFIED. SEE SV DATA)
```

```
 ! POWER TURBINE
 19 165100000.0  ! AUXILLARY POWER REQUIRED
 20 0.8          ! NON DIMENTIONAL MASS FLOW
 21 0.6          ! NON DIMENTIONAL SPEED
 22 0.90         ! ISENTROPIC EFFICIENCY
 23 -1.0         ! RELATIV ROTATIONAL SPEED
 24 1.0          ! COMPRESSOR NUMBER
 25 3.0          ! TURBINE MAP NUMBER
 26 1000.0       ! POWER INDEX N
 27 0.0          ! ANGLE
 ! NOZCON
 28 -1.0         ! AREA FIXED
 ! PERFORMANCE
 29 1.0          ! PROPELLER EFFICIENCY
 30 0.0          ! SCALLING INDEX
 31 0.0          ! REQUIRED DP NET THRUST OR POWER OUTPUT FOR PT

 310 3.0         ! COMPRESSOR 1, BD(820)=BD(820)*BD(317)
 311 -1.0
 312 820.0       ! ETASF FOR COMPRESSOR 1
 313 -1.0
 314 820.0
 315 -1.0
 316 317.0
 317 1.0         ! COMPRESSOR 1 DETERIORATION OF 0% IN EFFICIENCY

 320 3.0         ! COMPRESSOR 1, BD(830)=BD(830)*BD(327)
 321 -1.0
 322 830.0       ! WASF FOR COMPRESSOR 1
 323 -1.0
 324 830.0
 325 -1.0
 326 327.0
 327 1.0         ! COMPRESSOR 1 DETERIORATION OF 0% IN NON-
DIMENSIONAL MASS FLOW
 -1
 1 2 532.00      ! MASS FLOW
 5 6 1378.0      ! TURBINE ENTRY TEMPERATURE
 -1
                                                    Time Now 21:15:37

 ***********************************************




                 The Units for this Run are as follows:-

 Temperature = K   Pressure = Atmospheres   Length = metres

 Area = sq metres  Mass Flow = kg/sec       Velocity = metres/sec

 Force = Newtons   s.f.c.(Thrust) =  mg/N sec   s.f.c.(Power) = mug/J

 Sp. Thrust =    N/kg/sec     Power =   Watts
1

      ***** DESIGN POINT ENGINE CALCULATIONS *****
```

```
 ***** AMBIENT AND INLET PARAMETERS *****
 Alt. =      0.0      I.S.A. Dev. =    0.000       Mach No. =  0.00
 Etar = 0.9951        Momentum Drag =      0.00

 ***** COMPRESSOR  1 PARAMETERS *****
 PRSF =  0.41221E+01     ETASF =  0.12801E+01     WASF =  0.10776E+02
 Z = 0.85000             PR =  14.600             ETA = 0.88500
 PCN =   0.6000          CN = 0.60000             COMWK =
0.19960E+09

 ***** COMBUSTION CHAMBER PARAMETERS *****
 ETASF =  0.99800E+00
 ETA = 0.99800           DLP = 1.0170             WFB =  10.6464

 ***** TURBINE  1 PARAMETERS *****
 CNSF =  0.16852E+03     ETASF =  0.10039E+01     TFSF =  0.29182E+00
 DHSF =  0.14727E+05
 TF =  430.924            ETA = 0.90000            CN =  2.750
 AUXWK =  0.16510E+09

 ***** CONVERGENT NOZZLE  1 PARAMETERS *****
 NCOSF =  0.10000E+01
 Area = 11.5315          Exit Velocity =  104.24  Gross Thrust =
54947.68
 Nozzle Coeff. =  0.97144E+00



 Scale Factor on above Mass Flows, Areas, Thrusts & Powers =
1.0000



 Station  F.A.R. Mass Flow   Pstatic    Ptotal Tstatic  Ttotal
Vel    Area
     1   0.00000   532.000   1.00000   1.00000  288.15  288.15
0.0  ******
     2   0.00000   532.000    ******   0.99510  ******  288.15
******  ******
     3   0.00000   532.000    ******  14.52847  ******  653.49
******  ******
     4   0.00000   510.720    ******  14.52847  ******  653.49
******  ******
     5   0.02085   521.366    ******  13.51148  ****** 1378.00
******  ******
     6   0.02001   542.646    ******  13.51148  ****** 1351.90
******  ******
     7   0.02001   542.646    ******   1.02467  ******  786.84
******  ******
     8   0.02001   542.646   1.00000   1.02467  782.03  786.84
104.2 11.5315
     9   0.00000    21.280    ******  14.52847  ******  653.49
******  ******


   Shaft Power = 165100000.00
    Net Thrust = 54947.68
```

```
  Equiv. Power = 168642864.00
     Fuel Flow =  10.6464
        S.F.C. =  64.4846
     E.S.F.C. =  63.1299
 Sp. Sh. Power =    310338.34
 Sp. Eq. Power =    316997.84
 Sh. Th. Effy. =   0.3596
           Time Now 21:15:37

 ********************************************
 317 0.9503      ! COMPRE 1 DETERIORATION OF 4.970% IN EFFICIENCY
 327 0.98419     ! COMPRE 1 DETERIORATION OF 1.581% IN NON-
DIMENSIONAL MASS FLOW
 -1
 5 6 1100
 -1
                                                      Time Now 21:15:37

 ********************************************
 BERR( 1) =   -0.16064E-01
 BERR( 2) =    0.14480E+00
 BERR( 3) =   -0.13382E+00
 BERR( 4) =   -0.75745E+00

 Loop   1
 BERR( 1) =    0.11947E-01
 BERR( 2) =    0.55384E-02
 BERR( 3) =    0.44338E-01
 BERR( 4) =   -0.85567E-02

 Loop   2
 BERR( 1) =   -0.39292E-03
 BERR( 2) =    0.59184E-03
 BERR( 3) =    0.27685E-01
 BERR( 4) =   -0.94479E-02

 Loop   3
 BERR( 1) =   -0.52606E-03
 BERR( 2) =    0.81071E-04
 BERR( 3) =    0.17683E-01
 BERR( 4) =   -0.49542E-02

 Loop   4
 BERR( 1) =   -0.35383E-03
 BERR( 2) =   -0.52465E-05
 BERR( 3) =    0.11094E-01
 BERR( 4) =   -0.30408E-02

 Loop   5
 BERR( 1) =   -0.22645E-03
 BERR( 2) =   -0.21533E-04
 BERR( 3) =    0.69435E-02
 BERR( 4) =   -0.18843E-02

 Loop   6
 BERR( 1) =   -0.14328E-03
 BERR( 2) =   -0.19083E-04
 BERR( 3) =    0.43344E-02
 BERR( 4) =   -0.12029E-02
1
```

```
      ***** OFF DESIGN ENGINE CALCULATIONS. Converged after   6 Loops
*****



 ***** AMBIENT AND INLET PARAMETERS *****
 Alt. =      0.0      I.S.A. Dev. =    0.000       Mach No. =  0.00
 Etar = 0.9951        Momentum Drag =      0.00

 ***** COMPRESSOR  1 PARAMETERS *****
 PRSF =  0.41221E+01     ETASF =  0.12165E+01     WASF =  0.10605E+02
 Z = 0.79351             PR =  13.683             ETA = 0.84723
 PCN =   0.5995          CN = 0.59955             COMWK =
0.20028E+09

 ***** COMBUSTION CHAMBER PARAMETERS *****
 ETASF =  0.99800E+00
 ETA = 0.99800           DLP = 1.0784             WFB =   6.1945

 ***** TURBINE  1 PARAMETERS *****
 CNSF =  0.16852E+03     ETASF =  0.10039E+01     TFSF =  0.29182E+00
 DHSF =  0.14727E+05
 TF =  410.055            ETA = 0.89695            CN =  3.070
 AUXWK =  0.77492E+08

 ***** CONVERGENT NOZZLE  1 PARAMETERS *****
 NCOSF =  0.10000E+01
 Area = 11.5315          Exit Velocity =   81.61  Gross Thrust =
42430.90
 Nozzle Coeff. =  0.97132E+00



 Scale Factor on above Mass Flows, Areas, Thrusts & Powers =
1.0000



 Station  F.A.R. Mass Flow   Pstatic    Ptotal Tstatic  Ttotal
Vel    Area
     1   0.00000   529.050   1.00000   1.00000  288.15  288.15
0.0  ******
     2   0.00000   529.050    ******   0.99510  ******  288.15
******  ******
     3   0.00000   529.050    ******  13.61614  ******  656.66
******  ******
     4   0.00000   507.888    ******  13.61614  ******  656.66
******  ******
     5   0.01220   514.083    ******  12.53778  ****** 1100.00
******  ******
     6   0.01171   535.245    ******  12.53778  ****** 1083.45
******  ******
     7   0.01171   535.245    ******   1.01788  ******  623.93
******  ******
     8   0.01171   535.245   1.00000   1.01788  620.78  623.93
81.6 11.5315
     9   0.00000    21.162    ******  13.61614  ******  656.66
******  ******
```

```
   Shaft Power =  77492448.00
    Net Thrust = 42430.90
  Equiv. Power =  80228264.00
     Fuel Flow =   6.1945
        S.F.C. =  79.9365
     E.S.F.C. =  77.2106
 Sp. Sh. Power =    146474.62
 Sp. Eq. Power =    151645.81
 Sh. Th. Effy. =   0.2901
           Time Now 21:15:37

 ***********************************************
 -3
```

Preliminary performance deterioration by applying 254 microns particles (TET=1200 K)

```
***********************************************
 317 0.9503      ! COMPRE 1 DETERIORATION OF 4.970% IN EFFICIENCY
 327 0.98419     ! COMPRE 1 DETERIORATION OF 1.581% IN NON-
DIMENSIONAL MASS FLOW
 -1
 5 6 1200
 -1
                                                    Time Now 21:16:23

 ***********************************************
 BERR( 1) =   -0.16064E-01
 BERR( 2) =    0.93896E-01
 BERR( 3) =   -0.93891E-01
 BERR( 4) =   -0.56216E+00

 Loop   1
 BERR( 1) =    0.87522E-02
 BERR( 2) =    0.20001E-02
 BERR( 3) =    0.18068E-01
 BERR( 4) =    0.11622E-01

 Loop   2
 BERR( 1) =   -0.14248E-03
 BERR( 2) =    0.16553E-03
 BERR( 3) =    0.75373E-02
 BERR( 4) =   -0.45981E-02

 Loop   3
 BERR( 1) =   -0.22357E-03
 BERR( 2) =    0.50443E-04
 BERR( 3) =    0.44925E-02
 BERR( 4) =   -0.19010E-02
1

      ***** OFF DESIGN ENGINE CALCULATIONS. Converged after   3 Loops
*****


 ***** AMBIENT AND INLET PARAMETERS *****
```

```
 Alt. =      0.0      I.S.A. Dev. =    0.000       Mach No. =  0.00
 Etar = 0.9951        Momentum Drag =      0.00

 ***** COMPRESSOR  1 PARAMETERS *****
 PRSF =  0.41221E+01     ETASF =  0.12165E+01     WASF =  0.10605E+02
 Z = 0.80653             PR =  13.897             ETA = 0.84740
 PCN =   0.5997          CN = 0.59973             COMWK =
0.20153E+09

 ***** COMBUSTION CHAMBER PARAMETERS *****
 ETASF =  0.99800E+00
 ETA = 0.99800           DLP = 1.0623             WFB =   7.6643

 ***** TURBINE  1 PARAMETERS *****
 CNSF =  0.16852E+03     ETASF =  0.10039E+01     TFSF =  0.29182E+00
 DHSF =  0.14727E+05
 TF =  420.660            ETA = 0.90134            CN =  2.942
 AUXWK =  0.10591E+09

 ***** CONVERGENT NOZZLE  1 PARAMETERS *****
 NCOSF =  0.10000E+01
 Area = 11.5315          Exit Velocity =   89.19  Gross Thrust =
46410.66
 Nozzle Coeff. =  0.97134E+00


 Scale Factor on above Mass Flows, Areas, Thrusts & Powers =
1.0000



 Station  F.A.R. Mass Flow   Pstatic    Ptotal Tstatic  Ttotal
Vel    Area
     1   0.00000   528.019   1.00000   1.00000  288.15  288.15
0.0  ******
     2   0.00000   528.019    ******   0.99510  ******  288.15
******  ******
     3   0.00000   528.019    ******  13.82871  ******  659.57
******  ******
     4   0.00000   506.898    ******  13.82871  ******  659.57
******  ******
     5   0.01512   514.562    ******  12.76640  ****** 1200.00
******  ******
     6   0.01452   535.683    ******  12.76640  ****** 1180.08
******  ******
     7   0.01452   535.683    ******   1.01901  ******  681.59
******  ******
     8   0.01452   535.683   1.00000   1.01901  677.88  681.59
89.2 11.5315
     9   0.00000    21.121    ******  13.82871  ******  659.57
******  ******


   Shaft Power = 105910768.00
    Net Thrust = 46410.65
  Equiv. Power = 108903184.00
     Fuel Flow =   7.6643
        S.F.C. =  72.3661
     E.S.F.C. =  70.3776
```

```
 Sp. Sh. Power =    200581.42
 Sp. Eq. Power =    206248.69
 Sh. Th. Effy. =   0.3204
           Time Now 21:16:23

 ***********************************************
 -3
```

Preliminary performance deterioration by applying 254 microns particles (TET=1300 K)

```
 ***********************************************
 317 0.9503      ! COMPRE 1 DETERIORATION OF 4.970% IN EFFICIENCY
 327 0.98419     ! COMPRE 1 DETERIORATION OF 1.581% IN NON-
DIMENSIONAL MASS FLOW
 -1
 5 6 1300
 -1
                                                    Time Now 21:17:14

 ***********************************************
 BERR( 1) =   -0.16064E-01
 BERR( 2) =    0.48649E-01
 BERR( 3) =   -0.57662E-01
 BERR( 4) =   -0.32980E+00

 Loop   1
 BERR( 1) =    0.52799E-02
 BERR( 2) =    0.46682E-03
 BERR( 3) =    0.11167E-01
 BERR( 4) =    0.14987E-01

 Loop   2
 BERR( 1) =   -0.80900E-04
 BERR( 2) =    0.34486E-04
 BERR( 3) =    0.88705E-03
 BERR( 4) =   -0.31452E-02
1

      ***** OFF DESIGN ENGINE CALCULATIONS. Converged after   2 Loops
*****



 ***** AMBIENT AND INLET PARAMETERS *****
 Alt. =      0.0      I.S.A. Dev. =    0.000       Mach No. =  0.00
 Etar = 0.9951        Momentum Drag =      0.00

 ***** COMPRESSOR  1 PARAMETERS *****
 PRSF =  0.41221E+01     ETASF =  0.12165E+01     WASF =  0.10605E+02
 Z = 0.82377             PR =  14.176             ETA = 0.84536
 PCN =   0.5999          CN = 0.59987             COMWK =
0.20352E+09

 ***** COMBUSTION CHAMBER PARAMETERS *****
 ETASF =  0.99800E+00
 ETA = 0.99800           DLP = 1.0421             WFB =   9.1373
```

```
 ***** TURBINE  1 PARAMETERS *****
 CNSF =  0.16852E+03     ETASF =  0.10039E+01     TFSF =  0.29182E+00
 DHSF =  0.14727E+05
 TF =  427.388            ETA = 0.90169            CN =  2.829
 AUXWK =  0.13296E+09

 ***** CONVERGENT NOZZLE  1 PARAMETERS *****
 NCOSF =  0.10000E+01
 Area = 11.5315          Exit Velocity =   96.89  Gross Thrust =
50394.01
 Nozzle Coeff. =  0.97135E+00



 Scale Factor on above Mass Flows, Areas, Thrusts & Powers =
1.0000



 Station  F.A.R. Mass Flow   Pstatic    Ptotal Tstatic  Ttotal
Vel    Area
     1   0.00000   526.326   1.00000   1.00000  288.15  288.15
0.0  ******
     2   0.00000   526.326    ******   0.99510  ******  288.15
******  ******
     3   0.00000   526.326    ******  14.10695  ******  664.28
******  ******
     4   0.00000   505.273    ******  14.10695  ******  664.28
******  ******
     5   0.01808   514.410    ******  13.06485  ****** 1300.00
******  ******
     6   0.01736   535.463    ******  13.06485  ****** 1276.84
******  ******
     7   0.01736   535.463    ******   1.01959  ******  740.96
******  ******
     8   0.01736   535.463   1.00000   1.01959  736.66  740.96
96.9 11.5315
     9   0.00000    21.053    ******  14.10695  ******  664.28
******  ******


   Shaft Power = 132962048.00
    Net Thrust = 50394.01
  Equiv. Power = 136211296.00
     Fuel Flow =   9.1373
        S.F.C. =  68.7214
     E.S.F.C. =  67.0821
 Sp. Sh. Power =    252623.12
 Sp. Eq. Power =    258796.59
 Sh. Th. Effy. =   0.3374
           Time Now 21:17:14

 ********************************************
 -3
```

Preliminary performance deterioration by applying 254 microns particles (TET=1400 K)

```
 ***********************************************
 317 0.9503      ! COMPRE 1 DETERIORATION OF 4.970% IN EFFICIENCY
 327 0.98419     ! COMPRE 1 DETERIORATION OF 1.581% IN NON-
DIMENSIONAL MASS FLOW
 -1
 5 6 1400
 -1
                                                    Time Now 21:17:55

 ***********************************************
 BERR( 1) =   -0.16064E-01
 BERR( 2) =    0.80558E-02
 BERR( 3) =   -0.29352E-01
 BERR( 4) =   -0.61439E-01

 Loop   1
 BERR( 1) =    0.14659E-02
 BERR( 2) =   -0.19475E-04
 BERR( 3) =    0.98116E-02
 BERR( 4) =   -0.31813E-02

 Loop   2
 BERR( 1) =   -0.36856E-03
 BERR( 2) =    0.24042E-04
 BERR( 3) =   -0.71954E-02
 BERR( 4) =    0.81991E-02

 Loop   3
 BERR( 1) =    0.32916E-03
 BERR( 2) =   -0.20837E-04
 BERR( 3) =    0.60884E-02
 BERR( 4) =   -0.77392E-02

 Loop   4

 Loop   5
 BERR( 1) =   -0.15304E-03
 BERR( 2) =   -0.49903E-06
 BERR( 3) =    0.16930E-03
 BERR( 4) =    0.46020E-03
1

      ***** OFF DESIGN ENGINE CALCULATIONS. Converged after   5 Loops
*****



 ***** AMBIENT AND INLET PARAMETERS *****
 Alt. =      0.0      I.S.A. Dev. =    0.000       Mach No. =  0.00
 Etar = 0.9951        Momentum Drag =      0.00

 ***** COMPRESSOR  1 PARAMETERS *****
 PRSF =  0.41221E+01     ETASF =  0.12165E+01     WASF =  0.10605E+02
 Z = 0.84367             PR =  14.498             ETA = 0.84207
 PCN =   0.6000          CN = 0.59998             COMWK =
0.20596E+09
```

```
 ***** COMBUSTION CHAMBER PARAMETERS *****
 ETASF =  0.99800E+00
 ETA = 0.99800           DLP = 1.0198             WFB =  10.6226

 ***** TURBINE  1 PARAMETERS *****
 CNSF =  0.16852E+03     ETASF =  0.10039E+01     TFSF =  0.29182E+00
 DHSF =  0.14727E+05
 TF =  431.501            ETA = 0.89958            CN =  2.728
 AUXWK =  0.15864E+09

 ***** CONVERGENT NOZZLE  1 PARAMETERS *****
 NCOSF =  0.10000E+01
 Area = 11.5315          Exit Velocity =  104.79  Gross Thrust =
54449.79
 Nozzle Coeff. =  0.97145E+00



 Scale Factor on above Mass Flows, Areas, Thrusts & Powers =
1.0000



 Station  F.A.R. Mass Flow   Pstatic    Ptotal Tstatic  Ttotal
Vel    Area
     1   0.00000   524.257   1.00000   1.00000  288.15  288.15
0.0  ******
     2   0.00000   524.257    ******   0.99510  ******  288.15
******  ******
     3   0.00000   524.257    ******  14.42688  ******  670.07
******  ******
     4   0.00000   503.287    ******  14.42688  ******  670.07
******  ******
     5   0.02111   513.909    ******  13.40709  ****** 1400.00
******  ******
     6   0.02026   534.880    ******  13.40709  ****** 1373.70
******  ******
     7   0.02026   534.880    ******   1.02517  ******  802.55
******  ******
     8   0.02026   534.880   1.00000   1.02517  797.60  802.55
104.8 11.5315
     9   0.00000    20.970    ******  14.42688  ******  670.07
******  ******


   Shaft Power = 158636496.00
    Net Thrust = 54449.79
  Equiv. Power = 162147248.00
     Fuel Flow =  10.6226
        S.F.C. =  66.9621
      E.S.F.C. =  65.5123
 Sp. Sh. Power =    302593.03
 Sp. Eq. Power =    309289.69
 Sh. Th. Effy. =   0.3463
           Time Now 21:17:55

 ********************************************
 -3
```

Preliminary performance deterioration by applying 254 microns particles (TET=1500 K)

```
*********************************************
 317 0.9503      ! COMPRE 1 DETERIORATION OF 4.970% IN EFFICIENCY
 327 0.98419     ! COMPRE 1 DETERIORATION OF 1.581% IN NON-
DIMENSIONAL MASS FLOW
 -1
 5 6 1500
 -1
                                                    Time Now 21:18:42

 *********************************************
 BERR( 1) =   -0.16064E-01
 BERR( 2) =   -0.28655E-01
 BERR( 3) =    0.10992E-01
 BERR( 4) =    0.21145E+00

 Loop   1
 BERR( 1) =   -0.16199E-02
 BERR( 2) =    0.22914E-03
 BERR( 3) =    0.46969E-01
 BERR( 4) =   -0.81434E-01

 Loop   2
 BERR( 1) =   -0.32014E-02
 BERR( 2) =   -0.27115E-03
 BERR( 3) =   -0.49713E-01
 BERR( 4) =    0.64817E-01

 Loop   3

 Loop   4
 BERR( 1) =    0.33330E-02
 BERR( 2) =   -0.46247E-03
 BERR( 3) =    0.56151E-01
 BERR( 4) =   -0.63144E-01

 Loop   5
 BERR( 1) =   -0.13083E-02
 BERR( 2) =   -0.69308E-04
 BERR( 3) =    0.51608E-03
 BERR( 4) =    0.26339E-02
1

      ***** OFF DESIGN ENGINE CALCULATIONS. Converged after   5 Loops
*****



 ***** AMBIENT AND INLET PARAMETERS *****
 Alt. =      0.0      I.S.A. Dev. =    0.000       Mach No. =  0.00
 Etar = 0.9951        Momentum Drag =      0.00

 ***** COMPRESSOR  1 PARAMETERS *****
 PRSF =  0.41221E+01     ETASF =  0.12165E+01     WASF =  0.10605E+02
 Z = 0.86392             PR =  14.825             ETA = 0.83871
 PCN =   0.6001          CN = 0.60006             COMWK =
0.20839E+09
```

```
 ***** COMBUSTION CHAMBER PARAMETERS *****
 ETASF =  0.99800E+00
 ETA = 0.99800           DLP = 0.9979             WFB =  12.1374

 ***** TURBINE  1 PARAMETERS *****
 CNSF =  0.16852E+03     ETASF =  0.10039E+01     TFSF =  0.29182E+00
 DHSF =  0.14727E+05
 TF =  434.673            ETA = 0.89577            CN =  2.637
 AUXWK =  0.18394E+09

 ***** CONVERGENT NOZZLE  1 PARAMETERS *****
 NCOSF =  0.10000E+01
 Area = 11.5315          Exit Velocity =  112.85  Gross Thrust =
58574.78
 Nozzle Coeff. =  0.97152E+00



 Scale Factor on above Mass Flows, Areas, Thrusts & Powers =
1.0000



 Station  F.A.R. Mass Flow   Pstatic    Ptotal Tstatic  Ttotal
Vel    Area
     1   0.00000   522.134   1.00000   1.00000  288.15  288.15
0.0  ******
     2   0.00000   522.134    ******   0.99510  ******  288.15
******  ******
     3   0.00000   522.134    ******  14.75210  ******  675.92
******  ******
     4   0.00000   501.248    ******  14.75210  ******  675.92
******  ******
     5   0.02421   513.386    ******  13.75421  ****** 1500.00
******  ******
     6   0.02325   534.271    ******  13.75421  ****** 1470.64
******  ******
     7   0.02325   534.271    ******   1.02932  ******  865.56
******  ******
     8   0.02325   534.271   1.00000   1.02932  859.92  865.56
112.8 11.5315
     9   0.00000    20.885    ******  14.75210  ******  675.92
******  ******


   Shaft Power = 183943488.00
    Net Thrust = 58574.79
  Equiv. Power = 187720208.00
     Fuel Flow =  12.1374
        S.F.C. =  65.9843
      E.S.F.C. =  64.6568
 Sp. Sh. Power =    352292.00
 Sp. Eq. Power =    359525.25
 Sh. Th. Effy. =   0.3514
           Time Now 21:18:42

 ********************************************
 -3
```

Experimental related performance deterioration by applying 102 microns particles (TET=1100 K).

```
TURBOMATCH SCHEME - Windows NT version (October 1999)

 LIMITS:100 Codewords, 800 Brick Data Items, 50 Station Vector
 15 BD Items printable by any call of:-
 OUTPUT, OUTPBD, OUTPSV, PLOTIT, PLOTBD or PLOTSV

  Input "Program" follows

 ! INDUSTRIAL GAS TURBINE:

 ABB GT13E2 POWER GENERATION

 50 Hz SIMPLE CYCLE

 MODELLED BY P.SCHWABE / SME / AUGUST 1997


 OD SI KE CT XP
  -1
  -1
 INTAKE S1-2        D1-4               R300
 ARITHY             D310-317
 ARITHY             D320-327
 COMPRE S2-3        D5-11              R301      V5   V6
 PREMAS S3,4,9      D12-15
 BURNER S4-5        D16-18             R303
 MIXEES S5,9,6
 TURBIN S6-7        D19-26,301,27                V19  V20
 NOZCON S7-8,1      D28                R305
 PERFOR S1,0,0      D19,29-31,305,300,303,0,0,0,0,0,0,0
 CODEND



 BRICK DATA ITEMS
 ! INTAKE
 1 0.0           ! ALTITUDE
 2 0.0           ! ISA DEVIATION:Tamb=288.15 K, Pamb=1.01325 bar
 3 0.0           ! MACH NUMBER
 4 0.9951        ! PRESSURE RECOVERY
 ! COMPRESSOR
 5 -1.0          ! SURGE MARGIN
 6 0.6           ! DESIGN SPEED
 7 14.6          ! DESIGN PRESSURE RATIO
 8 0.885         ! ISENTRIOPIC EFFICIENCY
 9 1.0           ! ERROR SELECTION
 10 3.0          ! COMPRESSOR MAP NUMBER
 11 0.0          ! RELATIV TO DP VARIABLE STATOR ANGLE
 ! SPLITTER
 12 0.96         ! LAMBDA (W)
 13 0.0          ! DELTA (W)
 14 1.0          ! LAMBDA (P)
 15 0.0          ! DELTA (P)
 ! BURNER
 16 0.07         ! PRESSURE LOSS 0%
 17 0.998        ! EFFICIENCY
 18 -1.0         ! FUEL FLOW (-1 = TET SPECIFIED. SEE SV DATA)
```

```
 ! POWER TURBINE
 19 165100000.0  ! AUXILLARY POWER REQUIRED
 20 0.8          ! NON DIMENTIONAL MASS FLOW
 21 0.6          ! NON DIMENTIONAL SPEED
 22 0.90         ! ISENTROPIC EFFICIENCY
 23 -1.0         ! RELATIV ROTATIONAL SPEED
 24 1.0          ! COMPRESSOR NUMBER
 25 3.0          ! TURBINE MAP NUMBER
 26 1000.0       ! POWER INDEX N
 27 0.0          ! ANGLE
 ! NOZCON
 28 -1.0         ! AREA FIXED
 ! PERFORMANCE
 29 1.0          ! PROPELLER EFFICIENCY
 30 0.0          ! SCALLING INDEX
 31 0.0          ! REQUIRED DP NET THRUST OR POWER OUTPUT FOR PT

 310 3.0         ! COMPRESSOR 1, BD(820)=BD(820)*BD(317)
 311 -1.0
 312 820.0       ! ETASF FOR COMPRESSOR 1
 313 -1.0
 314 820.0
 315 -1.0
 316 317.0
 317 1.0         ! COMPRESSOR 1 DETERIORATION OF 0% IN EFFICIENCY

 320 3.0         ! COMPRESSOR 1, BD(830)=BD(830)*BD(327)
 321 -1.0
 322 830.0       ! WASF FOR COMPRESSOR 1
 323 -1.0
 324 830.0
 325 -1.0
 326 327.0
 327 1.0         ! COMPRESSOR 1 DETERIORATION OF 0% IN NON-
DIMENSIONAL MASS FLOW
 -1
 1 2 532.00      ! MASS FLOW
 5 6 1378.0      ! TURBINE ENTRY TEMPERATURE
 -1
                                                    Time Now 15:30:12

 ***********************************************




                 The Units for this Run are as follows:-

 Temperature = K   Pressure = Atmospheres   Length = metres

 Area = sq metres  Mass Flow = kg/sec       Velocity = metres/sec

 Force = Newtons   s.f.c.(Thrust) =  mg/N sec   s.f.c.(Power) = mug/J

 Sp. Thrust =    N/kg/sec     Power =   Watts
1

      ***** DESIGN POINT ENGINE CALCULATIONS *****
```

```
 ***** AMBIENT AND INLET PARAMETERS *****
 Alt. =      0.0      I.S.A. Dev. =    0.000       Mach No. =  0.00
 Etar = 0.9951        Momentum Drag =      0.00

 ***** COMPRESSOR  1 PARAMETERS *****
 PRSF =  0.41221E+01     ETASF =  0.12801E+01     WASF =  0.10776E+02
 Z = 0.85000             PR =  14.600             ETA = 0.88500
 PCN =   0.6000          CN = 0.60000             COMWK =
0.19960E+09

 ***** COMBUSTION CHAMBER PARAMETERS *****
 ETASF =  0.99800E+00
 ETA = 0.99800           DLP = 1.0170             WFB =  10.6464

 ***** TURBINE  1 PARAMETERS *****
 CNSF =  0.16852E+03     ETASF =  0.10039E+01     TFSF =  0.29182E+00
 DHSF =  0.14727E+05
 TF =  430.924            ETA = 0.90000            CN =  2.750
 AUXWK =  0.16510E+09

 ***** CONVERGENT NOZZLE  1 PARAMETERS *****
 NCOSF =  0.10000E+01
 Area = 11.5315          Exit Velocity =  104.24  Gross Thrust =
54947.68
 Nozzle Coeff. =  0.97144E+00



 Scale Factor on above Mass Flows, Areas, Thrusts & Powers =
1.0000



 Station  F.A.R. Mass Flow   Pstatic    Ptotal Tstatic  Ttotal
Vel    Area
     1   0.00000   532.000   1.00000   1.00000  288.15  288.15
0.0  ******
     2   0.00000   532.000    ******   0.99510  ******  288.15
******  ******
     3   0.00000   532.000    ******  14.52847  ******  653.49
******  ******
     4   0.00000   510.720    ******  14.52847  ******  653.49
******  ******
     5   0.02085   521.366    ******  13.51148  ****** 1378.00
******  ******
     6   0.02001   542.646    ******  13.51148  ****** 1351.90
******  ******
     7   0.02001   542.646    ******   1.02467  ******  786.84
******  ******
     8   0.02001   542.646   1.00000   1.02467  782.03  786.84
104.2 11.5315
     9   0.00000    21.280    ******  14.52847  ******  653.49
******  ******


   Shaft Power = 165100000.00
    Net Thrust = 54947.68
```

```
  Equiv. Power = 168642864.00
     Fuel Flow =  10.6464
        S.F.C. =  64.4846
     E.S.F.C. =  63.1299
 Sp. Sh. Power =    310338.34
 Sp. Eq. Power =    316997.84
 Sh. Th. Effy. =   0.3596
           Time Now 15:30:12

 ********************************************
 317 0.93428     ! COMPRE 1 DETERIORATION OF 6.572% IN EFFICIENCY
 -1
 5 6 1100
 -1
                                                  Time Now 15:30:12

 ********************************************
 BERR( 1) =    0.00000E+00
 BERR( 2) =    0.12321E+00
 BERR( 3) =   -0.13606E+00
 BERR( 4) =   -0.76274E+00

 Loop   1
 BERR( 1) =    0.10177E-01
 BERR( 2) =    0.36852E-02
 BERR( 3) =    0.43909E-01
 BERR( 4) =    0.27124E-02

 Loop   2

 Loop   3
 BERR( 1) =   -0.21523E-02
 BERR( 2) =   -0.76190E-04
 BERR( 3) =    0.68275E-04
 BERR( 4) =   -0.60276E-03
1

      ***** OFF DESIGN ENGINE CALCULATIONS. Converged after   3 Loops
*****



 ***** AMBIENT AND INLET PARAMETERS *****
 Alt. =      0.0      I.S.A. Dev. =    0.000       Mach No. =  0.00
 Etar = 0.9951        Momentum Drag =      0.00

 ***** COMPRESSOR  1 PARAMETERS *****
 PRSF =  0.41221E+01     ETASF =  0.11960E+01     WASF =  0.10776E+02
 Z = 0.80634             PR =  13.888             ETA = 0.83297
 PCN =   0.5995          CN = 0.59952             COMWK =
0.20816E+09

 ***** COMBUSTION CHAMBER PARAMETERS *****
 ETASF =  0.99800E+00
 ETA = 0.99800           DLP = 1.1068             WFB =   6.1580

 ***** TURBINE  1 PARAMETERS *****
 CNSF =  0.16852E+03     ETASF =  0.10039E+01     TFSF =  0.29182E+00
 DHSF =  0.14727E+05
 TF =  409.909            ETA = 0.89689            CN =  3.069
 AUXWK =  0.74412E+08
```

```
 ***** CONVERGENT NOZZLE  1 PARAMETERS *****
 NCOSF =  0.10000E+01
 Area = 11.5315          Exit Velocity =   82.49  Gross Thrust =
43466.54
 Nozzle Coeff. =  0.97134E+00


 Scale Factor on above Mass Flows, Areas, Thrusts & Powers =
1.0000



 Station  F.A.R. Mass Flow   Pstatic    Ptotal Tstatic  Ttotal
Vel    Area
     1   0.00000   536.315   1.00000   1.00000  288.15  288.15
0.0  ******
     2   0.00000   536.315    ******   0.99510  ******  288.15
******  ******
     3   0.00000   536.315    ******  13.81952  ******  665.64
******  ******
     4   0.00000   514.863    ******  13.81952  ******  665.64
******  ******
     5   0.01196   521.021    ******  12.71273  ****** 1100.00
******  ******
     6   0.01148   542.473    ******  12.71273  ****** 1083.76
******  ******
     7   0.01148   542.473    ******   1.01896  ******  622.31
******  ******
     8   0.01148   542.473   1.00000   1.01896  619.08  622.31
82.5 11.5315
     9   0.00000    21.453    ******  13.81952  ******  665.64
******  ******


   Shaft Power =  74412048.00
    Net Thrust = 43466.54
  Equiv. Power =  77214640.00
     Fuel Flow =   6.1580
        S.F.C. =  82.7554
      E.S.F.C. =  79.7517
 Sp. Sh. Power =    138746.81
 Sp. Eq. Power =    143972.45
 Sh. Th. Effy. =   0.2802
           Time Now 15:30:12

 ********************************************
 -3
```

Experimental related performance deterioration by applying 102 microns particles (TET=1500 K).

```
TURBOMATCH SCHEME - Windows NT version (October 1999)

 LIMITS:100 Codewords, 800 Brick Data Items, 50 Station Vector
 15 BD Items printable by any call of:-
 OUTPUT, OUTPBD, OUTPSV, PLOTIT, PLOTBD or PLOTSV

  Input "Program" follows

 ! INDUSTRIAL GAS TURBINE:

 ABB GT13E2 POWER GENERATION

 50 Hz SIMPLE CYCLE

 MODELLED BY P.SCHWABE / SME / AUGUST 1997


 OD SI KE CT XP
  -1
  -1
 INTAKE S1-2        D1-4               R300
 ARITHY             D310-317
 ARITHY             D320-327
 COMPRE S2-3        D5-11              R301      V5   V6
 PREMAS S3,4,9      D12-15
 BURNER S4-5        D16-18             R303
 MIXEES S5,9,6
 TURBIN S6-7        D19-26,301,27                V19  V20
 NOZCON S7-8,1      D28                R305
 PERFOR S1,0,0      D19,29-31,305,300,303,0,0,0,0,0,0,0
 CODEND



 BRICK DATA ITEMS
 ! INTAKE
 1 0.0           ! ALTITUDE
 2 0.0           ! ISA DEVIATION:Tamb=288.15 K, Pamb=1.01325 bar
 3 0.0           ! MACH NUMBER
 4 0.9951        ! PRESSURE RECOVERY
 ! COMPRESSOR
 5 -1.0          ! SURGE MARGIN
 6 0.6           ! DESIGN SPEED
 7 14.6          ! DESIGN PRESSURE RATIO
 8 0.885         ! ISENTRIOPIC EFFICIENCY
 9 1.0           ! ERROR SELECTION
 10 3.0          ! COMPRESSOR MAP NUMBER
 11 0.0          ! RELATIV TO DP VARIABLE STATOR ANGLE
 ! SPLITTER
 12 0.96         ! LAMBDA (W)
 13 0.0          ! DELTA (W)
 14 1.0          ! LAMBDA (P)
 15 0.0          ! DELTA (P)
 ! BURNER
 16 0.07         ! PRESSURE LOSS 0%
 17 0.998        ! EFFICIENCY
 18 -1.0         ! FUEL FLOW (-1 = TET SPECIFIED. SEE SV DATA)
```

```
 ! POWER TURBINE
 19 165100000.0  ! AUXILLARY POWER REQUIRED
 20 0.8          ! NON DIMENTIONAL MASS FLOW
 21 0.6          ! NON DIMENTIONAL SPEED
 22 0.90         ! ISENTROPIC EFFICIENCY
 23 -1.0         ! RELATIV ROTATIONAL SPEED
 24 1.0          ! COMPRESSOR NUMBER
 25 3.0          ! TURBINE MAP NUMBER
 26 1000.0       ! POWER INDEX N
 27 0.0          ! ANGLE
 ! NOZCON
 28 -1.0         ! AREA FIXED
 ! PERFORMANCE
 29 1.0          ! PROPELLER EFFICIENCY
 30 0.0          ! SCALLING INDEX
 31 0.0          ! REQUIRED DP NET THRUST OR POWER OUTPUT FOR PT

 310 3.0         ! COMPRESSOR 1, BD(820)=BD(820)*BD(317)
 311 -1.0
 312 820.0       ! ETASF FOR COMPRESSOR 1
 313 -1.0
 314 820.0
 315 -1.0
 316 317.0
 317 1.0         ! COMPRESSOR 1 DETERIORATION OF 0% IN EFFICIENCY

 320 3.0         ! COMPRESSOR 1, BD(830)=BD(830)*BD(327)
 321 -1.0
 322 830.0       ! WASF FOR COMPRESSOR 1
 323 -1.0
 324 830.0
 325 -1.0
 326 327.0
 327 1.0         ! COMPRESSOR 1 DETERIORATION OF 0% IN NON-
DIMENSIONAL MASS FLOW
 -1
 1 2 532.00      ! MASS FLOW
 5 6 1378.0      ! TURBINE ENTRY TEMPERATURE
 -1
                                                    Time Now 15:40:12

 ********************************************




                 The Units for this Run are as follows:-

 Temperature = K   Pressure = Atmospheres   Length = metres

 Area = sq metres  Mass Flow = kg/sec       Velocity = metres/sec

 Force = Newtons   s.f.c.(Thrust) =  mg/N sec   s.f.c.(Power) = mug/J

 Sp. Thrust =    N/kg/sec     Power =   Watts
1

      ***** DESIGN POINT ENGINE CALCULATIONS *****
```

```
 ***** AMBIENT AND INLET PARAMETERS *****
 Alt. =      0.0      I.S.A. Dev. =    0.000       Mach No. =  0.00
 Etar = 0.9951        Momentum Drag =      0.00

 ***** COMPRESSOR  1 PARAMETERS *****
 PRSF =  0.41221E+01     ETASF =  0.12801E+01     WASF =  0.10776E+02
 Z = 0.85000             PR =  14.600             ETA = 0.88500
 PCN =   0.6000          CN = 0.60000             COMWK =
0.19960E+09

 ***** COMBUSTION CHAMBER PARAMETERS *****
 ETASF =  0.99800E+00
 ETA = 0.99800           DLP = 1.0170             WFB =  10.6464

 ***** TURBINE  1 PARAMETERS *****
 CNSF =  0.16852E+03     ETASF =  0.10039E+01     TFSF =  0.29182E+00
 DHSF =  0.14727E+05
 TF =  430.924            ETA = 0.90000            CN =  2.750
 AUXWK =  0.16510E+09

 ***** CONVERGENT NOZZLE  1 PARAMETERS *****
 NCOSF =  0.10000E+01
 Area = 11.5315          Exit Velocity =  104.24  Gross Thrust =
54947.68
 Nozzle Coeff. =  0.97144E+00



 Scale Factor on above Mass Flows, Areas, Thrusts & Powers =
1.0000



 Station  F.A.R. Mass Flow   Pstatic    Ptotal Tstatic  Ttotal
Vel    Area
     1   0.00000   532.000   1.00000   1.00000  288.15  288.15
0.0  ******
     2   0.00000   532.000    ******   0.99510  ******  288.15
******  ******
     3   0.00000   532.000    ******  14.52847  ******  653.49
******  ******
     4   0.00000   510.720    ******  14.52847  ******  653.49
******  ******
     5   0.02085   521.366    ******  13.51148  ****** 1378.00
******  ******
     6   0.02001   542.646    ******  13.51148  ****** 1351.90
******  ******
     7   0.02001   542.646    ******   1.02467  ******  786.84
******  ******
     8   0.02001   542.646   1.00000   1.02467  782.03  786.84
104.2 11.5315
     9   0.00000    21.280    ******  14.52847  ******  653.49
******  ******


   Shaft Power = 165100000.00
    Net Thrust = 54947.68
```

```
  Equiv. Power = 168642864.00
     Fuel Flow =  10.6464
        S.F.C. =  64.4846
     E.S.F.C. =  63.1299
 Sp. Sh. Power =    310338.34
 Sp. Eq. Power =    316997.84
 Sh. Th. Effy. =   0.3596
           Time Now 15:40:12

 ********************************************
 317 0.93428     ! COMPRE 1 DETERIORATION OF 6.572% IN EFFICIENCY
 -1
 5 6 1500
 -1
                                                  Time Now 15:40:12

 ********************************************
 BERR( 1) =    0.00000E+00
 BERR( 2) =   -0.46939E-01
 BERR( 3) =    0.83802E-02
 BERR( 4) =    0.19650E+00

 Loop   1
 BERR( 1) =   -0.42225E-02
 BERR( 2) =    0.62948E-03
 BERR( 3) =    0.53498E-01
 BERR( 4) =   -0.87072E-01

 Loop   2

 Loop   3
 BERR( 1) =   -0.12678E-02
 BERR( 2) =   -0.71281E-04
 BERR( 3) =    0.80382E-03
 BERR( 4) =    0.46522E-02
1

      ***** OFF DESIGN ENGINE CALCULATIONS. Converged after   3 Loops
*****



 ***** AMBIENT AND INLET PARAMETERS *****
 Alt. =      0.0      I.S.A. Dev. =    0.000       Mach No. =  0.00
 Etar = 0.9951        Momentum Drag =      0.00

 ***** COMPRESSOR  1 PARAMETERS *****
 PRSF =  0.41221E+01     ETASF =  0.11960E+01     WASF =  0.10776E+02
 Z = 0.87674             PR =  15.030             ETA = 0.82243
 PCN =   0.6001          CN = 0.60006             COMWK =
0.21691E+09

 ***** COMBUSTION CHAMBER PARAMETERS *****
 ETASF =  0.99800E+00
 ETA = 0.99800           DLP = 1.0259             WFB =  12.1584

 ***** TURBINE  1 PARAMETERS *****
 CNSF =  0.16852E+03     ETASF =  0.10039E+01     TFSF =  0.29182E+00
 DHSF =  0.14727E+05
 TF =  434.834            ETA = 0.89541            CN =  2.637
 AUXWK =  0.18153E+09
```

```
 ***** CONVERGENT NOZZLE  1 PARAMETERS *****
 NCOSF =  0.10000E+01
 Area = 11.5315          Exit Velocity =  114.11  Gross Thrust =
60003.85
 Nozzle Coeff. =  0.97157E+00


 Scale Factor on above Mass Flows, Areas, Thrusts & Powers =
1.0000



 Station  F.A.R. Mass Flow   Pstatic    Ptotal Tstatic  Ttotal
Vel    Area
     1   0.00000   529.092   1.00000   1.00000  288.15  288.15
0.0  ******
     2   0.00000   529.092    ******   0.99510  ******  288.15
******  ******
     3   0.00000   529.092    ******  14.95606  ******  686.07
******  ******
     4   0.00000   507.929    ******  14.95606  ******  686.07
******  ******
     5   0.02394   520.087    ******  13.93019  ****** 1500.00
******  ******
     6   0.02298   541.251    ******  13.93019  ****** 1470.95
******  ******
     7   0.02298   541.251    ******   1.03205  ******  864.06
******  ******
     8   0.02298   541.251   1.00000   1.03205  858.28  864.06
114.1 11.5315
     9   0.00000    21.164    ******  14.95606  ******  686.07
******  ******


   Shaft Power = 181529392.00
    Net Thrust = 60003.85
  Equiv. Power = 185398256.00
     Fuel Flow =  12.1584
        S.F.C. =  66.9775
      E.S.F.C. =  65.5798
 Sp. Sh. Power =    343095.91
 Sp. Eq. Power =    350408.16
 Sh. Th. Effy. =   0.3462
           Time Now 15:40:12

 ********************************************
 -3
```